UNIVERSITY OF SOUTHAMPTON

FACULTY OF ENGINEERING, SCIENCES AND MATHEMATICS

School of Engineering Sciences

Aerodynamics and Flight Mechanics Research Group

Unsteadiness in shock-wave/boundary-layer interactions

by

Emile Touber

Thesis for the degree of Doctor of Philosophy

May 2010

UNIVERSITY OF SOUTHAMPTON

ABSTRACT

FACULTY OF ENGINEERING, SCIENCES AND MATHEMATICS
SCHOOL OF ENGINEERING SCIENCES

Doctor of Philosophy

UNSTEADINESS IN SHOCK-WAVE/BOUNDARY-LAYER INTERACTIONS

by Emile Touber

The need for better understanding of the low-frequency unsteadiness observed in shock wave/turbulent boundary layer interactions has been driving research in this area for several decades. This work investigates the interaction between an impinging oblique shock and a supersonic turbulent boundary layer via large-eddy simulations. Special care is taken at the inlet in order to avoid introducing artificial low-frequency modes that could affect the interaction. All simulations cover extensive integration times to allow for a spectral analysis at the low frequencies of interest. The simulations bring clear evidence of the existence of broadband and energetically-significant low-frequency oscillations in the vicinity of the reflected shock, thus confirming earlier experimental findings. Furthermore, these oscillations are found to persist even if the upstream boundary layer is deprived of long coherent structures.

Starting from an exact form of the momentum integral equation and guided by data from large-eddy simulations, a stochastic ordinary differential equation for the reflected-shock foot low-frequency motions is derived. This model is applied to a wide range of input parameters. It is found that while the mean boundary-layer properties are important in controlling the interaction size, they do not contribute significantly to the dynamics. Moreover, the frequency of the most energetic fluctuations is shown to be a robust feature, in agreement with earlier experimental observations. Under some assumptions, the coupling between the shock and the boundary layer is mathematically equivalent to a first-order low-pass filter. Therefore, it is argued that the observed low-frequency unsteadiness is not necessarily a property of the forcing, either from upstream or downstream of the shock, but simply an intrinsic property of the coupled dynamical system.

Contents

List of Figures

List of Tables

Declaration of Authorship

I, Emile Touber, declare that the thesis entitled "Unsteadiness in shock-wave/boundary-layer interactions" and the work presented in the thesis are both my own, and have been generated by me as the result of my own original research. I confirm that:

- this work was done wholly or mainly while in candidature for a research degree at this University;
- where any part of this thesis has previously been submitted for a degree or any other qualification at this University or any other institution, this has been clearly stated;
- where I have consulted the published work of others, this is always clearly attributed;
- where I have quoted from the work of others, the source is always given. With the exception of such quotations, this thesis is entirely my own work;
- I have acknowledged all main sources of help;
- where the thesis is based on work done by myself jointly with others, I have made clear exactly what was done by others and what I have contributed myself;
- parts of this work have been published as: Touber and Sandham (2008a,b, 2009a,b,c,d)

Signed: _____

Date: _____

Acknowledgements

The author would like to acknowledge the UK Turbulence Consortium EP/D044073/1 for the computational time provided on both the HPCx and HECToR facilities, the UKs national highperformance computing service, which is provided by EPCC at the University of Edinburgh and by CCLRC Daresbury Laboratory, and funded by the Office of Science and Technology through EPSRCs High End Computing Program. I am also grateful to the University of Southampton for the access to its high-performance computer, Iridis2. In addition, I would like to acknowledge the financial support of the European Union through the Sixth Framework Program with the UFAST project. Finally, I am grateful to the UFAST-project partners for kindly making their data available and to both Prof. N. D. Sandham and Dr. G. N. Coleman for their guidance.

Abbreviations

BL	**B**oundary **L**ayer
CTA	**C**onstant **T**emperature **A**nemometry
DF	**D**igital **F**ilter
DNS	**D**irect **N**umerical **S**imulation
DS	**D**ynamic **S**magorinsky eddy viscosity model
FTT	**F**low **T**hrough **T**ime
HWA	**H**ot **W**ire **A**nemometry
ITAM	**I**nstitute of **T**heoretical and **A**pplied **M**echanics
IUSTI	**I**nstitut **U**niversitaire des **S**ystèmes **T**hermiques **I**ndustriels
LES	**L**arge-**E**ddy **S**imulation
LHS	**L**eft-**H**and **S**ide
MIE	**M**omentum **I**ntegral **E**quation
MTS	**M**ixed-**T**ime-**S**cale eddy viscosity model
ODE	**O**rdinary **D**ifferential **E**quation
PDF	**P**robability **D**ensity **F**unction (sometimes written pdf)
PIV	**P**article **I**mage **V**elocimetry
PSD	**P**ower **S**pectral **D**ensity
RANS	**R**eynolds-**A**veraged **N**avier–**S**tokes
RDT	**R**apid **D**istortion **T**heory
RHS	**R**ight-**H**and **S**ide

RMS	**R**oot **M**ean **S**quare
SBLI	**S**hock-Wave/**B**oundary-**L**ayer **I**nteraction
SGS	**S**ub**G**rid **S**cale
SOTON	University of **SO**uthamp**TON**
SRA	**S**trong **R**eynolds **A**nalogy
ST	**S**ynthetic **T**urbulence
TBL	**T**urbulent **B**oundary **L**ayer
TUD	**D**elft **U**niversity of **T**echnology
TVD	**T**otal **V**ariation **D**iminishing
UAN	A.N. Podgorny Institute for Mechanical Engineering
UFAST	EU project, see: `http://www.ufast.gda.pl/`
URANS	**U**unsteady **R**eynolds-**A**veraged **N**avier–**S**tokes
VD	**v**an **D**riest
2D, **3D**	two (three) **D**imensional

Symbols

A	parameter in section 7.3
$\mathcal{A}_{\varepsilon_0,\Delta\sigma}$	set of instants, see (6.2a)
A_0	parameter, $q\,[L/(\bar{u}_1\phi)]^2$
B	parameter in section 7.3
C	Sutherland's law constant, $S/\bar{T}_1$, or a parameter in section 7.3 (see context)
C_f	skin friction, $2\tau_w/(\bar{\rho}_1\bar{u}_1^2)$
C_{f_0}	skin friction at reflected-shock foot
C_M	MTS model constant, 0.03
C_T	MTS model constant, 10
c	speed of sound
D	parameter in section 7.3
$\mathcal{D}$	compact subset of the $\mathbb{R}^3$ space
E_t	total energy
$\breve{E}_t$	resolved total energy
F	similarity thickness function, $[\delta_i(\xi) - \delta_i(\xi = 0)]/\Delta_i$, see (7.10)
F'	derivative of F, $\mathrm{d}F/\mathrm{d}\xi$
f	frequency
f_c	cutoff frequency
G, G^*	convolution kernels
H	reflected-shock mean and instantaneous shock-crossing point height, see figure 7.6

h	time-averaged zero streamwise velocity contour height or instantaneous shock-crossing height (see context)
h_0	time-averaged shock-crossing height (see figure 7.1)
K	streamwise distance between the time-averaged reflected-shock foot and the reflected-shock mean and instantaneous shock-crossing point, see figure 7.6
k	linear-dependence coefficient of s on ε, s/ε
k_{es}	SGS kinetic energy in the MTS model
k_x	stream-wise wavenumber
k_{ξ_r}	wavenumber in the reflected-shock direction
L	interaction length, $\bar{x}_0 - \bar{x}_{\text{imp}}$
L_x, L_y, L_z	streamwise, wall-normal and spanwise domain length
L_{sep}	separation length, $\bar{x}_{\text{at}} - \bar{x}_{\text{sep}}$
l_0	streamwise distance between the mean shock-foot and shock-crossing positions (see figure 7.1)
M	Mach number (flow-velocity to speed-of-sound ratio)
$\mathcal{M}$	momentum-thickness integrand, $\rho u[1 - u/\bar{u}_1]/[\bar{\rho}_1\bar{u}_1]$
$\dot{m}$	reversed mass flow rate per unit width, see (6.1)
N	number of periods covered by a sine wave at $f = 0.035\bar{u}_1/L$
N_x, N_y, N_z	streamwise, wall-normal and spanwise number of grid points
$\mathcal{N}$	measure of the set $\mathcal{A}_{\varepsilon_0,\Delta\sigma}$, see (6.2b)
Pr	Prandtl number (viscous to thermal diffusion rates ratio), 0.72
Pr_t	turbulent Prandtl number, 1.0
P_0	stagnation pressure
P_2	ratio $p_2^+/\bar{p}_1$
P_3	ratio $\bar{p}_3/\bar{p}_1$
p	pressure
q	proportionality coefficient in (7.54b), or variance of C''_{f_0} in (7.60)
$\mathbf{q}$	conservative-variable vector, $[\rho, \rho u, \rho v, \rho w, \rho E_t]^{\mathbf{T}}$
R	parameter in (7.45)
R_a	auto-correlation function, $R_a(\tau) = \overline{a'(t_0)a'(t_0+\tau)}/\overline{a'(t_0)a'(t_0)}$
Re	Reynolds number (inertial to viscous forces ratio)

$\mathrm{Re}_{\breve{\delta}_1}$	Reynolds number based on the code reference length, $\bar{\rho}_1 \bar{u}_1 \breve{\delta}_1 / \bar{\mu}_1$
Re_{δ_1}	Reynolds number based on the displacement thickness, $\bar{\rho}_1 \bar{u}_1 \delta_1 / \bar{\mu}_1$
Re_{δ_2}	Reynolds number based on the momentum thickness, $\bar{\rho}_1 \bar{u}_1 \delta_2 / \bar{\mu}_1$
Re_τ	Reynolds number based on the friction velocity, $\bar{\rho}_1 u_\tau \delta_0 / \bar{\mu}_1$
R_3	ratio $\bar{\rho}_3 / \bar{\rho}_1$
r, r', r''	model coefficients, see section 7.3
r_0	timescale ratio, t_f / t_s
S	Sutherland's temperature, 110.4 K
$\mathcal{S}$	power-spectral-density function
S_{ij}	strain-rate tensor, $(\partial u_i / \partial x_j + \partial u_j / \partial x_i)/2$
S^*_{ij}	deviatoric part of the strain-rate tensor
$\mathcal{S}_p$	wall-pressure power-spectral-density function
S_t	Strouhal number, $f L_{\mathrm{sep}} / \bar{u}_1$ or $f L / \bar{u}_1$ (see context)
s	mean to instantaneous shock-crossing points streamwise distance
T	total temperature, or a time interval (see context)
T_{aw}	adiabatic wall temperature
T_c	temperature computed using the Crocco-Busemann relation
T_S	MTS-model timescale
T_{sim}	simulation runtime
$\bar{T}_1$	freestream total temperature upstream of the interaction
T_0	stagnation temperature
t	time
$t^\star$	normalised time, $t \bar{u}_1 / L$
t_f	timescale associated with upstream turbulence structures, $\delta_0 / \bar{u}_1$
t_s	timescale associated with the low-frequency shock motions
t_0	a chosen startup time
U^+_{vd}	mean van Driest velocity profile in friction-velocity units
u, v, w	stream-wise, wall-normal and span-wise velocity
u_c	convection velocity (see context for details)
$\bar{u}_1$	freestream velocity upstream of the interaction
u_τ	friction velocity, $\sqrt{(\mu_w / \rho_w)[\partial u / \partial y]_w}$
x, y, z	stream-wise, wall-normal and span-wise direction
$\bar{x}_{\mathrm{at}}$	mean boundary-layer-reattachment location
$\bar{x}_{\mathrm{imp}}$	mean location of the extension of the impinging shock to the wall
$\bar{x}_{\mathrm{sep}}$	mean boundary-layer-separation location

$\bar{x}_0$	mean location of the extension of the reflected shock to the wall

Greek

α	time-averaged reflected-shock angle (see figure 7.1)
β	incident-shock angle or span-wise wave-number, $2\pi/\lambda_z$ (see context)
β_y	grid-stretching parameter in the wall-normal direction
Γ	Langevin force in (7.54a)
γ	specific-heat ratio, 1.4
Δ_i	thickness amplitude function, $\delta_i(\xi = 1) - \delta_i(\xi = 0)$, see (7.10)
Δt	time step
Δx, Δy, Δz	local grid spacing (stream-wise, wall-normal and span-wise direction)
$\overline{\Delta}$, $\widehat{\Delta}$, $\widehat{\overline{\Delta}}$	filter cutoff lengthscale
δ	Dirac function
δ_0	boundary-layer 99% thickness
δ_0^{imp}	boundary-layer thickness at the incident-shock impingement location in the absence of the shock
δ_1	displacement thickness, $\int_0^h [1 - \rho u/(\bar{\rho}_1 \bar{u}_1)]\,\mathrm{d}y$, $h > \delta_0$
δ_1^{imp}	boundary-layer displacement thickness at the incident-shock impingement location in the absence of the shock
$\check{\delta}_1$	inlet boundary-layer displacement thickness based on the van Driest velocity profile using the incompressible definition
δ_2	momentum thickness, $\int_0^h [\rho u/(\bar{\rho}_1 \bar{u}_1)]\,(1 - u/\bar{u}_1)\,\mathrm{d}y$, $h > \delta_0$
δ_p	pressure thickness, $\int_0^h [1 - p/p_h]\,\mathrm{d}y$, $h > \delta_0$
δ_ρ	density thickness, $\int_0^h [1 - \rho/\rho_h]\,\mathrm{d}y$, $h > \delta_0$
ε	reflected-shock foot displacement with respect to its mean position
$\dot{\varepsilon}$	reflected-shock foot velocity, $\mathrm{d}\varepsilon/\mathrm{d}t$
ζ	normalised reflected-shock foot displacement, ε/L
$\dot{\zeta}$	speed of the normalised reflected-shock foot displacement, $\mathrm{d}\zeta/\mathrm{d}t^\star$
η	vertical displacement of the shock-crossing point, $h - h_0$ (see figure 7.1)
η_r	reflected-shock displacement with respect to its mean position
Θ_i	mean thickness amplitude, $\overline{\Delta_i}$

θ	wedge angle
ϑ	velocity component in the reflected-shock normal direction
ι	instantaneous reflected-shock angle (see figure 7.6)
κ_i	linear-dependence coefficient of Δ_i on η, $[\Delta_i - \Theta_i]/\eta$
κ	von Karman constant (assumed to be 0.41)
$\varkappa$	$(\tan\alpha + \tan\beta)\sin(2\alpha)\sin[2(\alpha+\theta)] \,/\, (\tan\beta\,(1 - 1/\tan\alpha) - 1)$
Λ	linear-dependence coefficient of $\tilde{C}_{f_0}$ on ζ, $\tilde{C}_{f_0}/\zeta$
λ	length of a superstructure
λ_z	span-wise wavelength
μ	dynamic viscosity
$\bar{\mu}_1$	freestream dynamic viscosity upstream of the interaction
ν	kinetic viscosity, μ/ρ
ν_t	eddy viscosity
ξ	moving coordinate system, $(x + l_0 - \varepsilon)/(l_0 - \varepsilon + s)$
$\bar{\xi}$	normalised streamwise axis, $(x - \bar{x}_0)/L$
ξ_r	longitudinal position along the reflected shock
ξ'	normalised streamwise axis, $(x - \bar{x}_{\text{sep}})/L_{\text{sep}}$
Π	parameter, $\tan\beta/[2F'(0)\,(\tan\alpha + \tan\beta)]$
π	ratio of the circumference of a circle to its diameter $(3.141592\ldots)$
ϖ	velocity component along the reflected-shock direction
ρ	fluid density
$\bar{\rho}_1$	freestream density upstream of the interaction
σ	standard deviation of a signal
σ_{ij}	subgrid-scale stress tensor
ς	component of the sound speed along the reflected-shock direction
τ	correlation time
τ_c	characteristic correlation time
τ_{ij}	viscous shear stress
τ_s	system characteristic time scale, $1/\Phi$

τ_w	time-averaged wall shear-stress, $\mu_w[\partial u/\partial y]_w$
$\breve{\tau}$	resolved viscous shear stress
υ	steady term in (7.24)
Φ	ODE damping coefficient, $\bar{u}_1\phi/L$
ϕ	normalised ODE damping coefficient, see (7.26b) and (7.53b)
$\phi_{\max}$	ODE cutoff Strouhal number, $\phi/(2\pi)$
φ_p	disturbance phase angle with respect to a predefined reference
χ	parameter, $[2\gamma + \gamma\,(\gamma - 1)\,\mathrm{M}_1^2]/[\gamma + 1]$
Ψ_i	SGS heat flux
ψ	forcing in (7.26c)
Ω	power-law exponent, 0.67
ω_i	disturbance growth rate

Subscripts

$1, 2, 3$	the quantity is evaluated in the potential-flow region: 1 = upstream, 2 = after the incident shock but before the reflected shock, 3 = after interaction (not to confuse with vector indices, see context)
e	the quantity is evaluated at the boundary-layer edge
i, j, k	vector index: 1 = stream-wise, 2 = wall-normal and 3 = span-wise direction
max	quantity maximum-value
min	quantity minimum-value
w	the quantity is evaluated at the wall

Superscripts

$*$	denotes the deviatoric part of the tensor it is applied to
$\star$	denotes that the dimensional variable is used
$+$	denotes that the variable is expressed in wall-units, $y^+ = yu_\tau/\nu_w$ and $u^+ = u/u_\tau$, or denotes the top side of region 2 in chapter 7 (see figure 7.1)
$-$	denotes the bottom side of region 2 (see figure 7.1)

Operators

$\bar{a}$	time-averaged or grid-filtered variable (see context)
$\tilde{a}$	Favre-filtered variable, $\overline{\rho a}/\bar{\rho}$ (not to confuse with the triple decomposition, see context)
a', a'', $\tilde{a}$	triple decomposition, see (6.4a)
$\hat{a}$	test-filtered variable
$\widehat{\tilde{a}}$	result from test-filtering the Favre-filtered variable
$\widehat{\bar{a}}$	result from test-filtering the grid-filtered variable
$\langle a \rangle_\alpha$	α-averaged value of a
$\langle \cdot \rangle_{\varepsilon_0, \Delta\sigma}$	conditional-average operator, see (6.2c)
$\breve{a}$	van-Driest transformed field, $\int_{a(y=0)}^{a(y)} \sqrt{\rho/\rho_w}\, \mathrm{d}a'$
$\mathrm{Im}(a)$	imaginary part of a complex number a

1. Introduction

1.1 Motivation

On January 26, 1971, Concorde 001 was accomplishing its flight-test number 122 when it experienced "the most damaging incident of its development time" (Turcat, 2003). While cruising at Mach 2 over the Atlantic, upon switching off the reheat system, the third-engine-variable-inlet ramp (which can be seen in figure 1.1) was blown out due to "violent pressure fluctuations for about seven seconds"[1]. What Captain Defer and his crew experienced is known as inlet buzz. It is a low-frequency, high-amplitude pressure oscillation that is linked to shock-wave/boundary-layer and/or shock-wave/shock-wave interactions, affecting the engine intakes. It can seriously impair the integrity of the aeroplane, as demonstrated by Concorde 001.

According to Dolling (2001), the high-speed wind tunnel experiments on airfoils by Ferri (1940) are probably the first published observations of a shock-wave/boundary-layer interaction (SBLI). Although limited to a supersonic pocket embedded in a subsonic flow, additional experiments by Donaldson (1944), Liepmann (1946), Fage and Sargent (1947), Ackeret et al. (1947) quickly followed, demonstrating a sensitivity of such interactions to the state of the incoming boundary layer. However, given the peculiarity of the configuration (i.e. small supersonic pocket embedded in a subsonic flow with streamwise pressure gradients and surface curvature), these investigations may not have been sufficiently systematic to be conclusive.

In the late 1940's and early 1950's, further experiments were introduced to study the aforementioned interaction. This time, the experiments were run at fully supersonic speeds. The geometries used at that time consisted of an external shock generator, flat plate/flat ramp configurations or flat plates with steps, and axisymmetric bodies with flares/collars. Interestingly, these geometries are no different than the ones studied nowadays. These studies yielded a large data base of SBLI at various Reynolds numbers, Mach numbers and shock strengths, confirming the earlier observations of the importance of SBLI and their sensitivity to the state of the incoming boundary layer. Much of that work is summarised in Holder et al. (1954). However, unlike inviscid interactions between shocks and bodies, which have already been studied for more that two centuries

[1] Comments by the flight observer, Claude Durand.

FIGURE 1.1: Concorde G-BOAE on final at LHR airport (October 10, 2003). Photograph by Harm Rutten (`www.airliners.net`)

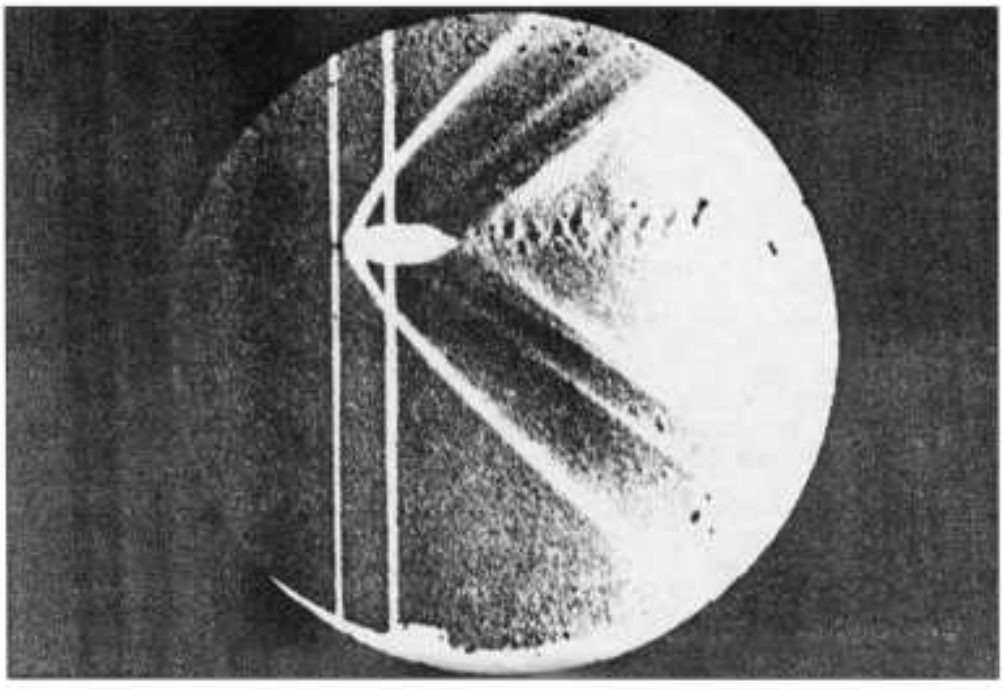

FIGURE 1.2: Photograph of a bullet in supersonic flight, published by Ernst Mach in 1887.

(see figure 1.2 and Anderson, 1990), no theory about viscous interaction is readily available, particularly in the case of turbulent interactions. Thus, not equipped with such theories, researchers have run many experiments, driven by the fact that most (if not all) of the supersonic flows involve, in one way or another, a (turbulent) SBLI.

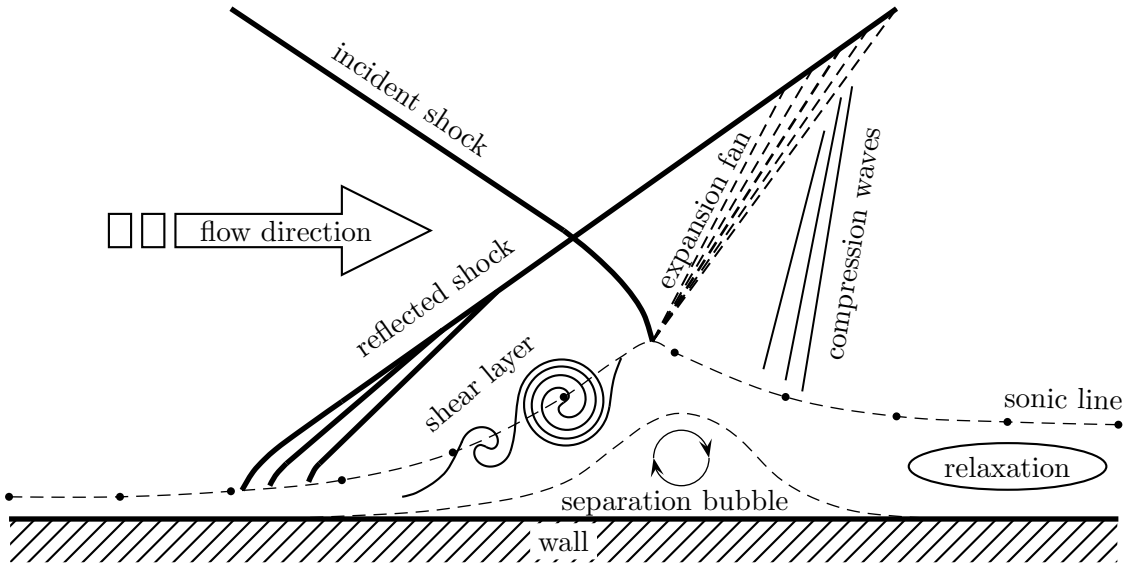

FIGURE 1.3: Sketch of the oblique shock / boundary-layer interaction

The broad aim of the present thesis is to use the technique of large-eddy simulation to shed light on the interaction between a turbulent boundary layer and an impinging oblique shock in order to identify the flow physics and develop modelling approaches for the observed low-frequency shock motions.

1.2 Introduction to the SBLI issue

Over the last 60 years, most of the research on two-dimensional SBLI has focused on three types of interaction: the case of an incident oblique shock wave impinging a flat-plate boundary layer (in this case, the initial shock is formed from an external device, like a wedge), the case of a normal shock interacting with a flat-plate boundary layer (similar to the previous case but fundamentally different since this interaction necessarily involves a large area of subsonic flow) and the case of a compression ramp or corner (in this case, the "reflected" shock is induced by the flow-deviation due to the ramp) — see Adamson and Messiter (1980) for a detailed review of all those cases. The compression-ramp case is by far the most studied occurrence of SBLI (Settles and Dodson, 1991). However, the present work is devoted to the oblique-shock reflection case, which is described below.

Figure 1.3 is a sketch of the shock-induced separation. If the pressure jump across the incident shock is sufficiently large, the associated adverse pressure gradient can lead to the separation of the incoming boundary layer which on average forms a separation bubble. At the leading edge of the separation bubble, the flow is deflected away from the wall, generating compression waves which eventually form the reflected shock, well upstream of where it would have been located for inviscid flow (Pirozzoli and Grasso,

2006). As the flow moves around the top of the bubble, an expansion fan is produced, quickly followed by compression waves near reattachment. Downstream of the interaction, the boundary layer is subject to a relaxation zone (Dupont et al., 2006), where it gradually goes back to the state of equilibrium. The recirculation bubble gives rise to a detached shear layer that is the focus of some more recent publications (Pirozzoli and Grasso, 2006; Dupont et al., 2007; Piponniau et al., 2009).

The aforementioned broad picture has been known for some time (Adamson and Messiter, 1980). As mentioned earlier, Ferri (1940) probably made the first observations of SBLI. Most of the early work on SBLI was experimental (Dolling, 2001). In the 1950's, the research focus was on mean wall-pressure and heating-rate measurements. From today's perspective, those measurements overlooked some of the key physics. However, the presence of a separation bubble was already identified and gave birth to the so-called "free-interaction theory", the basic ideas of which were first formulated by Lighthill (1953). At that time, the first scaling law for the wall-pressure evolution in the interaction zone was proposed and the question of the universal character of such interactions was raised. Chapman et al. (1958) noted that "certain characteristics of separated flows did not depend on the object shape or on the mode of inducing separation" and that such flow characteristics "are termed free interactions". The theory of the separation of a supersonic laminar boundary layer through the free interaction was first published by Stewartson and Williams (1969), who used triple-deck theory to derive the theoretical change in wall pressure. As noted by Adamson and Messiter (1980), Stewartson and Williams's final problem formulation contains no parameters and the solution is a universal solution. Later, Katzer (1989) confirmed through numerical simulation the local scaling laws of the free interaction in the vicinity of the separation point. Katzer distinguishes two mechanisms: a global mechanism that determines the separation-bubble length L_{sep} and a local mechanism that controls the free-interaction region, in the vicinity of the separation point. The former is found to depend linearly on the shock strength, defined as the ratio between the downstream freestream pressure p_3 and the upstream freestream pressure p_1, whereas the influences of the Mach number M and Reynolds number Re (based on the distance from the plate leading edge) on L_{sep} are given by the powers M^{-3} and $\mathrm{Re}^{1/2}$ for the range of values tested by Katzer (1989). The linear influence of the shock strength is somewhat different from the asymptotic theory (Neiland, 1971; Stewartson and Williams, 1973) where a power-law behaviour $(p_3/p_1)^{3/2}$ is found. This could be due to a finite versus infinite Reynolds-number effect. In contrast the free-interaction region is independent of the shock strength. The pressure at the separation point and the pressure plateau (note that we are considering laminar boundary layers here) are governed by the wall-shear stress at the beginning of the interaction region and the Mach number at the edge of the boundary layer, thus confirming the local scaling laws of the free interaction. Unfortunately, the asymptotic theory of the

triple deck could only be confirmed for the pressure scaling by Katzer whereas the length scales could not be verified for finite Reynolds numbers: at finite Reynolds numbers, the triple-deck theory tends to overestimate the length scale substantially, a discrepancy which increases with increasing Mach numbers (Katzer, 1989). More recently, Pagella et al. (2004) numerically investigated the cases of a 2D compression corner and 2D impinging shock at Mach 4.8 where they matched the bubble lengths. They find that the base flow properties were identical, in accordance with the free-interaction theory. They note that the physics of such flows are not determined by the type of SBLI but rather by the flow-field properties at the onset of the interaction. However, the authors report that when they considered the same comparison in 3D, the two flows were found to be different. Dolling (2001) notes that although the free-interaction theory appears successful at predicting the correct pressure scaling, the physics implicit in the theory are not what actually occurs.

In the 1950's, SBLI were described as relatively steady (Dolling, 2001). Today, this is known to be incorrect. In fact, some degree of unsteadiness could be seen in the early Schlieren pictures, but researchers had no means to study it until the mid 1960's, when the very first high-frequency pressure transducers became available. Kistler (1964) reports investigations on the unsteady aspect of shock-induced turbulent separation upstream of a forward-facing step and finds that such flows are characterised by relatively low frequencies (compared to $\bar{u}_1/\delta_0$). Up until the early 1990's, almost only surface measurements have been performed since intrusive techniques interfere with the flow. Nevertheless, those measurements clearly showed the existence of a low-frequency component in SBLI, but its cause still remains unanswered (Dolling, 2001). Unfortunately, the existence of low frequencies is a major issue in most (if not all) applications involving supersonic or hypersonic flows. As noted by Dolling (2001), the maximum mean and fluctuating pressure levels and the thermal loads that a structure is exposed to are found in regions of SBLI. The low-frequency unsteadiness of the reflected shock affects the structural integrity as it is a main source of fatigue which in turn becomes a major constraint in the choice of materials. Dolling (2001) writes: "the fluctuating pressure loads generated by translating shock waves, pulsating separated flows and expansions/ contractions of the global flow field can be severe enough to cause structural damage and cannot be ignored by designers of supersonic and hypersonic vehicles". That issue has thus been the major driver of SBLI research over the last decades. In the previous section, we mentioned the "buzz effect" in engine intakes, which is reported several times by the French test pilot, André Turcat, in his book about the design of Concorde (Turcat, 2003) as it was a major concern and the cause of important delays.

One of the fundamental questions about SBLI unsteadiness is to know whether or not the emergence of the low-frequency oscillations is independent of the type of interaction, like the pressure rise in the free-interaction theory for laminar interactions. Dussauge

et al. (2006) note that "the free-interaction theory and the experimental work showed that in such interactions the initial rise of mean pressure does not depend on the way it has been produced" but that "the initial rise reflects the intermittent motion of the initial shock". Based on this remark, the authors argue that "it may be hoped that this intermittent motion has rather general properties". They then collect available SBLI data for a wide range of Mach numbers and geometries and find that some aspects of the data tend to support this argument. For example, Dupont et al. (2006) find that, if scaled by the size of the interaction zone and the external velocity, the Strouhal number related to the shock unsteadiness is similar for a wide range of geometries. However, looking at figure 2 in Dussauge et al. (2006), one can argue that there exists a scattering of the data which is acknowledged by the authors themselves.

The need for a deeper physical understanding of the driving mechanisms of SBLI is not in doubt. Knight and Degrez (1998) looked at numerical prediction capabilities and find that although "accurate prediction of both aerodynamic and thermal loads" is achieved in the case of laminar interactions, turbulent interaction predictions are only "correct in the mean-pressure distribution" and that "skin friction and heat transfer distributions could differ by 100% for strong interactions". The success in the pressure distribution predictions may be related to the relative success of the free-interaction theory. Indeed, the wall-pressure comes from the top two decks in the triple-deck theory, whereas the heat transfer and skin friction are from the lower deck and thus will be sensitive to the turbulence model used in the simulation. Furthermore, Reynolds-averaged Navier–Stokes (RANS) simulations do not correctly capture the flow unsteadiness and thus are not expected to give the correct mean fields. However, it may be possible to add corrective terms in the RANS models to account for the low-frequency unsteadiness, as in Pasha and Sinha (2008). Pirozzoli et al. (2009) have also shown that RANS could be used to estimate the wall-pressure fluctuations at the shock foot.

With the recent rapid development of new laser-based methods (non-intrusive in nature), the increase in data acquisition rate, the post-processing capabilities of large volume data, not to mention the progress made in image processing of particle image velocimetry (PIV) data, combined with the development of numerical methods such as large-eddy simulation (LES), it is hoped that SBLI research will soon go from "a period of observation to a period of explanation" (Dolling, 2001).

1.3 Known facts on SBLI

Dolling (2001) summarises the current state of knowledge in SBLI by noting that over the last 60 years, "experiments from a wide range of facilities from continuous to intermittent, from transonic to hypersonic, have generated a data set that currently cannot

be understood within a common framework". This illustrates the lack of a proper theory and the following paragraphs aim at developing a picture of some important aspects of SBLI.

Thivet et al. (2000) report that in an unswept, separated-compression-ramp flow in which the free-stream velocity $\bar{u}_1$ is almost 800 $\mathrm{m\,s^{-1}}$ and the incoming boundary-layer thickness δ_0 is about 18 mm (giving a characteristic frequency $\bar{u}_1/\delta_0 \approx 40\,\mathrm{kHz}$), the expansion and contraction of the separated flow (often referred to "breathing") from $2\delta_0$ to $4\delta_0$ in extent is at a few hundred Hertz. The two orders of magnitude separating the characteristic frequency of the incoming boundary layer from the frequency of the "breathing" of the bubble is a common feature of all SBLI studies. This is the reason why the unsteadiness is qualified as being low frequency, relative to the higher characteristic frequency of the incoming turbulent boundary layer (TBL). The existence of the low-frequency motions, as mentioned earlier, is found in different experiments: in impinging-shock cases (Dussauge et al., 2006; Dupont et al., 2006, 2007; Souverein et al., 2008, 2009b,a; Polivanov et al., 2009; Humble et al., 2009), and in compression-ramp cases (Gramann, 1989; McClure, 1992; Ganapathisubramani et al., 2007b, 2009). Those two cases have also been investigated numerically, both from Direct Numerical Simulations (DNS) (Adams, 2000; Pirozzoli and Grasso, 2006; Wu and Martin, 2007, 2008a,b; Priebe et al., 2009) and LES (Garnier et al., 2002; Teramoto, 2005; Loginov et al., 2006; Pirozzoli et al., 2009; Garnier, 2009) point of view. However, most of the above numerical investigations could not demonstrate the existence of low-frequency shock motions, mainly because of integration times spanning at most one or two low-frequency cycles, which is insufficient given the broadband nature of the unsteadiness.

Dussauge et al. (2006) used the interaction length L and the upstream velocity $\bar{u}_1$ to scale the low-frequency unsteadiness. They argue that the interaction length, defined as the distance between the mean reflected-shock-foot position and the nominal inviscid impingement location, is probably the correct length scale to use. They applied this scaling to a wide range of data and find that it "would result in a sort of consensus on the order of magnitude of the Strouhal number". However, the frequencies found based on this scaling exhibit some scatter in the values, as noted by the authors. They then mention that one weak aspect of the scaling is probably the choice of the upstream velocity. Based on the aforementioned scaling, it is found that the Strouhal number ($S_t = fL_{\mathrm{sep}}/\bar{u}_1$) of the low-frequency oscillations in SBLI falls in the 0.02–0.05 range. Recently, Wu and Martin (2008a) have argued that the magnitude of the maximum-mean-reversed flow would be a proper choice for the velocity scale, leading to a Strouhal number of 0.8 in their DNS of a ramp-flow case. However, the Strouhal number would be of the order of 0.1 in the shock-reflection case considered in the present work.

From experimental investigations, Dupont et al. (2006) find that the reflected shock upstream of the interaction zone has an unsteady motion with $S_t \approx 0.03$. Furthermore,

they observe that the amplitude of the shock oscillations increases linearly with the shock intensity p_2/p_1, where p_2 is the freestream pressure behind the impinging shock but before the reflected shock. They also note that the second part of the interaction zone exhibits some degree of unsteadiness ($S_t \approx 0.04$) which is in quasi-linear dependence with the reflected-shock motion with a phase shift of π. This reinforces the idea that the separation bubble is in a breathing motion, although the slight mismatch in the two Strouhal numbers quoted suggests that the picture is not that straightforward. Finally, the authors conclude that a scaling for the relaxation zone cannot be achieved with only the upstream velocity and the interaction length scale. In fact, they notice that downstream of the interaction zone, large-scale structures are formed, a development which appears to be geometry-dependent (see also Dussauge, 2001).

The breathing motion of the bubble has been shown to contribute significantly to the mean-flow fields. In his PhD dissertation, Gramann (1989) finds that for a 28° unswept compression ramp at Mach 5, the separation bubble pulses from $2\delta_0$ to $4\delta_0$ and that the fraction of the root-mean-square (RMS) pressure fluctuations generated by frequencies lower than 5 kHz is as high as 60% to 70% of the total energy of the fluctuations. Similarly, Dupont et al. (2006) find that the unsteadiness in the second part of the interaction zone, responsible for the $S_t \approx 0.04$ value, contributes up to 30% of the total energy in the pressure fluctuations. It is tempting to say that the success of the free-interaction theory in predicting the mean-pressure rise in the interaction zone implies that the unsteadiness has a universal character, as argued earlier. This statement remains weak in light of the observed scatter in the available data. In addition, one must recall that the free-interaction theory makes use of the triple-deck theory and never considers the unsteadiness and turbulent nature of the flow. It is thus probably fortuitous that such a coincidence occurs, the physics implicit to the free-interaction theory being significantly different of what is actually occurring in the interaction zone (Dolling, 2001).

For laminar interactions, Katzer (1989) concluded that the length of the separation bubble depends linearly on the shock strength p_3/p_1 and that the influences of Mach and Reynolds numbers are given in powers of -3 and $+1/2$, respectively. For turbulent separation, such scaling still needs to be determined, but as mentioned earlier, Dupont et al. (2006) already observed that the amplitude of the shock oscillations and the interaction length increases linearly with the shock intensity p_2/p_1 (at constant Mach and Reynolds numbers), which would be consistent with the laminar scaling. Furthermore, Pagella and Rist (2003) looked at wall temperature effects and found that the bubble was smaller for cooled walls (they report bubble sizes up to 60% smaller) than for adiabatic walls. Indeed, they show through linear-stability theory that the first instability mode could be completely stabilised by wall cooling, but the authors also note that cooling destabilises higher acoustic modes. In a recent review on time-dependent numerical approaches for

SBLI, Edwards (2008) rightly points out the lack of, and need for, studies on the effect of wall heating in unsteady computations.

Up to this point, the description of the interaction has focused on statistical aspects of SBLI and the term unsteadiness was kept relatively vague. On the one hand, the bubble was said to be breathing, on the other hand, the reflected shock as well as the second part of the interaction were said to experience some degree of unsteadiness. One legitimate question would then be to wonder if those are the same. In Dussauge et al. (2006), one can read that the "flow separation is at the origin of the low-frequency fluctuation", and in Dupont et al. (2006) that there is "strong evidence of a statistical link between low-frequency shock movements and the downstream interaction", or again in Dolling (2001), that the "large-scale motion of the shock is the result of the expansion and contraction of the separation bubble". Whether the reflected shock controls the bubble or vice versa is an interesting question. The phase shift between the reflected-shock oscillations and the reattachment region mentioned in Dupont et al. (2006) may be an element of the answer.

What is known about shock-wave dynamics? Some useful insights are found from linear theory (McKenzie and Westphal, 1968; Culick and Rogers, 1983; Robinet, 1999, 2001; Robinet and Casalis, 2001). First of all, it is known that a shock wave can move under the influence of upstream and downstream conditions. Then, one can show that the transfer function of shock waves depends on the downstream flow (in particular, in the transonic regime). Depending on the downstream conditions, shocks may be frequency-selective or not. In general, shocks are found to be stable or neutral and can be seen as low-pass filters (i.e. they are less stable to lower frequencies). Their stability deteriorates as they become weaker. When an oblique shock is disturbed, the perturbations propagate along the shock with the direction of the tangential velocity (Robinet, 2001). With this in mind, Dussauge et al. (2006) give the following interpretation to what is seen in experiments when looking at the reflected shock: "the turbulent structures perturb randomly the foot of the shock, in a part where it can be considered as normal. It can be observed that the perturbations propagate along the shock to the outer flow where it is oblique and therefore stronger and more stable". Consequently, the authors note that fluctuations are expected to be damped as they move outwards, corresponding to usual observations or measurements in supersonic interaction. The picture just drawn by Dussauge et al. (2006) is a good description of what is seen in the current LES, to be discussed later.

From a more quantitative approach, Li (2007) has recently looked at the linear stability of a steady attached oblique shock wave from the Euler equations and analytically confirmed the so-called "sonic point criterion". The sonic-point criterion refers to a "predicted drastic change in the behaviour of oblique shock waves as shock strength increases such that the downstream flow becomes subsonic" (Li, 2007). In other words,

this is the mathematical confirmation of the aforementioned picture given by Dussauge et al. (2006): in the potential flow, the flow behind the oblique shock is supersonic and all stability criteria (see theorem 2.1 in Li, 2007) are met so that the shock system is linearly stable. However, as one approaches the near-wall region, the requirement for the flow behind the shock to be supersonic can easily be challenged and one could expect transition to Mach reflection. Since the sonic-point criterion is based on steady and purely geometrical considerations, it should be placed in the unsteady context of a turbulent boundary layer cautiously but one could argue that a particular disturbance can locally and temporarily trigger the sonic-point criterion, thus locally affecting the shock-reflection nature (from "regular" to "Mach" type). Large-scale/large-amplitude motions of the shock tips, as seen in the present LES simulations, could thus be generated.

One might ask whether or not linear theory is a good starting point to describe SBLI. If one thinks about the interaction as a whole, the answer is probably not, since SBLI are known to be highly non-linear. However, if one thinks about the response of a shock to disturbances, the answer is probably yes, as discussed in the previous paragraph. One further aspect on which linear-studies have been successful and worth mentioning here is the turbulence evolution behind a shock. Indeed, in the case of disturbances from isotropic, homogeneous turbulence, the work of Lee et al. (1997) and Mahesh et al. (1997) on comparing their DNS results with linear theory led the authors to conclude that "strikingly, linear theory is found to successfully reproduce most features observed in the interaction of isotropic vortical turbulence with a shock wave, including downstream turbulence evolution and turbulence modification across the shock wave". However, Boin et al. (2006) note that the amplification of isotropic and homogeneous turbulence through a shock wave, predicted by rapid distortion theory (RDT) is not valid for oblique interactions (see also Jacquin et al., 1993; Simone et al., 1997, amongst others).

It is worth mentioning here that compressibility affects the level of velocity fluctuations and the size of the energetic eddies (the contribution of small scales to the energy is larger in supersonic flows than in subsonic flows — Dussauge, 2001; Lele, 1994), but that the estimation of the timescales can be made from rules valid for solenoidal turbulence, suggesting that acoustic phenomena are not developed enough to modify the energy cascade. This is considered to be true for flows at convective Mach numbers below 0.6 (Dussauge, 2001; Lele, 1994). In fact, the importance of the acoustic pressure fluctuations in compressible turbulent boundary layers has been quantified by Borodai and Moser (2001), where the authors show that the turbulence quantities are decoupled from the acoustic fluctuations as long as the turbulent Mach number is small enough (interestingly, this provides a broader range of applicability than Markovin's hypothesis). Borodai and Moser (2001) findings are important as they show that the acoustic

fluctuations in the turbulent boundary layers considered in the present SBLI studies are not expected to interact with the turbulence structures. However, it is important to note that those results do not consider the presence of shock waves and are not valid very near the wall.

The amplification mechanism of turbulence in the interaction is a research topic in itself. In the past decade, there has been an increased interest in the shear layer that forms at the separation bubble edge. Pirozzoli and Grasso (2006) have run a DNS of an impinging shock on a Mach 2.25 and $\mathrm{Re}_{\delta_2} = 3725$ turbulent boundary layer. They find that the formation of the mixing layer is primarily responsible for the amplification of turbulence, which relaxes to an equilibrium state downstream of the interaction. From their compression-ramp LES, Loginov et al. (2006) conclude that the turbulence amplification in the external flow above the detached shear layer is due to downstream travelling shocklets. When comparing a ramp and a shock-reflection case at similar interaction strength p_3/p_1, Priebe et al. (2009) find significant differences in the turbulence amplification levels. Dupont et al. (2006) note that the mixing layer reattaching near the end of the interaction gives rise to developing large-scale structures as in subsonic separations (vortex shedding). In subsonic flows, this phenomenon is known to generate strong coupling between the shock zone and the flow far downstream (Dussauge et al., 2006).

1.4 Current speculations on the low-frequency unsteadiness in SBLI

1.4.1 Correlations with upstream events

1.4.1.1 Fast timescales

The previous paragraphs have mostly focused on observations and no attempt to describe the mechanisms which govern the unsteady interaction was made. One good reason is that until today, no such theory is available and only some speculations, sometimes conflicting, have been proposed. One of its kind, and probably the most common one, is to try to relate the reflected-shock unsteadiness to the coherent structures of the incoming turbulent boundary layer. For example, Andreopoulos and Muck (1987) suggest that the frequency of the shock motion scales on the bursting frequency of the incoming boundary layer. Indeed, when looking at high time-resolution animations of the interaction, it appears that there exists a strong correlation between the impact of a large eddy into the shock and the shock displacements. Erengil and Dolling (1993) have shown that the small-scale motions of the shock are caused by its response to the passage of turbulence

fluctuations through the interaction. The idea of a relationship between the shock-foot velocity and velocity fluctuations in the incoming boundary layer is supported by the very large-eddy simulation of Hunt and Nixon (1995). Similar high-frequency observations are made by Wu and Miles (2000), who looked at a Mach 2.5 compression corner flow at a very high sampling frequency rate. They show that large velocity fluctuations, due for example to the so-called hairpin structures, can have a significant impact on the shock. However, such events occur at higher frequencies than the ones of interest here and cannot yet be directly related to the large-scale/low-frequency motions of the reflected shock. For example, Thomas et al. (1994) find "no discernible statistical relationship between burst events and span-wise coherent shock-front motion".

The direct correlations between unsteady events due to the upstream turbulence and the shock motion are clear, since the impact of an eddy onto the shock will inevitably displace it. However, there is no particular reason to believe that such high-frequency dynamics are related to the low-frequency ones. Nevertheless the idea is not that incongruous since laminar interactions are not generally found to be unsteady[2], suggesting that the turbulent nature of the incoming boundary layer must play a role in the low-frequency motions. Furthermore, in light of the previous section, the shock can be thought of as a low-pass filter and one could imagine that the reflected shock filters the fluctuations in the incoming boundary layer up to a given cutoff frequency, which would lead to the observed low-frequency unsteadiness. This idea would be consistent with the observed similar Strouhal numbers for a wide range of interactions with some scatter due to the difference in geometry and shock strength, potentially modifying the cutoff frequency. This argument was suggested for example by Dussauge et al. (2006), as mentioned earlier.

The conceptual idea that the oblique shock could act as a low-pass filter was formally expressed by Plotkin (1975) who first modelled the shock as being randomly perturbed by upstream disturbances but subject to a relatively slow linear restoring mechanism, forcing the shock to come back to its initial position. Based on such assumptions, the shock motion follows a first-order ordinary equation which is forced stochastically to mimic the effect of the turbulence. This allowed Plotkin (1975) to match the expected wall-pressure spectra. Using experimental data to compute the model constants (i.e. the timescales of the restoring mechanism and correlation function of the incoming turbulence as well as the wall-pressure standard deviation at the shock foot) the obtained spectra was found to agree with the experimental results for frequencies sufficiently lower than the turbulence-related ones. Poggie and Smits (2001, 2005) have also compared experimentally-obtained spectra with the one derived by Plotkin (1975) and have found

[2]To the author's knowledge, the simulation by Robinet (2007) is the only reported case of unsteadiness in laminar SBLI.

excellent agreement in cases where the shock undergoes significant low-frequency oscillations. Conceptually, this mathematical model is attractive since it shows how broadband low-frequency motions can emerge by simply forcing the system with white noise. However, it lacks physically-sound justifications about whether the oblique shock/boundary-layer interaction can be modelled so simply and if so, on the key parameters responsible for the cutoff frequency. Furthermore, the low-pass filter behaviour of the model can only amplify existing low-frequency components from the forcing mechanism. In other words, the energetically-significant high frequencies found in the incoming boundary layer are not transferred to lower frequencies but instead are greatly damped while the low-frequency components are amplified. It is not clear if the energetically-insignificant low-frequency content from the upstream turbulent boundary layer is sufficient to be solely responsible for the observed important low-frequency shock motions, once the high frequencies have been cut off. Perhaps there exist alternative and more profound sources of low-frequency disturbances.

1.4.1.2 Slow timescales

Ünalmis and Dolling (1994) have investigated the correlations in a Mach 5 compression-corner flow between an upstream Pitot pressure and the shock-foot location, and found that an upstream shock position was correlated with higher upstream pressure, and vice versa. It was then argued that the shock position could be driven by a low-frequency thickening and thinning of the upstream boundary layer. Later, Beresh et al. (2002) looked at relatively low-frequency correlations in the same compression-corner flow and found significant correlations between upstream velocity fluctuations and the shock motions at 4–10 kHz, one order of magnitude smaller than the characteristic frequency of the large-scale structure of their incoming turbulent boundary layer ($\bar{u}_1/\delta_0 \sim 40\,\text{kHz}$). It should be noted that in the shock-reflection case of interest in the present work, the upstream boundary-layer characteristic frequency is about 50 kHz while the reported most energetic low-frequency shock motions are at about 0.4 kHz (Dupont et al., 2006).

Although Beresh et al. (2002) could find correlations between the shock motions and velocity fluctuations, they note that the "low-frequency thickening/thinning of the upstream boundary layer does not drive the large-scale shock motion", which seems to be in contradiction with the earlier suggestion of Ünalmis and Dolling (1994). A short time later, Hou et al. (2003) made a similar analysis as Beresh et al. (2002) but on a Mach 2 compression-corner flow and were able to confirm the existence of a correlation between the shock motion and a thickening/thinning of the upstream boundary layer. To add to the confusion the recent study by Piponniau et al. (2009), this time applied to shock-reflection experiments, does not show significant differences in the upstream

conditionally-averaged velocity profiles. Nonetheless, it appears logical that a change in the upstream mean boundary-layer properties would affect the shock position since a fuller velocity profile would be less prone to separation under the same adverse pressure gradient.

Despite some apparent desagreements, the aforementioned studies provide evidence of a connection between the shock position and the upstream conditionally-averaged boundary-layer profile. The events responsible for the substantial differences in the conditionally-averaged profiles in the ramp experiments will have to be clarified, and more importantly, the timescale on which they occur considered with care. Indeed, to be compatible with the shock-motion timescales, those events must be at least an order of ten-boundary-layer-thicknesses long. The emergence of time-resolved particle image velocimetry approaches made such considerations possible. For example, Ganapathisubramani et al. (2007b) have reported very long coherent structures of about fifty boundary-thicknesses long (termed "superstructures"), using PIV and Taylor's hypothesis (note that the use of Taylor's hypothesis may be valid as shown by Dennis and Nickels, 2008). In their paper, one can find the scaling argument that the low frequency induced by the superstructure scales on $\bar{u}_1/(2\lambda)$, where $\bar{u}_1$ is the upstream freestream velocity and λ the size of the superstructure. In the shock-reflection case, the energetically-significant low-frequency shock oscillations are at about $\bar{u}_1/(115\delta_0)$, where δ_0 is the upstream 99% boundary-layer thickness (Dupont et al., 2006). Using the above superstructure-scaling argument, the energetically-significant low frequencies seen in the shock-reflection experiment of Dupont et al. (2006) would be associated with structures with a length of the order of $50\delta_0$ long, consistent with the value quoted by Ganapathisubramani et al. (2007b). Interestingly, compression corner and shock-reflection experimental studies show (Dolling, 2001; Dussauge et al., 2006; Dupont et al., 2006; Piponniau et al., 2009) that for constant inflow conditions (and therefore for constant superstructure sizes) but different corner and wedge angles, the physical most-energetic low-frequency shock oscillations (not the Strouhal number) change markedly, making the upstream superstructures argument questionable unless the shock truly acts as a low-pass filter, as discussed earlier, with a cutoff frequency directly related to the corner or wedge angle.

It should be noted that it is uncertain whether such long events as the aforementioned superstructures are caused by an experimental artifact (such as Görtler-like vortices formed in the expansion section of the wind-tunnel nozzle, see Beresh et al., 2002). Although numerical simulations could, in theory, answer that question, it is not yet possible to perform DNS which can allow the development of such superstructures and at the same time cover long-enough time series to study the low-frequency shock motions. Ringuette et al. (2008) report long coherent structures up to the maximum domain size tested ($48\delta_0$) from their DNS investigations. However, it is also uncertain whether

the recycling/rescaling technique used by the authors could be forcing such structures. In the present work, particular care will be taken to avoid forcing any particular low-frequency/large-wavelength motions that may directly affect the reflected-shock low-frequency motions, if present in the simulations.

Furthermore, the following two remarks should be considered. First, it must be emphasized that the way the correlation functions are built will inevitably govern the level of understanding gained from the resulting correlation values. For example, the correlations mentioned above were built as follows: the motion of the shock or a predefined separation line is detected and then correlated to an earlier event in the incoming boundary layer, assuming that the upstream event has travelled the separating distance at a constant predefined velocity (usually the local mean velocity). This approach will by construction remove the possibility that the shock motion may be related to a downstream event. Second, such an algorithm always involves in one way or another the choice of arbitrary threshold values, which directly influence the level of correlations seen. For example, Ganapathisubramani et al. (2007b) define as the separation front the spanwise line from which the velocity is less than 187 $\mathrm{m\,s^{-1}}$, due to the difficulty in finding the zero-velocity contour line from the PIV, and the impossibility of using a criterion based on the zero skin-friction contour. With these assumptions, the authors find that the motion of the separation line is correlated to the presence of low- and high-speed regions. The analysis of DNS data allows the study of different possible correlation approaches, which may be difficult or impossible to implement experimentally, and the resulting effect on the interpretation of such correlations. For example, Wu and Martin (2008b) find that "the streamwise shock motion is not significantly affected by low-momentum structures in the incoming boundary layer". However, using a similar criterion as the one used by Ganapathisubramani et al. (2007b), the authors found much higher correlation values, similar to the ones found in the experiment. This demonstrates the sensitivity of the correlation techniques in the aforementioned experimental compression-corner investigations. Of course, the ability of numerical simulations to perform time- and space-resolved data greatly enhances the level of complexity the data analysis can reach. For example, one can look at possible upstream-propagating mechanisms using frequency/wave-number analysis of the wall-pressure distribution (as shown later).

The possibility that the aforementioned superstructures are the main source of low-frequency shock motions is still an active research topic. Emerging techniques such as tomographic particle image velocimetry could be useful at providing instantaneous three-dimensional snapshots of the interaction at Reynolds numbers not accessible to DNS or LES (Humble et al., 2009). In fact, considering the interaction in its full three-dimensional form raises one interesting question: are the low-frequency oscillations in phase along the shock front? In other words, does the shock oscillate as a block or

does it wrinkle in the spanwise direction? This is often not documented and the few studies considering this aspect have been performed for the compression-ramp case. For example, Wu and Miles (2000); Wu and Martin (2008a); Edwards et al. (2008) have shown evidences of spanwise shock wrinkling due to the passage of turbulent structures. Edwards et al. (2008) have computed the flow on a Mach 5 compression corner using a hybrid LES/RANS approach and find that large streamwise structures affect the shock front by producing spanwise wrinkles. These authors also report the existence of long coherent structures that could account for the low-frequency motions but they remain cautious about the use of Taylor's hypothesis as well as the possible artificial effect of the recycling technique used on the existence of those large-coherent structures. The time scale involved with those studies on the shock wrinkles differ from the larger time scales related to the low-frequency motions and the computational studies often suffer from the use of periodic boundary conditions combined with relativelly small spanwise extents (less than the separation-bubble length). Such spanwise confinements in the numerical simulations can have a large effect, as will be shown in the present work. Similarly, experiments are not free from artifacts produced by the wind-tunnel side walls, as shown by Dussauge et al. (2006) and Dussauge and Piponniau (2008), where corner flows are seen to produce "span-wise tornadoes" with associated timescales that can be comparable with the low-frequency motions. Garnier (2009) has recently performed stimulated detached eddy simulations to resolve the entire section of the wind tunnel. The corner-flow vortices present in his simulation are found to reduce the effective wind-tunnel section and strengthen the interaction but the author could not statistically connect the corner-flow low-frequency unsteady motions with those of the main separation.

1.4.2 Correlations with downstream flow features

The incoming boundary layer is not the only place where coherent structures occur. The idea that the vortical structures emerging from the shear layer could play an important role in the interaction is appealing. For example, Dussauge et al. (2006) write that the "eddies in the separated zone may be the source of excitation". Pirozzoli and Grasso (2006) go further and, based on a DNS of an impinging shock at Mach 2.25 and $\mathrm{Re}_{\delta_2} = 3725$, argue that the interaction mechanism works as follows: large coherent structures are shed close to the average separation point from the mixing layer, interacting with the incident shock to produce acoustic disturbances that propagate upstream (in the subsonic layer), thus inducing an oscillatory motion of the separation point and a subsequent branching and flapping motion of the reflected shock, enhancing the formation of discrete vortices. The large-scale low-frequency unsteadiness would then be

sustained by an acoustic resonance mechanism. The authors relate the aforementioned mechanism to the one responsible for the generation of tones in cavity flows. To support this, they developed a simplified model for the acoustic resonance and were successful at predicting the characteristic tones for the interaction they studied. Although appealing, this mechanism has not been explicitly confirmed using experimental or numerical data. In fact, the possibility that a resonance can occur is bound to the sensitive and selective nature of the shear layer. The receptivity of the particular shear layer to an acoustic field must be addressed. As mentioned earlier, Borodai and Moser (2001) have demonstrated the possible decoupling between the acoustic field and the turbulence so that the effect of the acoustic field on the turbulence could be neglected. Moreover, it is important to note that the integration time obtained by Pirozzoli and Grasso (2006) was much too short to cover any low-frequency oscillation, making the interpretation of the correlation functions subject to caution. Finally, the idea of a resonance-based mechanism seems rather surprising as it appears to oppose the experimental evidences of broadband oscillations.

Piponniau et al. (2009) have also considered the shear-layer as a key for the low-frequency shock motions and proposed a model based on the mass-entrainement timescale associated with the separation bubble and the developping mixing layer. The resulting timescale is of the same order of magnitude as the dominant shock-motion timescale and the model suggests that the main parameter controling the low-frequency shock motions is the spreading rate of the compressible mixing layer. Therefore, the authors argue that the low-frequency motions are closely related to the presence of a separated region downstream of the shock and that the geometry of the flow configuration (i.e. corner flow or shock reflection) does not influence them much, as long as the mean separation-bubble height is sufficiently large. Moreover, the authors find that the characteristic frequency of the shock motions are affected by the shock intensity p_2/p_1 and not directly related to any time scale from the upstream boundary layer.

Yet more alternative approaches have been suggested in the literature. One particularly interesting approach is to look at possible hydrodynamic instabilities. Boin et al. (2006); Boin and Robinet (2004) argue that the unsteadiness is intrinsic to the dynamics of the separated zone. They show that laminar SBLI can, under some assumptions, be the place of unsteady self-sustained low-frequency dynamics and that it is not necessary to have upstream disturbances to generate the unsteady motion. Their 3D calculations show that before becoming unsteady (when gradually increasing the shock angle), the SBLI goes through a phase were the flow becomes three-dimensional and stationary and that this state is unstable and leads to fully 3D and unsteady flows. They base their scenario on Dallman's conjecture (Dallmann, 1988), which states that before unsteady vortex shedding occurs, multiple recirculation zones occur inside the primary bubble

which finally leads to a global structural flow change with "multiple structurally unstable saddle-to-saddle connections". Theofilis et al. (2000) linked the 3D global instabilities in incompressible flows to Dallman's conjecture. Boin and Robinet (2004) believe that this extends to supersonic flows and SBLI and that it could explain the first stage of the establishment of the unsteady low frequency. In a relativelly recent paper, Robinet (2007) performs a BiGlobal analysis of the laminar shock-reflection case and reports that there exists a global mode (in the BiGlobal sense) for sufficiently strong shock strengths. The most unstable mode is reported to be three-dimensional with a wavelength scaling on the separation length while the 2D mode is found to be stable.

Finally, it is recalled that despite the numerous studies cited above, there remain uncertainties regarding possible external sources of unsteadiness. Dolling (2001) mentions possible stagnation chamber resonances, or vortices embedded with the test section (like the "span-wise tornadoes" mentioned by Dussauge et al., 2006) that could lead to the low-frequency unsteadiness. In fact, this led some researchers to believe that small changes in the incoming boundary layer thickness could be the cause of the unsteadiness (McClure, 1992; Ünalmis and Dolling, 1994). Beresh et al. (2002), Chan (1994) and Dupont et al. (2006) could not find such correlations but the latter authors could not rule out the idea that there could be "side wall effects" in their results. Similarly, numerical simulations suffer from the inevitable need for boundary conditions. In particular, LES and DNS of turbulent wall-bounded flows necessitate time-varying inflow boundary conditions which often introduce characteristic frequencies that could be of the same order of magnitude as the observed low-frequency oscillations. Would the simulations and experiments be both wrong for different reasons but still give comparable results? This is believed to be unlikely. Nevertheless, for the present simulations, a large amount of time was devoted in order to define inflow conditions that could not introduce any particular low frequency in the computational domain. This is thought to be the right start for numerical investigations on SBLI unsteadiness.

1.4.3 Objectives and thesis outline

Based on the above discussion, it is clear that shock/turbulent-boundary-layer interaction, and in particular the associated low-frequency unsteadiness, is still an active research field where no consensus on their origin can be found. The following work intends to shed some light on this enigma, using large-eddy simulations as the primary tool to generate the data that are then analysed to some extent. In particular we will:

- validate the LES approach through sensitivity studies and comparisons with experimental data

- adapt and assess a digital-filter based inflow generator to avoid forcing a particular frequency
- perform a stability analysis of time-averaged flows
- investigate low-frequency features from long LES runs
- develop a model for the low-frequency shock-foot motions

The thesis is organised as follows. The next chapter will introduce the governing equations with an emphasis on the filtered 3D compressible Navier–Stokes equations and the numerical strategy to solve them. In particular, the closure issue and the approximations made will be clearly stated in a first part, followed by a complete description and discussion of the boundary conditions, and more specifically the inflow-generator developed for this SBLI study. Then, the first SBLI computations will be presented with a grid, sub-grid-scale (SGS) model and domain sensitivity sensitivity study to gain confidence in the numerical approach. The results will be compared with other existing data wherever possible. The following chapter will then be devoted to time-averaged results using LES at various Mach numbers and wedge angles, together with comparisons with some available experimental data and some common properties between the different cases will be highlighted. Several time-averaged LES results will then be used as a basis for a linear-stability study to compare with the laminar interactions, which are found to be globally unstable. From there, the following chapters will be devoted to the unsteady data analysis, first by considering the wall-pressure fluctuations from four different LES and one experiment. Then, the shock system and interaction-region dynamics will be analysed, based on the generated LES data, by means of correlation functions, spectral analysis and conditional averages. Finally, the last chapter will introduce an approach to obtain a low-order stochastic model for the low-frequency shock motions and the proposed model will be compared with the LES and experimental data. A discussion about the low-frequency motions, based on the knowledge acquired from both the LES and the low-order model will be provided, followed by the conclusions and some suggestions for future work.

2. Governing equations and numerical method

This chapter describes the numerical approach that was implemented in order to perform the shock/boundary-layer interaction simulations to be presented throughout this dissertation. In particular, the large-eddy simulation technique used in this work will be detailed together with the challenging issue of the generation of the incoming turbulent-boundary-layer fluctuations.

2.1 Governing equations

2.1.1 The Navier–Stokes equations: DNS formulation

The dimensionless three-dimensional compressible Navier–Stokes equations (expressed in conservative form) are composed of one continuity equation, three momentum equations and the energy equation:

$$\frac{\partial \rho}{\partial t} + \frac{\partial \rho u_i}{\partial x_i} = 0, \tag{2.1a}$$

$$\frac{\partial \rho u_i}{\partial t} + \frac{\partial \rho u_i u_j}{\partial x_j} = -\frac{\partial p}{\partial x_i} + \frac{1}{\mathrm{Re}} \frac{\partial \tau_{ij}}{\partial x_j}, \tag{2.1b}$$

$$\frac{\partial E_t}{\partial t} + \frac{\partial (E_t + p) u_j}{\partial x_j} = \frac{1}{\mathrm{Re}} \frac{\partial u_i \tau_{ij}}{\partial x_j} - \frac{1}{(\gamma - 1)\,\mathrm{Re}\,\mathrm{Pr}\,\mathrm{M}^2} \frac{\partial}{\partial x_j} \left[\mu \frac{\partial T}{\partial x_j} \right], \tag{2.1c}$$

where ρ is the fluid density, u_i the instantaneous velocity vector, p the pressure, T the temperature, E_t the total energy and t the time. The streamwise, wall-normal and spanwise directions are denoted by x, y and z respectively. The fluid (air in practical applications) is assumed to be ideal. The equation of state, the total energy/pressure relation and the viscous shear-stress relation (for a Newtonian fluid) are:

$$p = \frac{1}{\gamma \mathrm{M}^2} \rho T, \tag{2.1d}$$

$$T = \gamma(\gamma - 1)\,\mathrm{M}^2 \left(\frac{E_t}{\rho} - \frac{1}{2} u_i u_i \right). \tag{2.1e}$$

$$\tau_{ij} = \mu \left(\frac{\partial u_j}{\partial x_i} + \frac{\partial u_i}{\partial x_j} - \frac{2}{3} \delta_{ij} \frac{\partial u_k}{\partial x_k} \right). \tag{2.1f}$$

The dynamic viscosity is taken to vary with temperature according to either a power law or Sutherland's law, depending on the simulation:

$$\mu = T^{\Omega} \text{ (power law), with } \Omega = 0.67 \tag{2.1g}$$

$$\mu = T^{3/2}\frac{1+C}{T+C} \text{ (Sutherland's law), with } C = S/\bar{T}_1^{\star},\ S = 110.4\,\text{K}. \tag{2.1h}$$

The Einstein summation convention was used in the above equations (and will be used everywhere in this report unless otherwise specified), δ_{ij} denotes the Kronecker-δ function, Re the Reynolds number, Pr the Prandtl number (taken to be 0.72), M the Mach number and γ the specific heat ratio (taken to be 1.4). The reference values to normalise the flow variables are taken in the potential flow, upstream of the interaction ($\bar{u}_1^{\star},\ \bar{\rho}_1^{\star},\ \bar{T}_1^{\star},\ \bar{\mu}_1^{\star}$). The reference length scale $l^{\star}$ will vary during the text and will be explicitly defined where it is used. The pressure p is normalised with $\bar{\rho}_1^{\star}\bar{u}_1^{\star^2}$ and the time t with $l^{\star}/\bar{u}_1^{\star}$.

2.1.2 The Navier–Stokes equations: LES formulation

Large-eddy simulation approaches are based on the definition of a scale separation. The conceptual idea is to fully resolve the large-scale most-energetic turbulence structures and only model the effect of the unresolved smaller scales. The main motivation is to reduce the number of degrees of freedom of the continuous system (2.1 *a*–*h*) as much as possible while maintaining the closest representation of the continuous system in order to reduce the computational cost associated with solving (2.1 *a*–*h*).

In practice, the scale separation is bound to the computational-grid resolution. From the Nyquist theorem, if Δx is the distance between two grid points on a homogeneous grid, no scale smaller than $2\Delta x$ can be captured. The error associated with the existence of these unresolved scales is called the *projection error*. In Fourier space, this is equivalent to cutting off the highest wavenumbers, where the cutoff wavenumber k_c is directly linked to the grid resolution: $k_c = \pi/\Delta x$. This sharp low-pass filter is referred to as the Nyquist filter.

The projection error should be made distinct from the *resolution* and *discretisation* errors: the discretisation error is the one associated with the approximation of the partial derivatives of the continuous problem by their discrete counterparts on the computational grid. The resolution error corresponds to the contribution of the missing scales via the non-linear terms. While the projection error reflects the error associated with the approximation of a continuous variable q by its discrete counterpart q_{d}, the resolution error is the difference between the exact solution $F(q)$, where F is a non-linear function, and its discrete counterpart $F(q_{\text{d}})$, arising from the contribution of the unresolved scales

through the non-linear terms. In a DNS, the resolution error must vanish but the projection error cannot be avoided. Furthermore, note that even if the discretisation error is reduced to zero, the resolution error would still be present. Therefore, the best LES approach possible is one where the resolution error cancels the discretisation error. This is generally attempted using one of the two different families of approaches: the first one where a forcing term (the sub-grid scale model) is introduced in the equations to cancel the resolution error and a second one where no sub-grid scale model is introduced but the numerical scheme is designed such that the discretisation error cancels the resolution error. The present work will make use of the former approach.

The formulation of the LES problem is a complex one and the reader is referred to Sagaut (2005) and Berselli et al. (2005) for much more complete descriptions. Mathematically, the LES problem is often formulated and modelled as the result of the application of a low-pass convolution filter to the Navier-Stokes equations. This is the approach undertaken here too. The properties of such filter are first described in the following section and then applied to the compressible Navier–Stokes equations (2.1 *a–h*).

2.1.2.1 Convolution filter: definition

The spatial-scale separation is represented by the convolution product defined below:

$$\bar{\mathbf{q}}(\mathbf{x}) = \int_D G\left(\mathbf{x}-\mathbf{z}\,;\,\overline{\Delta}\right)\,\mathbf{q}(\mathbf{z})\,\mathrm{d}^3\mathbf{z}, \tag{2.2a}$$

where $\mathbf{q}$ is a vector field, G the filter convolution kernel, and $\overline{\Delta}$ its associated characteristic cutoff lengthscale. The integration is performed on a compact subset of $\mathbb{R}^3$, denoted $\mathcal{D}$. Typically, the filter function is an infinitely differentiable function of bounded support in a bounded domain and normalised such that:

$$\int_D G\left(\mathbf{x}-\mathbf{z}\,;\,\overline{\Delta}\right)\,\mathrm{d}^3\mathbf{z} = 1. \tag{2.2b}$$

The property (2.2b) is to ensure the conservation of constants. Moreover, it is straightforward to see that the filter-operator (2.2a) is linear, independently of the characteristics of the kernel G. Finally, the filter is required to commute with the differentiation operator.

At this stage, it is important to distinguish the *grid filter* from the *test filter*. The grid filter corresponds to the implicit low-pass filter arising from the use a computational grid which is too coarse to resolve the smallest scales of the turbulent flow. This filter is represented as in (2.2 *a,b*) and denoted by the *overline* notation. The test filter corresponds to an explicit filtering operation which is performed on the resolved field in order to compute the subgrid-scale model terms. This filter is also of the same type as

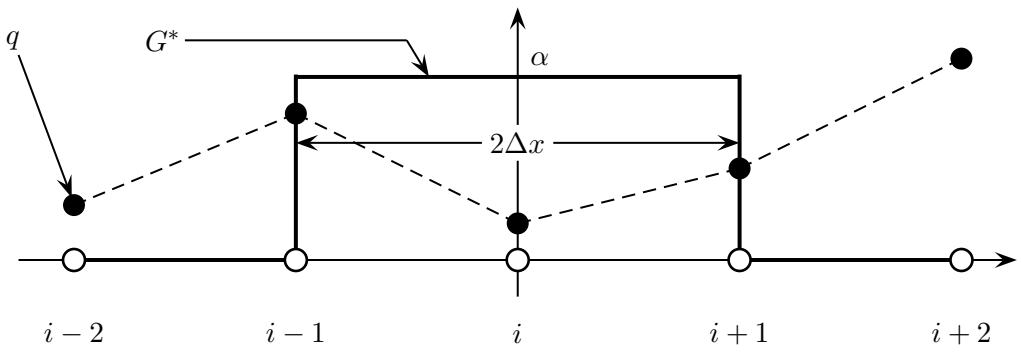

FIGURE 2.1: Discretised top-hat filter ($\widehat{\Delta} = 2\Delta x$)

(2.2 *a,b*). To avoid any confusion between the grid-filtered and test-filtered fields, the test-filtered field will be denoted by the *hat* notation $\hat{q}$. In the present work, the convolution kernel used for the test filter is a top-hat function (which is infinitely differentiable but not continuous):

$$G^*(\mathbf{x}-\mathbf{z}) = \begin{cases} 1/\widehat{\Delta} \text{ if } \parallel \mathbf{x}-\mathbf{z} \parallel \leq \widehat{\Delta}/2, \\ 0 \text{ otherwise.} \end{cases} \tag{2.3}$$

Note that (2.3) satisfies (2.2b).

In the following sections, the top-hat kernel used has a characteristic lengthscale set to $2\overline{\Delta}$ (i.e. in the case of a 1D homogeneous axis, $\widehat{\Delta} = 2\Delta x$ where Δx is the computational grid spacing). Since this test filter will only be applied in the homogeneous directions, issues related to varying grid spacing (as in the wall-normal direction) will not arise. However, the above definitions must be projected onto the discrete computational domain, as sketched in figure 2.1. If f denotes the integrand in (2.2a), its discrete counterpart can be expressed $g_{i+k} = G^*\left(x_k - x_i\right) \times q_{i+k}$, so that using the trapezoidal integration rule, one can write (2.2a) in the form:

$$\hat{q}_i = \frac{\Delta x}{2} \sum_{-\infty<k<\infty} \left\{ g_{i+k-1/2} + g_{i+k+1/2} \right\}. \tag{2.4}$$

Given the convolution kernel G^* in figure 2.1, the only non-zero terms in (2.4) are:

$$\begin{aligned} \hat{q}_i &= \alpha\Delta x \left(q_{i-1/2} + q_{i+1/2}\right) = \alpha\frac{\Delta x}{2}\left(\{q_{i-1} + q_i\} + \{q_i + q_{i+1}\}\right) \\ &= \alpha\frac{\Delta x}{2}\left(q_{i-1} + 2q_i + q_{i+1}\right). \end{aligned} \tag{2.5}$$

In order for G^* to satisfy (2.2b) in the particular case of figure 2.1, we must have $\alpha = 1/(2\Delta x)$. Hence:

$$\hat{q}_i = \frac{1}{4}\left(q_{i-1} + q_{i+1}\right) + \frac{1}{2}q_i. \tag{2.6}$$

2.1.2.2 Application of the filter to the governing equations

Starting from the grid-filtered field $\bar{q}$, the following Favre-filtered field may be defined:

$$\tilde{q} \equiv \frac{\overline{\rho q}}{\bar{\rho}}, \tag{2.7}$$

where the overline notation is defined in (2.2). After some algebraic manipulation (see Appendix A), the complete form of the grid-filtered dimensionless compressible Navier–Stokes equations (expressed in conservative form) is composed of one continuity equation, three momentum equations and the energy equation:

$$\frac{\partial \bar{\rho}}{\partial t} + \frac{\partial \bar{\rho}\tilde{u}_i}{\partial x_i} = 0, \tag{2.8a}$$

$$\frac{\partial \bar{\rho}\tilde{u}_i}{\partial t} + \frac{\partial \bar{\rho}\tilde{u}_i\tilde{u}_j}{\partial x_j} + \frac{\partial \bar{p}}{\partial x_i} - \frac{1}{\mathrm{Re}}\frac{\partial \breve{\tau}_{ij}}{\partial x_j} = -\mathrm{I}_i + \mathrm{II}_i, \tag{2.8b}$$

$$\begin{aligned}\frac{\partial \breve{E}_t}{\partial t} + \frac{\partial (\breve{E}_t + \bar{p})\tilde{u}_j}{\partial x_j} - \frac{1}{\mathrm{Re}}\frac{\partial \breve{\tau}_{ij}\tilde{u}_i}{\partial x_j} \\ + \frac{1}{(\gamma-1)\,\mathrm{Re}\,\mathrm{Pr}\,\mathrm{M}^2}\frac{\partial}{\partial x_j}\left[\tilde{\mu}\frac{\partial \tilde{T}}{\partial x_j}\right] &= -B_1 - B_2 - B_3 + B_4 \\ &\quad + B_5 + B_6 - B_7,\end{aligned} \tag{2.8c}$$

where the resolved equation of state, the resolved total energy/pressure relation and the resolved viscous shear-stress relations are:

$$\bar{p} = \frac{1}{\gamma \mathrm{M}^2}\bar{\rho}\tilde{T}, \tag{2.8d}$$

$$\breve{E}_t = \frac{\bar{p}}{\gamma - 1} + \frac{1}{2}\bar{\rho}\tilde{u}_i\tilde{u}_i, \tag{2.8e}$$

$$\breve{\tau}_{ij} = \tilde{\mu}\left(\frac{\partial \tilde{u}_j}{\partial x_i} + \frac{\partial \tilde{u}_i}{\partial x_j} - \frac{2}{3}\delta_{ij}\frac{\partial \tilde{u}_k}{\partial x_k}\right). \tag{2.8f}$$

The resolved dynamic viscosity is assumed to vary with the resolved temperature according to either a power law or Sutherland's law, depending on the simulation:

$$\tilde{\mu} = \left[\tilde{T}\right]^{\Omega} \text{ (power law), with } \Omega = 0.67, \tag{2.8g}$$

$$\tilde{\mu} = \left[\tilde{T}\right]^{3/2}\frac{1+C}{\tilde{T}+C} \text{ (Sutherland's law), with } C = S/\bar{T}_1^{\star},\ S = 110.4\,\mathrm{K}. \tag{2.8h}$$

The subgrid-scale (SGS) terms in (2.8 *b,c*) are (following the work of Vreman, 1995):

$$\mathrm{I}_i = \frac{\partial \sigma_{ij}}{\partial x_j}, \tag{2.9a}$$

$$\mathrm{II}_i = \frac{1}{\mathrm{Re}} \frac{\partial}{\partial x_j} \left[\bar{\tau}_{ij} - \breve{\tau}_{ij} \right], \tag{2.9b}$$

$$B_1 = \frac{1}{\gamma - 1} \frac{\partial}{\partial x_j} \left[\overline{p u_j} - \bar{p} \tilde{u}_j \right], \tag{2.9c}$$

$$B_2 = \overline{p \frac{\partial u_j}{\partial x_j}} - \bar{p} \frac{\partial \tilde{u}_j}{\partial x_j}, \tag{2.9d}$$

$$B_3 = \frac{\partial \sigma_{ij} \tilde{u}_i}{\partial x_j}, \tag{2.9e}$$

$$B_4 = \sigma_{ij} \frac{\partial \tilde{u}_i}{\partial x_j}, \tag{2.9f}$$

$$B_5 = \frac{1}{\mathrm{Re}} \left(\overline{\tau_{ij} \frac{\partial u_i}{\partial x_j}} - \bar{\tau}_{ij} \frac{\partial \tilde{u}_i}{\partial x_j} \right), \tag{2.9g}$$

$$B_6 = \frac{1}{\mathrm{Re}} \left(\frac{\partial \bar{\tau}_{ij} \tilde{u}_i}{\partial x_j} - \frac{\partial \breve{\tau}_{ij} \tilde{u}_i}{\partial x_j} \right), \tag{2.9h}$$

$$B_7 = \frac{1}{(\gamma - 1)\,\mathrm{Re}\,\mathrm{Pr}\,\mathrm{M}^2} \frac{\partial}{\partial x_j} \left[\overline{\mu \frac{\partial T}{\partial x_j}} - \tilde{\mu} \frac{\partial \tilde{T}}{\partial x_j} \right], \tag{2.9i}$$

where the subgrid-scale stress tensor is defined as:

$$\sigma_{ij} = \bar{\rho} \left(\widetilde{u_i u_j} - \tilde{u}_i \tilde{u}_j \right). \tag{2.9j}$$

2.1.2.3 The compressible shear-layer approximation

In principle, one should solve the full set of filtered equations (2.8 *a–h*), (2.9 *a–j*). However, this cannot be achieved unless the subgrid-scale terms (2.9 *a–j*) are modelled and related to the computed variables $[\bar{\rho}, \bar{\rho}\tilde{u}, \bar{\rho}\tilde{v}, \bar{\rho}\tilde{w}, \breve{E}_t]^{\mathbf{T}}$. In practice, this is difficult and one only models the most important terms. Vreman et al. (1995) looked at all the above subgrid scale terms from DNS-data analysis of a plane compressible mixing-layer at Mach numbers 0.2 and 0.6 (and Reynolds number 200). The DNS data were filtered using a top-hat filter with characteristic length $2\Delta x$. The authors categorised the subgrid scale terms as shown in table 2.1.

Although the classification was performed on a different flow at both lower Reynolds and Mach numbers than the ones considered in the present SBLI studies, one could assume that the classification by Vreman et al. (1995) still holds here, as suggested by the relative success of earlier SBLI LES studies (see Garnier et al., 2002; Teramoto, 2005; Loginov et al., 2006), which made use of the above classification. Furthermore, such an assumption is more and more justified as the computational grid is refined.

Relative importance		Subgrid scale term
Medium	$\mathcal{O}(10^{-1})$	I_i, B_1, B_2, B_3
Small	$\mathcal{O}(10^{-2})$	B_4, B_5
Negligible	$\mathcal{O}(10^{-3})$	II_i, B_6, B_7

TABLE 2.1: Classification of the subgrid scale terms (see Vreman et al., 1995)

Since I_i will be modelled, or more precisely, since the subgrid stress tensor σ_{ij} will explicitly be modelled (rather than its divergence), terms B_3 and B_4 can both be modelled. Thus, from the "small" term category, only B_5 is neglected whereas B_4 is integrated to B_3.

From the "medium" category, terms B_1 and B_2 have yet to be discussed. Vreman et al. (1995) have shown from their DNS data of a compressible mixing layer that B_1 and B_2 can be of the same order of magnitude. Looking at B_1 and B_2, it appears that those terms are directly related to compressibility effects and are thus expected to be sensitive to the Mach number. In fact, one can write:

$$B_2 = (\gamma - 1)B_1 + \tilde{u}_j \frac{\partial \bar{p}}{\partial x_j} - \overline{u_j \frac{\partial p}{\partial x_j}}, \tag{2.10}$$

so that B_1 and B_2 are explicitly correlated. Vreman et al. (1995) do report a Mach-number dependency for B_1 and B_2 and interestingly note that their relative magnitude remains the same. Looking at (2.10) with this observation in mind, it is argued that the global maximum of B_1 (noted $||B_1||$) over the global maximum of B_2 (noted $||B_2||$) may be scaling like $1/(\gamma - 1)$. From figure 5 in Vreman et al. (1995) one can notice that the time series of B_1 and B_2 peak at the same times and that the ratio $||B_1||/||B_2||$ is about 2.5, in excellent agreement with $1/(\gamma - 1) = 2.5$. If one considers the sum of B_1 and B_2:

$$B_1 + B_2 = \underbrace{\frac{\gamma}{\gamma - 1} \frac{\partial}{\partial x_j} [\overline{p u_j} - \bar{p} \tilde{u}_j]}_{\Phi} + \underbrace{\tilde{u}_j \frac{\partial \bar{p}}{\partial x_j} - \overline{u_j \frac{\partial p}{\partial x_j}}}_{D}, \tag{2.11}$$

the term D can be interpreted as the subgrid-scale pressure convection. Arguably, this is expected to be relatively small as the most energetic convected pressure fluctuations ought to be caused by large turbulence structures and acoustic radiations, two features that are commonly resolved in LES. In fact, term D is the term that previous works in compressible LES have neglected (Moin et al., 1991; Erlebacher et al., 1992; Garnier et al., 2002). Term Φ can be rearranged using the equation of state (both the filtered

and un-filtered versions):

$$\Phi = \frac{1}{(\gamma-1)\,\mathrm{M}^2}\frac{\partial}{\partial x_j}\left[\bar{\rho}\underbrace{\left(\widetilde{Tu_j}-\tilde{T}\tilde{u}_j\right)}_{\Psi_j}\right], \tag{2.12}$$

where the vector labelled Ψ_j is known as the subgrid-scale Reynolds heat flux and is commonly modelled through an eddy-diffusivity subgrid-scale model.

From the above discussion, the in-house SBLI code is set to only solve the approximate form of the aforementioned filtered normalised 3D compressible Navier–Stokes equations where terms II_i, B_5, B_6, B_7 and D are neglected and only the subgrid-scale stress tensor σ_{ij} and the subgrid-scale Reynolds heat flux Ψ_i are modelled. The SGS stress tensor and Reynolds heat flux modelling approach is the subject of the next section.

2.1.3 The closure problem

2.1.3.1 The SGS stress tensor

One of the most common approach to model the SGS stress tensor is to use an eddy viscosity approach:

$$\sigma_{ij} - \frac{1}{3}\delta_{ij}\sigma_{kk} = -2\bar{\rho}\nu_t\tilde{S}^*_{ij}, \tag{2.13a}$$

where ν_t is the eddy viscosity and $\tilde{S}^*_{ij}$ the deviatoric part of the strain-rate tensor computed from the filtered velocity field:

$$\tilde{S}_{ij} = \frac{1}{2}\left(\frac{\partial\tilde{u}_i}{\partial x_j}+\frac{\partial\tilde{u}_j}{\partial x_i}\right), \tag{2.13b}$$

$$\tilde{S}^*_{ij} = \tilde{S}_{ij} - \frac{1}{3}\delta_{ij}\tilde{S}_{kk}. \tag{2.13c}$$

Note that the isotropic part of the SGS stress tensor should also be modelled. Formally, the isotropic part of the SGS stress tensor can be included in the pressure term and its effect then appears as a modified pressure field. However, one can assume that the local turbulence Mach number is greater than the subgrid-scale turbulence Mach number. Since the local turbulence Mach number is rarely above 0.6, the thermodynamic pressure is expected to be the dominant term so that the isotropic part of the SGS stress tensor is simply neglected (see Erlebacher et al., 1992; Moin et al., 1991). However, the aforementioned argument is questionable in the SBLI context since the flow being filtered has embedded shock waves in it. The additional assumption is then to say that the significant numerical dissipation near the shocks is expected to exceed that of the

SGS model and that it is not necessary to worry about the isotropic part of the SGS stress tensor (see Garnier et al., 2002).

The eddy viscosity ν_t has been modelled in numerous ways. The present work will only be using the Dynamic Smagorinsky model (Germano et al., 1991a,b) and the Mixed-Time Scale model (Inagaki et al., 2005).

The Dynamic Smagorinsky eddy viscosity model In the Dynamic Smagorinsky (DS) case, the test filter is applied to the Favre-filtered field (see 2.1.2.1 and (2.7) for definitions), leading to the following hat-bar notation:

$$\widehat{\widetilde{q}}_i(\mathbf{x}) = \int_D G^*(\mathbf{x}-\mathbf{z}\,;\,\widehat{\Delta}) \left[\frac{\displaystyle\int_D G(\mathbf{x}-\mathbf{z}\,;\,\overline{\Delta})\,[\rho(\mathbf{z})q_i(\mathbf{z})]\;\mathrm{d}^3\mathbf{z}}{\displaystyle\int_D G(\mathbf{x}-\mathbf{z}\,;\,\overline{\Delta})\,\rho(\mathbf{z})\,\mathrm{d}^3\mathbf{z}} \right] \mathrm{d}^3\mathbf{z}. \tag{2.14}$$

In practice, the test filter is such that its characteristic width is larger than the grid filter in order to be able to test-filter the grid-filtered quantities. In this work, we have $\widehat{\Delta} = 2\overline{\Delta}$. Upon application of the test filter to the SGS stress tensor, one finds:

$$\hat{\sigma}_{ij} = \widehat{\overline{\rho u_i u_j}} - \widehat{\overline{\rho}\tilde{u}_i\tilde{u}_j}. \tag{2.15a}$$

Moreover, given the Favre-filtered field, it is possible to compute explicitly the non-linearity associated with test-filtering the velocity-velocity correlations:

$$L_{ij} = \widehat{\overline{\rho}\tilde{u}_i\tilde{u}_j} - \frac{\widehat{\overline{\rho}\tilde{u}_i}\,\widehat{\overline{\rho}\tilde{u}_j}}{\widehat{\overline{\rho}}}. \tag{2.15b}$$

By analogy with the SGS stress tensor, the test-filtered stress tensor can be defined:

$$F_{ij} = \widehat{\overline{\rho u_i u_j}} - \frac{\widehat{\overline{\rho}\tilde{u}_i}\,\widehat{\overline{\rho}\tilde{u}_j}}{\widehat{\overline{\rho}}}, \tag{2.15c}$$

which is nothing but the sum of (2.15a) and (2.15b):

$$L_{ij} = F_{ij} - \hat{\sigma}_{ij}. \tag{2.16}$$

Then, the SGS stress tensor and the test-filtered stress tensor are both assumed to relate to the deviatoric part of the respective strain-rate tensor via an eddy-viscosity model

using the same Smagorinsky constant C_S:

$$\begin{array}{rcl|rcl}
\sigma^*_{ij} & \equiv & \sigma_{ij} - \frac{1}{3}\delta_{ij}\sigma_{kk} = -2\bar{\rho}\nu_t\tilde{S}^*_{ij}, & F^*_{ij} & \equiv & F_{ij} - \frac{1}{3}\delta_{ij}F_{kk} = -2\widehat{\bar{\rho}}\nu'_t\widehat{\tilde{S}}^*_{ij}, \\
\nu_t & = & C_S\overline{\Delta}^2|\tilde{S}^*|, & \nu'_t & = & C_S\widehat{\overline{\Delta}}^2|\widehat{\tilde{S}}^*|, \\
\tilde{S}_{ij} & = & \frac{1}{2}\left(\frac{\partial\tilde{u}_i}{\partial x_j} + \frac{\partial\tilde{u}_j}{\partial x_i}\right), & \widehat{\tilde{S}}_{ij} & = & \frac{1}{2}\left(\frac{\partial\widehat{\tilde{u}}_i}{\partial x_j} + \frac{\partial\widehat{\tilde{u}}_j}{\partial x_i}\right), \\
\tilde{S}^*_{ij} & = & \tilde{S}_{ij} - \frac{1}{3}\delta_{ij}\tilde{S}_{kk}, & \widehat{\tilde{S}}^*_{ij} & = & \widehat{\tilde{S}}_{ij} - \frac{1}{3}\delta_{ij}\widehat{\tilde{S}}_{kk}, \\
|\tilde{S}^*| & = & \sqrt{2\tilde{S}^*_{ij}\tilde{S}^*_{ij}}, & |\widehat{\tilde{S}}^*| & = & \sqrt{2\widehat{\tilde{S}}^*_{ij}\widehat{\tilde{S}}^*_{ij}}.
\end{array} \tag{2.17}$$

Using the above system in (2.16) and assuming that both C_s and $\overline{\Delta}$ are constants over the test-filter characteristic length $\widehat{\Delta}$ yields:

$$L^*_{ij} = -2C_S \underbrace{\left[\widehat{\overline{\Delta}}^2\,\widehat{\bar{\rho}}\,|\widehat{\tilde{S}}^*|\widehat{\tilde{S}}^*_{ij} - \overline{\Delta}^2\widehat{\left\{\bar{\rho}\,|\tilde{S}^*|\tilde{S}^*_{ij}\right\}}\right]}_{M_{ij}}. \tag{2.18}$$

Since the tensors in (2.18) are symmetric, (2.18) corresponds to a system of six equations for the single unknown C_S. In the SBLI code, as in most publications (Germano et al., 1991a; Moin et al., 1991; Erlebacher et al., 1992), a least-square approach is used to solve for C_S:

$$C_S = -\frac{1}{2}\frac{L^*_{ij}M_{ij}}{M_{kl}M_{kl}}. \tag{2.19}$$

To avoid possible numerical instabilities arising from the dynamical approach, the above equation is averaged in the homogeneous (i.e. spanwise) direction (denoted by $\langle.\rangle_z$) and any negative value for C_S is set to zero:

$$C_S(x,y,t) = \max\left\{-\frac{1}{2}\frac{\langle L^*_{ij}M_{ij}\rangle_z}{\langle M_{kl}M_{kl}\rangle_z}\,;\,0\right\}. \tag{2.20}$$

The successive use of the convolution product (see (2.14)) with the kernels G and G^* having respectively a characteristic lengthscales $\overline{\Delta}$ and $\widehat{\Delta}$ raises the question of what the characteristic lengthscale $\widehat{\overline{\Delta}}$ of the resulting test filter is. Following the work of Vreman (1995) (pages 32–33), the best approximation of $\widehat{\overline{\Delta}}$ is:

$$\widehat{\overline{\Delta}} = \sqrt{\overline{\Delta}^2 + \widehat{\Delta}^2}. \tag{2.21}$$

Assuming that the characteristic length of the grid filter is $\sqrt{\Delta x\Delta z}$ and using $\widehat{\Delta} = 2\overline{\Delta}$ yields:

$$\widehat{\overline{\Delta}} = \overline{\Delta}\sqrt{5}, \quad \overline{\Delta} = \sqrt{\Delta x\Delta z}. \tag{2.22}$$

This completes the Dynamic Smagorinsky model.

The Mixed-Time Scale eddy viscosity model The Mixed-Time Scale (MTS) model is essentially based on a dimensionally-consistent physical argument relating to the asymptotic behaviour of the eddy viscosity as one approaches the wall and the potential flow (see Inagaki et al., 2005). Similarly to the DS model, the MTS model makes use of a test filter. The eddy viscosity ν_t in (2.13a) is modelled as:

$$\nu_t = C_M k_{es} T_S, \tag{2.23a}$$

where:

$$k_{es} = \left[\tilde{u}_i - \widehat{\tilde{u}}_i\right]\left[\tilde{u}_i - \widehat{\tilde{u}}_i\right], \tag{2.23b}$$

$$T_S^{-1} = \left(\frac{\overline{\Delta}}{\sqrt{k_{es}}}\right)^{-1} + \left(\frac{C_T}{|\tilde{S}^*|}\right)^{-1}, \tag{2.23c}$$

and $\widehat{\tilde{u}}_i$ and $\overline{\Delta}$ are defined by (2.14) and (2.22), respectively. The constants C_M and C_T were originally set to 0.05 and 10, respectively, by Inagaki et al. (2005) based on *a priori* tests in channel and backward-facing step flow data. However, in the current implementation of the model, we have used:

$$C_M = 0.03, \qquad C_T = 10, \tag{2.23d}$$

based on application of the SBLI code to compressible turbulent channel flow (Li, 2003).

This completes the MTS model. The main advantage of the MTS model over the DS one is that it is computationally less expensive because the constants are not computed dynamically. However, the DS approach is more elegant in the sense that it does not require any *ad-hoc* modelling constant.

2.1.3.2 The SGS heat flux

Once the eddy viscosity is obtained (from either one of the above SGS stress tensor models), the SGS heat flux (see (2.12)) is modelled as:

$$\Psi_i \equiv \widetilde{Tu_j} - \tilde{T}\tilde{u}_j = -\frac{\nu_t}{\mathrm{Pr}_t}\frac{\partial \tilde{T}}{\partial x_i}, \tag{2.24}$$

where ν_t is taken from the SGS stress-tensor model. The SGS turbulent Prandtl number Pr_t should in theory be computed dynamically as in Moin et al. (1991). However, it is considered constant in this study (as in Garnier et al., 2002). The value commonly used is $\mathrm{Pr}_t = 0.9$ but the current implementation has the SGS turbulent Prandtl number set to 1.0. This is exact in the SRA context but could lead to a slight underestimation of

the SGS heat flux in the more general case (assuming that an eddy-viscosity approach is valid and properly estimated by the SGS model).

2.1.4 Final problem formulation and numerical approach

Based on what was presented in the previous sections, the work described in this thesis is based on the solution of the following approximate form of the filtered 3D compressible Navier–Stokes equations:

$$\frac{\partial \bar{\rho}}{\partial t} + \frac{\partial \bar{\rho}\tilde{u}_i}{\partial x_i} = 0, \tag{2.25a}$$

$$\frac{\partial \bar{\rho}\tilde{u}_i}{\partial t} + \frac{\partial \bar{\rho}\tilde{u}_i\tilde{u}_j}{\partial x_j} + \frac{\partial \bar{p}}{\partial x_i} - \frac{1}{\mathrm{Re}}\frac{\partial \breve{\tau}_{ij}}{\partial x_j} \approx -\frac{\partial \sigma_{ij}}{\partial x_j}, \tag{2.25b}$$

$$\begin{aligned}\frac{\partial \breve{E}_t}{\partial t} + \frac{\partial (\breve{E}_t + \bar{p})\tilde{u}_j}{\partial x_j} - \frac{1}{\mathrm{Re}}\frac{\partial \breve{\tau}_{ij}\tilde{u}_i}{\partial x_j} \\ + \frac{1}{(\gamma-1)\,\mathrm{Re}\,\mathrm{Pr}\,\mathrm{M}^2}\frac{\partial}{\partial x_j}\left[\tilde{\mu}\frac{\partial \tilde{T}}{\partial x_j}\right] \approx -\tilde{u}_i\frac{\partial \sigma_{ij}}{\partial x_j} - \frac{1}{(\gamma-1)\,\mathrm{M}^2}\frac{\partial}{\partial x_j}\left[\bar{\rho}\Psi_j\right],\end{aligned} \tag{2.25c}$$

with:

$$\bar{p} = \frac{1}{\gamma \mathrm{M}^2}\bar{\rho}\tilde{T}, \tag{2.25d}$$

$$\breve{E}_t = \frac{\bar{p}}{\gamma - 1} + \frac{1}{2}\bar{\rho}\tilde{u}_i\tilde{u}_i, \tag{2.25e}$$

$$\breve{\tau}_{ij} = \tilde{\mu}\left(\frac{\partial \tilde{u}_j}{\partial x_i} + \frac{\partial \tilde{u}_i}{\partial x_j} - \frac{2}{3}\delta_{ij}\frac{\partial \tilde{u}_k}{\partial x_k}\right). \tag{2.25f}$$

$$\tilde{\mu} = \left[\tilde{T}\right]^{\Omega} \text{ or,} \tag{2.25g}$$

$$\tilde{\mu} = \left[\tilde{T}\right]^{3/2}\frac{1+C}{\tilde{T}+C}, \tag{2.25h}$$

$$\Psi_j = -\frac{\nu_t}{\mathrm{Pr}_t}\frac{\partial \tilde{T}}{\partial x_j}, \tag{2.25i}$$

$$\sigma_{ij} - \frac{1}{3}\delta_{ij}\sigma_{kk} = -2\bar{\rho}\nu_t\tilde{S}^*_{ij}, \tag{2.25j}$$

$$\tilde{S}_{ij} = \frac{1}{2}\left(\frac{\partial \tilde{u}_i}{\partial x_j} + \frac{\partial \tilde{u}_j}{\partial x_i}\right), \tag{2.25k}$$

$$\tilde{S}^*_{ij} = \tilde{S}_{ij} - \frac{1}{3}\delta_{ij}\tilde{S}_{kk}. \tag{2.25l}$$

$$\nu_t = C_M k_{es} T_S, \tag{2.25m}$$

$$k_{es} = \left[\tilde{u}_i - \widehat{\tilde{u}}_i\right]\left[\tilde{u}_i - \widehat{\tilde{u}}_i\right], \tag{2.25n}$$

$$T_S^{-1} = \left(\frac{\overline{\Delta}}{\sqrt{k_{es}}}\right)^{-1} + \left(\frac{C_T}{|\tilde{S}^*|}\right)^{-1}, \tag{2.25o}$$

$$\overline{\Delta} = \sqrt{\Delta x \Delta z}, \tag{2.25p}$$

$$|\tilde{S}^*| = \sqrt{2\tilde{S}^*_{ij}\tilde{S}^*_{ij}}, \tag{2.25q}$$

where $\mathrm{Pr} = 0.72$, $\mathrm{Pr}_t = 1.0$, $\Omega = 0.67$, $C = S/\bar{T}_1^\star$, $S = 110.4\,\mathrm{K}$, $C_M = 0.03$ and $C_T = 10$. The bar, tilde and hat notations are defined in (2.2), (2.7) and (2.14), respectively.

The equations above are solved using an explicit 4^{th}-order central spatial differencing scheme for the spatial derivatives and the 3^{rd}-order explicit Runge–Kutta scheme to integrate in time. The boundary treatment is also of 4^{th} order (see Carpenter et al., 1998). The code makes use of entropy splitting of the Euler terms (based on the work of Gerritsen and Olsson, 1996, 1998) and the laplacian formulation of the viscous terms to enhance the stability of the non-dissipative central scheme (see Sandham et al., 2002). In addition, a variant of the standard total variation diminishing scheme is used for shock capturing (Yee et al., 1999), coupled with the Ducros sensor (Ducros et al., 1999). At regular time intervals, the entire flow field is filtered using a 6^{th}-order explicit filter to remove possible grid to grid-point oscillations. The SBLI code was made parallel in all three directions using MPI libraries. Specific details on the implementations of the aforedescribed numerical strategy can be found in Jones (2008) and Li (2003). The choice of boundary conditions is the subject of the following section.

2.2 Boundary conditions

2.2.1 Wall, top and outflow boundary conditions

At the wall, the no-slip condition is enforced (i.e. $u_i = 0$). Furthermore, the wall is considered isothermal with a temperature close to the upstream adiabatic one (assuming a recovery factor of 1). Note that the test filter is not applied in the wall-normal direction so that the no-slip condition is directly applicable to the filtered velocity field. The top (free-stream) and outflow boundaries make use of an integrated characteristic scheme (see Thompson, 1987; Sandhu and Sandham, 1994) in order to minimise unwanted reflections from the computational-box boundaries. The oblique shock is introduced at the top boundary using the Rankine–Hugoniot relationships. The inflow condition is the boundary condition to which particular attention was devoted at the early stage of this work and is the subject of the remainder of this chapter.

2.2.2 The inlet boundary condition issue

Both LES and DNS approaches, when used to compute fully turbulent flows, are faced with one common issue: the need to prescribe realistic inflow conditions. Ideally, these conditions should be time and space dependent, with the correct statistical moments, phase information and spectrum of the real turbulent flow they reproduce. In practice, this is impossible and one needs to cope with a certain level of approximation. The

amount of publications on this issue is probably as dense as the number of publications on the different LES sub-grid scale models. However, almost all the methods proposed to date fall into two subcategories: precursor methods and synthetic turbulence methods (the explanations will follow). This reflects two issues. First, that a sufficiently accurate and efficient general inflow-generation method does not exist. Then, that the two families of techniques both suffer from serious drawbacks. There is no intention here to establish a complete and detailed literature review on the subject, but rather to recall some important facts.

The precursor type of technique consists essentially in running an auxiliary calculation to provide the correct and targeted inflow conditions of an actual simulation. They achieve among the most realistic results (in the sense that they are the most accurate solutions) and are easy to control (meaning that it is easy to match the inflow characteristics, e.g. skin friction and integral parameters like the displacement thickness). Furthermore, they are relatively easy to implement. A good introduction on the topic can be found in Lund et al. (1998). We focus here on the case of turbulent boundary layers. Perhaps the most famous approach is the one initiated by Spalart (1988), later extended and greatly simplified by Lund et al. (1998). These are the so-called periodic and recycling techniques. The main idea is to extract an instantaneous plane from an auxiliary simulation and rescale it to the correct flow properties of the inflow plane of the actual simulation. The auxiliary simulation would typically generate its own inflow conditions by means of periodic boundary conditions in the stream-wise direction. The auxiliary simulation is thus, by construction, limited to homogeneous flow in the stream-wise direction. However, Spalart (1988) elegantly applied it to a boundary-layer simulation by a change of variables accounting for the spatial growth of the boundary layer. This resulted in the addition of source terms in the equations, which is the main reason for Spalart's method to be said to be complex, as one needs to evaluate the growth terms beforehand. However, this was greatly simplified by Lund et al. (1998), who allowed the auxiliary simulation to be quasi-periodic. Their idea was to only work with the inflow and outflow boundary conditions of the auxiliary simulation. In practice, the outflow plane is rescaled back to the inflow by decomposition of the fields into the mean and fluctuating components, both rescaled in a different and ingenious way (see Lund et al., 1998). To make it work, one only needs an empirical relation to relate the inflow wall shear to the solution downstream. By doing so, Lund et al. (1998) were able to generate inflow data for boundary layers at $\mathrm{Re}_{\delta_2} \in [1530\text{–}2150]$ with reported high accuracy and little or no adjustment of the flow at the inlet (due to errors introduced when rescaling the fields).

The drawbacks of such methods are readily mentioned in the literature – see Smirnov et al. (2001); Keating et al. (2004); Kornev and Hassel (2007); Klein et al. (2003); di Mare et al. (2006); Kempf et al. (2005); Veloudis et al. (2007); Jarrin et al. (2006) and

the references therein. Some of these are not relevant to the case of a fully turbulent boundary layer (e.g. issues with complex geometries, non-fully developed flows etc...) so that only the ones of direct relevance to the SBLI study are mentioned here. One of these is known as the pressure-drift issue. The method was first developed for incompressible boundary layers, and later extended to compressible boundary layers by Urbin and Knight (2001) and others – see Sagaut et al. (2004) for details. It is known that the compressible-boundary-layer versions of the method of Lund et al. (1998) can produce a drift either in the targeted boundary-layer thickness or in the displacement thickness. The rescaling of the thermodynamic quantities is in fact an issue and a correction was proposed by Sagaut et al. (2004). Perhaps the most significant drawback of the recycling/rescaling technique for the purposes of studying the possible low-frequency oscillations in SBLI, is the low frequency content introduced by the recycling process (for interesting plots of the velocity spectrum, see Keating et al., 2004). This could impair and mislead the SBLI investigations[1] (Adams, 1997; Edwards et al., 2008). This is the main motivation for not using this approach in the current work.

The second family of inflow-generation methods is fundamentally different. The idea here is to prescribe an artificial inflow field which mimics real turbulence (hence the name "synthetic"). The matching is usually performed on the first/second order statistical moments and on the velocity spectrum. One major consequence of the high level of approximation used is that the flow will be unphysical for some distance downstream of the inflow plane. In the boundary-layer case, such unphysical transients are usually of the order of ten to twenty inflow-boundary-layer thicknesses long. Indeed, although one can easily prescribe the right statistical moments and spectrum, it is unlikely that the phase information contained by such synthetic fields will also match that of real turbulence. The unphysical prescribed phase information will thus have to adjust itself downstream of the inlet plane until it becomes physically correct. Moreover, it is inherently difficult to predict the skin-friction and displacement-thickness values downstream of this transient regime. Despite the aforementioned drawbacks, synthetic inflow conditions are increasingly popular and numerous current research efforts seem to head towards synthetic methods. The number of papers on such techniques over the last five years is rather convincing.

The simplest approach would be to add random disturbances to the mean profiles and let them evolve to turbulence. Unfortunately, this is known to lead to relaminarisation of the flow (see Keating et al., 2004; Veloudis et al., 2007). Indeed, such an approach uniformly distributes the energy in the wave-number space and not enough energy is put into larger wavelengths. One possibility is to prescribe the correct spectral densities with random phase and perform an inverse Fourier transform (see Lee et al., 1992). This yields good results but applicable at reasonable cost only on uniform grids and it is not

[1]Private communication with Dr. Eric Garnier, ONERA (2007)

clear how to cope with non-homogeneous fields (Jarrin et al., 2006). However, Smirnov et al. (2001) have successfully enhanced a variant of the spectral approach for inhomogeneous, anisotropic turbulence. They were also able to achieve close to divergence-free velocity fields for inhomogeneous turbulence and truly divergence-free velocity fields for homogeneous turbulence, which may be of interest for aeroacoustic studies.

An alternative technique is to filter a random data field to achieve targeted spatial and temporal correlations. This technique is often called the "Digital Filter" approach (see the original paper of Klein et al., 2003). Improvements of the digital filter technique have been made by di Mare et al. (2006) where a more detailed method to obtain the coefficients of the filter is given. Veloudis et al. (2007) looked at the influence of using various filter widths in an attempt to better describe the different length-scales present in boundary layers as one moves in the wall-normal direction and concluded that the results with a single filter length-scale could still produce good-quality results. They also proposed an elegant way of decreasing the computational cost of the method (where a full 3D field has to be filtered) by performing the convolution in Fourier space. Xie and Castro (2008) have also greatly reduced the computational cost of the digital-filter approach by avoiding filtering in 3D. Instead, they correlate the previous 2D inflow plane data with the new one using an exponential function based on two weight factors.

It is worth mentioning a couple of other interesting approaches. For example, Kempf et al. (2005) have proposed to filter a random field using a diffusion equation and have found that it can lead to the same result as the digital-filter approach (which usually makes use of Gaussian filters), but with the interesting advantage of its simple use in complex geometries and inhomogeneous turbulence (as opposed to the use of a set of filters in the digital-filter approach which can be expensive on refined grids). Jarrin et al. (2006) report relatively short transients with their synthetic-eddy approach, which brings advantages over the digital-filter approach for complex geometries and inhomogeneous turbulence. Attempts to provide the right phase information rather than the first/second order one-point statistics were made by focusing more on known structures of turbulent boundary layers, as in Sandham et al. (2003) (discussed in more details in the next section). Johansson and Andersson (2004) also published an interesting alternative, somehow bridging the gap between the two families. In their paper, they use an auxiliary simulation to compute the evolution of the most energetic eddies using proper orthogonal decomposition. They then add random low-energy small-scale modes for the inflow condition of the actual simulation. The transient is thus relatively small since it only affects the small-scale modes, which recover relatively fast. However, this approach suffers from the need for a large enough database to compute the proper orthogonal decomposition basis. Finally, it is important to note that synthetic-inflow conditions based on filtering random numbers must use sufficiently large filters to represent the large-scale turbulent structures. It is shown in Keating et al. (2004) for example that

if eddies at least four times larger than the integral length-scale are not included, the flow can exhibit a longer transient or worst, relaminarise. The smaller the characteristic length of the filter is, the more random the perturbation field becomes, which is known to potentially lead to the relaminarisation issues.

In the following sections, the detailed procedure to generate both the mean inlet profiles and the fluctuating fields using either the synthetic turbulence or the digital filter approaches is provided.

2.2.2.1 Mean inflow profiles

In the following paragraphs, we will need to distinguish dimensional variables from normalised ones. The dimensional variables will be denoted by the superscript *star* as in $a^\star$, whereas the non-dimensional variables will have no superscript. Let us define the following integral transform:

$$\check{q}(y) = \int_{q(y=0)}^{q(y)} \sqrt{\frac{\rho}{\rho_w}} \mathrm{d}q', \tag{2.26}$$

which will be referred to as the van Driest transform. In the SBLI code, the reference lengthscale used is the inflow van Driest displacement thickness, defined as:

$$\check{\delta}_1 = \int_0^\infty [1 - \check{u}(\check{y})] \, \mathrm{d}\check{y}. \tag{2.27}$$

One main motivation to use the van Driest transform is that it is known to provide a useful approximation to transform the mean velocity profile of a compressible turbulent boundary layer into its incompressible counterpart (at least for the range of Mach numbers considered in this work).

The superscript *plus* as in a^+ will be used when the variable a is expressed in the standard wall-unit system. The subscript e denotes that the variable is evaluated at the boundary-layer edge while the subscript w indicates that the evaluation is performed at the wall. Stagnation variables are denoted by the subscript *zero*.

Mean velocity profile in the van Driest coordinate system — $\check{u}(\check{y})$ The semi-analytical mean velocity profile[2] in the van Driest coordinate (VD) system is generated following the operations below, for which the original motivations can be found in Sandham (1991) and its extension to compressible flows in Li's PhD thesis (Li, 2003):

[2]In this work, time-averaged quantities will usually be explicitly indicated using the usual *overline* notation (e.g. $\bar{u}$). However, since this paragraph focuses on the mean inlet profiles, the overline notation is not used to lighten the notation but it is implied that the variables considered in this paragraph are the time-averaged quantities (e.g. $u \equiv \bar{u}$).

1. Guess the value of the edge velocity (in the VD coordinate system), which will be denoted $\check{u}_e^+$ throughout this section.

2. Lay out a grid (in terms of velocity), i.e. spread out velocities between 0 and $\check{u}_e^+$: $\check{u}^+ \in [0, \check{u}_e^+]$.

3. Compute the corresponding $\xi^+(\check{u}^+)$ according to the formula proposed by Spalding (1961):

$$\xi^+(\check{u}^+) = \check{u}^+ + e^{-\kappa b}\left[e^{-\kappa\check{u}^+} - 1 - \left(\kappa\check{u}^+\right) - \frac{1}{2}\left(\kappa\check{u}^+\right)^2 - \frac{1}{6}\left(\kappa\check{u}^+\right)^3\right], \tag{2.28}$$

where κ is the von Karman constant and b the additive constant in the log-law (we assume $\kappa = 0.41$ and $b = 5.17$).

4. Change coordinate system according to:

$$\check{y}^+(\check{u}^+) = \frac{\xi^+(\check{u}^+)\xi_e^+}{\xi_e^+ - \xi^+(\check{u}^+)}, \text{ where } \xi_e^+ = \xi^+(\check{u}_e^+). \tag{2.29}$$

5. Let $\check{y}^\star$ be the physical distance from the wall. In the code, the reference length-scale is the displacement thickness computed on the VD velocity profile ($\check{\delta}_1$). The Reynolds number is defined as:

$$\check{\mathrm{R}}\mathrm{e}_{\check{\delta}_1^\star} \equiv \frac{\check{\rho}_e\check{u}_e^\star\check{\delta}_1^\star}{\check{\mu}_e}. \tag{2.30}$$

Then, note that in the incompressible-like VD-space, thermodynamic quantities are fixed so that $\check{\rho}_e^\star = \check{\rho}_w^\star$ and $\check{\mu}_e^\star = \check{\mu}_w^\star$. By definition, $\check{u}_e^+ = \check{u}_e^\star/\check{u}_\tau^\star$. One can write that $\check{y}^+ \equiv \check{y}^\star\check{u}_\tau^\star/\check{\nu}_w^\star = \check{y}^\star\check{\mathrm{R}}\mathrm{e}_{\check{\delta}_1^\star}/(\check{u}_e^+\check{\delta}_1^\star)$. Hence:

$$\check{y} \equiv \frac{\check{y}^\star}{\check{\delta}_1^\star} = \frac{\check{y}^+\check{u}_e^+}{\check{\mathrm{R}}\mathrm{e}_{\check{\delta}_1^\star}}. \tag{2.31}$$

6. The boundary thickness δ_0 (normalised by $\check{\delta}_1^\star$) is computed from:

$$\delta_0 = \frac{\check{u}_e^+\xi_e^+}{\alpha\check{\mathrm{R}}\mathrm{e}_{\check{\delta}_1^\star}} \quad \text{with} \quad \frac{1}{2}\ln(1+\alpha) = \frac{\check{\mathrm{R}}\mathrm{e}_{\check{\delta}_1^\star}}{690 + 1.5\check{\mathrm{R}}\mathrm{e}_{\check{\delta}_1^\star}}. \tag{2.32}$$

7. The velocity profile (normalised by the free-stream velocity) in the VD coordinate system is obtained from:

$$\check{u}(\check{y}) = 1 - f + \frac{\check{u}^+}{\check{u}_e^+}f, \tag{2.33}$$

where:

$$f = \exp\left\{-c\left[\exp\left(\eta^{1/\kappa}\right) - 1\right]\right\}, \quad \eta = \frac{\check{y}}{\delta_0} \quad \text{and} \quad c = 3.0. \tag{2.34}$$

8. The aforementioned process is repeated by changing the guessed edge-velocity value $\breve{u}_e^+$ in step 1 until:

$$\breve{\delta}_1 = \frac{\breve{\delta}_1^\star}{\breve{\delta}_1^\star} = \int_0^\infty (1 - \breve{u}(\breve{y}))\,\mathrm{d}\breve{y} = 1. \tag{2.35}$$

Mean velocity, temperature and density profiles — $u(y)$, $T(y)$, $\rho(y)$. The mean velocity profile computed in the previous paragraph is expressed in the VD space and one now needs to perform the inverse transform. The adiabatic wall temperature is:

$$T_{aw} = 1 + \frac{\gamma - 1}{2}\mathrm{M}_1^2. \tag{2.36}$$

The temperature-velocity relation is given by the Crocco–Busemann equation (White, 1991):

$$T = T_w + (T_{aw} - T_w)u - \frac{\gamma - 1}{2}\mathrm{M}_1^2 u^2. \tag{2.37}$$

If the wall is adiabatic, then $T_w = T_{aw}$. To remain general, let us proceed as if the wall was not adiabatic. The Crocco–Busemann relation is:

$$T = a + bu + cu^2 \quad \text{with} \quad a = T_w, \quad b = T_{aw} - T_w, \quad c = 1 - T_{aw}. \tag{2.38}$$

The VD transform is defined by the following integral:

$$\breve{u}^+ = \int_0^{u^+} \sqrt{\frac{\rho}{\rho_w}}\mathrm{d}u'^+. \tag{2.39}$$

Assuming that the pressure is constant across the boundary layer (the usual boundary-layer-equation approximation), the ideal gas law can be written $\rho T = \text{constant}$, so that the Crocco–Busemann relation can be substituted into the above integral to give:

$$\begin{aligned}\breve{u}^+ = u_e^+\sqrt{T_w}\int_0^u \frac{\mathrm{d}u'}{\sqrt{a + bu' + cu'^2}} \\ = u_e^+\sqrt{\frac{T_w}{-c}}\left[\sin^{-1}\left(\frac{b}{\sqrt{b^2 - 4ac}}\right) - \sin^{-1}\left(\frac{2cu + b}{\sqrt{b^2 - 4ac}}\right)\right].\end{aligned} \tag{2.40}$$

Solving the above equation at the boundary-layer edge yields:

$$u_e^+ = \frac{\breve{u}_e^+\sqrt{-c}}{\sqrt{T_w}\left[\sin^{-1}\left(\frac{b}{\sqrt{b^2 - 4ac}}\right) - \sin^{-1}\left(\frac{2c + b}{\sqrt{b^2 - 4ac}}\right)\right]}. \tag{2.41}$$

The x-component of the velocity profile is then:

$$u(\breve{u}) = \frac{\sqrt{b^2-4ac}\,\sin\left[\sin^{-1}\left(\frac{b}{\sqrt{b^2-4ac}}\right) - \breve{u}\frac{\breve{u}_e^+}{u_e^+}\sqrt{\frac{-c}{T_w}}\right] - b}{2c}. \tag{2.42}$$

The temperature and density profiles can then be computed from the velocity profile using the above Crocco–Busemann relation and the ideal-gas law (assuming the pressure to be constant across the boundary layer). One last operation is needed, however, to transform the VD coordinate $\breve{y}$ back to the normal coordinate y. As seen in the previous paragraph:

$$\breve{y}^+ = \frac{\breve{y}\breve{\mathrm{Re}}_{\breve{\delta}_1^\star}}{\breve{u}_e^+}. \tag{2.43}$$

Recall the following definitions:

$$y^+ = \frac{y^\star u_\tau^\star}{\nu_w^\star},\quad u_\tau^\star = \frac{u_e^\star}{u_e^+},\quad \breve{\mathrm{Re}}_{\breve{\delta}_1^\star} = \frac{\breve{u}_e^\star \breve{\delta}_1^\star}{\breve{\nu}_e^\star},\quad y = \frac{y^\star}{\breve{\delta}_1^\star}. \tag{2.44}$$

Using these definitions, one can write:

$$y^+ = \frac{y\breve{\mathrm{Re}}_{\breve{\delta}_1^\star}}{u_e^+}\frac{\breve{\nu}_e^\star}{\nu_w^\star}\frac{u_e^\star}{\breve{u}_e^\star}. \tag{2.45}$$

With $\breve{\nu}_e^\star/\nu_w^\star = \nu_e^\star/\nu_w^\star = \rho_w/\mu_w$, $u_e^\star/\breve{u}_e^\star = 1$ and $\breve{y}^+ = y^+$:

$$y = \frac{u_e^+}{\breve{u}_e^+}\frac{\mu_w}{\rho_w}\breve{y}. \tag{2.46}$$

Assuming a power-law dependence for the dynamic viscosity ($\mu = T^\Omega$, see (2.1g)):

$$y = \frac{u_e^+}{\breve{u}_e^+}T_w^{\Omega+1}\breve{y}. \tag{2.47}$$

Mean profile for the wall-normal component of the velocity — $v(y)$. Despite the fact that boundary-layer growth is an important feature to be simulated, it is common practice to set the wall-normal velocity to zero at the inflow plane. Such a crude approximation will unavoidably result in an unphysical boundary-layer growth in the first grid points of the computational box. In addition, the inconsistency produced by this approximation can generate an oblique shockwave at the inlet plane that will modify the targeted upstream flow conditions. However, one may argue that the synthetic turbulent inflow boundary conditions will also generate unphysical results and that it is questionable whether prescribing the correct BL growth is of significant importance. Nevertheless, although the added disturbances will result in unphysical fields, it is felt that prescribing the correct growth in the mean profile is helpful to reduce the inflow

transient and the strength of the aforementioned shockwave emanating from the inflow plane.

To prescribe the BL growth, a second stream-wise velocity profile is generated slightly downstream of the first profile. From those two profiles $u(y)$, one can evaluate the stream-wise velocity gradient. Once determined, this gradient is then used to integrate the continuity equation (the mean span-wise velocity being zero). The second velocity profile needs to be related to the first one. Unfortunately, this can only be done with the help of empirical relations. For the present simulations, we have used equations (6.68) and (6.69) on page 430 of White (1991): $\mathrm{Re}_{\delta_0} = (C_f/0.02)^{-6}$ and $\mathrm{Re}_x = (\mathrm{Re}_{\delta_0}/0.16)^{7/6}$. For further details, please refer to the copy of the in-house routine to generate the aforementioned inflow mean profiles, made available in Appendix B.

Once the inflow mean profiles are obtained using the above method, the fluctuating fields can be generated and added to the mean profiles to produce the final time-dependent inflow conditions.

2.2.2.2 Fluctuations

Added perturbations: the synthetic turbulence approach In this section, the synthetic turbulence (ST) approach to generate the fluctuations for the TBL generation is described in detail. The general idea of the method is to prescribe inflow disturbances that mimic the accepted deterministic features of turbulent boundary layers by introducing specific inner- and outer-layer disturbances with associated phase information (see Yao and Sandham, 2002; Sandham et al., 2003). Disturbances in the inner region (denoted $u_{i<}$) represent lifted streaks (with a peak location at $\mathring{d}_1^+$) while the outer-region disturbances (denoted $u_{i>}$) represent three-dimensional vortices.

In Sandham et al. (2003), these disturbances were expressed as for an incompressible boundary layer and the method was then extended to supersonic boundary-layer flows (Mach 2) by Li (2003). The extension to compressible boundary layer is based on the semi-local scaling proposed by Huang et al. (1995) and demonstrated for example by Coleman et al. (1995) in channel-flow simulations. Data expressed using this semi-local scaling appear to match well with incompressible data (Morkovin's hypothesis) as shown for example in the Mach 2.5 DNS of a turbulent boundary layer by Guarini et al. (2000). Therefore, the disturbances previously expressed for an incompressible turbulent boundary layer can be simply re-scaled to the case of a compressible boundary layer.

Inner-layer modes Semi-local quantities will be denoted[3] by $\mathring{a}$. We have:

$$\mathring{u}_\tau^\star \equiv \sqrt{\frac{\mu_w^\star}{\rho^\star(y)}\left.\frac{\partial u^\star}{\partial y^\star}\right|_{y^\star=0}} = \sqrt{\frac{\rho_w}{\rho(y)}}u_\tau^\star, \tag{2.48}$$

$$\mathring{y}^+ \equiv \frac{y^\star \mathring{u}_\tau^\star}{\nu(y)^\star} = \sqrt{\frac{\rho_w}{\rho(y)}}\frac{y^\star u_\tau^\star}{\nu_w^\star}\frac{\nu_w^\star}{\nu(y)^\star} = y^+\frac{\mu_w\rho(y)}{\mu(y)\rho_w}\sqrt{\frac{\rho_w}{\rho(y)}} = \frac{y\check{\mathrm{Re}}_{\check{\delta}_1^\star}}{u_e^+}\frac{\rho(y)\sqrt{\rho_w}}{\mu(y)\sqrt{\rho(y)}}. \tag{2.49}$$

Assuming the power-law relation $\mu = T^\Omega$ and recalling that $\rho = 1/T$ (if the pressure is assumed constant across the boundary layer), one finds:

$$\mathring{y}^+ = \frac{y\check{\mathrm{Re}}_{\check{\delta}_1^\star}}{u_e^+}\frac{1}{\sqrt{T_w}T(y)^{\Omega+1/2}}. \tag{2.50}$$

Note that we have u_e^+ in the above expression and not $\check{u}_e^+$.
Similarly:

$$\mathring{u}^+ = \frac{u^\star}{\mathring{u}_\tau^\star}, \quad u^+ = \frac{u^\star}{u_\tau^\star}, \tag{2.51}$$

$$\mathring{u}^+ = u^+\sqrt{\frac{T_w}{T(y)}}. \tag{2.52}$$

The angular frequency ϖ_1 of the disturbances sets the stream-wise distance λ_x they cover at a convective velocity u_c over one period τ:

$$\varpi_1 = \frac{2\pi}{\tau}, \quad \tau = \frac{\lambda_x}{u_c}. \tag{2.53}$$

Note the following:

$$\mathring{\lambda}_x^+ \equiv \frac{\lambda_x^\star \mathring{u}_\tau^\star}{\nu(y)^\star} = \frac{\lambda_x\check{\mathrm{Re}}_{\check{\delta}_1^\star}}{u_e^+}\frac{\rho(y)\sqrt{\rho_w}}{\mu(y)\sqrt{\rho(y)}}, \tag{2.54}$$

$$\mathring{u}_c^+ = u_c^+\sqrt{\frac{\rho(y)}{\rho_w}} = u_e^+ u_c\sqrt{\frac{\rho(y)}{\rho_w}}, \tag{2.55}$$

$$\tau = \frac{\mathring{\lambda}_x^+}{\mathring{u}_c^+}\frac{{u_e^+}^2}{\check{\mathrm{Re}}_{\check{\delta}_1^\star}}\frac{\mu(y)}{\rho_w}. \tag{2.56}$$

The convective velocity $\mathring{u}_c^+$ can be expressed as a fraction of the friction velocity:

$$\mathring{u}_c^+ = \chi\mathring{u}_\tau^+, \quad \mathring{u}_\tau^+ = u_\tau^+\sqrt{\frac{\rho(y)}{\rho_w}} \equiv \frac{u_\tau^\star}{u_\tau^\star}\sqrt{\frac{\rho(y)}{\rho_w}} = \sqrt{\frac{\rho(y)}{\rho_w}}. \tag{2.57}$$

[3]Most of the notations introduced in this paragraph are not reported in the nomenclature since their use is strictly limited to this paragraph.

In Sandham et al. (2003), $\chi = 10$ and $\mathring{\lambda}_x^+ = 500\pi$.
Hence (using a power law for μ):

$$\varpi_1 = \underbrace{\left[\frac{2\pi\chi}{\mathring{\lambda}_x^+}\right]}_{\omega_1} \frac{\check{\mathrm{Re}}_{\check{\delta}_1^\star}}{u_e^{+2}} \frac{\sqrt{\rho(y)\rho_w}}{\mu(y)} = \omega_1 \frac{\check{\mathrm{Re}}_{\check{\delta}_1^\star}}{u_e^{+2}} \frac{1}{\sqrt{T_w} T(y)^{\Omega+1/2}}. \tag{2.58}$$

Finally, we want N_1 near-wall streaks in the span of length L_z spaced by $\mathring{\lambda}_z^+$ ($\mathring{\lambda}_z^+ = 100$ in Sandham et al., 2003). The z-dependence of the disturbances is in $\cos(\zeta_1 z)$. Hence:

$$\zeta_1 = \frac{2\pi N_1}{L_z} \quad \text{and} \quad \mathring{\lambda}_z^+ = \frac{L_z \check{\mathrm{Re}}_{\check{\delta}_1^\star}}{u_e^+} \frac{\rho_w}{\mu_w} = \frac{L_z \check{\mathrm{Re}}_{\check{\delta}_1^\star}}{u_e^+} \frac{1}{T_w^{\Omega+1}}. \tag{2.59}$$

L_z should thus be chosen such that $\mathring{\lambda}_z^+$ is of the order of 100.

The inner-layer perturbations in Sandham et al. (2003) (equations (5) and (6)) are (in their incompressible-like form):

$$\mathring{u}_<^+(x=0,y,z,t) = c_{1,1}\mathring{y}^+ \exp\left(-\mathring{y}^+/\mathring{d}_1^+\right) \sin(\varpi_1 t)\cos(\zeta_1 z + \phi_1), \tag{2.60a}$$

$$\mathring{v}_<^+(x=0,y,z,t) = c_{2,1}\mathring{y}^{+2} \exp\left[-\left(\mathring{y}^+/\mathring{d}_1^+\right)^2\right] \sin(\varpi_1 t)\cos(\zeta_1 z + \phi_1). \tag{2.60b}$$

Note that the velocities are expressed in wall units. The conversion to normal units is:

$$\mathring{u}_{i_<} = \frac{1}{u_e^+}\sqrt{\frac{T_w}{T(y)}}\mathring{u}_{i_<}^+ = u_{i_<}. \tag{2.61}$$

In the present simulations, the above original equations were slightly modified, based on the argument that the second mode used in Li (2003) is also located in the inner-layer. The definition of the coefficients was also modified to make them Reynolds-number independent. A summary of the equations being currently used to generate the perturbations will follow.

Outer-layer modes The modifications from the incompressible form of the outer-layer modes (Sandham et al., 2003) is straightforward as one only needs to ensure that lengths are made dimensionless using the displacement thickness computed on the VD velocity, which is the case here.

The equations at glance and the parameter values The present variant of the ST approach proposed by Sandham et al. (2003) is given below. In the original version, the span-wise fluctuations were computed from the stream-wise and wall-normal fluctuations via the continuity equation. However, this is found to produce rather sharp and

severe oscillations in the RMS profile of the spanwise fluctuations. Instead, the continuity equation is not used and spanwise fluctuations are prescribed in the same manner as for the streamwise and wall-normal fluctuations.

Inner-layer mode:

$$u_{i_<}(0,y,z,t) = 2\exp(1)\sqrt{\frac{\rho_w}{\rho(y)}}\sum_{j=1}^{2} c_{i,j}\left[F(y)\frac{y}{d_j}\right]^{p_{i,j}} \exp\left[-\left(F(y)\frac{y}{d_j}\right)^{p_{i,j}}\right] \times \sin\left[\omega_j \frac{F(y)}{u_e^+} t\right] \cos\left[\frac{2\pi N_j}{L_z} z + \phi_j\right], \quad (2.62a)$$

where:

$$F(y) = \frac{\check{\mathrm{R}}\mathrm{e}_{\check{\delta}_1^\star}}{u_e^+\sqrt{T_w}T(y)^{\Omega+1/2}}, \quad \Omega = 0.67, \quad (2.62b)$$

$$u_e^+ = \check{u}_e^+ \frac{\sqrt{(T_{aw}-1)/T_w}}{\sin^{-1}\left[\frac{T_{aw}-T_w}{\sqrt{(T_{aw}+T_w)^2-4T_w}}\right] - \sin^{-1}\left[\frac{2-T_{aw}-T_w}{\sqrt{(T_{aw}+T_w)^2-4T_w}}\right]}, \quad (2.62c)$$

$$T_{aw} = 1 + \frac{\gamma-1}{2}\mathrm{M}_1^2. \quad (2.62d)$$

Outer-layer mode:

$$u_{i_>}(0,y,z,t) = 2\exp(1)\sqrt{\frac{\rho_w}{\rho(y)}}\sum_{j=3}^{4} c_{i,j}\left[\frac{y}{d_j}\right]^{p_{i,j}} \exp\left[-\left(\frac{y}{d_j}\right)^{p_{i,j}}\right] \times \sin(\omega_j t) \cos\left[\frac{2\pi N_j}{L_z} z + \phi_j\right]. \quad (2.62e)$$

	j	$c_{1,j}$	$c_{2,j}$	$c_{3,j}$	$p_{1,j}$	$p_{2,j}$	$p_{3,j}$	d_j	ω_j	N_j	ϕ_j
Inner modes	1	0.10	-0.025	-0.09	1	2	2	12.0	1/25	8	0.00
	2	0.10	-0.06	-0.09	1	2	2	45.0	1/4	6	0.00
Outer modes	3	0.05	-0.05	-0.07	2	2	2	2.0	1/8	4	0.10
	4	0.08	-0.045	-0.05	2	2	2	4.0	1/16	3	0.15

TABLE 2.2: Parameters used for the synthetic turbulence inflow conditions (2.62 *a,e*)

Results from the above procedure will be given together with the results from the second technique that was implemented. This second method is the digital-filter approach and is the subject of the next paragraph.

Added perturbations: the digital filter approach The digital-filter (DF) method is a statistical approach to the inflow-condition specification problem where the turbulence first- and second-order statistical moments are imposed by means of filtered random data sets. It offers the possibility to prescribe both the Reynolds-stress tensor and the energy spectra. However, it does not allow for a direct control on the instantaneous fields, which are generally unphysical and responsible for the observed transient states downstream of the inflow plane. This will be discussed further, after the following DF-approach presentation, in a comparative study between the DF and ST methods.

Let $\{r_k\}_{1\leq k\leq p}$ be a set of p random numbers with zero-mean ($\overline{r_k} \equiv \sum_{k=1}^{p} r_k/p = 0$) and unit-variance ($\overline{r_k r_k} = \sum_{k=1}^{p} r_k^2/p = 1$)[4]. Let N be a positive integer and F_N the following discrete filter operator[5]:

$$v_k \equiv F_N(r_k) = \sum_{j=-N}^{N} b_j r_{k+j}, \tag{2.63}$$

where $\{b_j\}_{-N\leq j\leq N}$ is a set of real numbers to be defined later. Noting that the above filter operator is linear, making the averaging and filtering operations commute, and that the set $\{r_k\}_{1\leq k\leq p}$ is composed of zero-mean and unit-variance random numbers, one can easily show that:

$$\overline{v_k} = 0, \text{ and } \overline{v_k v_{k+q}} = \sum_{j=-N+q}^{N} b_j b_{j-q}. \tag{2.64}$$

The two-point-correlation function is modelled (in 1D for simplicity):

$$R(x_k + x) = \exp\left(-\frac{\pi x}{2I_x}\right), \tag{2.65}$$

where x_k is a reference point, x some distance away from the reference point and I_x a given integral length scale. Note that in the original paper of Klein et al. (2003), the authors assume a Gaussian auto-correlation function. However, Xie and Castro (2008) argue that auto-correlation functions have a form closer to exponential than Gaussian, hence the current choice of exponential correlation function. This will inevitably produce an energy-decay rate of -2 in place of the expected -5/3 law. However, it is argued that this choice of function is correct for the large-scale structures and that most of the discrepancies will occur at the smallest scales (Xie and Castro, 2008), which are found to recover the modelling errors more rapidly than the large-scale structures.

[4]Note that the *overline* notation has a different meaning in this paragraph where it no longer stands for the grid-filter operator but for the arithmetic mean operator.

[5]Similarly to the previous paragraph, most of the numerous notations introduced here are not reported in the nomenclature since their use is strictly limited to this paragraph.

On the computational grid, if n is such that $I_x = n\Delta x$ and that $x = q\Delta x$, the two-point-correlation function becomes:

$$R(x_k + q\Delta x) \equiv \frac{\overline{v_k v_{k+q}}}{\overline{v_k v_k}} = \exp\left(-\frac{\pi q}{2n}\right), \tag{2.66}$$

leading to the system:

$$\frac{\sum_{j=-N+q}^{N} b_j b_{j-q}}{\sum_{j=-N}^{N} b_j^2} = \exp\left(-\frac{\pi q}{2n}\right), \tag{2.67}$$

the solution of which can be approximated by:

$$b_k \approx \frac{b'_k}{\left(\sum_{j=-N}^{N} {b'_j}^2\right)^{1/2}} \quad \text{with } b'_k = \exp\left(-\frac{\pi k}{n}\right). \tag{2.68}$$

Klein et al. (2003) find the above approximation to be good if $N \geq 2n$ (this is not found to be a computationally expensive requirement).

Upon application of the F_N-operator with the above definition for the convolution coefficients, the initial random field of zero-mean and unit-variance has been given a coherence integral length scale I_x. Note that the above 1D description can be extended to 2D by simply defining the 2D convolution coefficients as: $b_{jk} = b_j b_k$.

The step-by-step procedure to produce the inlet flow-variable fluctuations is as follows. First, the integral lengthscales I_x, I_y, I_z to prescribe must be known. Given the grid spacing, these lengthscales are converted into an equivalent number of grid points, i.e. $n_{I_x} = I_x/\Delta x$. This sets the filter size: $N_{F_x} = 2n_{I_x}$. In the current implementation, a zonal approach is used by defining two different sets of filters in the near-wall region and the outer-region, as in Veloudis et al. (2007). Then, the convolution coefficients $\{b_k\}_{-N_{F_x} \leq k \leq N_{F_x}}$ are computed as shown in the above equation (in 1D).

Next, a set of random numbers with a normal distribution about zero and unit variance is acquired. Since a large number of such sets will be needed, it is worth noting the following improvement over the commonly used approach to obtain a normal distribution. Most pseudo-random number generators will generate uniformly distributed numbers and one usually achieves a normal distribution simply by adding many (12 in Xie and Castro, 2008) of those uniformly distributed sets and invoking the central limit theorem. However, using the Box–Muller transform, one only needs two sets: if a and b are two independent numbers uniformly distributed in $(0, 1]$, combining them such that $c = \cos(2\pi b)\sqrt{-2\ln(a)}$ and $d = \sin(2\pi b)\sqrt{-2\ln(a)}$ will make c and d be two independent numbers from a normal distribution of unit standard deviation.

Once the normally-distributed random numbers with zero-mean and unit-variance are obtained, they are filtered using the previously-computed convolution coefficients: $v_k \equiv F_{N_{F_x}}(r_k) = \sum_{j=-N_{F_x}}^{N_{F_x}} b_j r_{k+j}$ (in 1D). The pseudo velocity field v_k has now the prescribed lengthscale I_x. Next, the computed field v_k is correlated with the previous

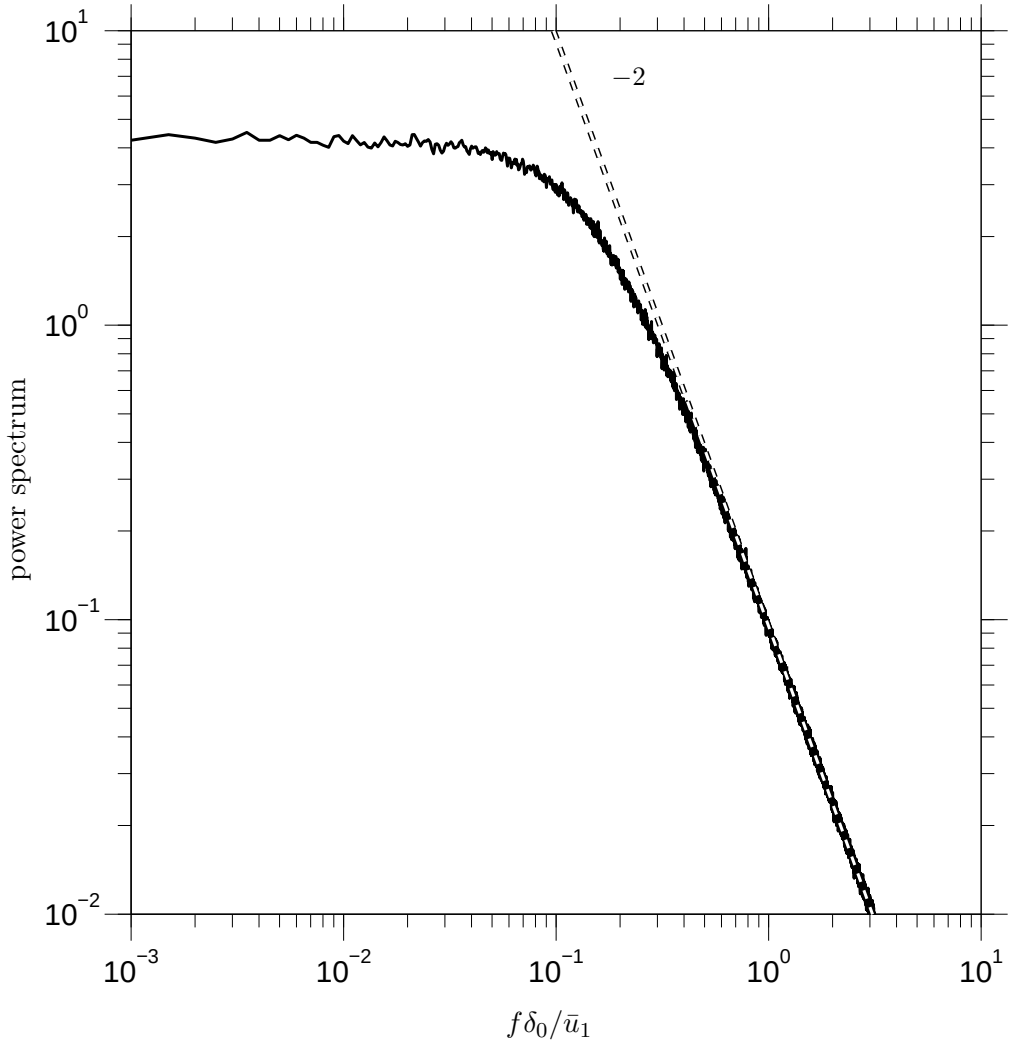

FIGURE 2.2: Spectrum of $\varrho_k(t)$ obtained from (2.69) using $I_x = \delta_0$ and $\bar{u} = 0.6\bar{u}_1$

one, v_k^{old}. (Except of course when performing the very first time step.) The following correlation function was suggested by Xie and Castro (2008) to avoid having to filter a 3D field as in the original paper of Klein et al. (2003):

$$\varrho_k = \varrho_k^{\text{old}} \exp\left(-\frac{\pi\Delta t}{2\tau}\right) + v_k \sqrt{1 - \exp\left(-\frac{\pi\Delta t}{\tau}\right)}, \tag{2.69}$$

where Δt is the time step and τ the Lagrangian timescale ($\tau = I_x/\bar{u}$ in the present implementation, where $\bar{u}$ and I_x are the prescribed inlet mean stream-wise velocity and integral length scale, respectively). Figure 2.2 illustrates the power spectrum obtained using (2.69). As mentioned earlier, the spectrum rolls off with a -2 slope in place of the expected $-5/3$ law.

The field ϱ_k now contains all the enforced two-point correlation functions as well as the prescribed stream-wise correlation. The single-point correlations can now be

specified, as originally proposed by Lund et al. (1998). In 3D, it can be written:

$$\begin{bmatrix} u(0,y,z,t) \\ v(0,y,z,t) \\ w(0,y,z,t) \end{bmatrix} = \underbrace{\begin{bmatrix} \langle u(0,y,z)\rangle_t \\ \langle v(0,y,z)\rangle_t \\ \langle w(0,y,z)\rangle_t \end{bmatrix}}_{\bar{u}_i(0,y)} + \underbrace{\begin{bmatrix} \sqrt{R_{11}} & 0 & 0 \\ R_{21}/\sqrt{R_{11}} & \sqrt{R_{22}-\left(R_{21}/\sqrt{R_{11}}\right)^2} & 0 \\ 0 & 0 & \sqrt{R_{33}} \end{bmatrix} \begin{bmatrix} \varrho_1(y,z) \\ \varrho_2(y,z) \\ \varrho_3(y,z) \end{bmatrix}}_{u_i'(0,y,z,t)}, \quad (2.70)$$

where $\{R_{ij}\}_{(i,j)\in\{1,2,3\}}$ is the prescribed Reynolds-stress tensor.

The inflow time-dependent velocity field has now been built and there remains to specify the thermodynamic variables. To generate the thermodynamic fluctuations, the previously determined velocity perturbations u_i' are used, invoking the Strong Reynolds Analogy (SRA):

$$\frac{T'}{\bar{T}} = -(\gamma-1)\mathrm{Ma}^2\frac{u'}{\bar{u}}, \quad \text{with} \quad \mathrm{Ma}^2 = \frac{\bar{u}^{\star 2}}{\gamma^\star R^\star \bar{T}^\star} = \mathrm{M}^2\frac{\bar{u}^2}{\bar{T}}, \quad (2.71)$$

where the *overline* notation is used to denote that the variable is time averaged.

The validity of the SRA is debatable. In fact, from the DNS of Guarini et al. (2000), it is known that the above equation is wrong in general. However, it is also shown to be correct in a weaker sense, in that it provides the correct RMS correlation (see Guarini et al., 2000). Recently, Martin (2007) obtained good results using the SRA as a means to initialise the flow in a DNS. The use of the SRA is thus deemed acceptable as a first approach.

Once T' is computed from the above equation, assuming that the pressure is constant across the boundary layer (invoking the boundary-layer approximation) and that the pressure fluctuations are negligible compared to the velocity, density and temperature fluctuations (an hypothesis already used in the SRA), one finds:

$$\frac{\rho'}{\bar{\rho}} = -\frac{T'}{\bar{T}}. \quad (2.72)$$

All the inflow variables are now prescribed and one can go through the above procedure again at the following time step.

In this work, the uniformly-distributed pseudo-random numbers are obtained from the Mersenne Twister generator (see Matsumoto and Nishimura, 1998). Using the Box–Muller transform, each time step will require two sets of $3 \times N_y \times N_z$ random numbers (3 velocity components in the inflow plane with N_y and N_z both in the order of 10^2).

Given the Mersenne Twister generator period of $2^{19937} - 1$, we are guaranteed not to introduce any cyclic behaviour in the computational domain, which is a desired feature for the low-frequency study in SBLI. In addition, the combined use of the Box–Muller theorem, the Mersenne Twister generator and the 2D filtering approach of Xie and Castro (2008) (as opposed to the 3D approach by Klein et al., 2003) produce an efficient method which is not found (in practice) to be slower than the analytical ST approach of Sandham et al. (2003).

The digital-filter coefficients used in the current simulations are provided in table 2.3. Note that a TBL simulation is performed prior to the SBLI simulations in order to compare the DF and ST approaches for a computationally less expensive configuration. The DF settings differ slightly between the TBL and SBLI cases. However, it was found while implementing the DF approach that this technique is relatively robust to the choice of filter coefficients, which is an interesting and desirable feature. This is true as long as the prescribed coherence lengthscales are larger than the integral lengthscales of the real flow. Failing to meet that requirement can lead to laminarisation issues (Keating et al., 2004; Veloudis et al., 2007), as when only white noise is added to the flow (see the earlier discussion on this issue). The prescribed mean-velocity profile is obtained from the semi-analytical method described at the beginning of this section and the prescribed Reynolds stresses were obtained from an earlier simulation under similar flow conditions as the ones to be considered here. A copy of the digital-filter Fortran routines is available in appendix C.

Velocity component		u		v		w	
		TBL	SBLI	TBL	SBLI	TBL	SBLI
$I_x/\check{\delta}_1$		10	10	4	4	4	4
$N_{F_y} = 2I_y/\Delta y,$	if $y \leq \check{\delta}_1$	35	20	45	25	30	15
	if $y > \check{\delta}_1$	65	35	85	45	40	20
$N_{F_z} = 2I_z/\Delta z$		15	20	15	20	30	30

TABLE 2.3: Digital Filter coefficients

2.2.2.3 Test on a flat plate turbulent boundary layer

The previously described DF and ST inflow-generation techniques are compared for a Mach 2 and $\mathrm{Re}_{\check{\delta}_1} \approx 2500$ turbulent flat-plate boundary-layer flow. The numerical details are given in table 2.4.

Axis direction		x	y	z
Domain size	L_x, L_y, L_z in $\breve{\delta}_1$	400	50	20
	L_x, L_y, L_z in δ_0	28	3.5	1.7
Number of points	N_x, N_y, N_z	401	151	81
Grid resolution	Δx^+, $\Delta y^+_{\min}$, Δz^+	33	1.6	10

TABLE 2.4: Numerical details for the turbulent-boundary-layer simulations

Figure 2.3 compares the skin-friction evolution obtained for both the DF and the ST inlet methods. The two techniques produce a transient of about 20 boundary-layer thicknesses, as expected for such approaches (Keating et al., 2004). Despite the fundamental differences in the formulation of each technique, the skin friction appears to converge to the expected levels at a similar stream-wise location. This indicates that the near-wall region is not sensitive to the prescribed inlet method. This is probably because the near-wall turbulence structures recover from the modelling errors fairly quickly and neither of the two approaches perform better there. However, figure 2.4 compares the van Driest velocity profiles obtained at $x/\delta_0 \approx 15$ and some differences are found in the outer-region. Although both approaches produce the expected near-wall asymptotic behaviour of a turbulent flow, the wake-region does not appear to be realistic in the case of the synthetic turbulence. This is further seen in the turbulence statistics at the same stream-wise station, as shown in figures 2.5 and 2.6. In figure 2.5, the inner-layer scaling with the compressibility correction of Huang et al. (1995) is used for comparison with the DNS data of an incompressible turbulent boundary layer (Spalart, 1988) whereas figure 2.6 is plotted using the displacement thickness. Both figures exhibit the presence of a second spurious peak in the RMS profiles for the synthetic-turbulence method. This unexpected distribution of the turbulence energy is due to the presence of a low-frequency, large-wavelength mode, which was introduced at the inlet, and is found to survive for long stream-wise distances, even up to the outflow boundary. Further downstream, the ST results eventually converge to the DF ones. The ability of the last outer mode to survive for such distances was not observed in Sandham et al. (2003). This may be due to the higher Mach and Reynolds numbers used here, potentially stabilising this outer mode, since the method was found to be successful for a subsonic boundary layer.

With respect to the SBLI simulations, we clearly do not wish to force a particular low-frequency/long-wavelength mode as this could directly impair the low-frequency study in the interaction. This is the main reason for choosing the DF, since it is able to produce realistic inflow conditions with the guarantee to avoid any cyclic pattern. In fact, the DF formulation is convenient since it provides a direct control on the size of the coherent structures introduced at the inlet. In the present SBLI study, the integral

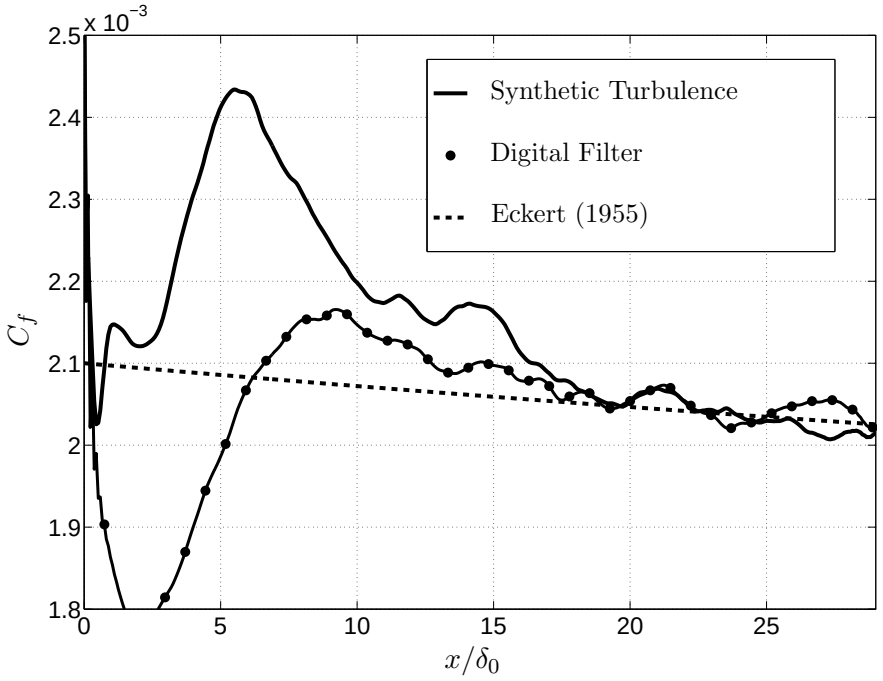

FIGURE 2.3: Skin-friction evolution: digital filter *vs* synthetic turbulence

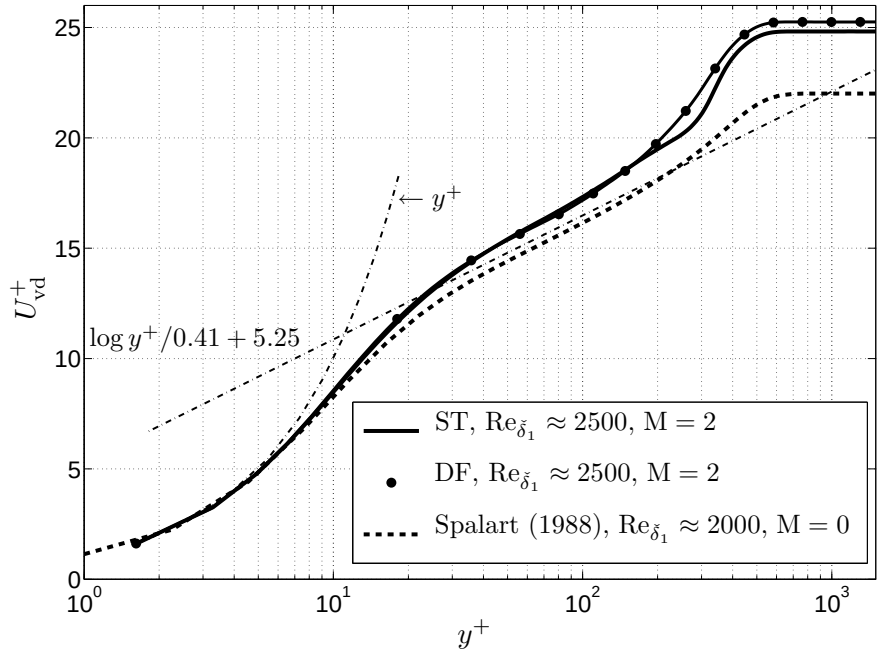

FIGURE 2.4: Velocity profiles at $x/\delta_0 \approx 15$: digital filter *vs* synthetic turbulence

lengthscale used in the exponential correlation function is set to be less than $0.6\delta_0$. Of course, larger structures can develop in the domain by the time the flow reaches the interaction. However, since the available domain before the interaction will be of the order of $10\delta_0$ long, no structure longer than about ten boundary-layer-thicknesses long

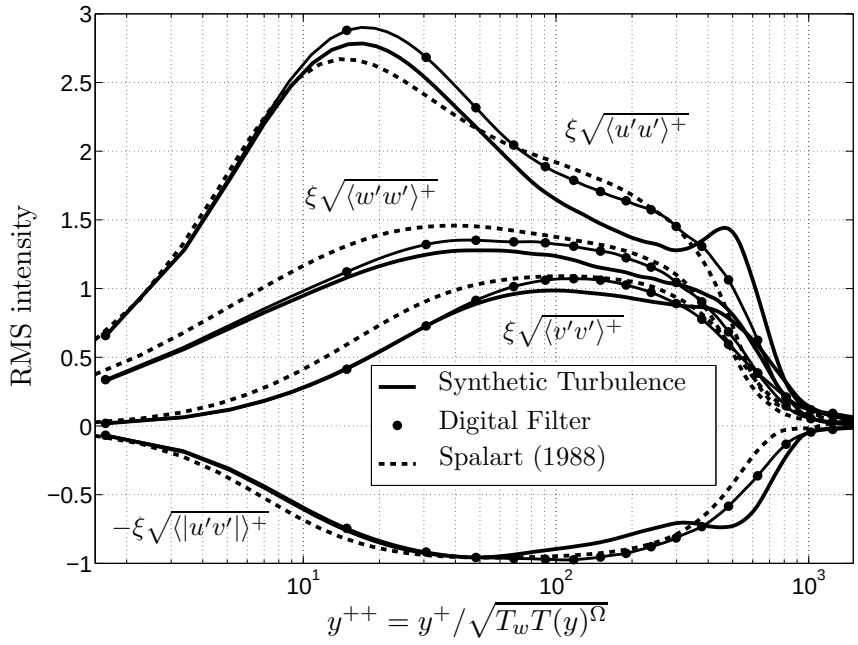

FIGURE 2.5: Turbulence intensities at $x/\delta_0 \approx 15$: digital filter *vs* synthetic turbulence. Note that the density correction $\xi = \sqrt{\rho(y)/\rho_w}$ was applied

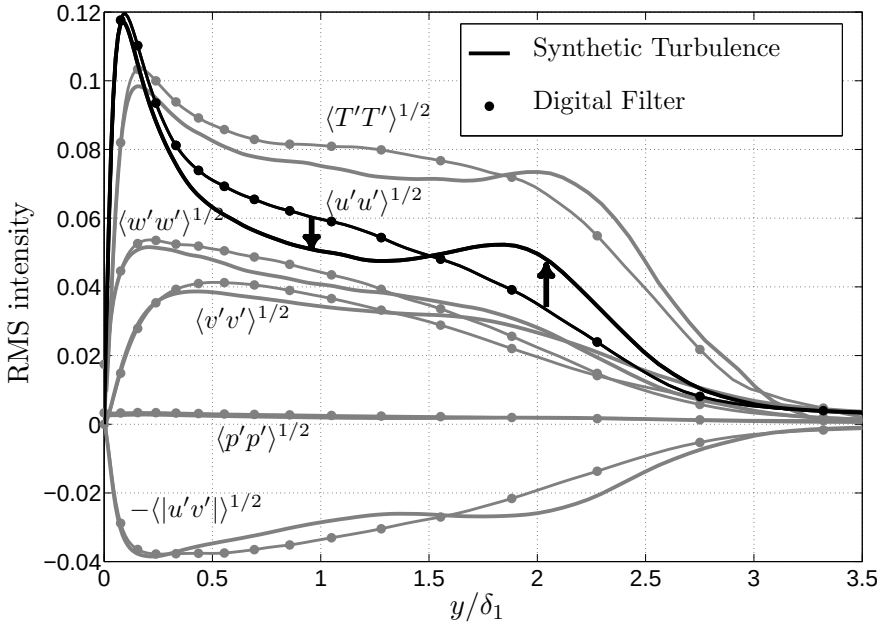

FIGURE 2.6: Turbulence intensities at $x/\delta_0 \approx 15$: digital filter *vs* synthetic turbulence

can form upstream of the interaction. Evidences on the absence of any upstream low-frequency forcing will be provided in a later chapter.

In this chapter, the numerical procedure and in particular the LES formulation together with the choice of inlet conditions has been described in detail. Now, equipped with the numerical strategy, the first SBLI LES can be performed in order to validate and gain confidence in this approach. Thus, the next chapter is devoted to the validation of the code through grid/domain convergence studies, SGS-model-effect studies as well as comparisons with existing data (LES and PIV).

3. Validation of the numerical strategy

In this chapter, eight different LES of the same flow configuration will be presented as the basis for the code validation, together with PIV and LES results from earlier independent studies. The main objective is to gain sufficient experience and confidence with the numerical approach to justify the choices of grid resolution, sub-grid scale model and domain sizes to be used in the final shock/boundary-layer simulations.

3.1 Flow conditions and numerical settings

The flow considered in this chapter corresponds to an experiment performed by the supersonic research group at the "Institut Universitaire des Systèmes Thermiques Industriels" (IUSTI). It consists in a Mach 2.3 flat-plate TBL impinged by an oblique shock-wave generated by an 8° turning angle wedge placed in the potential flow. The Reynolds number based on the displacement thickness δ_1^{imp} evaluated at the impingement point in the absence of the shock is about 21×10^3. The PIV data used in this chapter for this configuration are described in Dupont et al. (2008). The same shock-reflection configuration was studied using LES by Garnier et al. (2002), where the authors had also looked at grid-size and SGS-model effects on the time-averaged results.

As shown in tables 3.1 and 3.2, the eight LES differ in the choice of grid resolution, SGS model and spanwise extent. The choice of the reference grid is largely based on the findings of Garnier et al. (2002). The grid refinement study is limited to one direction at a time. In addition to limiting the increase of the computational cost of each single refinement, this approach is advantageous in that it allows for the identification of the most sensitive direction. Moreover, this can highlight situations where errors cancel in a favourable way. Refining the grid in all three directions at a time by the same amount may fail to detect such patterns. However, the refinement in the wall-normal direction is not uniquely defined because of the grid stretching. As shown in table 3.1, it was decided to use the additional grid points to relax the stretching coefficient so that the near-wall resolution stayed the same whereas the outer-region resolution was improved by nearly a factor two. The benefit of this is to focus on the effect of the shock-system

Case	Reference	Refined in x	Refined in y	Refined in z
Domain size				
L_x, L_y, L_z in $\check{\delta}_1$	450, 70, 24	450, 70, 24	450, 70, 24	450, 70, 24
L_x, L_y, L_z in δ_1^{imp}	71.9, 11.2, 3.8	71.9, 11.2, 3.8	70.0, 10.7, 3.6	72.3, 11.3, 3.8
L_x, L_y, L_z in δ_0	25.4, 4.0, 1.4	25.5, 4.0, 1.4	25.4, 4.0, 1.4	25.4, 4.0, 1.4
Number of points				
N_x, N_y, N_z	451, 81, 73	901, 81, 73	451, 161, 73	451, 81, 145
Grid resolution[a]				
Δx^+, Δy^+_{min}, Δz^+	40.6, 1.6, 13.5	20.3, 1.6, 13.5	40.6, 1.5, 13.5	40.6, 1.6, 6.8
Grid stretching[b] β_y	5.50	5.50	4.75[c]	5.50
Statistics				
sampling rate[d]	5	5	5	5
$\Delta t\, \bar{u}_1/\check{\delta}_1$	0.025	0.045	0.045	0.045
number of FTT[e]	9	6	11	7
SGS model	MTS	MTS	MTS	MTS
Dynamic viscosity	PL[f]	PL[f]	PL[f]	PL[f]

[a] measured upstream of the interaction and at the wall for the y direction
[b] the stretching function used is: $y = L_y \sinh(\beta_y(j-1)/(N_y-1))/\sinh(\beta_y)$
[c] note that the stretching is relaxed to keep the same reference near-wall resolution while doubling N_y to increase the outer-layer resolution and better capture the shocks
[d] the quoted number corresponds to the number of time steps between each record
[e] Flow-Through-Time: time it takes to go across the computational domain at the upstream freestream velocity
[f] power law, see (2.25g)

TABLE 3.1: Numerical details for the grid sensitivity study

resolution on the results rather than on the near-wall-resolution effects since the settings used do not differ from the usual LES values for wall-bounded flows. To study the SGS-model effects, the MTS model will be compared to the DS model. In addition, the case where the SGS terms are simply neglected is considered to gain some insights about their overall contribution to the solution. This case will be labelled "implicit" LES but it must be noted that the numerical scheme was not modified in any particular way so that the discretisation error would act as a SGS model. Finally, the choice of the domain spanwise extent is critical in separated turbulent flows and this effect will be quantified. Before comparing the LES cases, it is interesting to see how the LES approach performs as a predictive tool with respect to PIV experimental data.

Case	Large span	Small span	DS	Implicit
Domain size				
L_x, L_y, L_z in $\check{\delta}_1$	450, 70, 120	450, 70, 12	450, 70, 24	450, 70, 24
Number of points[a]				
N_x, N_y, N_z	451, 81, 361	451, 81, 37	451, 81, 73	451, 81, 73
Grid stretching[b] β_y	5.50	5.50	5.50	5.50
Statistics				
sampling rate[c]	5	5	5	5
$\Delta t\, \bar{u}_1/\check{\delta}_1$	0.045	0.045	0.045	0.045
number of FTT[d]	9	73	16	8
SGS model	MTS[e]	MTS[e]	DS[e]	None[e]
Dynamic viscosity	PL[f]	PL[f]	PL[f]	PL[f]

[a] the grid resolutions are kept the same as the reference grid (see table 3.1)
[b] the stretching function used is: $y = L_y \sinh(\beta_y(j-1)/(N_y-1))/\sinh(\beta_y)$
[c] the quoted number corresponds to the number of time steps between each record
[d] Flow-Through-Time: time it takes to go across the computational domain at the upstream freestream velocity
[e] a 6^{th}-order filter was applied every 5 iterations to remove spurious numerical oscillations
[f] power law, see (2.25g)

TABLE 3.2: Numerical details for the domain and SGS model sensitivity study

3.2 Comparison with PIV data

In this section, the flow statistics obtained from the large-span LES are compared against the PIV data from Dupont et al. (2008). Figure 3.1 gives the time-averaged[1] streamwise-velocity field. The left-hand side of the figure is a superposition of the PIV field (in filled contours) and the LES field (thick solid lines). The contours were taken at exactly the same levels to allow a direct comparison of both the spatial structure and amplitude level of the velocity fields. The right-hand side of the figure provides a comparison of the PIV and LES velocity profiles at four different streamwise locations. Overall, the LES results are in good agreement with the PIV data. One noticeable difference is in the separation area (highlighted in the contourmaps) where the PIV shows a taller mean separation bubble with a slightly stronger reversed flow (about 5% of the upstream freestream velocity in the PIV against 3% in the LES). The boundary-layer thickening, however, is well captured.

Figure 3.2 is a similar comparison to the one in the previous paragraph but for the wall-normal velocity component. The initial part of the interaction is in good agreement with the PIV. In the recovery region the agreement near the wall is satisfactory,

[1] In this chapter, the *overline* notation refers to the time-averaged field and not to the grid-filtered field. Of course, for the LES data, the time average is performed on the resolved field, which is grid-filtered.

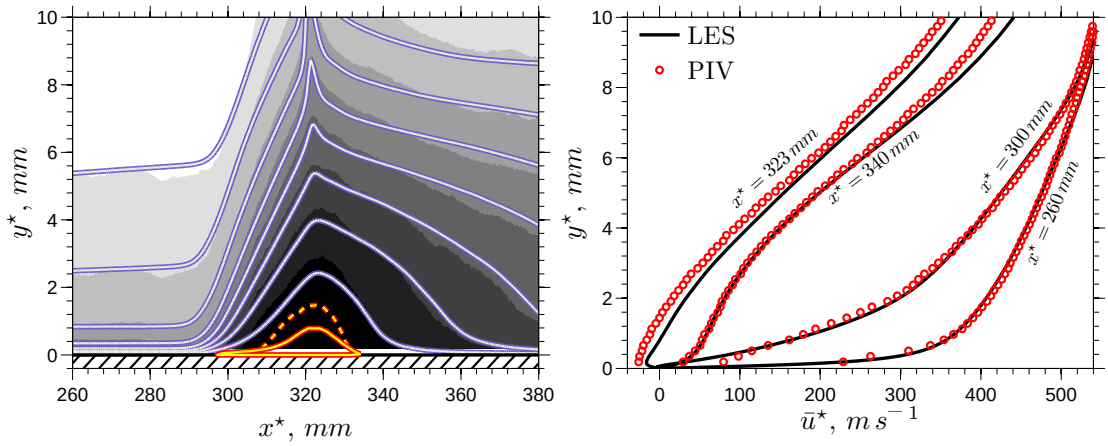

FIGURE 3.1: Mean streamwise velocity: PIV *vs* LES. Two-dimensional distribution showing the PIV in *filled contours* and the LES in *solid lines* at exactly the same contour levels (*left*). The *solid* and *dashed red/yellow lines* correspond to $\bar{u} = 0$ in the LES and the PIV fields, respectively. Profiles at different streamwise locations (*right*)

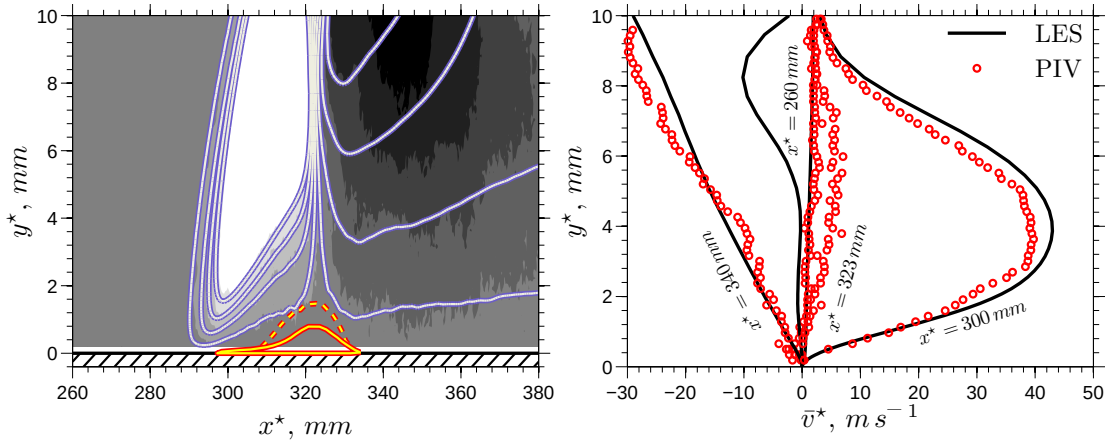

FIGURE 3.2: Mean wall-normal velocity: PIV *vs* LES. Two-dimensional distribution showing the PIV in *filled contours* and the LES in *solid lines* at exactly the same contour levels (*left*). The *solid* and *dashed red/yellow lines* correspond to $\bar{u} = 0$ in the LES and the PIV fields, respectively. Profiles at different streamwise locations (*right*)

but deteriorates in the outer part of the boundary layer. Larger differences are seen in the separation bubble, as mentioned in the previous paragraph. It should be noted that the PIV is less well converged for the wall-normal velocity than for the streamwise velocity and that near-wall PIV measurements are usually less reliable. Furthermore, the flow inside the bubble is highly unsteady and the bubble can be nonexistent at times and much bigger than its mean size at other times. The velocity fluctuations inside the bubble can thus be large compared to the mean velocity value, producing high Reynolds-stress values. Therefore, a good agreement between the LES and the PIV inside the mean separation region is not expected.

Figure 3.3 gives the streamwise-velocity RMS fluctuation map. The LES results are seen to capture a structure similar to the PIV inside the interaction. In particular,

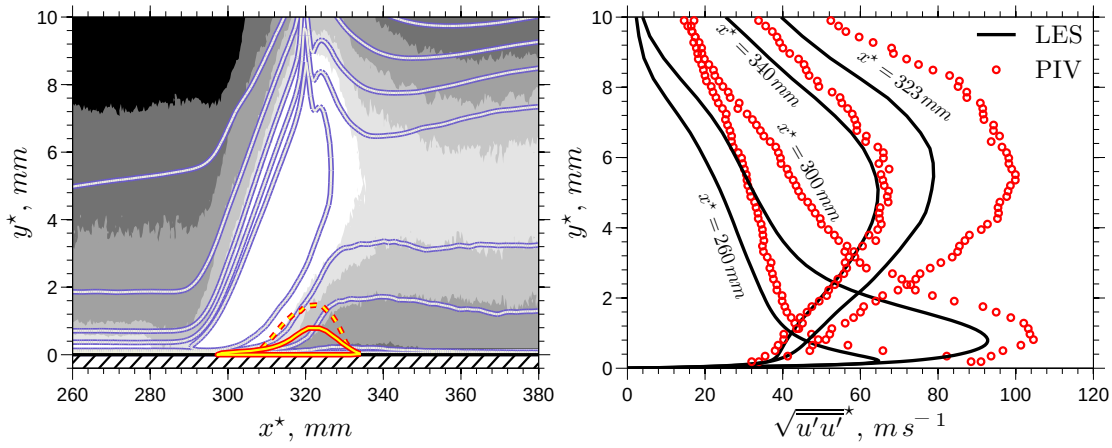

FIGURE 3.3: RMS of the streamwise velocity fluctuations: PIV *vs* LES. Two-dimensional distribution showing the PIV in *filled contours* and the LES in *solid lines* at exactly the same contour levels (*left*). The *solid* and *dashed red/yellow lines* correspond to $\bar{u} = 0$ in the LES and the PIV fields, respectively. Profiles at different streamwise locations (*right*)

the inclination angle of the high-intensity ridge found inside the interaction region is in good agreement with the PIV findings. The ridge corresponds to the energetic shear layer formed at the bubble interface. However, the LES shear layer is slightly thinner than the PIV one. It should also be noted that the fluctuations in the LES upstream of interaction do not penetrate as far into the flow as in the PIV. This is due to the digital-filter settings, which assigned too little energy in the outer part of the boundary layer. This was improved in a second large-span LES, which is described in the following chapter. However, the lack of incoming outer-layer fluctuations does not seem to survive past the interaction and the profiles at $x^\star = 340\,mm$ are in good agreement.

Figure 3.4 shows a comparison of the wall-normal velocity fluctuations. It can be seen that the comparison deteriorates compared to the previous figures: the LES fluctuations are slightly stronger in the post-interaction region and the local maximum seems to be closer to the wall than in the PIV. The shift in the height of the ridge of maximum wall-normal velocity fluctuations seems to correlate well with the taller PIV bubble. It is unclear why the experimental bubble is taller, but one can speculate this to be related to the presence of the wind-tunnel side walls, which tend to enhance the size of the separation bubble[2]. However, note that the contourmap indicates a good match for the shock-system position, suggesting that the size of the interaction as found by the LES is in good agreement with the experiment.

Finally, figure 3.5 gives the Reynolds shear-stress distributions. It must be emphasised that the shear stress is not easily obtained using PIV. Nevertheless, despite the lack of convergence in the PIV data, the qualitative and to some extent the quantitative agreement between the PIV and the LES is remarkably good. It is interesting to note

[2]Private communication with Dr. Jean-Paul Dussauge, IUSTI (2008).

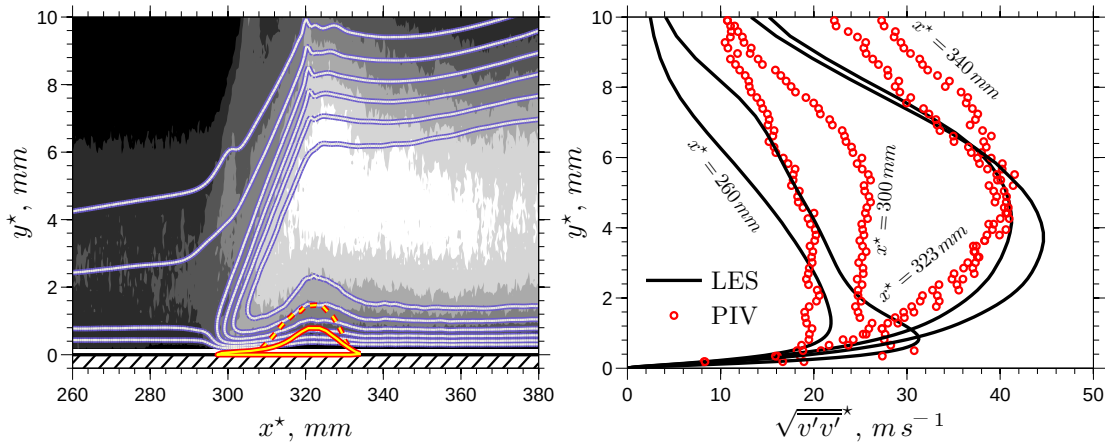

FIGURE 3.4: RMS of the wall-normal velocity fluctuations: PIV *vs* LES. Two-dimensional distribution showing the PIV in *filled contours* and the LES in *solid lines* at exactly the same contour levels (*left*). The *solid* and *dashed red/yellow lines* correspond to $\bar{u} = 0$ in the LES and the PIV fields, respectively. Profiles at different streamwise locations (*right*)

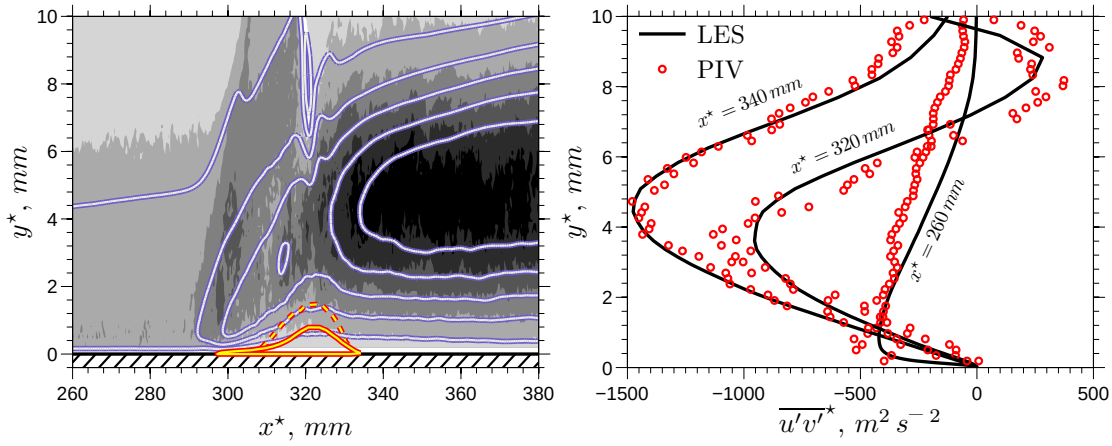

FIGURE 3.5: Reynolds shear stress: PIV *vs* LES. Two-dimensional distribution showing the PIV in *filled contours* and the LES in *solid lines* at exactly the same contour levels (*left*). The *solid* and *dashed red/yellow lines* correspond to $\bar{u} = 0$ in the LES and the PIV fields, respectively. Profiles at different streamwise locations (*right*)

the small but clear region of high positive shear-stress values (near $x^\star = 320\,mm$ and $y^\star \in [7\,mm, 10\,mm]$). This corresponds to the flapping motion of the incident-shock tip. Also, one can detect the mean position of the reflected shock, which is seen to be correctly predicted by the LES.

Generally speaking, the PIV and LES data agree sufficiently well to deem the LES approach capable of reproducing this complex flow field. Also, the good agreement with the PIV data, taken from the median plane of the wind tunnel, suggests that the 8-degree-wedge-angle experiment is close to being statistically two-dimensional, as claimed by Dussauge and Piponniau (2008), and that the wind-tunnel-corner flows are not too important in this case. However, it was shown here that the separation-bubble

predictions were good with respect to the bubble length but that the bubble height was underpredicted by the LES. This is believed to be a sign of some level of three-dimensionality in the experiment. In fact, the interaction-length prediction would not agree so well if the experiment had been strongly affected by the side walls, as shown for example in the 9.5-degree case (see Dussauge and Piponniau, 2008). In the 9.5-degree case, the success of a statistically two-dimensional LES would not be guaranteed and would probably have to account for the wind-tunnel side-wall effects.[3]

3.3 Grid-refinement, domain- and subgrid-scale-sensitivity study

In this section, the effects of the tested grid resolutions, choice of domain widths and SGS model on the interaction length are presented. Figure 3.6 gives the skin friction evolution inside the interaction for different grid resolutions and domain widths, as defined in tables 3.1 and 3.2. Although the statistics were not acquired over the same amount of samples, the number of samples used in this study was large enough to consider the results to be statistically converged. From figure 3.6(a), it is seen that the tested grid resolutions do not produce significant differences in the size of the separation bubble and skin-friction levels. In table 3.3 the length of the separation bubble is reported to be insensitive to the different grids tested to within 7%, suggesting that the solution is nearly grid converged. Garnier et al. (2002) also looked at the sensitivity of their results to the grid resolution and could not find any significant differences at similar resolutions to the present ones (note that they used the local boundary-layer-edge conditions to normalise the skin friction and Sutherland's law for the dynamic viscosity whereas the upstream boundary-layer-edge conditions and a power law is used in this study). We are thus confident that the grid resolution used for the present work is sufficiently fine to only have marginal effects on the statistical results.

Figure 3.6(b) compares the skin-friction evolution for the different domain widths considered (see table 3.2). Contrary to the grid-resolution sensitivity tests, the results are found to be very sensitive to the computational-box width. Previous simulations of the IUSTI 8-degree shock-reflection case made use of spanwise widths of $1.4\delta_0$ (Garnier et al., 2002) and $2.2\delta_0$ (Pirozzoli and Grasso, 2006), whereas the experimental separation-bubble length is $\mathcal{O}(4\delta_0)$-long (Dupont et al., 2006). In this domain-size effect study, the tested spanwise lengths range from $0.7\delta_0$ to $7\delta_0$. The separation point is found to move upstream as the spanwise extent is reduced while the reattachment point moves further downstream, leading to longer bubbles and slower recovery rates. Figure 3.7(a) further

[3]Private communication with Dr. Eric Garnier, ONERA (2007).

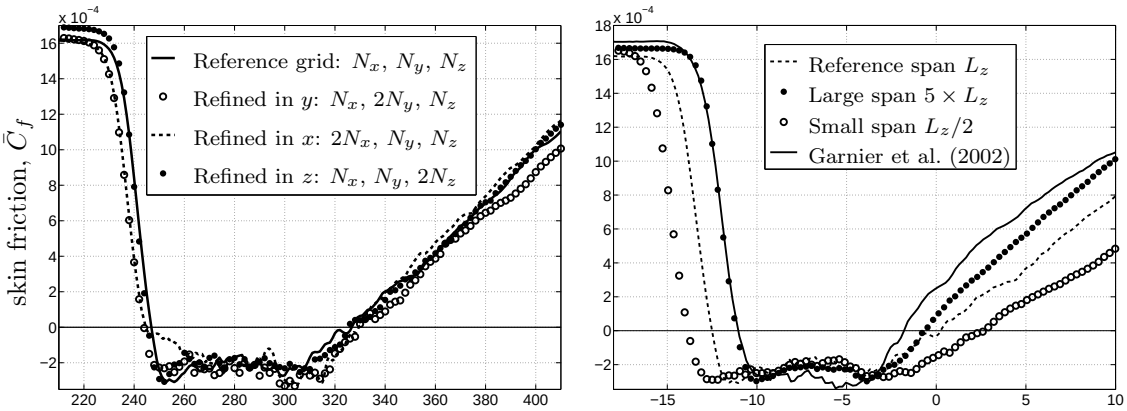

(a) grid-resolution effect (b) domain-width effect

FIGURE 3.6: Skin-friction sensitivity to the grid resolution and the domain width. The skin friction is normalised with the upstream potential-flow properties and the dynamic viscosity is computed using the power law

confirms the changes by looking at the wall-pressure distribution (normalised by the upstream pressure). The wall-pressure distribution is seen to develop a plateau as the domain width is reduced. This is reminiscent of laminar interactions, but we are certain that the flow remained fully turbulent in the small-span simulations. In fact, the small-span LES was chosen such that despite the increased spanwise coherence (forced by the periodic boundary conditions) a fully turbulent flow could be maintained. The existence of a pressure plateau is thus a direct consequence of the bubble extension due to the high level of spanwise coherence. Finally, it is interesting to note that the increased interaction length due to the reduced size of the domain width does not seem to affect the initial rate of change of the wall-pressure distribution. This is reminiscent of the free-interaction theory in laminar interactions (Stewartson and Williams, 1969; Katzer, 1989).

Table 3.3 shows the bubble and interaction lengths for the different grids and domain sizes, compared with the values obtained by Garnier et al. (2002) (LES) and Dupont et al. (2006) (experiment). This further quantifies the sensitivity of the bubble to the domain width, with an extension of the bubble of about 35% between the large and small-span cases. In addition, table 3.3 suggests that the simulated normalized shock intensity is higher than in the experiment, probably due to a slightly lower level in the incoming skin friction. In the table, p_2 refers to the theoretical freestream pressure after the incident shock but before the reflected shock and τ_w is the wall shear-stress before the interaction. Finally, table 3.3 quantifies the differences found between the interaction length L and the separation length $L_{\rm sep}$. The interaction length is defined as the distance between the location of the reflected-shock extension to the wall $\bar{x}_0$ and

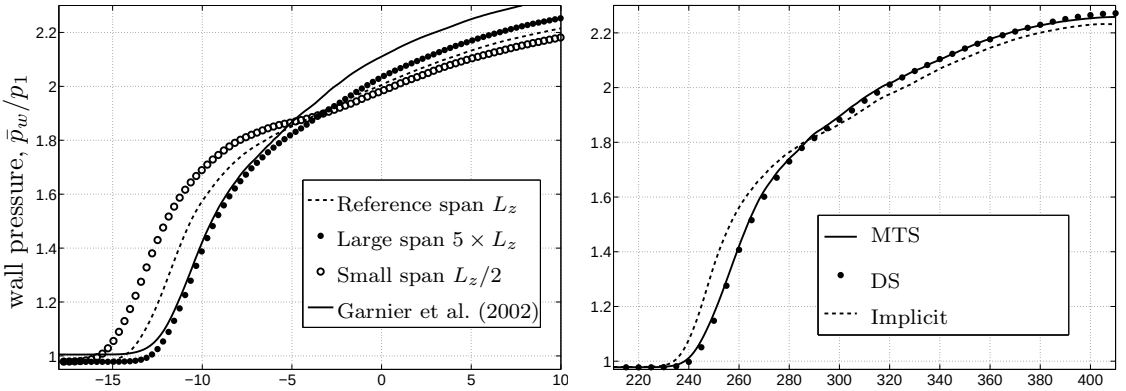

streamwise direction, $(x - \bar{x}_{\text{imp}})/\check{\delta}_1$
(a) domain-width effect

streamwise direction, $x/\check{\delta}_1$
(b) subgrid-scale model effect

FIGURE 3.7: Wall pressure sensitivity to the domain width and the subgrid-scale model

Case	Ref.	$2N_x$	$2N_y$	$2N_z$	$L_z/2$	$5L_z$	LES[a]	Exp[b]
$(p_2 - p_1)/(2\tau_w)$	50.2	50.9	50.5	48.6	49.3	48.9	47.5	40.5
L/δ_0	5.1	5.4	5.3	5.1	5.9	4.8	4.5	4.2
L_{sep}/δ_0	4.5	4.8	4.8	4.5	6.1	3.9	3.1	3.5[c]
$(\bar{x}_{\text{sep}} - \bar{x}_0)/\delta_1^{\text{imp}}$	2.0	2.4	2.1	1.7	2.1	2.0	2.5	–
$(\bar{x}_{\text{at}} - \bar{x}_{\text{imp}})/\delta_1^{\text{imp}}$	0.2	0.7	0.7	0.0	2.7	−0.7	−1.8	–

[a] from Garnier et al. (2002)
[b] from Dupont et al. (2006)
[c] this value is not in the original paper of Dupont et al. (2006) but was estimated based on the LES results taking $(\bar{x}_{\text{sep}} - \bar{x}_0)/\delta_1^{\text{imp}} \sim 2$, giving an experimental value of $L_{\text{sep}} \approx 39\,mm$

TABLE 3.3: Interaction lengths and normalised shock intensity

the inviscid-impingement location of the incident oblique shock $\bar{x}_{\text{imp}}$, while the separation length is the distance between the separation point $\bar{x}_{\text{sep}}$ and the reattachment point $\bar{x}_{\text{at}}$. Experimentalists prefer to use the interaction length while computationalists favor the use of the separation length, which is readily available. To allow a consistent comparison with the experiment, the experimental separation length was evaluated to be around $39\,mm$. This will be used when considering the unsteady aspects.

The SGS model effect was investigated by comparing the MTS model with the DS model and an implicit LES approach. Figure 3.7(b) gives the wall-pressure rise in the interaction obtained from the different models. The MTS and DS models give similar results, whereas the implicit LES appears to stand out. The good agreement between the two SGS models suggests that the grid is fine enough so that the particular choice of eddy-viscosity model has little importance. However, the larger separation found by the implicit LES, as shown in figure 3.8(a), and steeper increase in the wall-pressure streamwise evolution (figure 3.7(b)) suggests that simply neglecting the SGS terms for

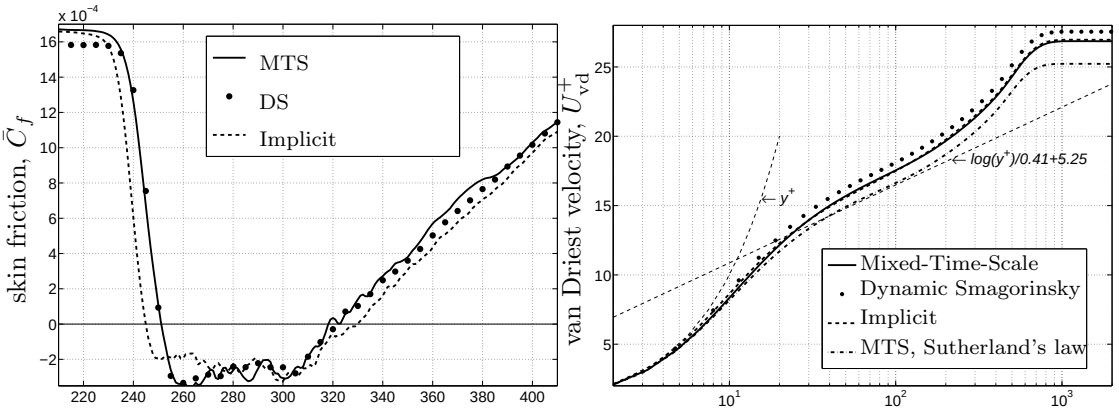

(a) SGS model effect on the skin friction (b) SGS model effect on the upstream velocity profile

FIGURE 3.8: SGS model effect on the interaction length and upstream velocity profile

that particular grid and numerical approach would not be adequate.

The SGS model effect on the incoming velocity profile is shown in figure 3.8(b). The DS model gives a slightly lower friction velocity than the MTS and implicit LES, as already noticed from the upstream skin-friction values. The apparent overshoot of the log-law constant is not believed to be related to a resolution issue, since the grid-refinement study did not show any strong deviations in the results as the grid was refined. In fact, the overshoot seems mainly due to the choice of dynamic-viscosity law. In the present LES, a power law with exponent 0.67 was used. If instead, one uses Sutherland's law (as in Garnier et al., 2002), it can easily be shown that the dynamic viscosity at the wall would be about 13% greater. To estimate the effect of a 13% difference in the dynamic-viscosity value at the wall, the van Driest velocity profile from the MTS model was re-processed using Sutherland's law and the result is shown in figure 3.8(b). The difference is noticeable and the agreement with the log-law appears to be improved. Furthermore, it should be noted that there exists some variations on the value of the additive constant used in the literature (van Driest used 5.24 van Driest, 1956). Based on the above discussion about the improvement of Sutherland's law over the power law used in the current simulations, all new large-eddy simulations to be presented in the following chapters will be performed using Sutherland's law.

Finally, figure 3.9 provides the eddy-viscosity field for the two SGS models tested. The asymptotic behavior of the models in the upstream boundary layer as one approaches the wall differ, as shown in figure 3.9(a). The eddy viscosity from the MTS model approaches the wall as y^{+^2}, which is a factor y^+ away from the expected asymptotic behavior, which is properly captured by the DS model. This issue is reported in Inagaki et al. (2005). Despite the wrong near-wall behavior of the MTS model, the skin friction in the relaxation part of the interaction (see figure 3.7(a)) is close to the DS result, suggesting that the incorrect asymptotic behavior of the MTS model has little importance.

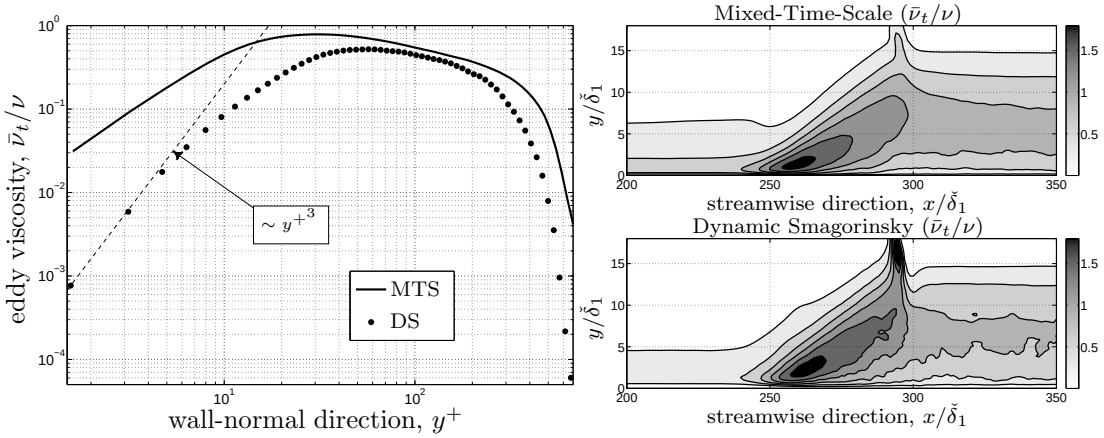

(a) model effect on the upstream eddy-viscosity profile (b) model effect on the eddy-viscosity distribution

FIGURE 3.9: SGS model effect on the eddy viscosity to kinematic viscosity ratio

Figure 3.8(b) confirms the overall similar eddy-viscosity distribution between the two models inside the interaction, with some discrepancies near the shocks.

Since the DS model is significantly more computationally intensive than the MTS model, for no obvious additional improvements in the SBLI predictions, and that the implicit-LES results differ from the ones with the SGS model on, the choice of the MTS model in the present SBLI studies appears justified.

In this chapter, we have demonstrated that the numerical approach presented in chapter 2 is capable of producing results in good agreement with earlier experimental (PIV) and numerical (LES) data. Furthermore, grid resolutions of $4.1 \cdot 10^1 \times 1.6 \times 1.4 \cdot 10^1$ were shown to produce nearly grid-independent results with the choice of eddy-viscosity model having no noticeable influence on the interaction. The use of a subgrid-scale model, however, was seen to be preferable to an implicit LES approach. By contrast, the choice of domain width was found to strongly influence the interaction length. With the experience gained from the above validation campaign, the numerical approach is now applied to actual SBLI investigations.

4. Time-averaged flow-field characteristics

This chapter focuses on the properties of the time-averaged flow fields of three different shock-reflection configurations. All cases were obtained using the large-eddy simulation approach presented in the previous chapters. Unsteady aspects of those simulations are covered in chapter 6. Each case is based on actual experimental configurations studied in the context of the UFAST project (discussed below). The simulation results are first compared with their experimental equivalents and a cross-comparison is then performed with a particular section on the properties of the developing mixing layer in the interaction.

4.1 Description of the UFAST project

As mentioned in the acknowledgement section, this work was partially funded by the European Union with the Sixth Framework program through the UFAST project. From the project presentation page (`http://www.ufast.gda.pl/`), one can read: "the UFAST project aims to foster experimental and theoretical work in the highly non-linear area of unsteady shock wave boundary layer interaction". The University of Southampton (SOTON) was one among 21 partners involved in this project. Our particular role was to make use of the LES approach in order to simulate three different shock-reflection configurations. The simulations were run in parallel with experiments from three partners: the "Institut Universitaire des Systèmes Thermiques Industriels" (IUSTI) — Marseille (France), the "Institute of Theoretical and Applied Mechanics" (ITAM) — Novosibirsk (Russia), and the TUD - Aerodynamics Laboratory, Faculty of Aerospace Engineering, Delft University of Technology — Delft (Netherlands). The aim was twofold: first, to assess the capabilities and limitations of LES to simulate these three experimental cases. Second, to provide physical insights (not available from RANS/URANS approaches but at a lower cost than DNS approaches) into the driving mechanisms of the unsteadiness observed in SBLI.

The experimental and numerical flow conditions are summarised in table 4.1. Because of the prohibitive computational cost of the TUD case, the LES of this flow case was not run at the actual experimental Reynolds number, and a value close to the ITAM

Flow case	IUSTI	ITAM	TUD
Mach number	2.3	2.0	1.7
Wedge angle	8°	7°	6°
Stagnation pressure $P_0\,(bar)$	0.5	0.8	2.3
Stagnation temperature $T_0\,(K)$	300	288	273
Reynolds number[a], $\mathrm{Re}_{\delta_1} \times 10^4$	2	1	12[b]/1[c]
Sutherland's law C value[d]	0.76	0.68	0.64

[a] based on the upstream freestream velocity $\bar{u}_1$, the boundary-layer edge dynamic viscosity and the boundary-layer displacement thickness δ_1 (upstream of interaction)
[b] experimental value
[c] simulated value
[d] see (2.25h)

TABLE 4.1: UFAST experimental and numerical flow conditions

flow case was chosen instead. The IUSTI case is the strongest interaction studied, followed by the ITAM and the TUD cases. Figure 4.1 provides an instantaneous side-view of the temperature field for the three cases. One can see that the interaction length (relative to δ_0^{imp}, the boundary-layer 99% thickness at the inviscid shock-impingement point, $\bar{x}_{\mathrm{imp}}$, in the absence of the shock) reduces going from IUSTI to ITAM to TUD. The δ_0^{imp} value could be evaluated from a separate canonical boundary-layer simulation. However, in the present work, it was evaluated based on a linear extrapolation of the upstream-of-interaction boundary layer (where it is no longer under the influence of the inlet condition but not yet under the influence of the interaction). Such an approach is reasonable given the short streamwise distances considered (only few boundary-layer thicknesses).

Table 4.2 gives the relevant numerical details of the grid and domain size of each LES as well as information about the timestep and runtime. Such grid resolutions were shown in the previous chapter to be sufficient for the results to be considered nearly grid and SGS-model independent. In fact, it was shown in chapter 3 that the most critical grid parameter at such grid resolutions is the spanwise extent of the computational domain, and that the simulated bubble can artificially increase in size if the domain width is too small. This occurs when the computational-box width is too narrow to resolve the low and energetically significant spanwise wavenumbers found in the interaction region. It is recommended that the domain spanwise extent be longer than the separation-bubble length. Unfortunately, such constraints on the grid greatly reduce the possibility to integrate the LES over many low-frequency cycles. The following section focuses on the individual three time-averaged flow fields by comparing the obtained statistics with other experimental and/or computational results wherever possible. Then, a cross comparison of the present LES data is presented.

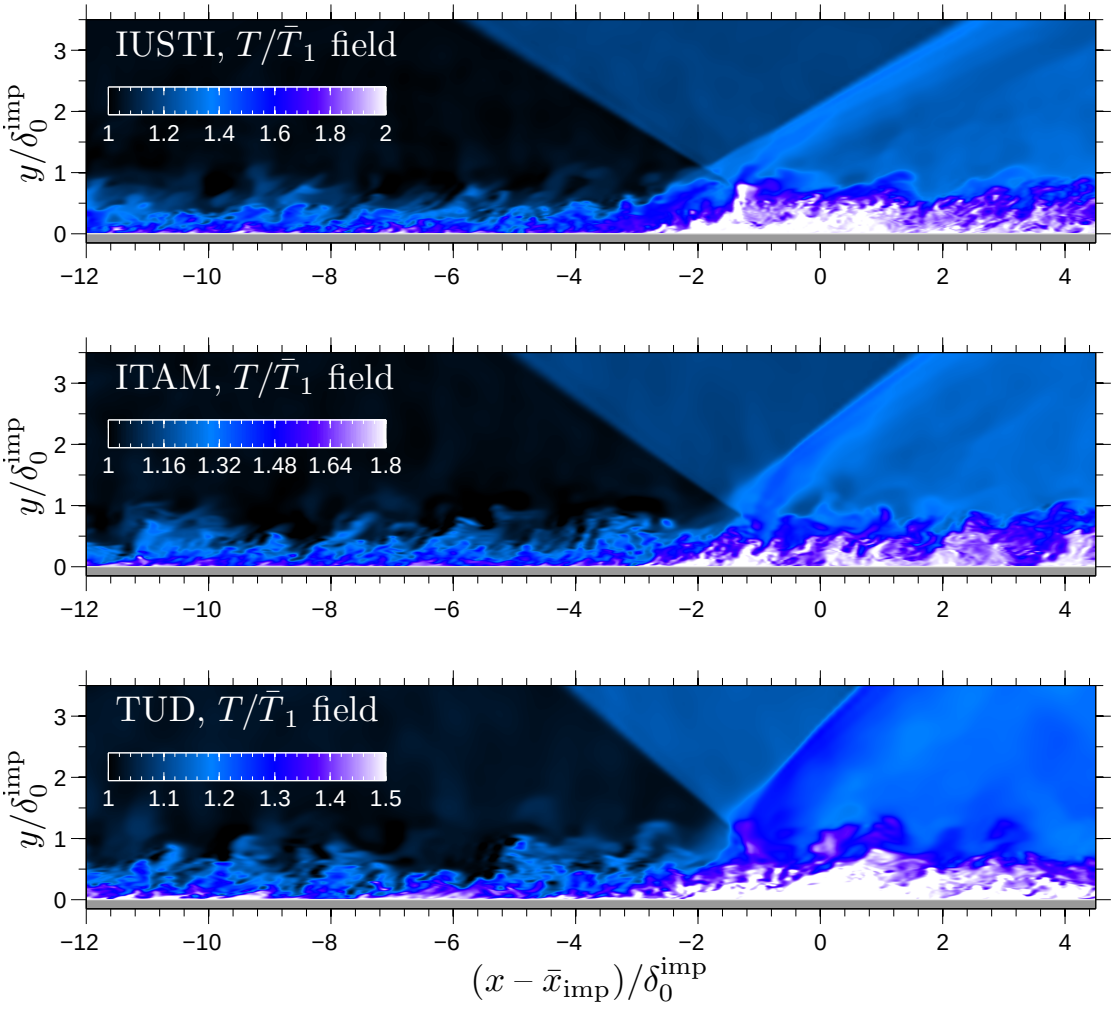

FIGURE 4.1: Instantaneous side views of the temperature field from the present LES

4.2 Case by case comparisons

4.2.1 The IUSTI case

A comparison between LES and PIV results of the IUSTI 8° case was already provided in chapter 3 for the large-span case presented in table 3.2. Since a new large-span case is introduced in table 4.2, the PIV/LES comparison is repeated here. The new large-span LES[1] differs from the earlier one mostly in an enhanced resolution in the wall-normal direction (longer L_y, smaller stretching β_y for a doubled N_y value), the choice of Sutherland's law for the dynamic viscosity and a modification of the imposed upstream Reynolds stress profiles used in the digital-filter approach to improve the observed lack of fluctuations in the outer-layer part of the incoming TBL (see chapter 3).

[1]From this chapter onward, the large-span LES refers to the IUSTI case described in table 4.2.

Flow case	IUSTI	ITAM	TUD
Domain size			
L_x, L_y, L_z, in δ_0^{imp}	20.3, 4.1, 4.7	23.9, 4.8, 2.7	26.9, 5.4, 3.0
L_x, L_y, L_z, in L_{sep}	6.9, 1.4, 1.6	11.6, 2.3, 1.3	20.3, 4.1, 2.2
L_x, L_y, L_z, in L	5.6, 1.1, 1.3	7.9, 1.6, 0.9	10.5, 2.1, 1.2
Number of points, N_x, N_y, N_z	451, 151, 281	451, 151, 141	451, 151, 141
Grid stretching coefficient[a], β_y	5.0	5.0	5.0
Grid resolution			
Δx^+, Δy^+_{min}, Δz^+	33, 1.3, 12	30, 1.2, 11	39, 1.6, 14
Runtime[b], T_{sim}			
$T_{\text{sim}}\bar{u}_1/\delta_0^{\text{imp}}$	2.65×10^3	2.25×10^3	2.18×10^3
$T_{\text{sim}}\bar{u}_1/L$	726	748	852
$\Delta t\bar{u}_1/\delta_0^{\text{imp}}$	2.0×10^{-3}	2.4×10^{-3}	2.7×10^{-3}
Number of cycles[c], N	25.4	26.2	29.8
Sampling rate for the statistics[d], n	5	5	5
Dynamic viscosity law	Sutherland	Sutherland	Sutherland

[a] where $y = L_y \sinh(\beta_y(j-1)/(N_y-1))/\sinh(\beta_y)$, $j \in \{1, \ldots, N_y\}$
[b] excluding the relatively long start-up transient
[c] number of low-frequency cycles covered by a sine wave beating a frequency $f = 0.035\bar{u}_1/L$
[d] the flow is probed once every n iteration(s)

TABLE 4.2: UFAST simulation settings

Figures 4.2 and 4.3 compare the LES reference profiles (at $x^\star = 260\,mm$) with the PIV results. One can see that the agreement for the velocity profiles is excellent, while the agreement for the velocity fluctuations is reasonably good. The reduced streamwise fluctuations around $y^\star = 5\,mm$ in the LES is mainly due to the recovery effects due to the digital-filter approach. If the reference station was moved further downstream, the LES profile would be expected to fill in, as found in earlier simulations without shocks. Figures 4.4 and 4.5 show the time-averaged streamwise and wall-normal velocity fields from the PIV (grey-colour background) and the LES (super-imposed solid lines). The selected contour levels in the LES field are exactly the same as in the PIV field. The overall agreement is satisfactory. The most striking differences are the taller PIV bubble and the unexplained poorer agreement in the $x^\star \in [320\,mm, 360\,mm]$, $y^\star \in [6\,mm, 13\,mm]$ region.

Figures 4.6 and 4.7 give the velocity-fluctuation fields, where the qualitative agreement is found to be satisfactory. The amplitude can be slightly off, for example in the recovery region of the wall-normal velocity-fluctuation map, where the LES levels are found to be higher. However, the streamwise velocity-fluctuation levels are in better agreement and the spatial distribution of the ridge of maximum fluctuation is seen to

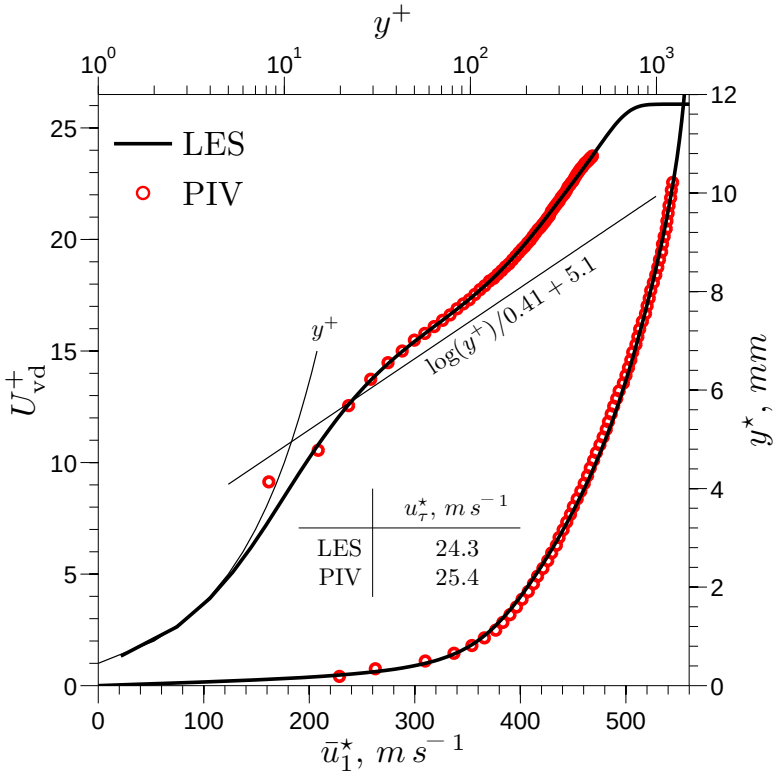

FIGURE 4.2: Upstream velocity profiles (at $x^\star = 260\,mm$): LES *vs* PIV

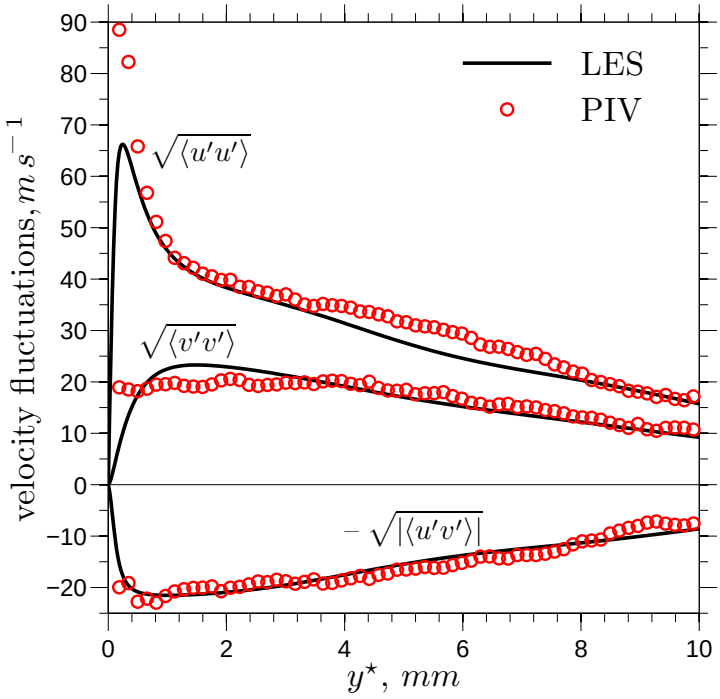

FIGURE 4.3: Upstream Reynolds stress profiles (at $x^\star = 260\,mm$): LES *vs* PIV

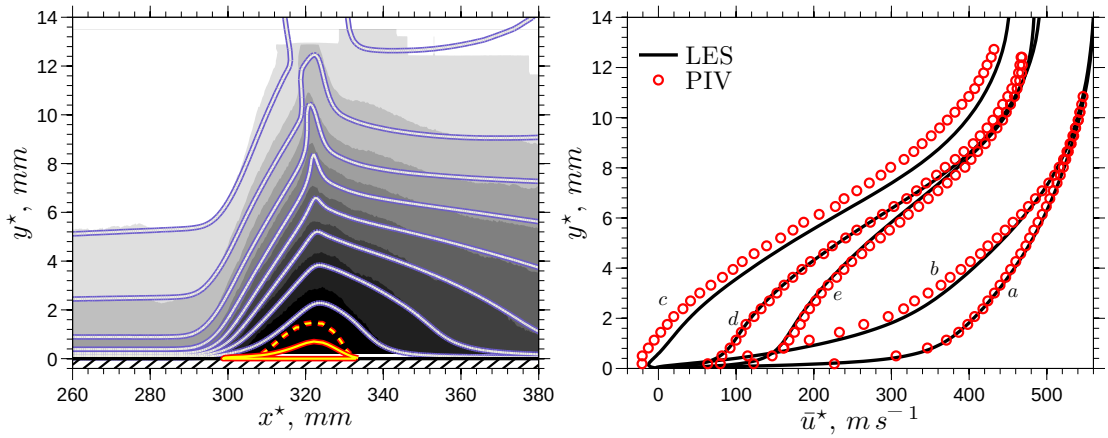

FIGURE 4.4: Mean streamwise velocity field: PIV (*filled contours*) *vs* LES (*solid lines*) at exactly the same contour levels (*left*). The *solid* and *dashed red/yellow lines* correspond to $\bar{u} = 0$ in the LES and the PIV fields, respectively. Profiles at different streamwise locations where a, b, c, d, e correspond to $x^\star = 275\,mm$, $300\,mm$, $325\,mm$, $350\,mm$, $375\,mm$, respectively (*right*)

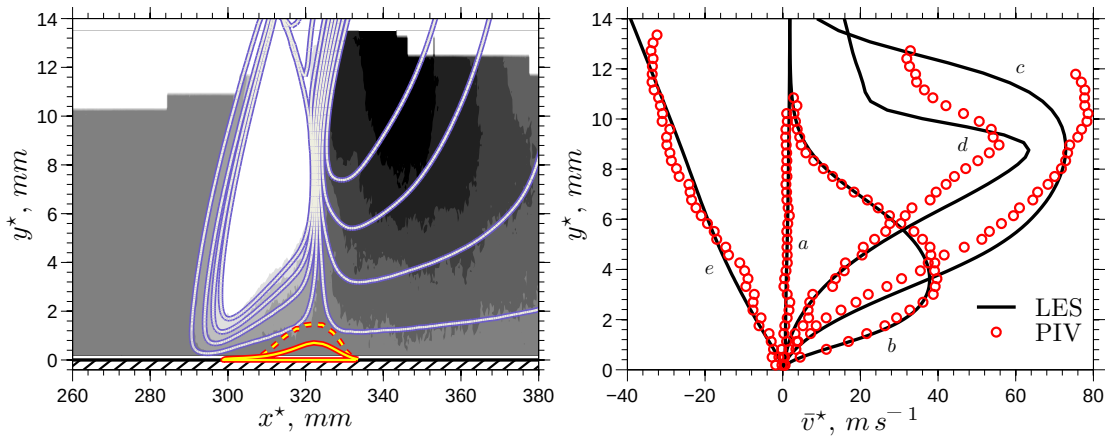

FIGURE 4.5: Mean wall-normal velocity field: PIV (*filled contours*) *vs* LES (*solid lines*) at exactly the same contour levels (*left*). The *solid* and *dashed red/yellow lines* correspond to $\bar{u} = 0$ in the LES and the PIV fields, respectively. Profiles at different streamwise locations where a, b, c, d, e correspond to $x^\star = 280\,mm$, $300\,mm$, $310\,mm$, $320\,mm$, $340\,mm$, respectively (*right*)

match the PIV results. Furthermore, the modification of the imposed Reynolds stress profiles in the digital-filter approach has improved the comparison of the upstream RMS distribution (see figure 3.3 for reference). From figure 4.7, it is possible to infer the position of the reflected shock, which is in good agreement.

Figure 4.8 shows the Reynolds shear-stress field, with a satisfactory agreement between the LES and the PIV, despite the difficulties in measuring it experimentally. Similarly to figure 4.7, the location of the shock system agrees well, leading to the conclusion that the interaction length found in the LES matches with the experimental one. The separation length should also be close to the experimental one and, although the PIV

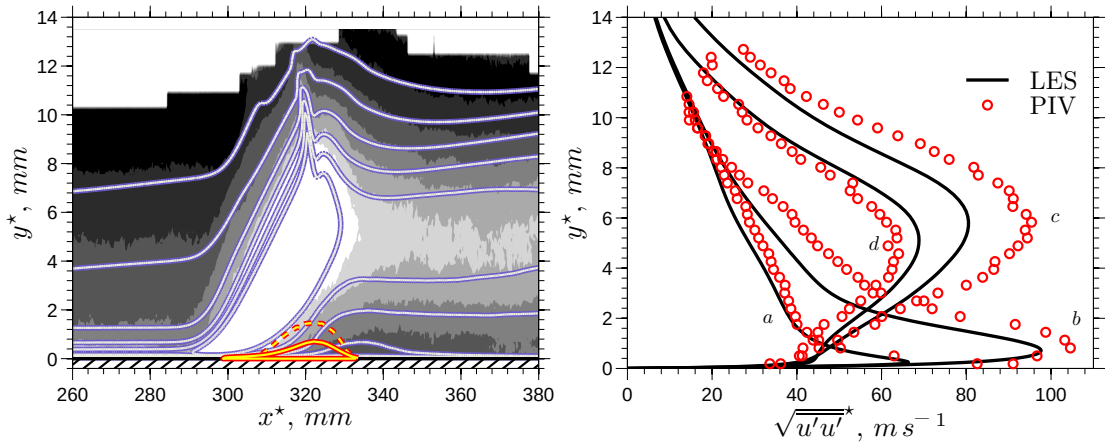

FIGURE 4.6: Streamwise-velocity fluctuations: PIV (*filled contours*) *vs* LES (*solid lines*) at exactly the same contour levels (*left*). The *solid* and *dashed red/yellow lines* correspond to $\bar{u} = 0$ in the LES and the PIV fields, respectively. Profiles at different streamwise locations where a, b, c, d correspond to $x^\star = 275\,mm$, $300\,mm$, $325\,mm$, $350\,mm$, respectively (*right*)

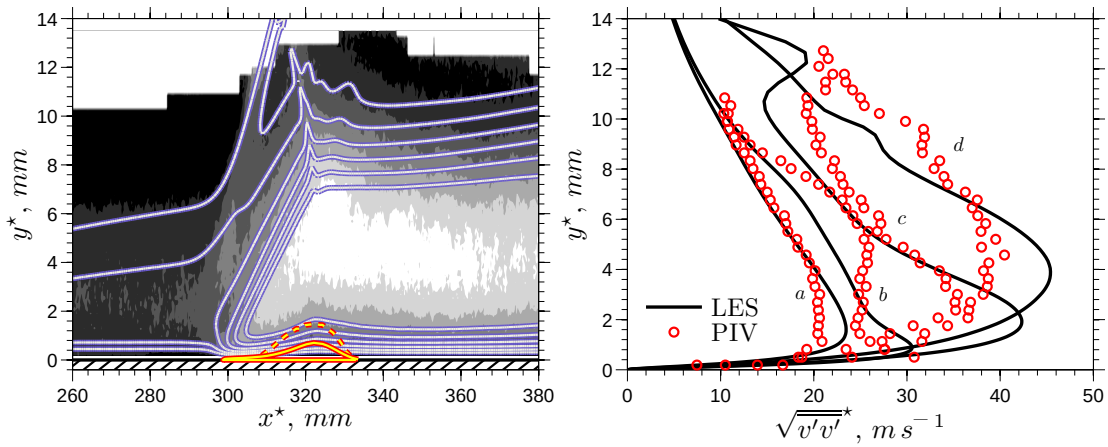

FIGURE 4.7: Wall-normal-velocity fluctuations: PIV (*filled contours*) *vs* LES (*solid lines*) at exactly the same contour levels (*left*). The *solid* and *dashed red/yellow lines* correspond to $\bar{u} = 0$ in the LES and the PIV fields, respectively. Profiles at different streamwise locations where a, b, c, d correspond to $x^\star = 280\,mm$, $300\,mm$, $310\,mm$, $320\,mm$, respectively (*right*)

does not come close enough to the wall to verify this, the trends look similar. However, it is recalled that the bubble heights found in the LES and the PIV differ by a significant amount.

The aforementioned figures were generated using the PIV data presented in Dupont et al. (2008). It is interesting to note that an earlier PIV data set exists, corresponding to the wall-pressure measurements published in Dupont et al. (2006). Although those two[2] PIV sets are supposed to be performed under the same experimental flow conditions, significant differences are found, as shown in figure 4.9. The interaction

[2]The older PIV set will be referred as the 2006 PIV set.

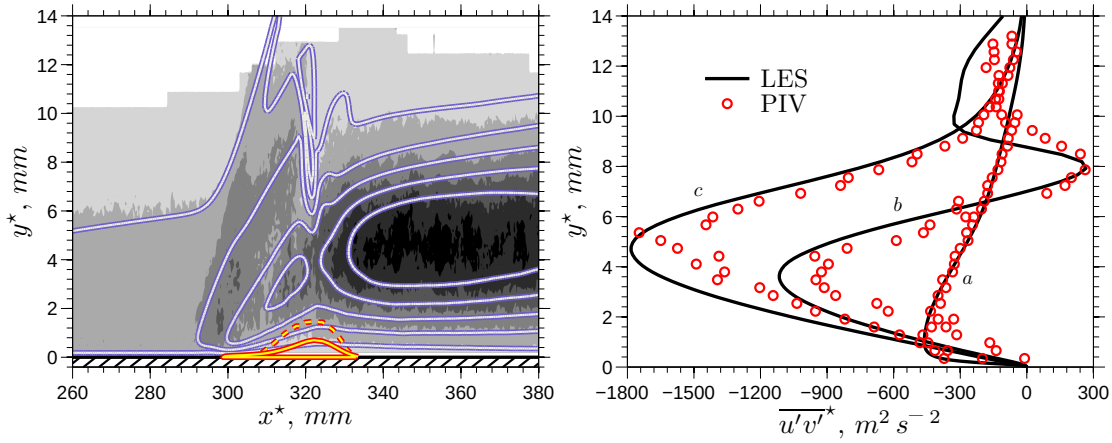

FIGURE 4.8: Reynolds shear-stress field: PIV (*filled contours*) *vs* LES (*solid lines*) at exactly the same contour levels (*left*). The *solid* and *dashed red/yellow lines* correspond to $\bar{u} = 0$ in the LES and the PIV fields, respectively. Profiles at different streamwise locations where a, b, c correspond to $x^\star = 280\,mm$, $321\,mm$, $345\,mm$, respectively (*right*)

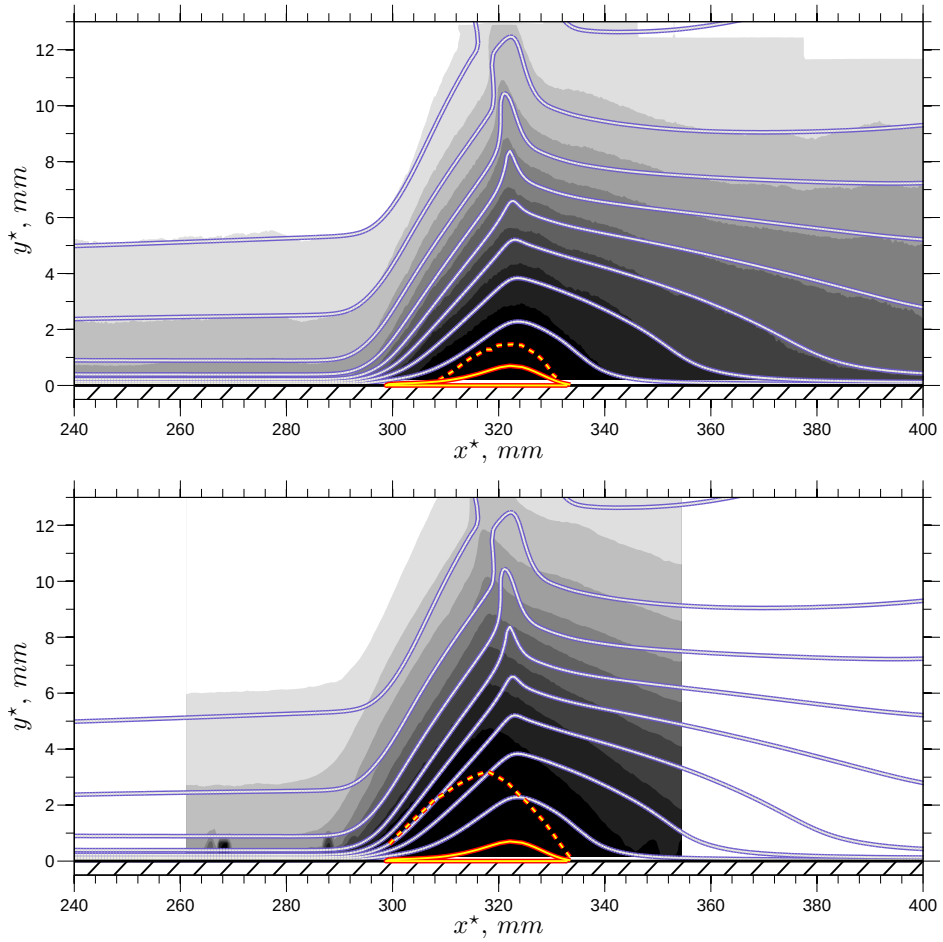

FIGURE 4.9: Mean streamwise velocity field: PIV (*filled contours*) *vs* LES (*solid lines*) at exactly the same contour levels. The *top* PIV data are the same as in figure 4.4 while the *bottom* PIV data are taken from a campaign prior to the UFAST project (in 2006), corresponding to the study which led to the wall-pressure measurements published in Dupont et al. (2006)

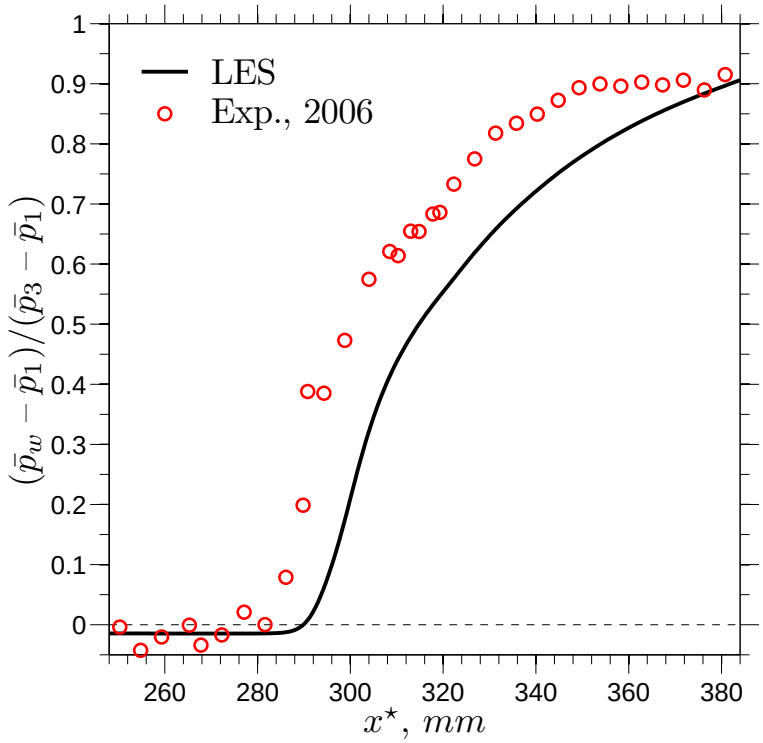

FIGURE 4.10: Wall-pressure distribution

length in the 2006 PIV data is seen to expand about $1\,cm$ more upstream than the later set, with a much larger and taller bubble. The IUSTI group relates these differences to a slight change in the inflow conditions between 2006 and 2008 (a 10% decrease in boundary-layer thickness) which may result from a modification in the way the particles are injected in the windtunnel[3]. Unfortunately, more details would be needed to explain such a large modification of the interaction itself but it reflects the sensitivity of the interaction to the flow conditions.

Figure 4.10 compares the 2006 experimental wall-pressure evolution (see Dupont et al., 2006) with the LES results. Since the LES inflow is matched to the 2008 experimental campaign (Dupont et al., 2008), the LES wall-pressure increase is delayed by about $1\,cm$, which is consistent with the shift between the 2006 and more recent PIV fields. It is speculated that the wall-pressure evolution in the newer experimental run (unfortunately not available) would be closer to the LES findings based on the relatively good comparison between the LES and PIV fields. In addition, a pressure plateau can be observed in the experimental data towards the end of the figure. This feature is not present in the LES data and could be a consequence of the influence of the expansion fan originating from the trailing edge of the wedge, which is not included in the simulation.

[3]Private communication with Dr. J.-P. Dussauge, December 2008.

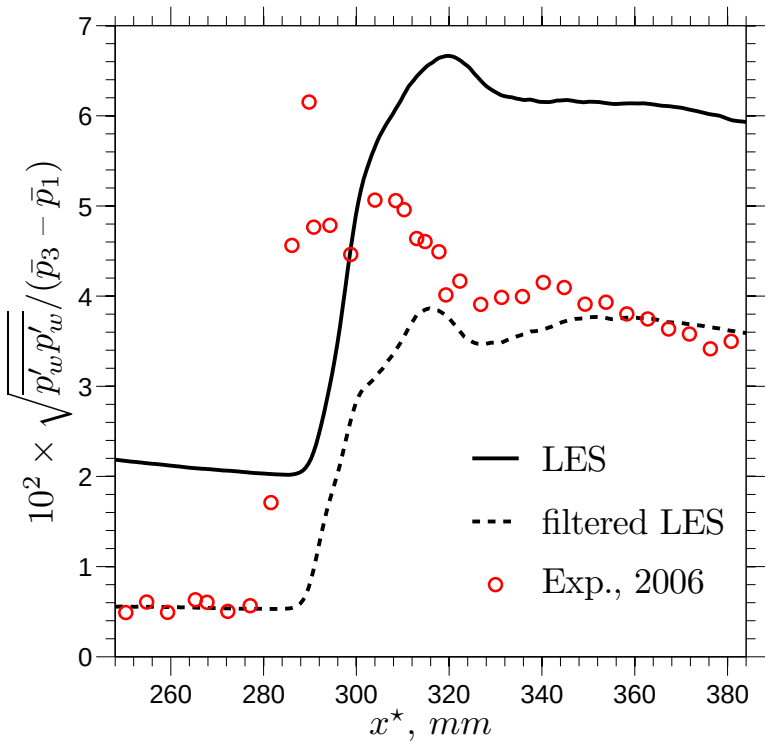

FIGURE 4.11: Wall-pressure fluctuations distribution

Figure 4.11 gives the root-mean-square distribution of the wall-pressure fluctuations. Here again, a shift of $\mathcal{O}(1\,cm)$ is expected. Aside from the separation-point-location issue, there are other significant differences between the LES and the experiment. One striking difference is the disagreement in the levels of pressure fluctuations. It is suspected that the main reason for such disagreement in the RMS levels originates in the way the experimental signals were acquired. In particular, the high-frequency content may not have been resolved. To test that idea, the LES signals were low-pass filtered with a 6^{th}-order low-pass non-causal Butterworth filter with a cutoff frequency of 80 kHz. The computed RMS from the filtered signals are in much better agreement with the experimental results, suggesting that the non-resolved higher frequencies in the measurements may significantly contribute to the overall energy of the wall-pressure fluctuations. However, near the shock foot, it is known that the low-frequency fluctuations can be responsible for up to a third of the total energy (Dupont et al., 2006).

It is not just in experiments where large variations of the separation-bubble size occur, despite the use of similar flow conditions. As shown in chapter 3, varying the computational-domain width can modify the predicted separation by significant amounts. For example, figure 4.12 shows the large difference between the earlier narrow-span LES and the latest large-span LES where the span was increased by almost a factor

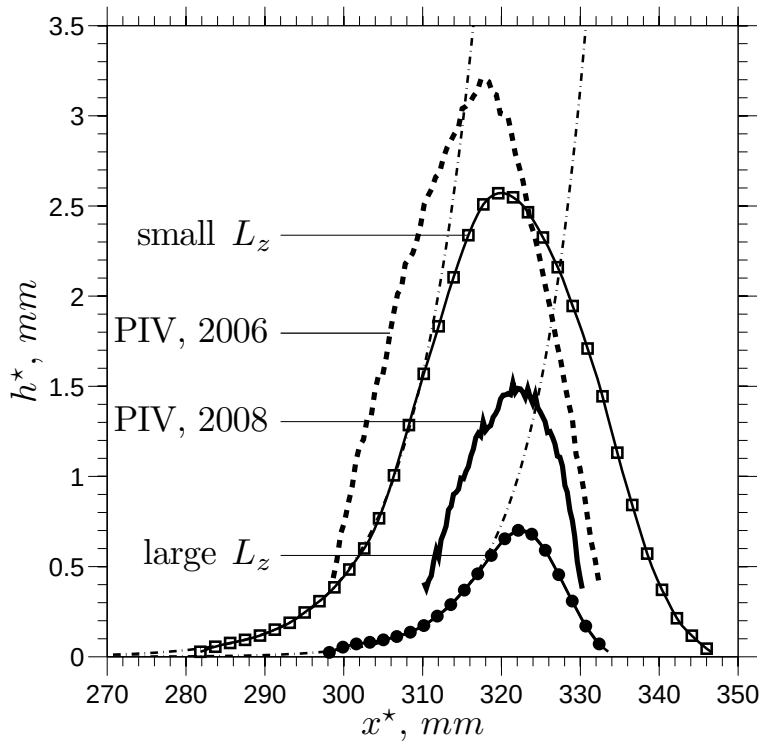

FIGURE 4.12: Mean zero-u-velocity contours

nine. The effect on the bubble is impressive, with the narrow-span bubble about 60% longer and 300% taller. One other striking aspect is that the narrow-span bubble height is very close to the 2006 experimental campaign.

The bubble sensitivity to the spanwise length may be related to the level of spanwise coherence. Figure 4.13 illustrates the important difference between the two LES by looking at the Fourier transform of the spanwise correlation function of the streamwise velocity component. One can see that the narrow-span LES is sufficiently wide to resolve all the significant structures of the incoming TBL but that the most energetic spanwise modes are cut-off inside the interaction, forcing the bubble to remain two dimensional. This artificial two-dimensional bubble topology was shown to lead to significant differences in the predicted interaction lengths. It is therefore possible that the spanwise coherence between the 2006 and newer experiments was significantly affected by a change in the seeding conditions which eventually lead to a 25% change in the interaction length. We shall come back to some properties of the bubble topology in chapters 5 and 6.

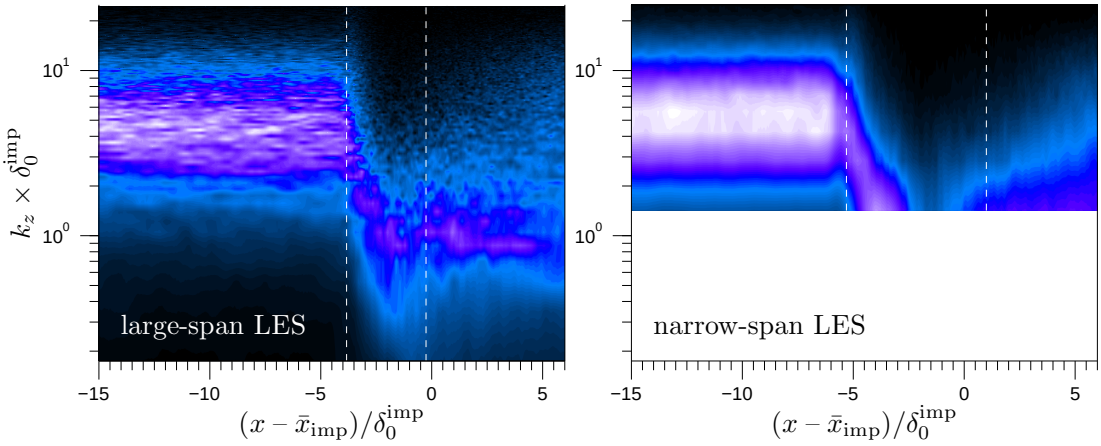

FIGURE 4.13: One-dimensional weighted spectra maps of the span-wise correlations of the streamwise-velocity component at $y/\delta_0^{\mathrm{imp}} \approx 0.02$: large- *vs* narrow-span LES. Contours show $k_z \cdot |E_{uu}|$, where $E_{uu}(k_z) = (1/L_z) \int_{-L_z/2}^{L_z/2} R_{uu}(z) \exp(-2i\pi k_z z) \mathrm{d}z$, with $R_{uu}(z) = \overline{u'(z_0,t)u'(z_0+z,t)}/\overline{u'(z_0,t)u'(z_0,t)}$. The *white dashed lines* indicate the location of separation and reattachment

4.2.2 The ITAM case

In the early stages of the UFAST project, the ITAM case was set up with a wedge angle at 8° and an even lower Reynolds number, but the first half of the project raised a number of difficulties. First, the choice of a low Reynolds number resulted in major experimental issues, where it was not possible to obtain a canonical incoming TBL. Second, preliminary simulation runs evidenced large discrepancies between the simulated and experimental interaction lengths. Therefore, it was decided to increase the Reynolds number and reduce the shock strength by setting the wedge angle to 7°. This thesis only briefly reports the latest results from the 7° case. Figure 4.14 provides the incoming reference profiles. Although the comparison is better than in the early stages of the project, it is not completely satisfactory. Note that the 2D/3D RANS results from the partner Podgorny Institute for Mechanical Engineering Problems (UAN) are also reported in the figure. Those 2D/3D RANS simulation results were performed using the UAN in-house solver FlowER. The 3D compressible Reynolds-averaged Navier–Stokes equations are solved using an implicit time-integration scheme combined with a second-order accurate finite volume approach for the spatial discretisation. The code uses an exact Riemann-problem solver. The turbulence model chosen for this study is the k-ω SST model.

Figure 4.15 compares the streamwise RMS velocity fluctuations from the hot-wire anemometry (HWA) measurements and the LES. The RMS levels are scaled according to Morkovin's scaling and compared with the incompressible DNS data of Spalart (1988). The disagreement between the LES and HWA was discussed at length in the

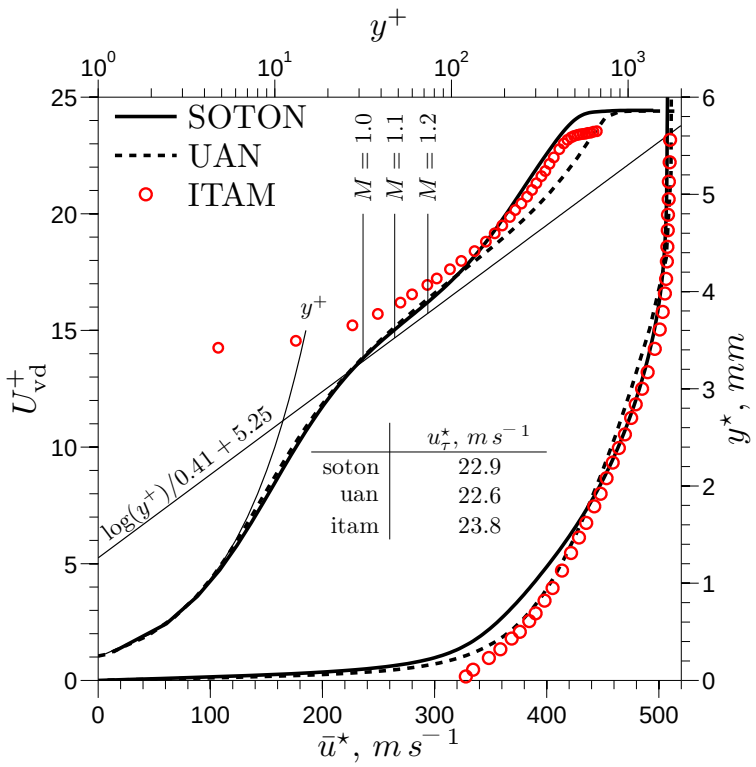

FIGURE 4.14: Upstream velocity profiles (at $x^\star = 260\,mm$)

course of the UFAST project. In summary, the lack of fluctuations in the HWA data is due to poor performance of the constant-temperature-anemometry (CTA) system at high frequencies, therefore cutting off the near-wall high-frequency turbulent fluctuations. ITAM has corrected the high-frequency response of the CTA measurements using a transfer function. The data presented in figure 4.15 include this correction. It can be seen that the fluctuations in the inner region are still underestimated. However, the outer-layer region is close to the DNS data and the correction seems to be applicable there. The LES shows the opposite trend. The inner layer is relatively near the DNS data but the outer region is overestimated. The higher LES levels can be explained by the position of the reference plane, which is too close to the inflow plane. The boundary layer at the reference station is still recovering from the inlet conditions. It was shown in chapter 2 that the outer-layer region recovers more slowly than the inner layer. In fact, if the reference plane had been further downstream from the inlet plane, the outer profile would have a shape closer to the DNS. Finally, the LES inflow plane produces a weak shock in addition to being relatively noisy, with values of $\sqrt{\overline{p'_w p'_w}}/\tau_w \approx 5$, artificially increasing the RMS levels.

Figure 4.16 compares the wall-pressure evolution along the interaction for the experiment, the LES and the 2D/3D RANS calculations of UAN. Despite the use of a reduced

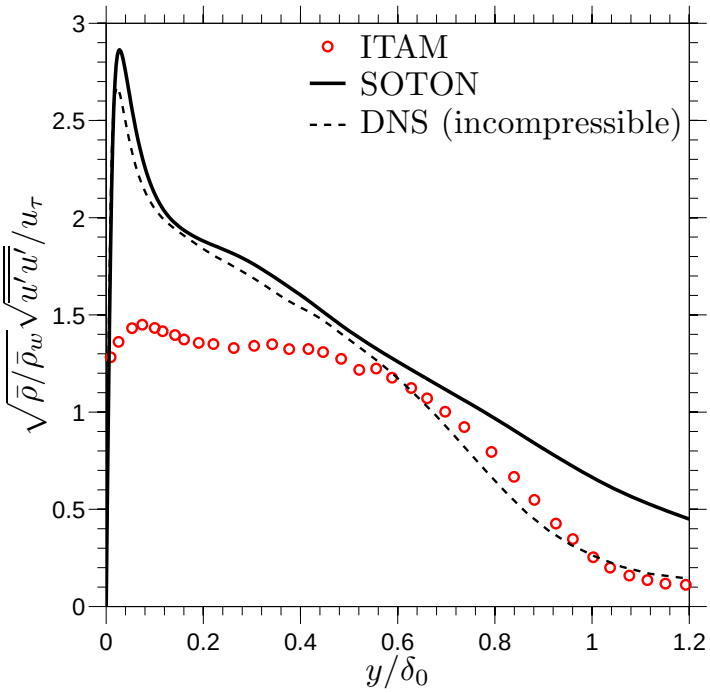

FIGURE 4.15: Upstream streamwise velocity fluctuations (at $x^\star = 260\,mm$)

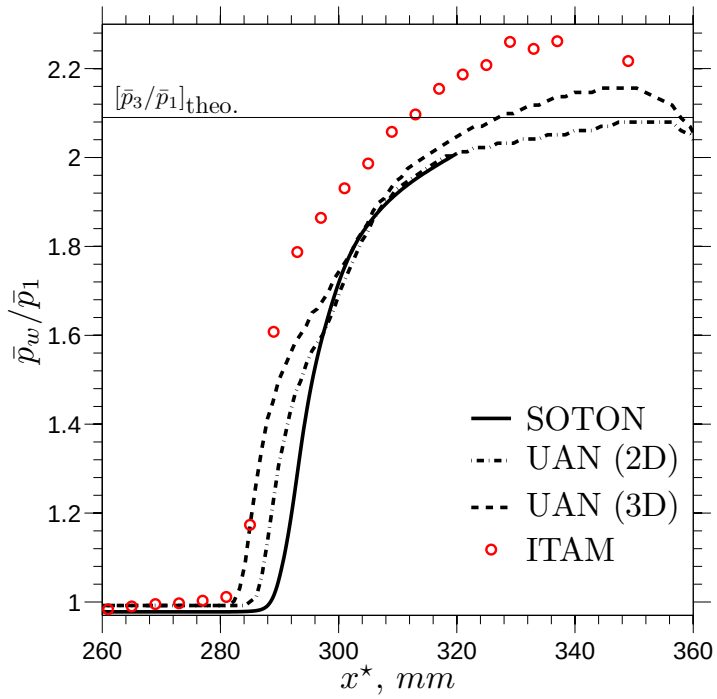

FIGURE 4.16: Wall-pressure distribution

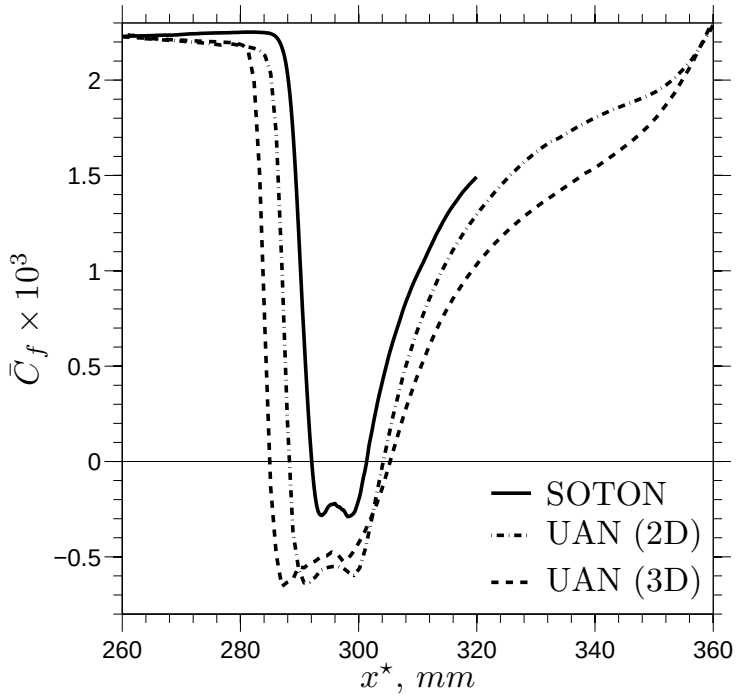

FIGURE 4.17: Skin-friction distribution

wedge angle, the interaction length in the experiment is still longer than in the simulations. There are several interesting observations to make here. First, the interaction length is seen to correlate with the back-pressure level. In this respect, the experiment overshoots the theoretical back-pressure value which could force the separation to move upstream. The reason why the back pressure overshoots the theoretical value is not fully understood but the 3D RANS calculations of UAN offer some useful insight since the presence of the side-wall boundary layers and the associated corner flows is responsible for at least part of this pressure overshoot, as shown in the 3D RANS wall-pressure distribution, compared to the 2D RANS findings. The 3D-RANS pressure overshoot is not as strong as in the experiment, but is sufficient to produce a pressure gradient that is closer to the experiment, perhaps bringing the separation point closer to the experimental one. This is further shown in the skin-friction distribution in figure 4.17. One other aspect of the wall-pressure distribution is the apparent pressure decrease near the end of the graph, a feature not captured by the LES. This is believed to be due to the expansion fan originating from the wedge trailing edge, which is included in the RANS but not in the LES. This can be seen in figure 4.18. It should be noted that the incident-shock impingement point found in the experiment does not exactly

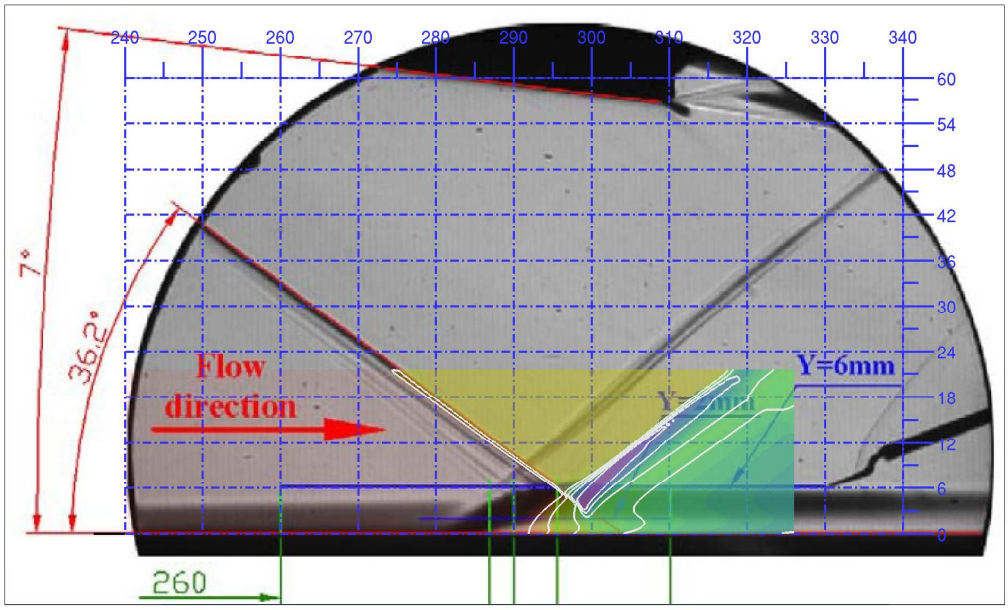

FIGURE 4.18: LES pressure field *vs* Schlieren picture

match the theoretical values. After discussing this with the ITAM group, the experimental incident-shock impingement point was found to be about $2.2\,mm$ earlier than the expected theoretical location. The difference mainly comes from the fact that the actual leading edge of the wedge is not perfectly sharp. All the plots presented here already account for this shift. Figure 4.18 clearly illustrates the difference in the predicted interaction length by the LES and experimental findings. The 3D RANS investigations of UAN tend to suggest that the failure of statistically 2D simulations (as in the LES) to reproduce the wind-tunnel experiments is related to the presence of strong side-wall corner flows inside the wind tunnel.

4.2.3 The TUD case

As mentioned at the beginning of this chapter, the TUD case is the only LES where the experimental flow conditions are not fully matched. The Reynolds number, based on the momentum thickness, is about 3×10^3 in the LES while it is about 5×10^4 in the actual setup. A detailed description of the experimental data that are reproduced here can be found in Souverein et al. (2008) and Souverein et al. (2009b). The large Reynolds-number difference is easily seen in figure 4.19 with the van Driest velocity profiles, expressed in wall units. The Reynolds-number effect is not visible using the velocity-defect scaling, where the profiles collapse well on one single profile (see figure 4.19). This confirms the turbulent character of both the simulated and the actual boundary layers. Similarly, using Morkovin's scaling for the friction velocity and the boundary-layer thickness

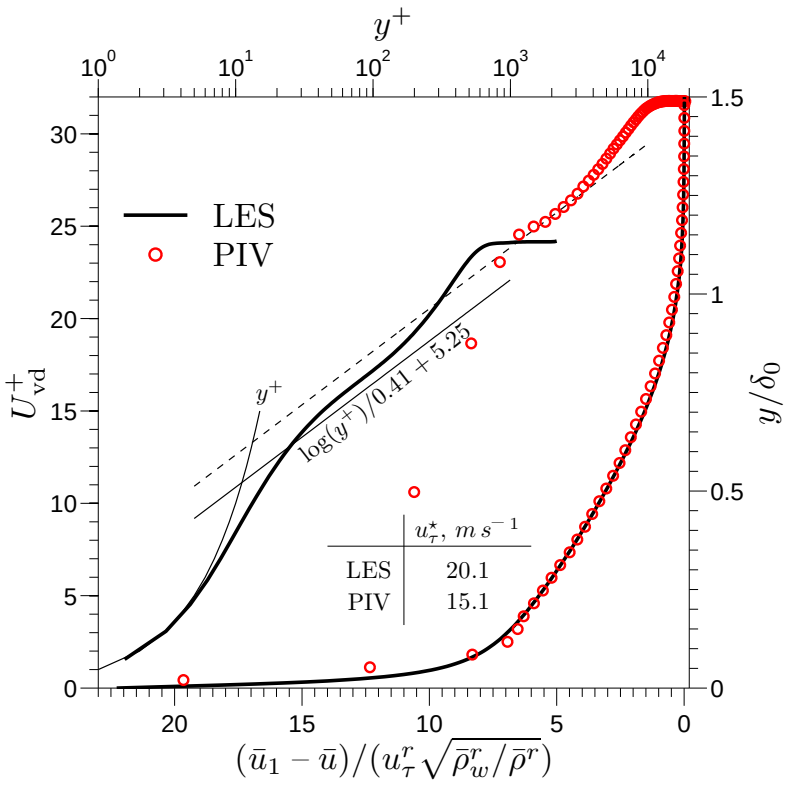

FIGURE 4.19: Velocity profiles at $(x-\bar{x}_{\mathrm{imp}})/\delta_0^{\mathrm{imp}}=-4.5$

as the reference lengthscale, one can make the streamwise-velocity fluctuation profiles obtained with the LES agree reasonably well with the PIV results (figure 4.20). The wall-normal-velocity fluctuations give greater differences. It is believed that the PIV underestimates the wall-normal-velocity fluctuations near the wall while the LES may be over-estimating them. The higher levels of fluctuations found by the PIV outside the boundary layer can be inferred to the wind-tunnel freestream turbulence[4].

Figure 4.21 gives a side-by-side comparison of the defect-velocity field across the interaction, where the same contours are plotted and the defect-velocity scale makes use of the upstream boundary-layer properties (as in figure 4.19, which we term reference profiles – hence the superscript "r" in the figure captions). Note that the reference lengthscale used here is the 99% boundary-layer thickness and that the streamwise axis has its origin at the incident-shock-impingement location. Overall, the two figures look similar, although one can note the larger boundary-layer thickening and interaction length in the LES. However, the larger interaction length in the LES is relative to the choice of reference lengthscale. For example, figure 4.22 compares the mean wall-normal-velocity field using the reference boundary-layer thickness (left) or the reference displacement thickness (right). Since the Reynolds numbers are significantly different, the ratio δ_0/δ_1

[4]Private communication with Louis Souverein, December 2008.

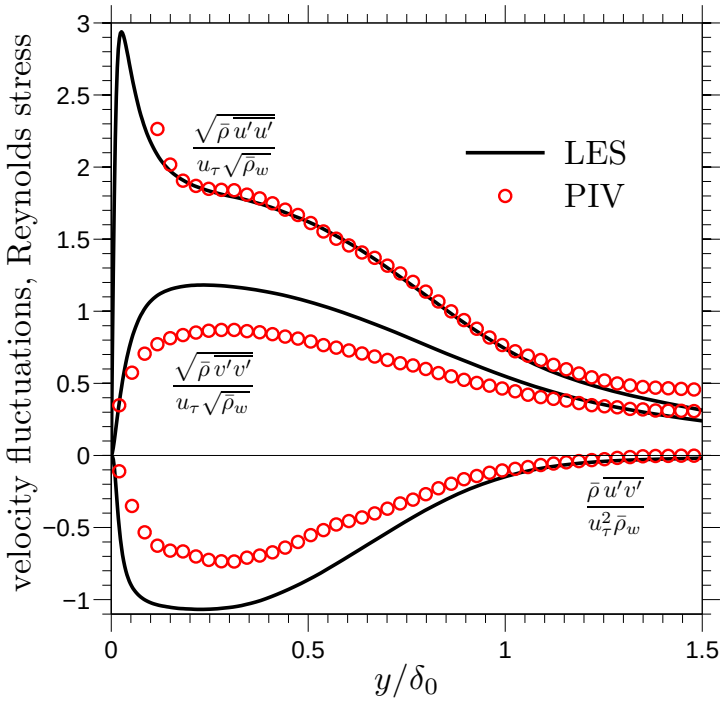

FIGURE 4.20: Reynolds stress profiles at $(x - \bar{x}_{\text{imp}})/\delta_0^{\text{imp}} = -4.5$

in the experiment is different from the LES, making the choice of lengthscale important for the interpretation. In figure 4.22, the displacement thickness seems to perform well at collapsing the LES on top of the PIV. However, in figure 4.20, the boundary-layer thickness was clearly seen to be a good choice for the Reynolds stresses. This is why figures 4.23 to 4.25 make use of the boundary-layer thickness. Overall, the velocity-fluctuation contour plots give similar qualitative distributions. However, there are some differences. For example, near the reflected-shock foot, the PIV field has more energetically significant fluctuations. Similarly, the fluctuations due to the presence of the shockwaves in the potential flow are more visible in the PIV. The fact that the incident shock can be seen in the PIV fields suggests that the PIV may overestimate the fluctuations near shocks.

In addition to studying each flow case separately, it is interesting to compare all the LES results and see whether a consistent picture arises from the different flow cases. This is the focus of the following sections.

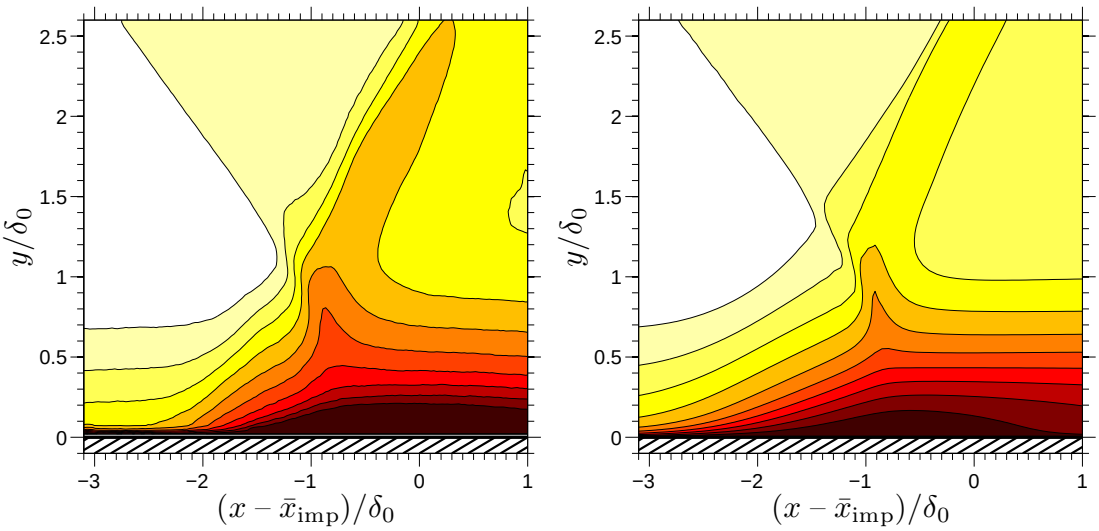

FIGURE 4.21: Mean streamwise velocity field: PIV (*left*) *vs* LES (*right*). Contours are based on the velocity defect field $(\bar{u}_1 - \bar{u})/(u_\tau^r \sqrt{\bar{\rho}_w^r/\bar{\rho}^r})$ and are taken at exactly the same levels in both the PIV and LES fields

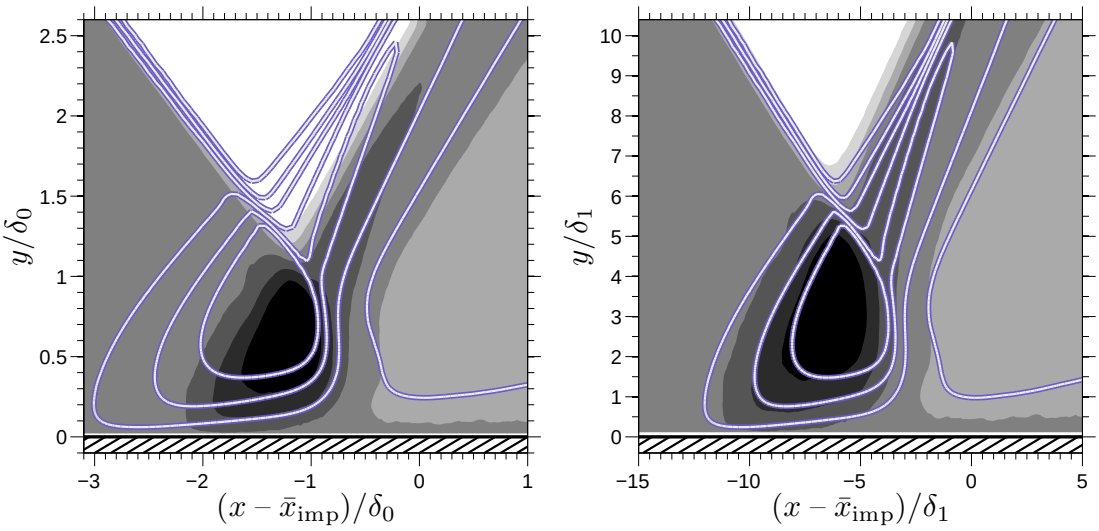

FIGURE 4.22: Mean wall-normal velocity field: PIV (*filled contours*) *vs* LES (*solid lines*), using δ_0 as reference lengthscale (*left*) or δ_1 (*right*)

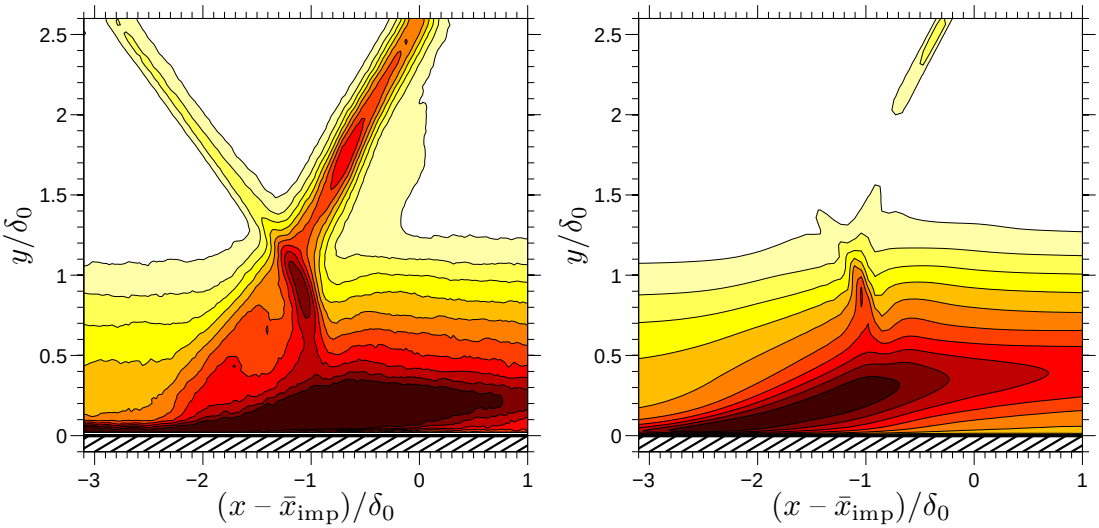

FIGURE 4.23: Streamwise velocity fluctuations field: PIV (*left*) *vs* LES (*right*). Contours are based on the RMS velocity field using the upstream Morkovin's scaling $\sqrt{\bar{\rho}^r \overline{u'u'}}/(u_\tau^r \sqrt{\bar{\rho}_w^r})$ and are taken at exactly the same levels in both the PIV and LES fields

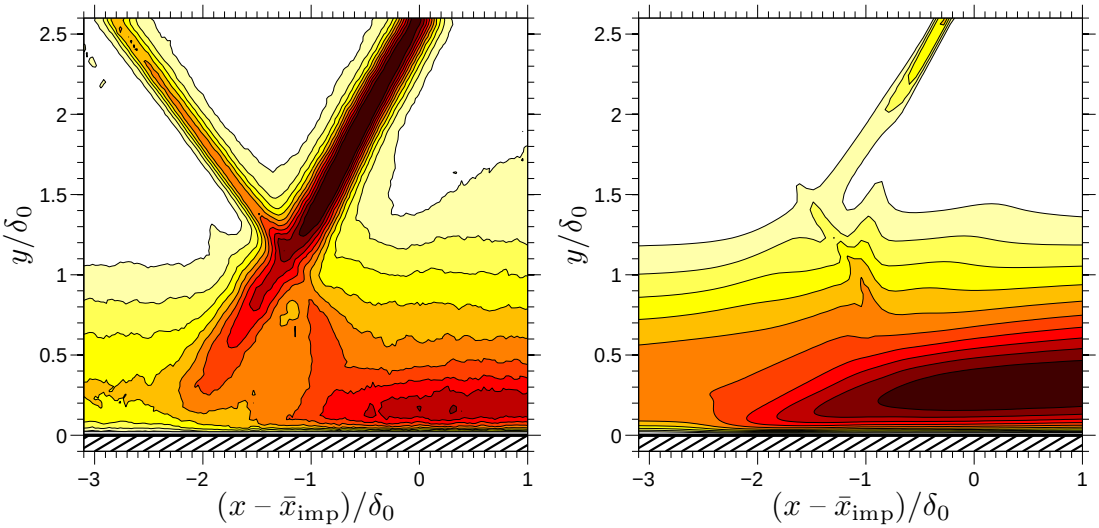

FIGURE 4.24: Wall-normal velocity fluctuations field: PIV (*left*) *vs* LES (*right*). Contours are based on the RMS velocity field using the upstream Morkovin's scaling $\sqrt{\bar{\rho}^r \overline{v'v'}}/(u_\tau^r \sqrt{\bar{\rho}_w^r})$ and are taken at exactly the same levels in both the PIV and LES fields

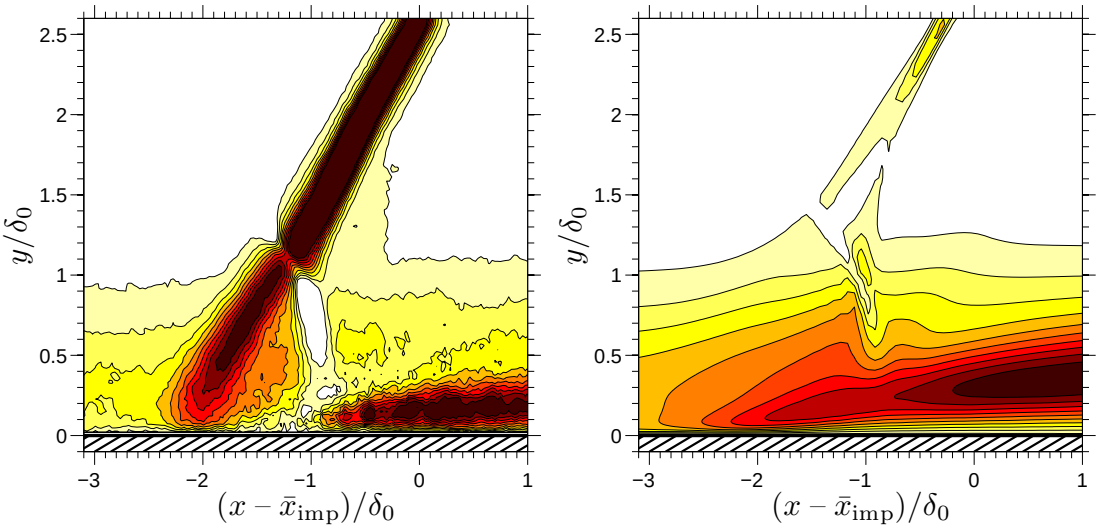

FIGURE 4.25: Reynolds shear-stress field: PIV (*left*) *vs* LES (*right*). Contours are based on the shear-stress field using the upstream Morkovin's scaling $\bar{\rho}^r\overline{u'v'}/(u_\tau^{r\,2}\bar{\rho}_w^r)$ and are taken at exactly the same levels in both the PIV and LES fields

4.3 Cross comparisons

In this section, the time-averaged properties of the previously defined LES are compared. In addition to the UFAST cases, a 4°-wedge-angle ITAM case has been added, where the simulation was set up such that the impingement point matches the one in the 7° case. The upstream van Driest-transformed velocity profiles are shown in figure 4.26. The IUSTI case has the highest Mach and Reynolds numbers, while the ITAM and TUD cases have similar Reynolds number, but different Mach number. It should be noted that at constant Reynolds number, the constraint on the grid resolution increases as the Mach number decreases, simply because of the temperature dependence of the dynamic viscosity. Therefore, running the ITAM case at the TUD resolution is less expensive than running the TUD case.

Figure 4.27 provides the Reynolds stresses at the same station as for the velocity profiles. Apart from being rescaled to the simulated displacement thickness, all the digital-filter settings were exactly the same in all three cases. It is shown in chapter 2 that the digital-filter approach requires approximately ten to twenty boundary-layer thicknesses to recover the introduced modelling errors at the inlet. In particular, the outer region of the boundary layer was found to exhibit the slowest recovery and this effect appeared to be stronger as the Mach number was increased. This can explain the small hump one can see in the outer-layer region of the IUSTI Reynolds stress profile. As the reference station is moved further downstream, an equilibrium state is reached and the hump slowly disappears. A trade-off between the domain size and the possibility

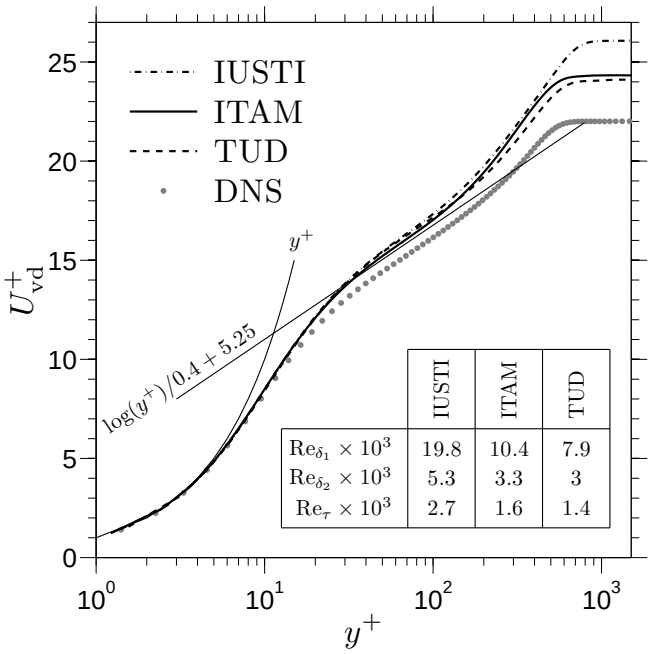

FIGURE 4.26: van Driest-transformed velocity profiles of the UFAST cases upstream of interaction at $(x-\bar{x}_{\mathrm{imp}})/\delta_0^{\mathrm{imp}} = -4.5$. The DNS data corresponds to the incompressible simulations of Spalart (1988) at $\mathrm{Re}_{\delta_2} = 1410$. The Reynolds numbers quoted in the figure are defined as: $\mathrm{Re}_{\delta_1} = \bar{\rho}_1\bar{u}_1\delta_1/\bar{\mu}_1$, $\mathrm{Re}_{\delta_2} = \bar{\rho}_1\bar{u}_1\delta_2/\bar{\mu}_1$ and $\mathrm{Re}_{\tau} = \bar{\rho}_1 u_\tau\delta_0/\bar{\mu}_1$

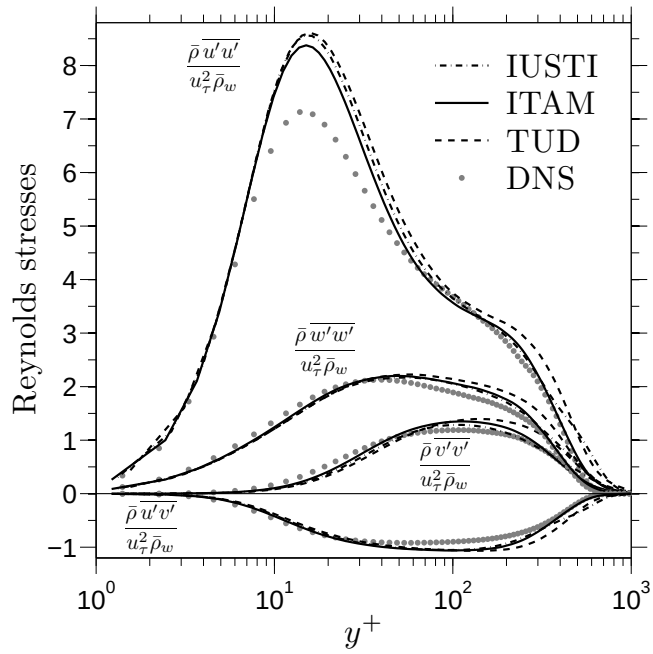

FIGURE 4.27: Reynolds-stresses profiles of the UFAST cases, expressed using Morkovin's representation and taken at $(x - \bar{x}_{\mathrm{imp}})/\delta_0^{\mathrm{imp}} = -4.5$. The DNS data corresponds to the incompressible simulations of Spalart (1988) at $\mathrm{Re}_{\delta_2} = 1410$

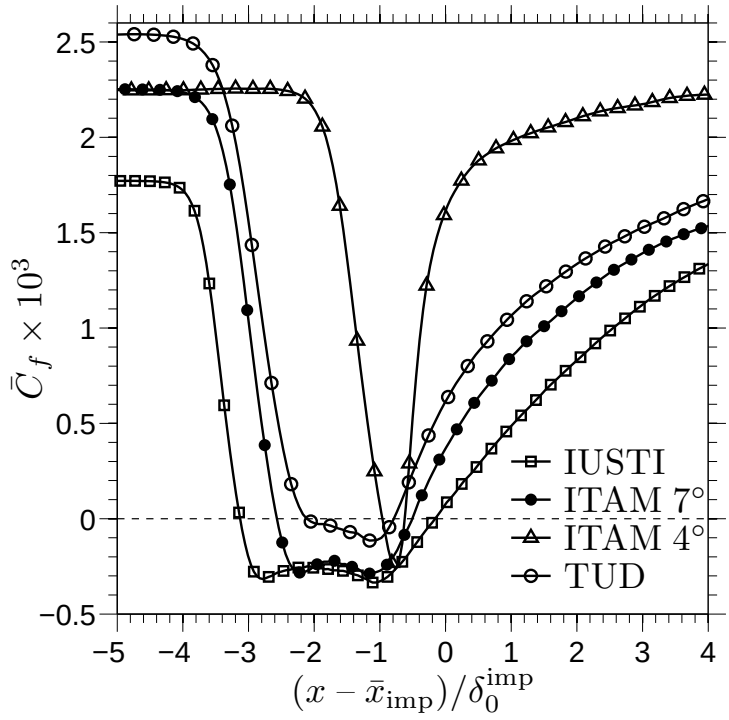

FIGURE 4.28: Mean skin-friction distributions of the UFAST cases

to run the simulation for very long times is required.

Figures 4.28 and 4.29 give the time- and span-averaged skin-friction and wall-pressure distributions. The Reynolds number effect on the skin friction upstream of interaction is clearly seen. All flow cases exhibit a mean separation although the TUD case could be considered as marginally separated. The separation length relative to the boundary-layer thickness is: $L_{\mathrm{sep}}/\delta_0^{\mathrm{imp}} = 2.97$ (IUSTI), 2.06 (ITAM 7°) and 1.33 (TUD). The interaction length, computed from the theoretical inviscid impingement point and the mean position of the reflected-shock (determined by linearly extrapolating to the wall the ridge seen in the Reynolds-shear-stress field inside the potential flow) is found to be: $L/\delta_0^{\mathrm{imp}} = 3.64$ (IUSTI), 3.01 (ITAM 7°) and 2.56 (TUD). Note the relatively large differences (93% for the TUD case) between the separation length and the interaction length. Those differences should be considered with care when comparing shock-reflection configurations with ramp-corner flows.

Interestingly, the rate of decrease in skin friction (figure 4.28) is similar in all cases compared to the differences in the recovery rates. The apparent similarity in the skin-friction drop is reminiscent of the free-interaction theory (Stewartson and Williams, 1969; Katzer, 1989). However, contrary to what figure 4.28 could suggest, the separation point is not solely governed by the incoming skin-friction level, and of course

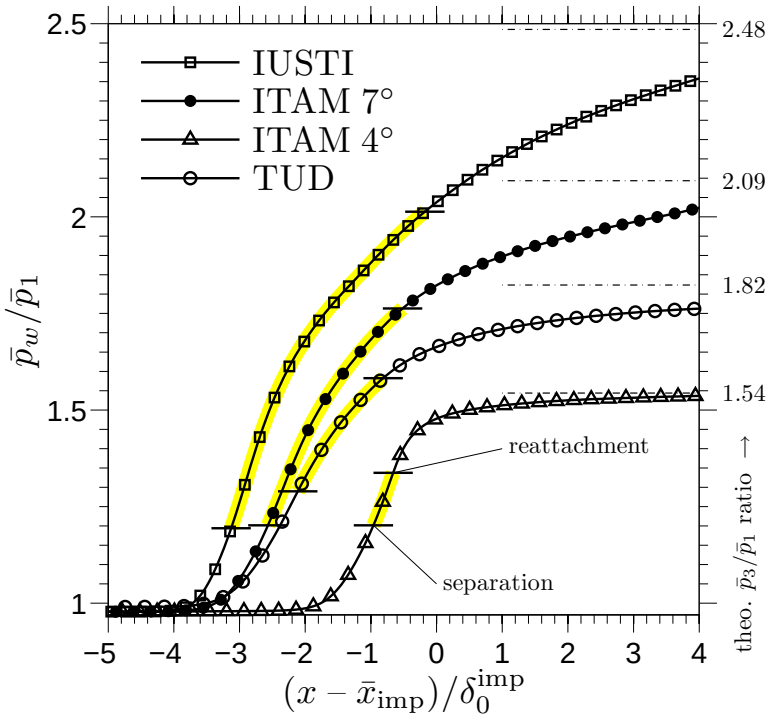

FIGURE 4.29: Mean wall-pressure distributions of the UFAST cases, normalised with upstream pressure. In addition, the separation and reattachment locations are indicated on the wall-pressure distributions. On the right-hand side of the figure, the theoretical pressure increase across the shock-reflection system as predicted by inviscid theory is provided for each flow case

the pressure increase plays a significant role and should be accounted for. This is for example confirmed by the ITAM 4° and 7° cases where the upstream boundary-layer is identical but subject to a significantly different pressure increase (see figure 4.29). In fact, figure 4.29 shows that separation occurs at the same excess-pressure level $\bar{p}_w/\bar{p}_1$ in the ITAM 7° and 4° cases. Interestingly, the IUSTI and TUD cases also separate at a similar excess-pressure level to the ITAM case ($\bar{p}_{\mathrm{sep}}/\bar{p}_1 = 1.19$ for IUSTI, $\bar{p}_{\mathrm{sep}}/\bar{p}_1 = 1.20$ for ITAM, $\bar{p}_{\mathrm{sep}}/\bar{p}_1 = 1.29$ for TUD), with the TUD case slightly departing from the other cases. Since the TUD-case Reynolds number is closer to the ITAM one than the ITAM one is to the IUSTI one, this difference could be interpreted as a small Mach-number effect.

One other aspect of the mean separation bubble is its height. Figure 4.30 shows the span- and time-averaged zero streamwise-velocity contours of the different flow cases. The bubbles are found to be very shallow, with aspect ratios from 5×10^1 to 5×10^2. The TUD bubble does not even rise above the incoming viscous-sublayer height ($y^+ = 8$), making its experimental detection rather challenging. Of course, instantaneous snapshots (as in figure 4.1) exhibit occurrences of much taller bubbles and what is shown

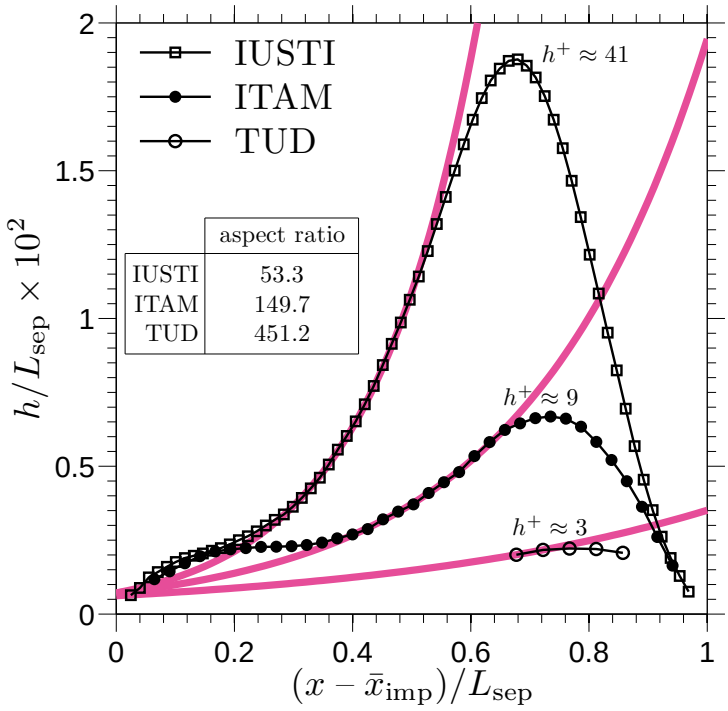

FIGURE 4.30: Mean zero-streamwise-velocity contours of the UFAST cases. The h^+ values indicate the maximum height reached by the contour expressed in wall units taken at the same reference plane as in figures 4.27 and 4.28. The *thick coloured lines* indicate an exponential best-fit lines on a particular section of the contours. The contours aspect ratios, defined as $L_{\mathrm{sep}}/h_{\mathrm{max}}$, are also provided in the figure

in figure 4.30 is a time and span average. The maximum reversed flow recorded in the instantaneous LES flowfields was $.60\bar{u}_1$ (IUSTI), $.43\bar{u}_1$ (ITAM) and $.58\bar{u}_1$ (TUD) while the span- and time-averaged maximum reversed flow is $.027\bar{u}_1$ (IUSTI), $.007\bar{u}_1$ (ITAM) and $.0007\bar{u}_1$ (TUD). Therefore, the intermittent and marginal nature of the TUD separation bubble does not prevent the occurrence of similar reversed-flow magnitudes to the IUSTI case. This is important to note when considering the low-frequency shock oscillations (discussed in chapter 6). Finally, the bubble contours (at least for the IUSTI and ITAM cases) are found to exhibit a section which grows exponentially in the streamwise direction, before the maximum height is reached.

Dupont et al. (2008) have synthesised the experimental investigations performed at IUSTI (figure 7 in Dupont et al., 2008) for various flow conditions and measurement techniques. Despite the data scatter, their figure suggests a possible linear relationship (for the weakest interactions) between the interaction length (expressed in upstream boundary-layer thickness) and the ratio between the pressure jump across the impinging shockwave and the upstream wall-shear stress. The same relation is plotted in figure 4.31 with both the LES and the experimental data (only for adiabatic-wall conditions).

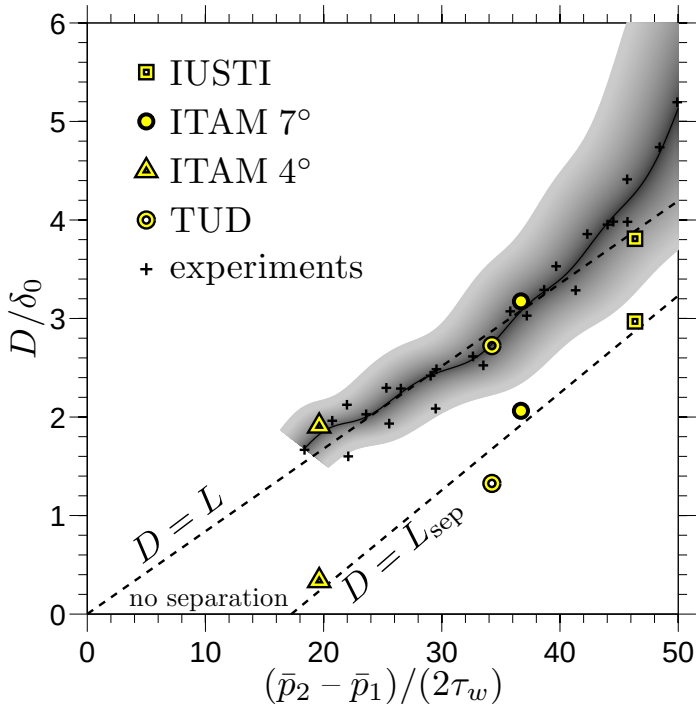

FIGURE 4.31: Relationship between the interaction lengths and the upstream wall-shear stress to pressure jump ratios. D is either the separation-bubble length or the interaction length. The pressure difference $\bar{p}_2 - \bar{p}_1$ is the theoretical pressure jump across the impinging oblique shockwave. The experimental data are from Dupont et al. (2008) (where only the adiabatic-wall cases are reproduced). The *dashed lines* indicate the best-fit line passing through the LES data. In the case of $D = L$, the best-fit line was forced to go through the origin. The *solid black line* comes from filtering the set of experimental data using a 6^{th}-order low-pass non-causal Butterworth filter with cutoff at $\tau_w/(\bar{p}_2 - \bar{p}_1) \approx 0.05$

It can be argued that in the absence of the shock ($\bar{p}_2 - \bar{p}_1 = 0$), the interaction length vanishes and therefore the origin of the graph is also a data point. Using the LES data (including the ITAM 4° case), a best-fit line passing through the origin was computed (dashed line) and the LES data points do not seem to be far off the linear relationship. It must be noted that the experimental data from Dupont et al. (2008) have been rescaled using the LES boundary-layer-thickness and wall-shear-stress values, which are more reliably obtained from the simulation than measured experimentally. This resulted in a shift (of about 5% along the y-axis and 10% along the x-axis) towards the suggested linear relationship. However, the experimental data are seen to depart from the suggested linear relationship for stronger interactions. This could be due to some wind-tunnel side-wall effects which are known to considerably change the topology of the separation bubble for strong interactions (Dussauge and Piponniau, 2008), leading to an increased interaction length. The grey region in the figure delimits the region spanned by the

solid black line assuming a realistic level of uncertainty in the data ($\pm 5\%$ in evaluating L and δ_0 combined with an error of $\pm 10\%$ in evaluating the wall-shear stress – with the worst-case combination considered). Finally, the case where the chosen reference length is the separation length is shown. The intersection of the line with the abscissa indicates the onset of separation and the $(\bar{p}_2 - \bar{p}_1)/(2\tau_w) \approx 17$ value is found to correspond well with the $\bar{p}_w/\bar{p}_1$ values at separation from figure 4.29 (taking $\bar{p}_2 = \bar{p}_w$).

4.4 Mixing-layer properties

As mentioned in chapter 2, Piponniau et al. (2009) have recently considered the shear layer forming above the separation bubble as playing a key role in the observed low-frequency shock motions and proposed a model based on the mass-entrainement timescale associated with the separation bubble and the developing mixing layer. With this scaling argument and empirical relations, the authors find that the resulting timescale is of the same order of magnitude as the dominant low-frequency shock-motion timescale. In this section, the shear-layer properties as found in the LES data are reported, to check whether the scaling arguments and empirical relations used by Piponniau et al. (2009) agree with the numerical results.

Figure 4.32 gives the location of the mixing-layer centreline for all three cases (IUSTI, ITAM and TUD). It was computed following the local inflection point in the wall-normal distribution of the mean streamwise momentum component[5]. The distances in figure 4.32 were normalised by the respective interaction length L to remove the important differences in the L/δ_0^{imp} values between the three simulated cases. Using this scaling, the mixing-layer centreline in all three cases follows a similar pattern with two main sections: a first one ranging from the reflected-shock foot to the incident-shock tip with a relatively important inclination angle with respect to the wall ($\mathcal{O}(20°)$) and a second one starting at the incident-shock tip and continuing in the recovery region with a smaller inclination angle. Note that as the incident-shock strength is weakened (from IUSTI to TUD), the transition from the first to the second section of the mixing-layer centreline is smoother.

In this section, the path described by the mixing-layer centreline defined in figure 4.32 will be used as local coordinate system with ξ and ζ the local tangential and normal components, respectively. Therefore, the time-averaged velocity components in this curvilinear system are denoted $\bar{u}_\xi$ and $\bar{u}_\zeta$. The velocity distribution $\bar{u}_\xi(\zeta)$ at several ξ locations (along the mixing-layer centreline) is provided in figure 4.33. Those profiles are

[5]Note that several inflection points occur in the $\overline{\rho u}(y)$ profiles, especially in the recovery region where three inflection points may be found. In this study, we chose the one that is the farthest from the wall as this is the one that was most likely used in Piponniau et al. (2009).

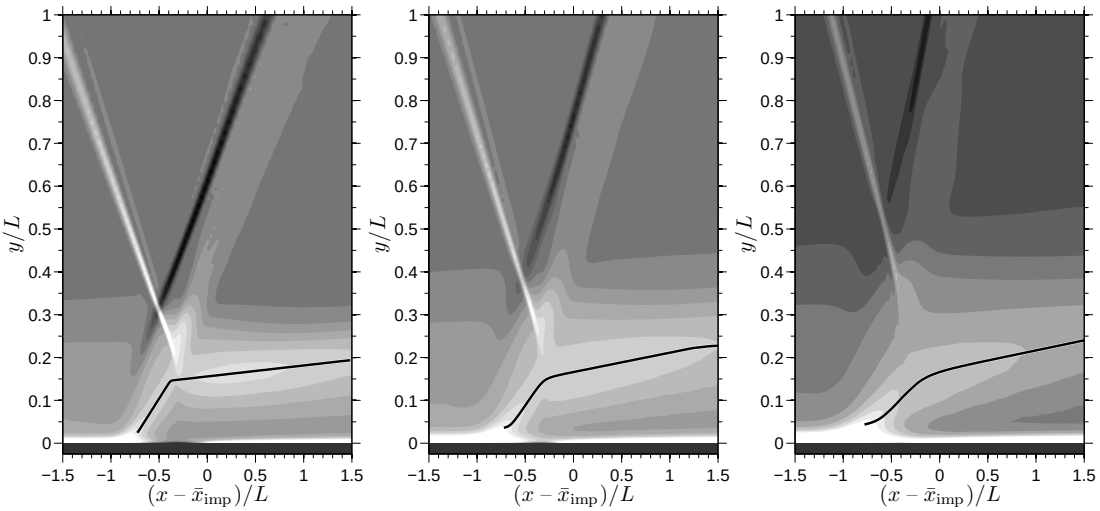

FIGURE 4.32: Shear-layer centreline location: IUSTI (*left*), ITAM (*middle*), TUD (*right*). The *filled contours* give the $\partial\overline{\rho u}/\partial y$ field. The *solid lines* indicate the location of inflection points of interest (i.e. $\partial^2\overline{\rho u}/\partial y^2 = 0$)

used to define several quantities of interest, which are needed to estimate some parameters employed in Piponniau et al. (2009). The high velocity $\bar{u}_\xi^u$ is defined as the first local maximum of the relative velocity component $\bar{u}_\xi - \bar{u}_\xi^c$ as one goes in the positive ζ direction, where $\bar{u}_\xi^c$ is the ξ-component of the mean velocity at the mixing-layer centreline ($\zeta = 0$). The low velocity $\bar{u}_\xi^d$ is defined as the relative velocity at the next inflection point in the $\bar{u}_\xi - \bar{u}_\xi^c$ velocity profile as one goes to negative ζ values. If no inflection point is found, the first local minimum in $\bar{u}_\xi - \bar{u}_\xi^c$ is used instead. Those two definitions are identified by the black dots in figure 4.33. The difference between the high velocity $\bar{u}_\xi^d$ and the low velocity $\bar{u}_\xi^d$ is called the velocity deffect accross the mixing layer. The shear-layer vorticity thickness is defined as the ratio between the velocity deffect and the rate of velocity increase at the mixing-layer centreline: $(\bar{u}_\xi^u - \bar{u}_\xi^d)/\left[\mathrm{d}\bar{u}_\xi/\mathrm{d}\zeta\right]_{\zeta=0}$. The mixing-layer velocity profiles on the left of figure 4.33 are rescaled using the local velocity deffect and the vorticity thickness. The results are shown on the right of figure 4.33. If the mixing layer were canonical, this choice of similarity scaling would make the profiles collapse onto one single curve which is represented by the error function (shown in dashed line in the figure). The particular configuration due to the presence of the shockwaves does not allow the mixing layer to be of a canonical nature and the similarity scaling is not found to be effective at collapsing the profiles, except near the centreline.

Figure 4.34 shows the vorticity-thickness evolution along the mixing-layer centreline as well as the isentropic convective Mach number M_c, defined as the ratio between the velocity deffect and the sum of the local speeds of sound evaluated at the same locations as the velocities used to compute the velocity deffect (see Piponniau et al., 2009). Furthermore, the velocity ratio $r = (\bar{u}_\xi^c + \bar{u}_\xi^d)/(\bar{u}_\xi^c + \bar{u}_\xi^u)$ and density ratio $s = \bar{\rho}^d/\bar{\rho}^u$ as

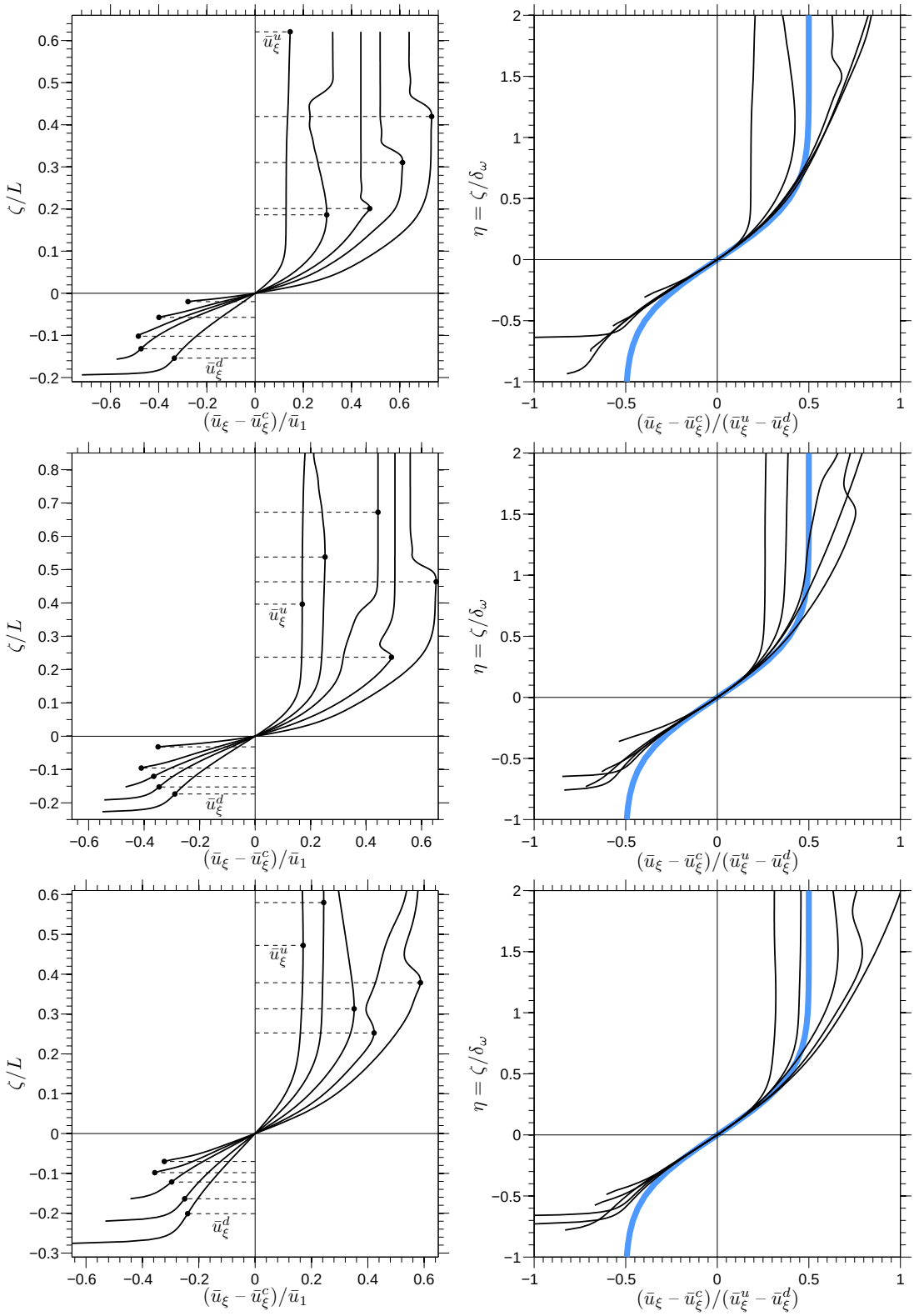

FIGURE 4.33: Velocity profiles at different stations along the shear-layer centreline: IUSTI (*top*), ITAM (*middle*), TUD (*bottom*). The figures on the *left* are normalised using global quantities whereas the figures on the *right* make use of local quantities. The *thick blue lines* correspond to erf $\left(\eta\sqrt{\pi}\right)/2$. The shear-layer vorticity thickness δ_ω is estimated using $(\bar{u}^u_\xi - \bar{u}^d_\xi)/\left[\mathrm{d}\bar{u}_\xi/\mathrm{d}\zeta\right]_{\zeta=0}$

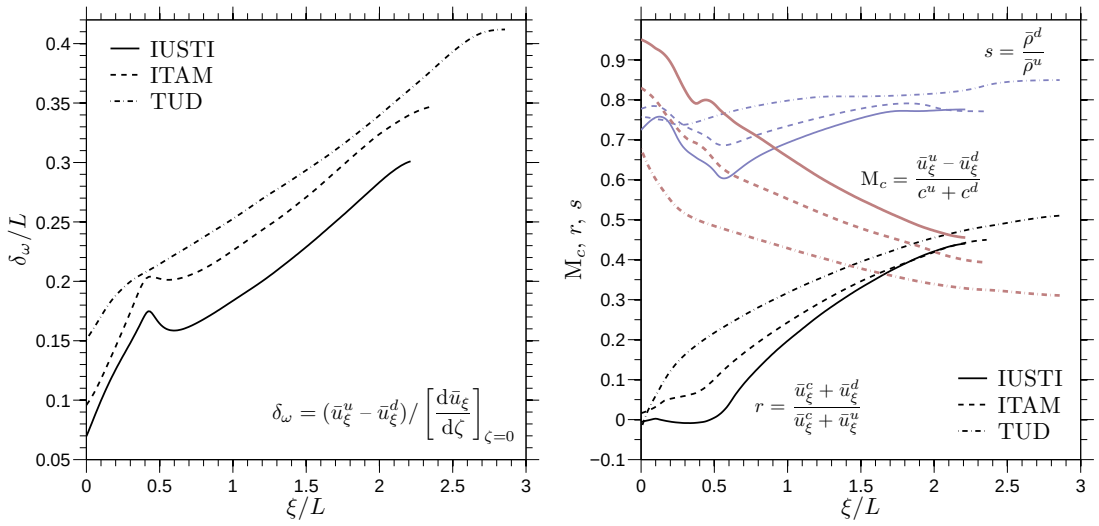

FIGURE 4.34: Shear-layer properties: vorticity thickness δ_ω (*left*), isentropic convective Mach number M_c, external velocity and density ratio (r and s, respectively, see Piponniau et al., 2009) (*right*)

a function of the position ξ along the mixing-layer centreline are also provided. These quantities are consistent with the notations introduced by Piponniau et al. (2009) which are used to evaluate the growth rate of the mixing layer following the empirical relation:

$$\delta'_\omega \equiv \frac{\mathrm{d}\delta_\omega}{\mathrm{d}\xi} = \frac{\delta'_{ref}}{2}\frac{(1-r)(1+\sqrt{s})}{1+r\sqrt{s}}\Phi(\mathrm{M}_c), \tag{4.1}$$

with $\delta'_{ref} \approx 0.16$ and where $\Phi(\mathrm{M}_c)$ is the normalised spreading rate (see Piponniau et al., 2009).

The above empirical relation can be compared against the LES results shown in figure 4.35 (for all the flow cases). Let us assume that Φ is 0.3, 0.35 and 0.45 for the IUSTI, ITAM and TUD cases respectively, based on M_c values of 0.9, 0.8 and 0.7 (see figure 4.34 at $\xi = 0$) and figure 2 in Piponniau et al. (2009). Combined with the results for r and s, one finds that $\delta'_\omega \sim 5 \times 10^{-2}$ using the empirical relation from canonical compressible mixing layers. This is different from the results shown in figure 4.35 where the LES spreading rates are significantly larger. The faster growth rate of the mixing layer in the SBLI case is believed to be due to the presence of the reflected shock, significantly affecting the flow at least on the faster-velocity side of the mixing layer.

In Piponniau et al. (2009), the most energetic low-frequency oscillations are evaluated using:

$$S_t \equiv fL/\bar{u}_1 = \frac{L}{H}\delta'_\omega\left[(1-r)C + \frac{r}{2}\right], \tag{4.2}$$

where $C \approx 0.14$ and H is approximately the largest height reached by the shear-layer centreline inside the interaction. From figure 4.32, one finds $H/L \sim 0.15$ (to compare with 0.12 in Piponniau et al., 2009). From figure 4.34, we have (for the IUSTI case) at

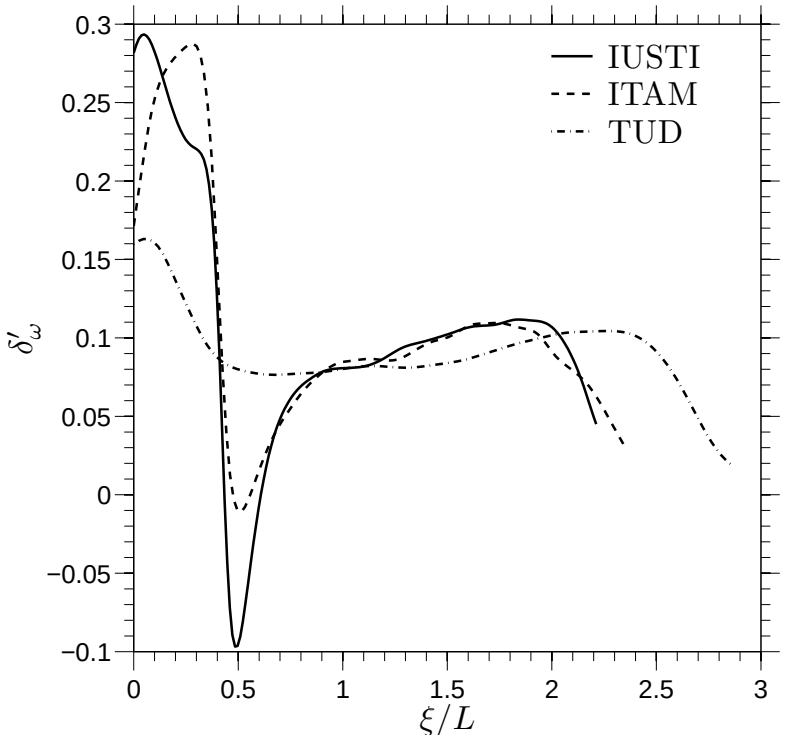

FIGURE 4.35: LES shear-layer spreading rates

the begining of the interaction: $s \sim 0.8$ and $r \sim 0$ (to compare with 0.56 and -0.11 in Piponniau et al., 2009). The convective Mach numbers are similar in both the LES and the experiment, hence $\Phi(\mathrm{M}_c) \approx 0.3$ in both cases. This gives $\delta'_\omega \sim 0.05$ using the values from Piponniau et al. (2009), 0.05 using (4.1) with the r and s LES values[6], and 0.3 using the LES data directly (see figure 4.35 at $\xi \approx 0$). From (4.2), one finds $S_t \sim 0.042$ in Piponniau et al. (2009), against 0.046 using the LES data with (4.1) to estimate δ'_ω or 0.28 if δ'_ω is computed directly from the LES data. The actual Strouhal number is 0.03 in the experiment (see Dupont et al., 2006) as well as in the LES (as will be shown in chapter 6).

The above shear-layer analysis thus reveals that the empirical relationship for the mixing-layer growth rate is not supported by the LES results with a difference of almost one order of magnitude. Therefore, the success of (4.2) to predict the low-frequency shock unsteadiness in Piponniau et al. (2009) seems fortuitous as it is bound to the use of (4.1) for the estimation of the growth rate. If the actual growth rate were used, the scaling for the low-frequency insteadiness would be about an order of magnitude larger than it actually is. This does not mean that the mechanism proposed by Piponniau et al. (2009) does not exist, but in light of the above results, it is believed to be acting at a higher frequency than the one of interest in this thesis.

[6]Note the good but fortuitous agreement at this point since there exist large differences in the s and r values.

In this chapter, we have focused on the time-averaged fields of three different shock-impingement configurations for which experimental data are available. It appeared that although the large-eddy simulation results of the IUSTI 8° case compared relatively well with the experimental findings, comparing LES results with experimental data is generally difficult. For example, it was shown that a change in the seeding of the PIV could greatly affect the interaction region and that the flow could be strongly influenced by the presence of the wind-tunnel side walls. The expansion fan originating from the wedge, and which is not included in the LES, could also interact with the boundary layer to modify the back pressure which can then influence the primary interaction. Therefore, the relative sensitivity of the interaction to experimental artifacts makes the comparison between experimental and numerical results rather uncertain. To reduce the level of uncertainties it is best to simulate the full experimental setup (i.e. include the wind-tunnel geometry). Unfortunately, the computational cost of such approach is not currently acceptable. Moreover, attempting to include potential experimental artifacts in simulations is not necessarily the correct approach if the purpose of the simulation is to study and understand the underlying mechanism responsible for the low-frequency shock motions.

Thus, a more consistent comparison was performed by comparing the LES with itself. Given the range of separation bubbles, including a marginal separation, it was best to use L as the reference lengthscale instead of L_{sep}. This distinction should be considered when comparing shock-reflection configurations with ramp flows. Upon plotting the L/δ_0 ratio against $(\bar{p}_2 - \bar{p}_1)/(2\tau_w)$, a linear relationship (as suggested in figure 7 of Dupont et al., 2008) is possible. Of particular interest was the remark that the very beginning of the interaction is rather similar in all the tested cases, which is reminiscent of the free-interaction theory. In all cases, separation occurred at about the same excess-pressure level of $\bar{p}/\bar{p}_1 \sim 1.2$, independently of the wedge angle and Mach number. This demonstrates that the onset of separation is primarily related to the boundary-layer properties and its ability to sustain adverse pressure gradients.

In all cases, the separation bubbles were very shallow with aspect ratios of the order of fifty to five hundred. The maximum height achieved was in the IUSTI case with the top of the bubble reaching the beginning of the logarithmic region of the incoming boundary layer. This is to contrast with instantaneous snapshots, where the bubble can be much taller, giving an indication of the relatively intermittent nature of the separated flow.

Finally, particular attention was given to the mixing layer that develops inside the interaction. It is composed of two main sections: an inclined upstream section going from the reflected-shock foot to the incident shock tip (with an inclination angle of about twenty degrees) and a more horizontal section in the recovery region. The mixing-layer growth was found to be greater than for canonical compressible cases (at least in the

first section). This is probably due to the strong pressure gradient imposed by the shock. Consequently, the mechanism proposed in Piponniau et al. (2009) would in fact be acting at a Strouhal number nearly one order of magnitude larger than the value associated with the low-frequency motions of interest and which are the main focus of this thesis from this point onward. The next chapter will not be directly concerned by the unsteady aspects of the LES data but will instead present some stability-analysis results which will often be referred to in the subsequent chapters.

5. Linear-stability analysis

Before focusing on the unsteady aspects of the previously introduced LES runs, it is of interest to consider the linear-stability properties of the time-averaged flowfields. As mentioned in the introduction, Robinet (2007) has recently performed a Bi-Global analysis of an oblique shock impinging on a laminar boundary layer, and found that for a sufficiently large wedge angle, the flow could become absolutely unstable to span-wise wavelengths of the order of the separation-bubble length. It is then questionable whether an absolute instability could be playing an important role in the origin of the low-frequency oscillations. This chapter considers the base-flow linear-stability properties of the IUSTI flow case to see if it shares similar properties to its laminar counterpart, provided that the linear-stability analysis can be extended to this turbulent flow. To address this issue, the same SBLI code as the one used to run the LES will be used, but in a slightly modified form, to allow the detection of the most unstable and/or least damped mode of any given (3D) base flow.

5.1 Description of the method

As described in chapter 2, the in-house code solves the 3D compressible Navier–Stokes equations, which may be written in the following generic way:

$$\frac{\partial \mathbf{q}}{\partial t} = \mathrm{RHS}(\mathbf{q}), \tag{5.1}$$

where $\mathbf{q}$ is the conservative variable vector $[\rho, \rho u, \rho v, \rho w, \rho E_t]^{\mathbf{T}}$. Let $\mathbf{q}_b$ be the time and span-averaged field obtained from the LES results, which will be referred to as the *base flow*. If this base flow is used as the initial condition of a simulation, one can obtain the rate of change of $\mathbf{q}$ needed to satisfy the equilibrium. In other words:

$$\frac{\partial \mathbf{q}_b}{\partial t} = \mathrm{RHS}(\mathbf{q}_b). \tag{5.2}$$

If the flow $\mathbf{q}$ is decomposed into its base-flow component $\mathbf{q}_b$ and a perturbation $\mathbf{q}'$ (i.e. $\mathbf{q} = \mathbf{q}_b + \mathbf{q}'$), one can write:

$$\frac{\partial \mathbf{q}'}{\partial t} = \mathrm{RHS}(\mathbf{q}) - \mathrm{RHS}(\mathbf{q}_b), \tag{5.3}$$

where RHS($\mathbf{q}_b$) acts like a forcing term in the governing equations. Thus, it is possible to track the time and spatial evolution of the prescribed initial disturbance on the base flow, while maintaining the base flow at its initial state. Therefore, the most unstable (or least damped) mode can directly be detected. The above forcing was introduced in the code with no inclusion of the SGS terms to run the stability analysis as a DNS. However, the TVD-Ducros filter and the integrated characteristic schemes were used and modified in a similar way to the governing equations given above.

By definition, the base flow is the span- and time-averaged flowfield, which is not a solution to the Navier-Stokes equations (otherwise the left-hand side of (5.2) would strictly be zero). In fact, the forcing term introduced can be thought of as the divergence of a Reynolds-stress tensor in the RANS equations. Thus, the above stability-analysis formulation is at first sight similar to the linear-stability analysis of the RANS equations, if the perturbations considered are sufficiently small. It could then be argued that such analysis corresponds to the initial stage of an unsteady RANS calculation started from the steady-RANS solution, but with the major difference that no modelling is applied to the disturbances. There are cases where the large-scale flow unsteadiness are found to be relatively well predicted by linear theory. For example, Gaster et al. (1985) compare their experimental measurements of a forced turbulent mixing layer with the results of classical linear-stability theory, and report a good agreement between the two in both the amplitude and phase distribution. A more recent successful attempt is the application of the BiGlobal analysis to predict the shock-induced transonic-buffet onset by Crouch et al. (2007). It can thus be argued that the SBLI case may also be a candidate for the application of linear-stability theory. Indeed, the low-frequency shock motions are known to occur on timescales two orders of magnitude larger than the characteristic timescale of the turbulence. The separation of timescales, which appears to be needed for a successful extension of linear-stability theory, is clearly present in the SBLI case. In such a framework, the turbulent nature of the flow would only be needed to produce the base flow.

5.2 Results

To check the validity of the above modifications of the code, the stability simulation was first performed with no initial disturbance and the base flow could be maintained for as long as the test was run for (about six flow-through-times, longer than is needed for this study). Then, white noise disturbances were introduced with a maximum amplitude four, six or eight orders of magnitude smaller than the free-stream quantities. The white noise was introduced upstream of the interaction inside a square cylinder of section five

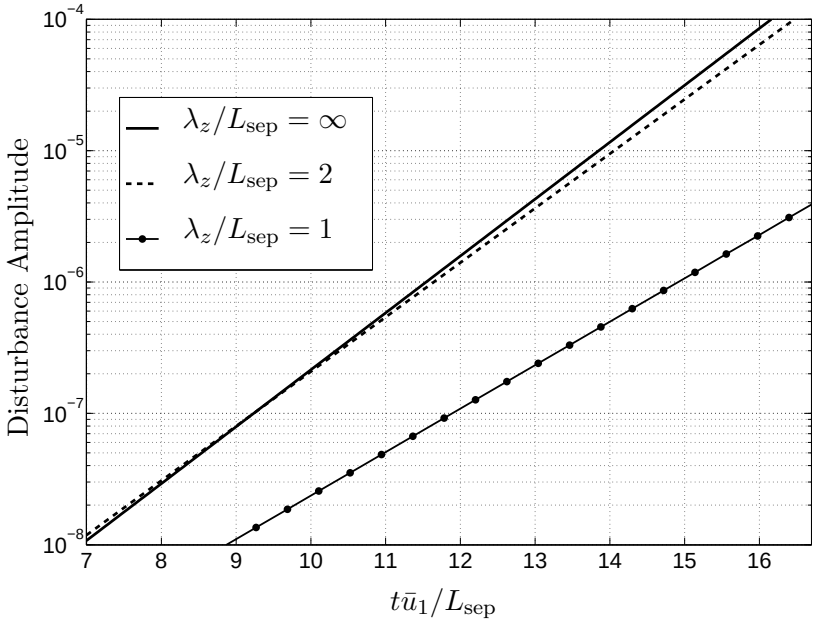

FIGURE 5.1: Example of the disturbances exponential growth (linear stage) for three different span-wise wavelengths λ_z

by five grid points and spanning the entire simulation-domain spanwise extent. Alternatively, specific spanwise wavenumbers were excited using sine waves for the initial condition. The linear-stability simulations were performed for various domain widths, ranging from 0 to 8 times the separation-bubble lengths. The original LES grid resolution was kept in the streamwise and wall-normal directions whereas the spanwise resolution was set to 20 and 40 points per separation-bubble wavelength (two resolutions were tested to make sure that the results are grid independent). The base flows considered here were obtained by time and span-averaging the conservative variables of the small (see table 3.2) and large-span (see table 4.2) IUSTI 8° LES runs. To remove spurious oscillations in the time- and span-averaged data, the base flows were all low-pass filtered prior running the stability simulations.

After a transient state, all the tested cases have shown that the disturbances end up picking up a globally unstable mode (following an exponential growth in time as shown in figure 5.1), the structure of which is shown in figure 5.2. The mode was found to be stationary until saturation of the linear regime was reached.

Contrary to the results of Robinet (2007) for a laminar interaction, the global mode is found to be present in 2D (i.e. at zero spanwise wavenumber) for the current turbulent SBLI case. Furthermore, when trying to enhance higher wavenumbers in the initial disturbance, the smaller spanwise wave-numbers were consistently seen to grow faster. Figure 5.3 provides the growth rates obtained at different wavenumbers from the time evolution of the amplitude of different spanwise-Fourier modes. First, the 2D mode is found to be the most unstable, although 3D modes with wavelengths of the order of, or

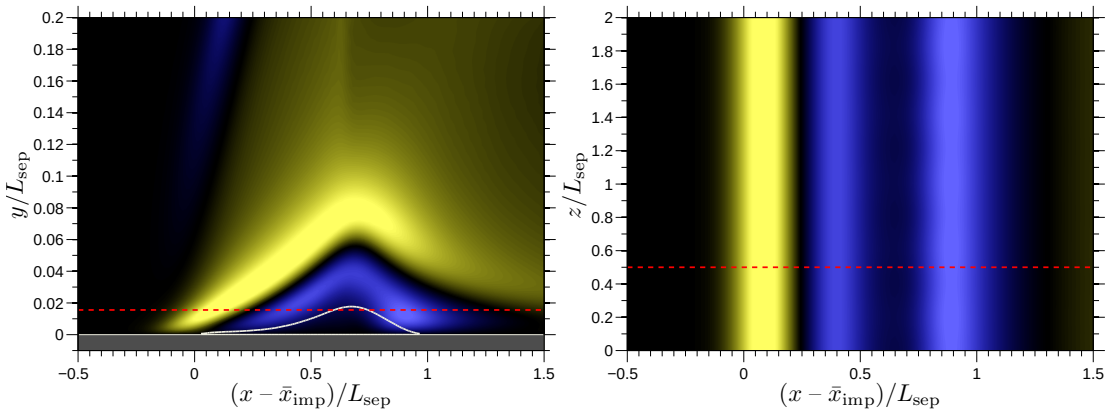

FIGURE 5.2: Global-mode amplitude function for the streamwise momentum disturbance (ρu mode): side view (*left*) and top view (*right*). The *solid line* indicates the base-flow zero-velocity contour while the *dashed line* gives the position of the plane cut for the side and top views. The contours are taken between $\pm 1.3 \times 10^{-6}$ and shown on a non-linear scale to highlight the positive (*yellow*) and negative (*blue*) regions

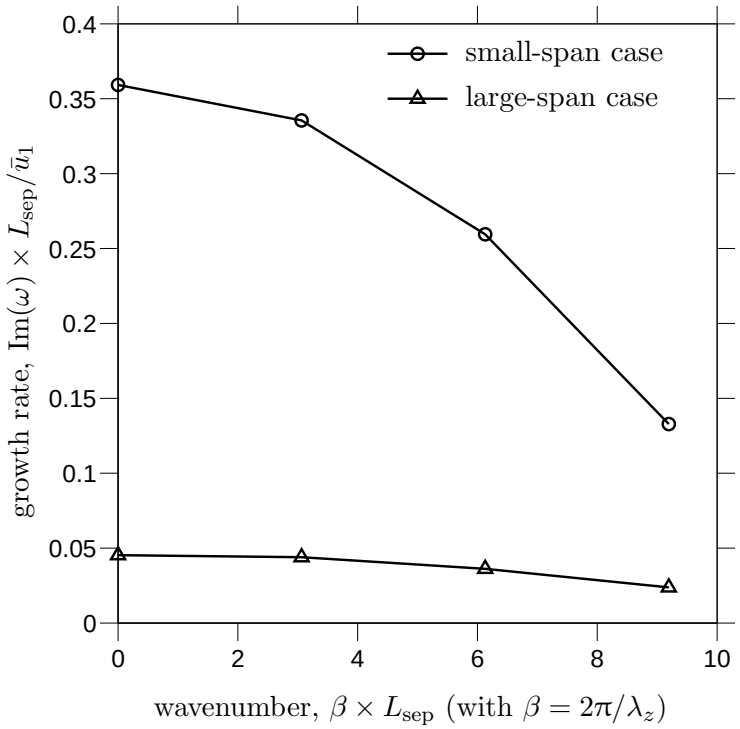

FIGURE 5.3: Global-mode growth rates for different spanwise wavenumbers, where $\{\rho u\}' = A(x,y)\exp(i\beta z - i\omega t)$, with $A(x,y)$ the amplitude function and i the imaginary number ; for the different base flows tested

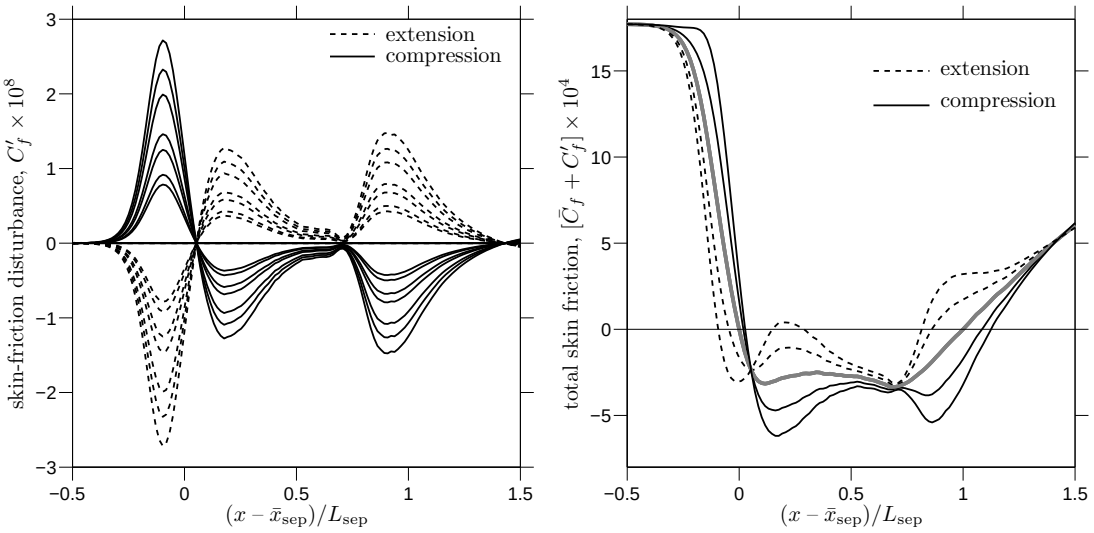

(a) (b)

FIGURE 5.4: Global-mode effect on the separation bubble (for the large-span case) (a) Global mode fingerprint on the skin friction (curves plotted at different times) (b) Global change in the skin friction (amplified to a non-linear level for demonstration purpose)

larger than, the separation-bubble length have quite similar growth rates. Second, the growth rates are low compared to the inverse time scales involved in the turbulence. In fact, the growth rates are found to be smaller than an inverse time scale based on the free-stream velocity and the separation length. However, the values provided in figure 5.3 should be considered with care as they are shown to be sensitive to the base flow used. Nevertheless, it may be argued that if the 2D global mode is active, the associated amplification mechanism would scale on several bubble-flow-through times.

If we now consider the 2D structure of the global mode, it is worth noting that the sign of the amplitude function is arbitrary. Indeed, changing the sign of the initial disturbance leads to the same picture as in figure 5.2 with the difference that the sign of the amplitude function is reversed. The effect of the global-mode structure on the skin friction is given in figure 5.4. Depending on the sign of the amplitude function, one can show that the separation and reattachment points are either moved upstream or downstream (in phase). Furthermore, as shown in figure 5.4(b), the bubble can either break up or the separation can be amplified in the initial portion of the separation under the influence of the global mode (note that the disturbance amplitude levels were increased to a non-linear level to make the global-mode effect visible). The relevance of this remark will be made clearer later in the discussion of the LES data.

Thus, an unstable global mode was found in the span- and time-averaged flow field of the turbulent SBLI, the growth rate of which is greatest at zero spanwise wavenumber. Based on the above study, the global-mode growth rates are found to be at most $\mathcal{O}(0.5L_{\text{sep}}/\bar{u}_1)$, which converts to $\omega_i \sim \mathcal{O}(0.1\delta_0/\bar{u}_1)$ (assuming $L_{\text{sep}} \sim \mathcal{O}(5\delta_0)$). This implies that if we consider the case where the initial disturbance was four orders of magnitude smaller than the base flow, the linear regime will span a time $t \approx \ln(10^3)/\omega_i \sim \mathcal{O}(70\bar{u}_1/\delta_0)$. Therefore, the linear regime involves timescales about two orders of magnitude larger than the characteristic timescale associated with the incoming turbulence. This is consistent with the earlier argument that the stability analysis would be meaningful if it involved timescales larger than the turbulence, so that the turbulence only acts to produce the base flow but does not play a significant role in the development of large-scale motions, just like in the investigations of Gaster et al. (1985). Of course, this does not constitute a proof, but the stability results are found to be consistent with the underlying assumptions made earlier. Based on the results of Gaster et al. (1985) and Crouch et al. (2007), one cannot rule out the possibility that the aforementioned global mode is meaningful and plays a role in the observed low-frequency shock motions in the IUSTI 8-degree shock-reflection case. Note that at this stage, the existence of the low-frequency shock motions is based on the available experiment evidence (see Dupont et al., 2006). Characterising the LES low-frequency content is the main point of interest of the following chapter.

6. Unsteady aspects

In chapter 1, the need for a better understanding of the driving mechanism for the observed low-frequency unsteadiness in shock wave/turbulent boundary layer was discussed. This was shown to have been driving research in this area for several decades. However, as noted by Dolling (2001), this period can be considered as a period of observation rather than a period of explanation, and the unsteady character of SBLI remains an important practical challenge for external and internal flow problems such as airframe design and turbomachinery. Moreover, the case of the reflected shock was shown to have received much less attention than the case of a ramp flow, despite being more academically suited, at least in appearance, due to the absence of wall curvature which can remove complexities related to the inherent flow topology and associated instabilities. Additionally, for a given incoming turbulent boundary layer, ramp-flow cases usually exhibit higher low-frequency shock motions compared to the shock-reflection configuration (by about one order of magnitude). The latter configuration is advantageous in the sense that the low-frequency shock motions are more decoupled from the timescales of the incoming turbulence. This can be good from the point of view of an experimentalist, because of difficulties in measuring higher frequencies, but it is more challenging from a computational point of view due to the need to obtain longer time series to resolve the low-frequency motions.

At the time of this project and to the best of the author's knowledge, no simulation of the shock-impingement case had been performed to confirm the experimental evidence by unambiguously showing that the SBLI region is indeed the place of significant low-frequency oscillations. Among the flow cases considered in this thesis (see chapter 4) only the IUSTI 8° case had been studied using LES by Garnier et al. (2002) and DNS by Pirozzoli and Grasso (2006) (but at a lower Reynolds number). These two earlier works are compared to the present simulations in table 6.1. Of main interest is the last line of the table, where the times spanned by the various simulations are compared. Based on the scaling proposed in Dupont et al. (2006) for S_t, the relevant scales are the freestream velocity $\bar{u}_1$ and separation-bubble length L_{sep}. From Dupont et al. (2006), the most energetic low frequencies are expected to occur at $S_t \sim 0.035$. The comparison is thus based on the number of periods of this particular frequency covered by the simulation. As mentioned in chapter 1, the reflected-shock motions are not harmonic but broadband in nature. Therefore, one should cover several (if not many) periods of this

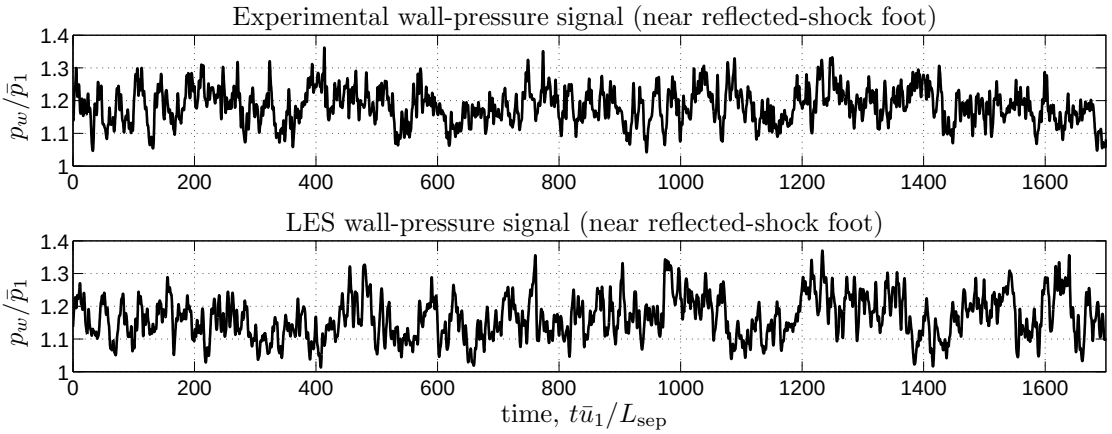

FIGURE 6.1: Wall-pressure time signals: experimental and numerical. Both the LES and experimental data have been filtered with a 6^{th}-order low-pass Butterworth filter with a cutoff Strouhal number of 2, and the LES signal has then been projected – via linear interpolation – on the experimental time axis

particular frequency to properly capture it[1]. As can be seen from table 6.1, the earlier simulations by Garnier et al. (2002) and Pirozzoli and Grasso (2006) could not properly capture the low-frequency shock motions. In the present work, we have tried to run the simulations as long as possible, given the computing power available, while following the constraint on the spanwise extent of the computational box that was presented in chapter 3, with the exception of the narrow-span case, where the relatively inexpensive grid allowed the simulation to cover about 60 low-frequency cycles. Due to the need to resolve most of the turbulence timescales, the present LES typically cover a dynamic range of 7 decades, representing in the narrow-span case over 5×10^6 time steps.

This chapter is comprised of three main sections. In the first section, the LES results are investigated from wall-pressure signals and compared to the available experimental results. At this point, we will comment on the effect of using short time series and on the performances of the digital-filter approach to generate the inflow data. The second section will focus on the mass flow rate per unit width of the reversed flow with particular attention given to the spanwise distribution. In the last section, the LES database is used to extract the shock position in time. This is then used to produce conditionally-averaged data, which will be extensively used in chapter 7.

6.1 Wall-pressure data analysis

6.1.1 Narrow-span case and experimental results

Figure 6.1 provides an experimental wall-pressure signal obtained from Dupont et al. (2006) and its LES equivalent obtained from the narrow-span case. Both signals were

[1]We shall be more specific about what is meant by "many" in this chapter.

Case	IUSTI 8°				ITAM 7°	TUD 6°
	Narrow span	Large span	GSD[a]	P&G[a]		
Upstream Reynolds number Re_{δ_2}	5×10^3	5×10^3	5×10^3	4×10^3	3×10^3	3×10^3
Domain size L_x, L_y, L_z in L_{sep}	4.3, 0.7, 0.1	6.9, 1.4, 1.6	5.5, 2.1, 0.5	78, 6.8, 2.3	11.6, 2.3, 1.3	20.3, 4.1, 2.2
Grid size N_x, N_y, N_z	451, 81, 37	451, 151, 281	255, 151, 55	2650, 111, 255	451, 151, 141	451, 151, 141
Grid resolution Δx^+, $\Delta y^+_{\mathrm{min}}$, Δz^+	41, 1.6, 14	33, 1.3, 12	50, 1, 18	15, 1, 6.5	30, 1.2, 11	39, 1.6, 14
Ratio $L_{\mathrm{sep}}/\delta_0^{\mathrm{imp}}$	$\mathcal{O}(6)$	$\mathcal{O}(3)$	$\mathcal{O}(3)$	$\mathcal{O}(1)$	$\mathcal{O}(2)$	$\mathcal{O}(1)$
SGS model	MTS	MTS	MSM[b]	none (DNS)	MTS	MTS
Dynamic viscosity law	Power	Sutherland	Sutherland	Sutherland	Sutherland	Sutherland
Inflow conditions	DF	DF	Recycling	BT[c]	DF	DF
Time step $\Delta t \bar{u}_1/\delta_0^{\mathrm{imp}}$	2×10^{-3}	2×10^{-3}	6×10^{-4}	8×10^{-4}	2×10^{-3}	2×10^{-4}
Number of low-frequency cycles[d]	$\mathcal{O}(6 \times 10^1)$	$\mathcal{O}(3 \times 10^1)$	$\mathcal{O}(1)$	$\mathcal{O}(1)$	$\mathcal{O}(3 \times 10^1)$	$\mathcal{O}(3 \times 10^1)$

[a] GSD stands for Garnier et al. (2002); P&G stands for Pirozzoli and Grasso (2006)
[b] Mixed-Scale Model (see Sagaut, 2005; Garnier et al., 2002)
[c] Bypass Transition (a laminar profile is used at the inlet and the BL is tripped using blowing and suction)
[d] number of low-frequency cycles covered by a sine wave at frequency $f = 0.035\bar{u}_1/L_{\mathrm{sep}}$

TABLE 6.1: Numerical details for the low-frequency study: present calculations and earlier ones

normalised with the upstream pressure and filtered with a 6^{th}-order low-pass Butterworth filter with a cutoff Strouhal number of 2. Note that we use the separation-bubble length as the reference length and not the interaction length. Then, the filtered LES pressure signal was projected by linear interpolation onto the experimental time axis. This allows a direct comparison of the two signals. One can see that they share similar properties, suggesting that the LES reproduces the dynamics reasonably well. A closer look at the signals reveals that the experimental signal is slightly richer at frequencies near cutoff, but overall, the resemblance is striking.

Figure 6.2 compares the two signals in a more rigorous way, from a spectral point of view. Figure 6.2(a) gives the power spectral density (PSD) of the aforementioned two signals, with an additional LES wall-pressure signal taken upstream of the interaction. This time, the LES signals were not low-pass filtered so that the high-frequency content is retained. However, all signals were segmented using Welch's method (with 50% overlaps and Hanning windows). In order to obtain a smooth PSD at high frequencies, the LES signal was processed several times with an increasing number of segments, going from about ten segments for the lowest frequency end to several thousands for the highest frequencies. The entire frequency range was reconstructed to obtain the plots in figure 6.2(b). Figure 6.2(a) confirms the good agreement suggested in figure 6.1 between the experiment and the LES at low-frequencies. Furthermore, the upstream probe from the LES confirms that the energetic low-frequencies observed near the reflected shock were not introduced by the inlet conditions and thus that the digital-filter approach met our expectations in that aspect.

Figure 6.2(b) gives the weighted PSD. It is obtained by multiplying the PSD by the frequency (the Strouhal number in our case) and normalising by the integration of the PSD over a given frequency (Strouhal number) range. This representation is convenient to highlight the frequencies which contribute most to the variance of the signal. However, the normalization is arbitrary and one should be careful when comparing the LES and the experiment as the available frequency ranges of the two signals differ. In figure 6.2(b), a hybrid normalisation is provided (labelled "hybrid norm"), where one accounts only for the common frequency range covered between the experimental and LES signals (i.e. between the lowest frequency covered by the LES up to the cutoff frequency of the experimental signal). As can be seen from this figure, the agreement between the LES and the experiment using the hybrid-frequency range is satisfactory.

These results imply the following. First, that the region under the reflected shock exhibits significant low-frequency oscillations. These so-called low frequencies are broadband and cover at least one frequency decade around $S_t \approx 0.03$, giving the reflected shock a very random-like motion. Furthermore, these frequencies are two orders of magnitude smaller than the energetic frequencies related to the turbulence. Since the fluctuations related to the turbulence contribute to the signal-variance nearly as much as the

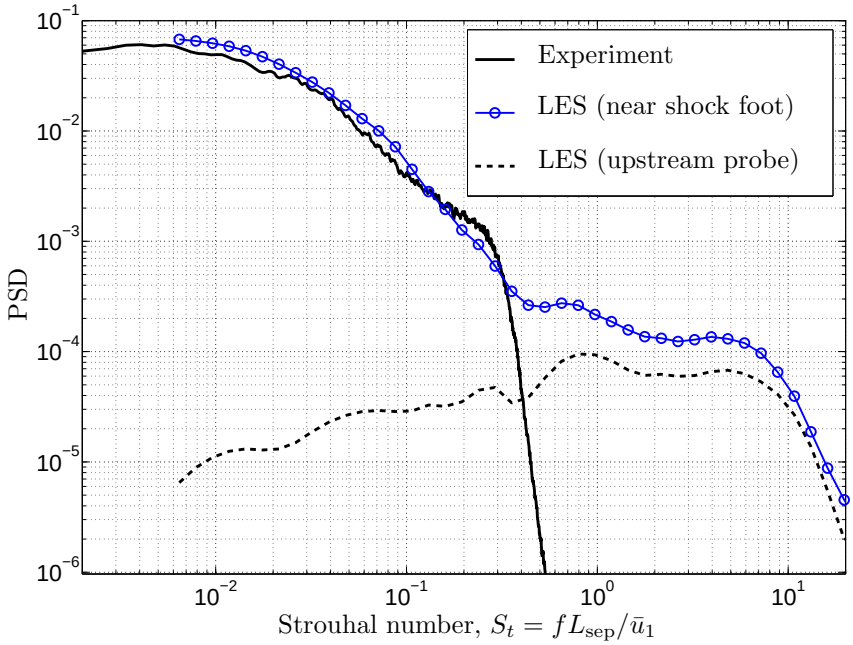

(a) power-spectral density

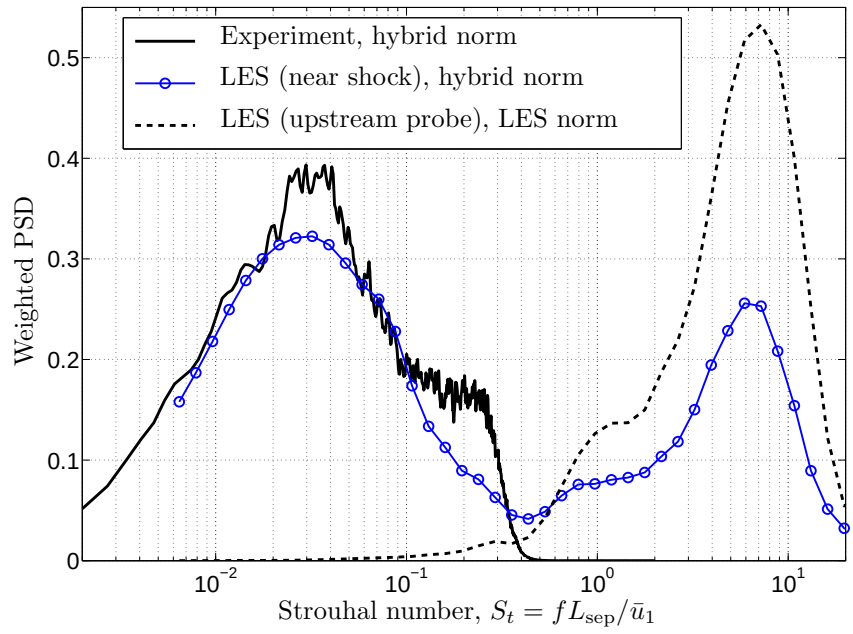

(b) weighted-power-spectral density

FIGURE 6.2: Spectral analysis of the wall-pressure signals: experiment *vs* LES

low-frequencies, it makes the distinction between low-frequency and turbulence-related events extremely difficult when looking at a raw time-signal as in figure 6.1. Second, the good agreement of the LES with the experimental data suggests that the present LES does capture the important dynamics of this interaction: namely, the frequency of the most energetic low-frequency unsteadiness and the bandwidth of the low-frequency content. However, the LES slightly underestimates the amount of energy around $S_t \approx 0.3$. Nevertheless, the overall good agreement suggests that the experimental observations of the existence of low-frequency shock motions are not due to an artifact of the experimental arrangement.

However, it should be recalled that the present low-frequency analysis is obtained from the narrow-span LES, which was shown to significantly overestimate the separation-bubble length. One could wonder why the agreement with the experiment is so good. As mentioned in chapter 1, Dussauge et al. (2006) have shown that the low-frequency unsteadiness scaled relatively well with the interaction length[2] and it is possible that the narrow-span LES benefits from this choice of lengthscale in the definition of the Strouhal number. In fact, the agreement would be poor if we had used the boundary-layer thickness as the reference lengthscale. Second, assuming that the global mode found in the previous section is related to the low-frequency oscillations, and in light of the experienced sensitivity of the growth rates to the amount of reversed flow, it would not be surprising that the low-frequency oscillations are related to the separation-bubble properties, and more precisely, to the amount of reversed flow, which is related to the bubble height. It was shown earlier that the large-span LES underestimated the bubble height and consequently the magnitude of the reversed flow. Since the narrow-span bubble is longer and taller than the one found in the large-span case, it is likely that the amount of reversed flow in the narrow-span LES closely matches the experiment, artificially leading to a good agreement for the low-frequency dynamics.

The LES wall-pressure signals are further analysed from two sets of wall-pressure probes. The first set, which is referred to as the high-spatial/low-temporal resolution one, is made of the 451 available grid points in the streamwise direction, along the median-line of the computational-box floor, where the pressure was recorded every one hundred iterations. The second set, which is referred to as the low-spatial/high-temporal resolution one, is made of one pressure measurement every five grid points along the same line, but at a sampling rate of one record every ten iterations.

Figure 6.3(a) is obtained from the low-spatial/high-temporal resolution array and is simply an extension of figure 6.2(b) to all the available streamwise locations. The contours are isovalues of the weighted PSD. This is similar to figure 5 in Dupont et al. (2006), except that the high-frequency end of the current figure is higher than in their paper, owing to the inclusion of the energetically significant high-frequency oscillations

[2]In this flow configuration, the interaction length and separation length are similar.

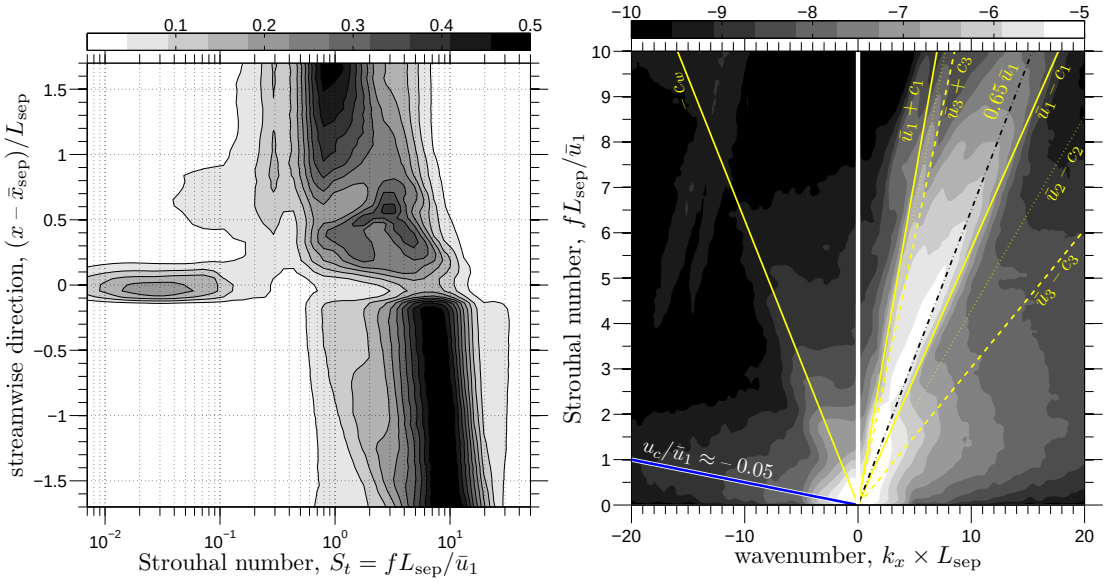

(a) Weighted-power-spectral density map (b) Frequency/wave-number diagram

FIGURE 6.3: Energetically significant frequencies as found in the wall-pressure signals (a) weighted-power-spectral density map (b) frequency/wave-number diagram (where the contour levels – shown on a logarithmic scale – are the premultiplied PSD levels obtained from the two-dimensional Fourier transform of the space-time correlation function of the wall-pressure probe array. The reference probe to compute the space-time correlation function was located at $(x-\bar{x}_{\rm sep})/L_{\rm sep} = 0.3$). The PSDs are premultiplied by (a) the frequency divided by the total resolved power (as in figure 6.2(b)) for each individual streamwise location, (b) the frequency)

related to the turbulence. Figure 6.3(a) can be interpreted as the map of the most dominant wall-pressure fluctuations as one moves along the streamwise direction. From this point of view, the separation region clearly stands out. More precisely, it is worth noticing that the energetic broadband low-frequency peak mentioned earlier is very localised about the separation point $\bar{x}_{\rm sep}$. In the remaining part of the separation bubble, the energy is distributed over three decades of Strouhal numbers. This is in good agreement with Dupont et al. (2006). After the interaction, a new ridge starts forming, similar to the upstream ridge, but at lower Strouhal numbers. This is due to the thicker post-interaction boundary layer, where similar turbulence structures to the upstream boundary-layer ones are produced, but of larger sizes, leaving a similar footprint in the spectrum but at lower Strouhal numbers.

Figure 6.3(b) was obtained from the high-spatial/low-temporal resolution array. First, a reference point is chosen at $(x-\bar{x}_{\rm sep})/L_{\rm sep} \approx 0.3$ and the two-point correlation function in space and time is computed. The resulting space-time correlation function is then Fourier-transformed in space, with a Hanning window to remove end-effects, followed by a Fourier transform in time to obtain the PSD at different streamwise wavenumbers k_x, using Welch's method (with 50% overlaps and Hanning windows). Finally, the PSD

was filtered to remove spurious oscillations with a non-causal filter and weighted by the frequency. This gives the frequency/wavenumber diagram shown in figure 6.3(b) where the contours are the weighted PSD levels. In addition, all possible acoustic dispersion relations are indicated on the figure, where $\bar{u}_i$, c_i, $i \in \{1, 2, 3\}$ refer to the theoretical potential freestream velocities and local speeds of sound, where region 1 is upstream of interaction, 2 after the incident shock but before the reflected shock and 3 after the interaction. c_w is the speed of sound at the wall[3].

Several observations can be made from figure 6.3(b), firstly, on the positive wavenumber side, where a large amount of energy is found for wave speeds ranging from $\bar{u}_1 - c_1$ to $\bar{u}_1 + c_1$. Looking more closely at this region, a ridge corresponding to waves propagating at $0.65\bar{u}_1$ seems to emerge. This ridge is related to the shedding of coherent structures in the shear-layer at the bubble interface. It must be recalled that the reference point to build the correlation function was at $(x - \bar{x}_{\text{sep}})/L_{\text{sep}} \approx 0.3$ so that in this case, the shedding of the shear-layer structures at the beginning of the interaction turns out to be the most important contributor to the wall-pressure fluctuations. However, if we had used as the reference point a position upstream of the interaction, the downstream acoustic waves $\bar{u}_1 + c_1$ would have been relatively more important than the shear-layer structures (this is not shown here). This remark is important to stress that the relative importance (amplitude level) of the structures seen in figure 6.3(b) depends on the choice of reference point and should thus be considered carefully. However, the structure of the frequency-wavenumber diagram itself does not depend on the location of the reference point within the region considered. In addition to the aforementioned distinct ridges on the positive-wavenumber side, one can see more spatially-distributed structures such as the wide lobe for positive wavenumbers which is related to the turbulence-induced pressure fluctuations. The second set of observations concerns the negative-wavenumber side of the figure, where upstream acoustic waves are clearly detected, supporting the possibility of the feedback-loop mechanism proposed by Pirozzoli and Grasso (2006). However, for such a mechanism to be present, one would need to explicitly show that the shear layer is sensitive to this upstream-propagating acoustic field. Finally, of interest to the present discussion is the ridge at low frequencies corresponding to upstream-propagating low-frequency waves. A best fit to the ridge gives a convection speed of $-0.05\bar{u}_1$. Note that replacing the freestream velocity by this convection speed in the definition of the Strouhal number would make the energetic low-frequency oscillations have a Strouhal number of the order of unity.

One disadvantage of the frequency/wavenumber diagram is that it cannot tell us where the aforementioned slowly-upstream propagating waves come from. It could, if

[3]The speed of sound at the wall is constant along the flat plate due to the choice of isothermal boundary condition.

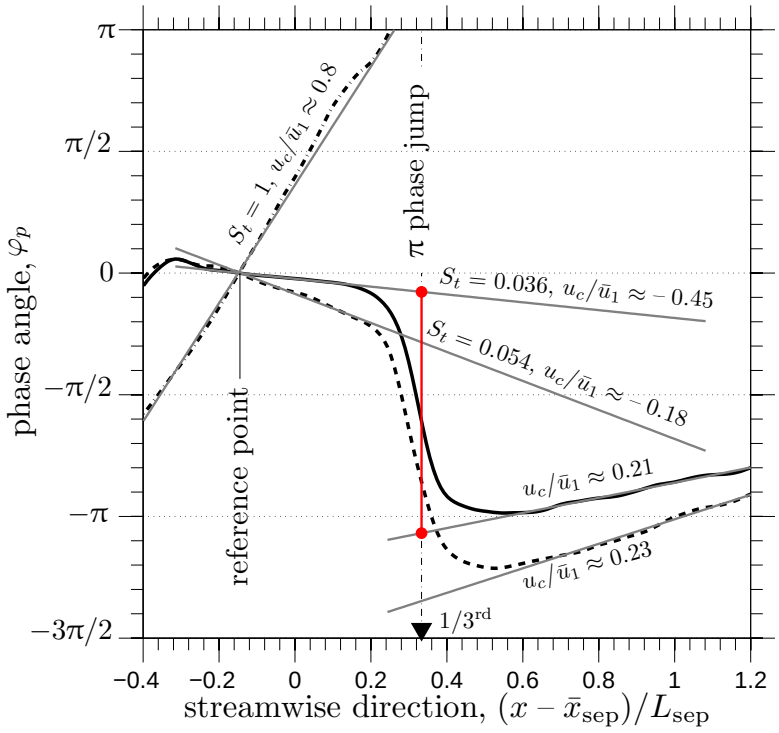

FIGURE 6.4: Phase evolution at different frequencies with respect to a reference probe at $(x - \bar{x}_{\mathrm{sep}})/L_{\mathrm{sep}} \approx -0.2$

we were to restrict the streamwise extent on which the analysis is performed and successively move this frame downstream, since past the source point of those waves one would not find their presence in the diagram anymore. However, this is not a convenient approach. Instead, we prefer to look at the phase evolution of the wall-pressure disturbances at a given frequency. For this, a reference point at $(x - \bar{x}_{\mathrm{sep}})/L_{\mathrm{sep}} \approx -0.2$ is picked using the pressure probes from the high-spatial/low-temporal resolution array. The results for three different frequencies are given in figure 6.4. Note that the phase data were unwrapped so that jumps of 2π were removed. In addition, the phase evolution was filtered to remove the noise. One disadvantage of this approach is of course that the obtained phase is contaminated by all streamwise wavenumbers (note that the level of contamination can be estimated from the frequency-wavenumber map described in the previous paragraph).

One can see in figure 6.4 that for the $S_t \approx 1$ case, the phase increases nearly linearly. The convection velocity u_c can be deduced from the slope since $u_c/\bar{u}_1 = 2\pi S_t / [\mathrm{d}\varphi_p/\mathrm{d}\xi']$, where $\xi' = (x - \bar{x}_{\mathrm{sep}})/L_{\mathrm{sep}}$. However, at lower Strouhal number, interesting changes in the phase evolution can be observed, which cannot be explained by the modulo-2π factor. In particular, for $(x - \bar{x}_{\mathrm{sep}})/L_{\mathrm{sep}} \in [-0.3, 0.3]$, the phase decreases linearly

while it increases linearly everywhere else. Furthermore, the change of slope around $(x - \bar{x}_{\text{sep}})/L_{\text{sep}} \sim 1/3$ is abrupt with a phase-jump of about π. Before the jump, an upstream propagation speed is found whereas after the jump, one finds a downstream propagation speed. This means that the source of the slow-upstream propagating wave discovered in the frequency/wavenumber diagram is located about one third of the way down the bubble. Interestingly, this is reminiscent of the global-mode effect on the initial part of the bubble as described in chapter 5. Hudy et al. (2003) have investigated the flow behind a fence by mean of wall-pressure measurements and report the existence of a phase jump of π in the middle of the separation bubble, similar to the one observed here. Moreover, the authors suggest that this jump could be related to the presence of a globally unstable mode. Our stability analysis results combined with the above analysis of the LES data seem to argue in favour of such a connection.

6.1.2 Short-signal length effects

As shown in the above section, the low-frequency pressure fluctuations near the shock foot are broadband in nature. This implies that in order to guarantee the convergence of the spectral-analysis results, one must capture "several times" the most significant period. Although the term several times is relatively vague, the above results suggest that covering about 60 cycles can give a good estimate. However, in order to obtain the smooth spectra shown in figures 6.2 and 6.3, different window sizes were successivelly applied. Generally, a single window size is employed. In the remainder of this work, the classical single-size windowing approach will be mostly used and it is therefore of interest to evaluate the level of confidence one can have on the final spectrum on the basis of the number of low-frequency cycles covered by the LES (as indicated in table 6.1).

In this section, we make use of the large-span LES of the IUSTI case and the LES of the ITAM and TUD cases. Figure 6.5 shows the evolution of the streamwise momentum (ρu) at a fixed point near the reflected shock and inside the potential-flow region (at the simulation-box midplane). The shock wave is either upstream or downstream of the numerical probe. All signals have also been low-pass filtered with the same 6^{th}-order low-pass noncausal Butterworth filter with cutoff frequency $0.5L/\bar{u}_1$ to highlight the low-frequency content. The autocorrelation functions obtained from the filtered signal were computed and are provided in figure 6.6. High levels of correlations are seen over time lags of order $100\bar{u}_1/L$. Undoubtedly, the reflected shocks in all three configurations exhibit energetic low-frequency shock motions which are significantly below the characteristic frequencies of structures the size of the boundary layer.

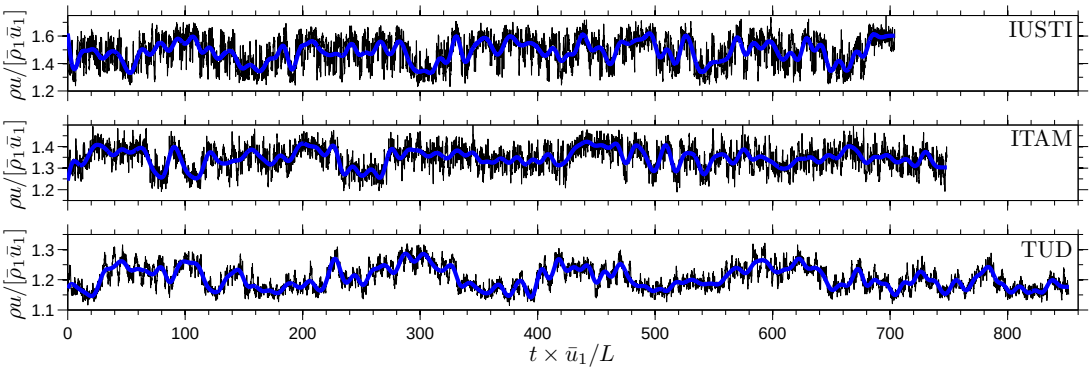

FIGURE 6.5: Numerical hot-wire signals from the simulation-box midplane and at a point crossed by the reflected shockwave, which is taken above the incoming boundary-layer height. The *thick blue line* was obtained by filtering the LES signal with a 6^{th}-order low-pass non-causal Butterworth filter with cutoff frequency of $0.5 \times L/\bar{u}_1$ (using Matlab `idfilt` function)

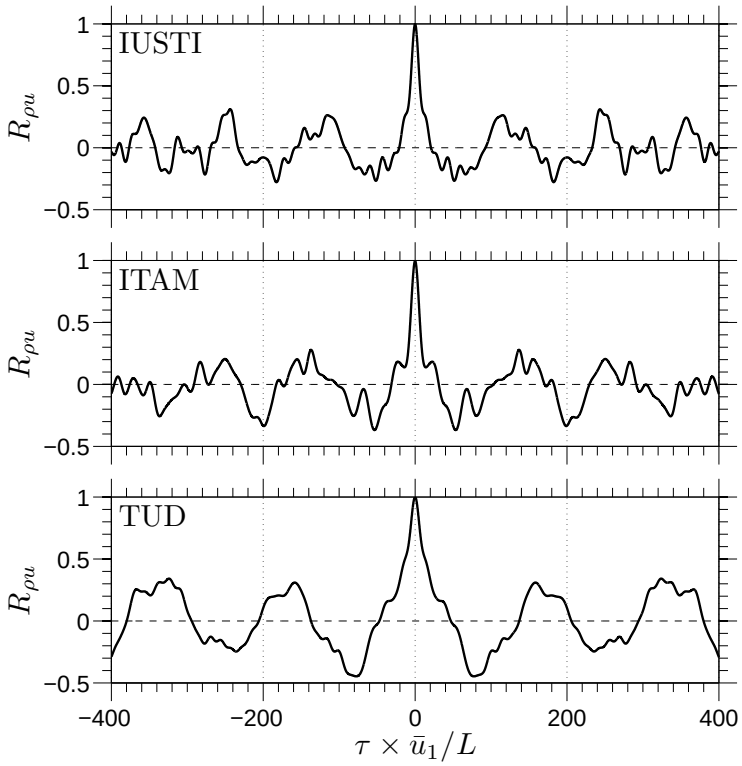

FIGURE 6.6: Autocorrelation functions obtained from filtered numerical hot-wire signals, where the function is defined as: $R_{\rho u}(\tau) = \overline{[\rho u]'(t)[\rho u]'(t+\tau)}/\overline{[\rho u]'(t)[\rho u]'(t)}$

The shape of the autocorrelation functions is of particular interest. Wavy structures with clear local maxima and minima are characteristic of harmonic motions. However, it is known from the previous section that the shock motions are broadband. If the low-frequency motions had really been broadband, then the autocorrelation would not have produced a wavy structure and would decay to zero (this is shown later in figure 6.7). This indicates either that the LES finds the low-frequency shock motions to be made of harmonic motions or that the LES is not yet converged at low frequencies. Given the earlier results, the latter is the most likely to be true. To illustrate this, we shall make use of the long near-shock-foot wall-pressure experimental signal from Dupont et al. (2006).

The experimental signal was cut into 79 segments and each segment was post-processed in exactly the same way as for the LES data. The choice of the individual segment length is such that it matches the length of the large-span LES data. In parallel, the post-processing was applied to the full experimental signal. This gives the set of grey lines and the thick dashed black line in figure 6.7. For comparison, the LES auto-correlation function from figure 6.6 is superimposed (dash-dotted blue line). The difference between the full experimental signal and the LES is large, with the experimental correlation function remaining at low correlation levels for long time lags. However, the individual experimental segments resemble the LES results. This illustrates the limitation of the short-signal analysis. Indeed, the apparent disagreement between the analysis of the LES and the full experimental signal does not mean that the LES did not correctly capture the flow unsteadiness. In fact, some of the experimental segments would suggest it did (see segment 45).

By definition, the PSD corresponds to the Fourier transform of the autocorrelation function. The lack of convergence of the LES data and the associated wavy structure of the autocorrelation function (as seen in figure 6.6) will have severe consequences on the PSD analysis by producing peaky structures in the spectra (see figure 6.7). It is tempting to associate those peaks with a physical explanation, all the more since the spikes can sometimes appear as harmonics of a main one. In light of the analysis of the experimental results, it appears that interpreting individual spikes in the LES spectra is not meaningful. From the narrow-span LES and experimental results, a longer (at least twice as long) LES signal is required in order to fill in the low-frequency spectra. This remark is important since it shows that covering more than 60 cycles is required to be able to quantify the most energetic low frequencies. Although the large-span LES were run for about 30 low-frequency cycles (which is already longer than previous works), the low-frequency data analysis can only provide estimates.

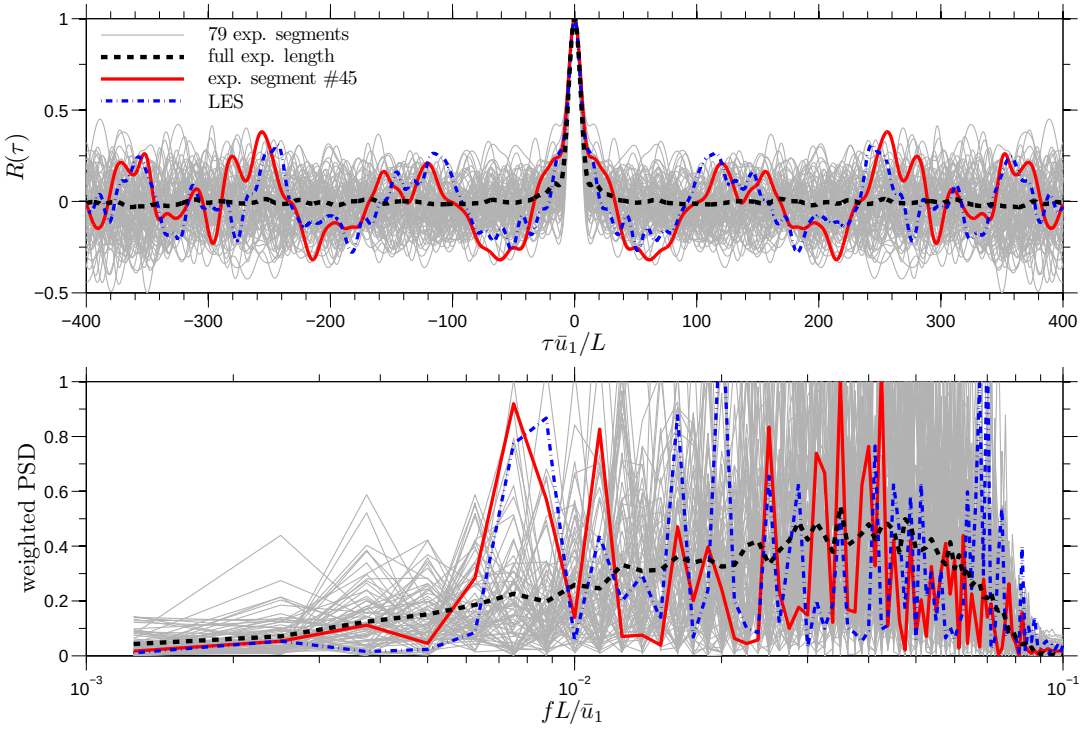

FIGURE 6.7: Effect of short-length signals on the analysis of broadband low-frequency motions. The *top plot* gives the correlation function obtained from various time series. All listed time series have been low-pass filtered in the same manner as for figure 6.5. The experimental signal corresponds to the IUSTI wall-pressure measurements near the reflected-shock foot as described in Dupont et al. (2006). It spans a time about 79 times longer than the time covered by the LES of the IUSTI case. The autocorrelation functions obtained from the 79 sequential experimental segments spanning the LES time are provided in *light grey*. The *thick dashed line* corresponds to the result obtained using the full experimental signal. The autocorrelation function of the LES of the IUSTI case provided in figure 6.6 is repeated with a *dash-dotted line*. A particular segment (labelled segment #45) is provided for illustration purposes (*red solid line*). The *bottom plot* is the premultiplied Fourier transform of the autocorrelation functions shown on the top figure

6.1.3 Upstream influence and digital filter

Before investigating the different LES results, the upstream influence and the use of the digital-filter approach are briefly discussed in this section. Figure 6.8 shows snapshots of the streamwise velocity-fluctuation field in a plane parallel to the wall at two different altitudes: at $y^+ \approx 12$ and $y/\delta_0 \approx 0.2$. The colourmap highlights the region of the flow with a velocity deficit. At $y^+ \approx 12$, a streaky structure is clearly seen. However, the timescales associated with these near-wall turbulence structures are small compared to the timescales associated with the low-frequency shock oscillations. At $y/\delta_0 = 0.2$, no obvious large-scale coherent structure is apparent. To be more convinced of the absence of such structure in the present LES investigations, one can develop the time history

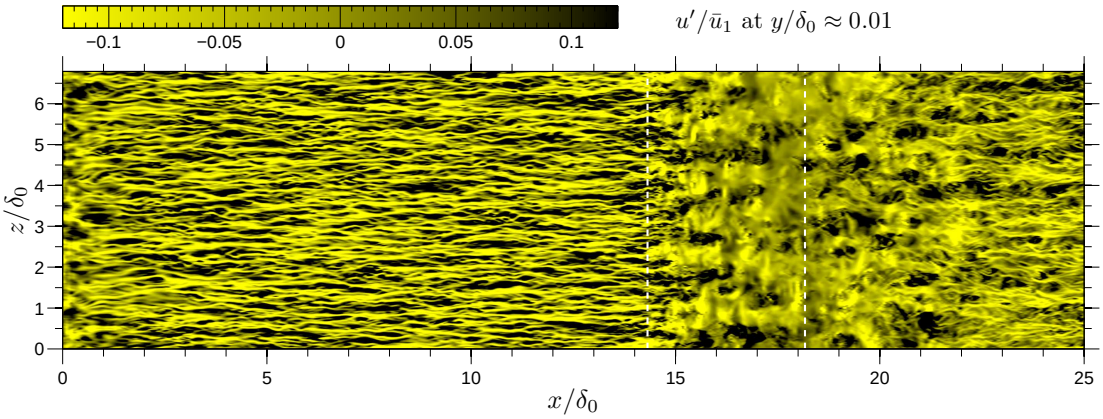

(a) at $y^+ \approx 12$, $u_c/\bar{u}_1 \approx 0.35$

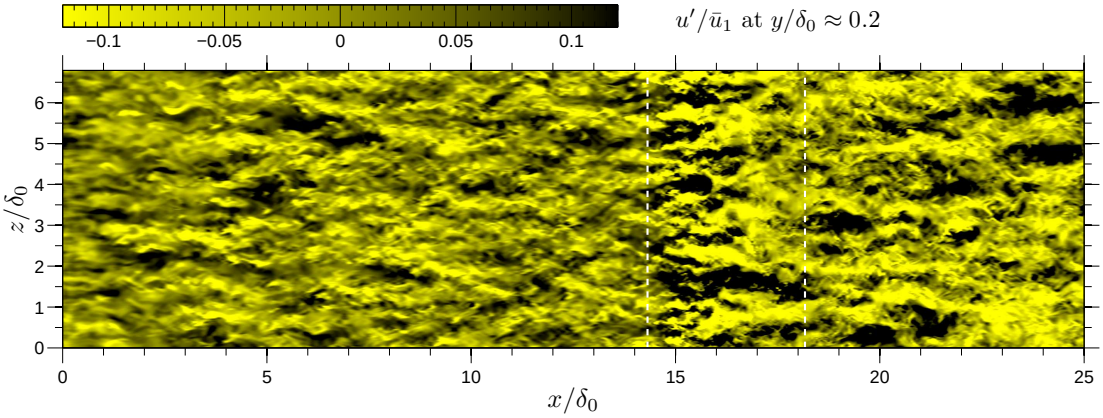

(b) at $y/\delta_0 \approx 0.2$, $u_c/\bar{u}_1 \approx 0.73$

FIGURE 6.8: Instantaneous snapshot of $u'/\bar{u}_1$ from the (old) large-span LES case at two different heights. The dash lines indicate the mean separation and reattachment positions

of the velocity fluctuations seen along a numerical wire just before the interaction (corresponding to $x^\star = 260\,mm$) and at $y/\delta_0 = 0.2$, as shown in figure 6.9, where time is converted into space assuming the fluctuations are convected at the local mean velocity u_c, as in figure 4 in Ganapathisubramani et al. (2007a) (Taylor's hypothesis). The colormap was designed to highlight any large-scale velocity deficit in the reconstructed flow field. The longest structures one can see are of order $10\delta_0$ long.

An autocorrelation function (computed from the narrow-span LES at $x^\star = 260\,mm$, $y/\delta_0 = 0.2$ and in the middle plane of the computational box) is shown in figure 6.10, where the same time-to-space transform as in the previous paragraph was applied. Note that the space axis is given on a logarithmic scale to cover long distances. The correlation function is seen to drop to zero in about one boundary-layer thickness. Note that it drops faster than the prescribed correlation in the digital filter. This is expected since the correlation lengthscales were deliberately overestimated to ensure that the simulated

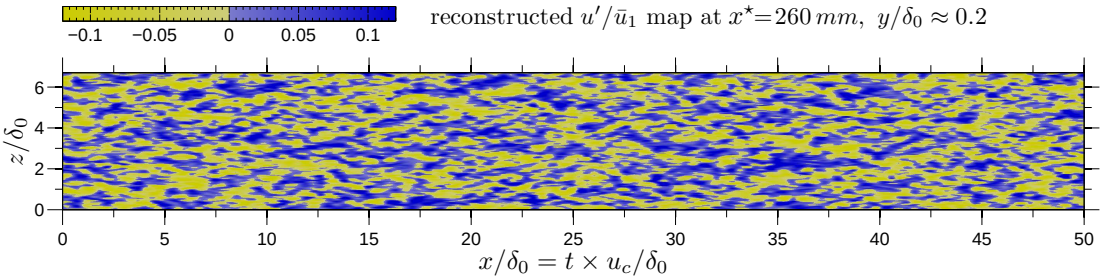

FIGURE 6.9: Reconstructed $u'/\bar{u}_1$ field from a numerical transverse wire located at $x^\star = 260\,mm$ and $y/\delta_0 = 0.2$. u_c is the mean streamwise velocity at $x^\star = 260\,mm$ and $y/\delta_0 = 0.2$ ($u_c/\bar{u}_1 \approx 0.73$)

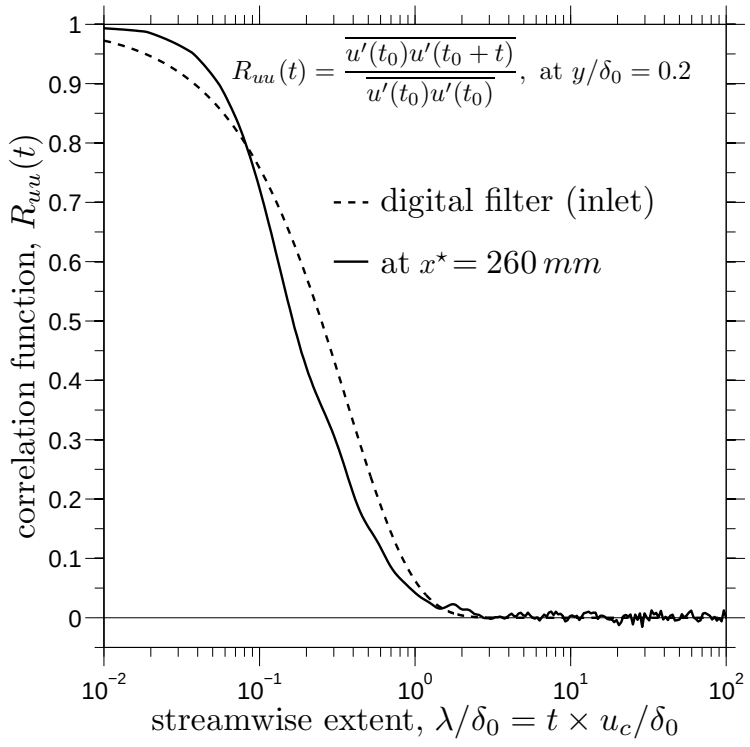

FIGURE 6.10: Streamwise-velocity correlation at $x^\star = 260\,mm$ (about $11\delta_0$ downstream of the inlet) and $y/\delta_0 = 0.2$, compared with the specified correlation at inlet (see equation (2.69)). u_c is the mean streamwise velocity at $x^\star = 260\,mm$ and $y/\delta_0 = 0.2$ ($u_c/\bar{u}_1 \approx 0.73$)

flow does not relaminarise (see chapter 2). Also, it is expected that the correlation function in a turbulent boundary layer drops slightly faster than the prescribed exponential function at the inlet. What is most important for the present study is that the correlation function remains at zero for large time intervals. This was the main objective that motivated the choice of the digital-filter approach, where no cyclic pattern is enforced, as shown by the correlation function. In contrast, the correlation function in the DNS of Wu and Martin (2007) (figure 4) does not drop to zero and does not extend to the period of the recycling/rescaling technique used by the authors.

From the point of view of the digital filter, the current settings ensured that no structure longer than $\mathcal{O}(\delta_0)$ was introduced and this is confirmed by the observed correlation function. However, once inside the computational domain, nothing can prevent larger structures developing, and from figure 6.9 one can see that structures up to $10\delta_0$ long may develop, corresponding to the size of the available computational domain before interaction. As shown earlier, the narrow-span bubble is about $6\delta_0$ long, while the most energetic low-frequency oscillations are at $fL_{\text{sep}}/\bar{u}_1 \approx 0.03$. Using the boundary-layer thickness as the lengthscale, the energetic low-frequency oscillation converts to $f\delta_0/\bar{u}_1 \approx 0.005$. The timescale associated with this frequency is $200\bar{u}_1/\delta_0$. Since $u_c/\bar{u}_1 \approx 0.73$, the lengthscale covered during this time using Taylor's hypothesis is about $150\delta_0$. Using the scaling argument of Ganapathisubramani et al. (2007b), one would thus need to have $75\delta_0$-long superstructures in the narrow-span LES to explain the observed energetic low-frequency oscillations. This is nearly ten times the size of the longest structures present in the present LES, making the superstructures or the incoming flow unlikely to be directly responsible for the low-frequency shock motions observed in this study. This does not mean that long coherent upstream disturbances are not important when present in practical applications but they are not found to be necessary to observe the low-frequency shock motions.

6.1.4 All three large-span LES

In this section, the LES wall-pressure fluctuations are analysed in the same way for all three flow cases in order to highlight possible common characteristics. It was shown in figure 4.31 that the interaction length could be linearly correlated with the ratio between the pressure jump and the wall-shear stress. Therefore, the interaction length appears to be the prefered choice of lengthscale for a cross comparison, as opposed to the separation length, which is nearly zero in the TUD case. Hence the choice of L in the following figures.

The wall-pressure signals were recorded at every streamwise and spanwise grid points in all three LES. At each station, the autocorrelation was computed and then averaged

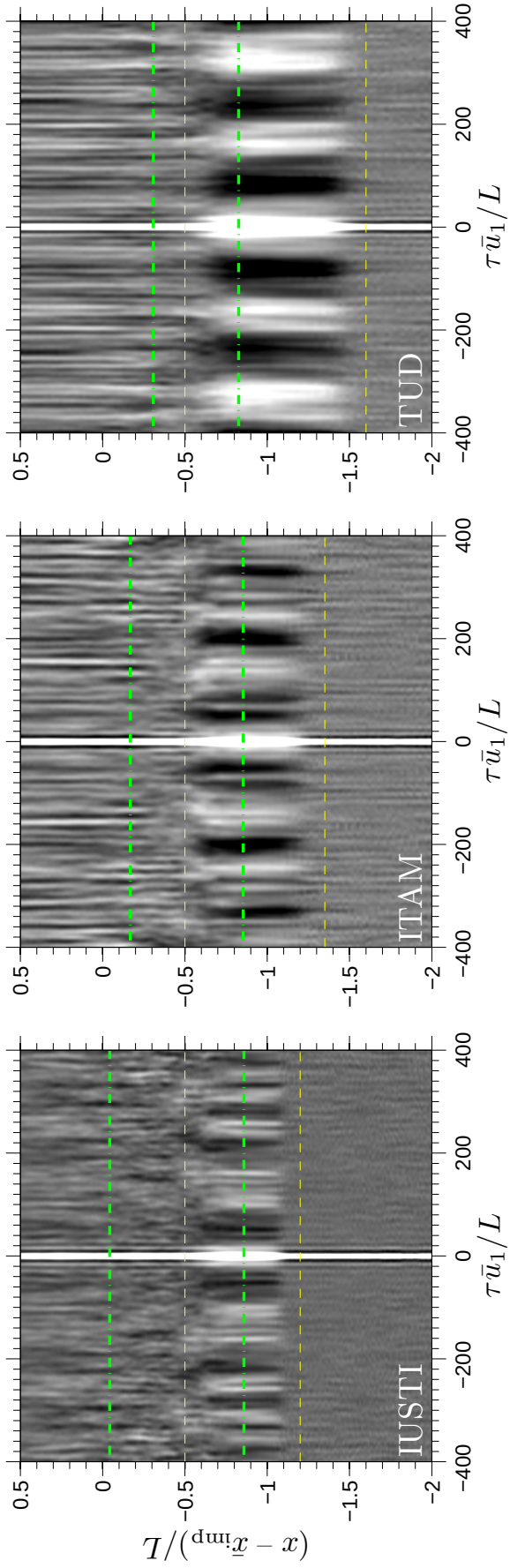

FIGURE 6.11: Wall-pressure autocorrelation functions, as a function of streamwise location. The autocorrelation function was computed in the same way as in figure 6.6 with the wall pressure instead of the streamwise momentum flux. Also, all the spanwise stations are included so that the correlation function is also averaged in the spanwise direction. As in figure 6.6, the signals were low-pass filtered prior to computing the autocorrelation function using the same filter. The *greyscale* is linearly distributed between correlation levels ranging from -0.1 (*black*) to +0.1 (*white*) using 256 intensity increments. The *dashed lines* delimit a region exhibiting significant low-frequency motions. Those limits will be used in figure 6.12. The *dash-dotted lines* indicate the mean separation and reattachment positions

in the spanwise direction to obtain the autocorrelation maps shown in figure 6.11. A clear band with large-scale black and white structures, corresponding to high levels of correlation over large time lags, is seen for all three cases[4]. These larger-scale structures are seen to stop in the middle of the interaction for all three cases but their starting points differ. This implies that the low-frequency motions are more energetic in the first part of the interaction and that the shock-foot low-frequency motions do not span the same distance relative to the interaction length in each case. A clear streaky structure is also seen in the second part of interaction, with what would correspond to a richer frequency content in the IUSTI case given the greater level of "noise".

The absence of large-scale structures upstream of the interaction reflects the absence of particular low-frequency modes, which is expected given the digital-filter settings (see previous section). Furthermore, the fact that in all three cases the large black and white bands stop before $(x-\bar{x}_{\mathrm{imp}})/L = 0.5$ suggests that the source of the low-frequency source is inside the interaction region. This is consistent with the narrow-span LES results (figure 6.4), where low-frequency wall-pressure fluctuations were shown to originate in the first section of the separation bubble, a property that was found to be consistent with the presence of a globally unstable mode, suggesting that the low-frequency motions could be originating from a hydrodynamic instability mechanism. From figure 6.11, the large-span LES results seem consistent with this idea given the spatial confinement of the energetically significant frequencies.

Figure 6.12 gives the contribution of each frequency band to the wall-pressure variance relative to the upstream wall-pressure fluctuations. In this way, the build-up of low-frequency fluctuations, as perceived in figure 6.11, is further quantified. Significant fluctuations for $fL/\bar{u}_1 < 0.03$ emerge in the initial part of the interaction. Furthermore, the fact that all three cases exhibit a relatively similar build-up below this Strouhal number implies that the choice of the velocity-scale $\bar{u}_1$ and length-scale L to quantify the low-frequency motions (as proposed by Dussauge et al., 2006) is appropriate.

A frequency/streamwise-wavenumber analysis of the wall-pressure fluctuations inside the interaction, similar to the one in figure 6.3(b), has been performed and is shown in figure 6.13. Features common to all three cases can be found, namely, the presence of convecting coherent structures such as the vortices shed by the shear layer as well as acoustic radiation. In addition, one can see relatively similar lobed contours characteristic of the broadband time and spatial scales of the turbulence. The presence of upstream propagating acoustic waves can also be detected in all cases as well as upstream-propagating waves at a convective speed of about $u_c/\bar{u}_1 = -0.05$. Replacing $\bar{u}_1$ by u_c for the velocity-scale in the Strouhal-number definition for the most energetic

[4]Note that the presence of those stripes is symptomatic of short-signal effects when the spectral content should be broadband, as shown in section 6.1.2. However, despite the lack of convergence of the LES data, it is still possible to study some aspects of the low-frequency motions.

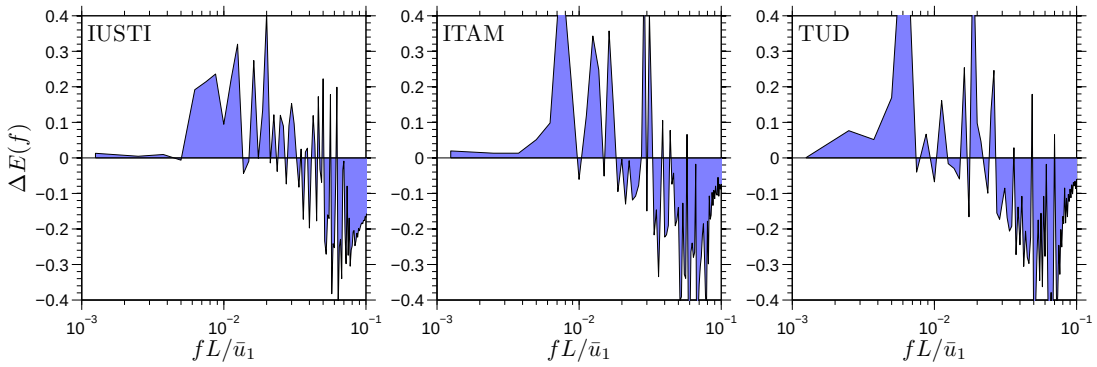

FIGURE 6.12: Difference in the weighted PSD between the first half of the interaction region with the region immediately upstream of interaction. $\Delta E(f) = G_I(f) - G_U(f)$ where $G_I(f)$ is the premultiplied PSD ($f \times PSD(f)$) integrated over the region embedded between the two *dashed lines* in figure 6.11 and normalised by the total resolved power in the same region. $G_U(f)$ is computed in the same manner as $G_I(f)$ with the difference that the integration is performed other the region spanning from $(x - \bar{x}_{\text{imp}})/L = -2$ to the first dashed line in figure 6.11. The resulting quantity highlights the contribution of each frequency band to the wall-pressure variance in the initial part of interaction relatively to the incoming boundary layer. It is aimed at quantifying the build-up of significant low-frequency oscillations as perceived in figure 6.11

low-frequency motions would make this close to unity.

From the above results, all the tested cases have shown evidence of the presence of low-frequency shock oscillations, including the case with a marginal separation. At the wall, the low-frequency oscillations are mainly confined in the first half of the interaction region and no energetically significant low-frequency motions were introduced in the upstream boundary layer. Although the spectral analysis is not fully converged at low frequencies, the build-up of energetic low-frequency motions was found to occur below a Strouhal number of 0.03 ($S_t = fL/\bar{u}_1$). In the next section, additional comparisons will be provided on the basis of other quantities than the wall pressure. In particular, some of the HWA and Schlieren-image-processing results from the ITAM group will be used. Then, the narrow- and large-span LES of the IUSTI flow case will be used to comment on the three-dimensionality of the flow and the possible effect of the domain spanwise extent on the low-frequency unsteadiness.

6.2 Additional cross comparisons and 3D aspects

6.2.1 The ITAM case

As shown in chapter 4, the interaction length predicted by the LES of the ITAM flow case did not match the experimental findings. This discrepancy was mainly attributed to the presence of corner flows produced by the wind-tunel side walls. Independently of

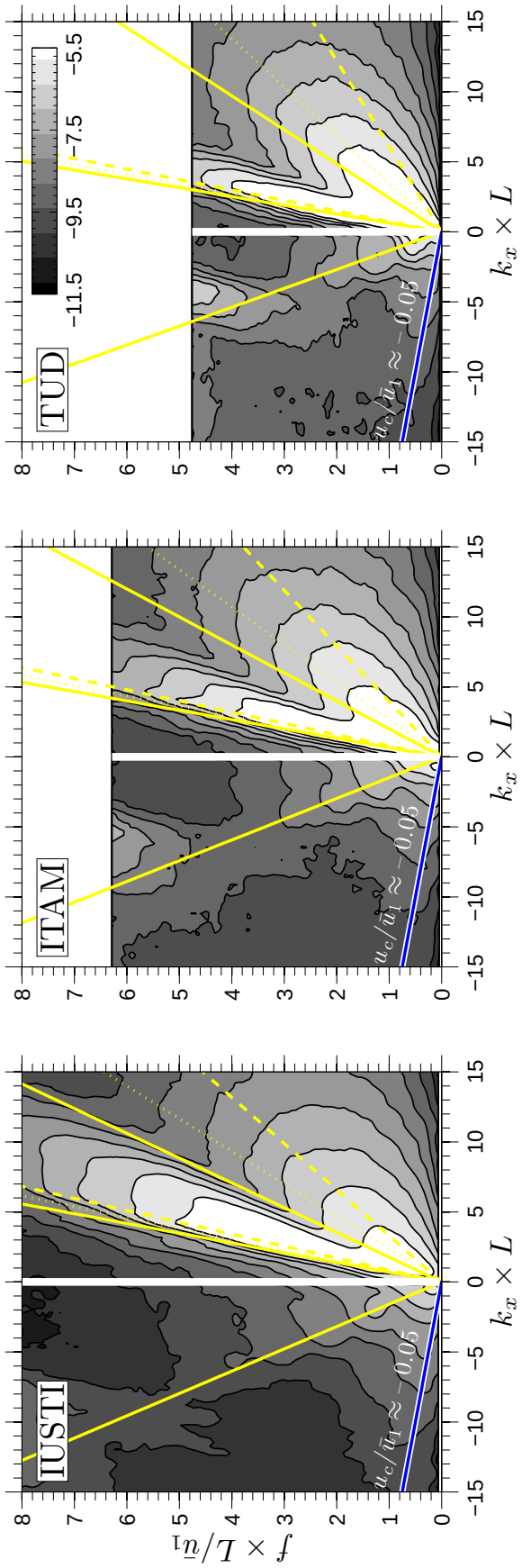

FIGURE 6.13: Wall-pressure frequency/wavenumber diagrams, derived from the 2D Fourier transform of the 2-point correlation function, where the reference point was taken at $(x - \bar{x}_{\text{sep}})/L_{\text{sep}} \approx 0.3$. The *contours* show the premultiplied PSD on a logarithmic scale. In contrast to the previous figures, the turbulence content was retained (no low-pass filter was applied) to build the 2-point correlation function. However, the contours of the premultiplied PSD were made smoother by filtering out the high-frequency fluctuations in the contour lines to lighten the figure. Similarly to figure 6.11, the 2-point correlation is also averaged in the spanwise direction. Hence, only the streamwise wavenumbers are considered here. The *yellow lines* indicate the dispersion relation for various acoustic waves. The *solid lines* correspond to an acoustic wave travelling in the upstream potential flow ($\bar{u}_1 \pm c_1$) for the positive-wavenumber quadrant. The ($-c_w$) upstream-propagating acoustic wave at the wall is also shown in the negative-wavenumber quadrant. The equivalent relations for regions 2 and 3 are shown with *dotted* and *dashed lines*, respectively, where region 2 is the potential flow located between the oblique impinging and reflected shockwaves while region 3 is the potential flow located after the shock system. Finally, the *thick solid blue* and *white lines* indicate an upstream propagation at 5% of the upstream freestream velocity

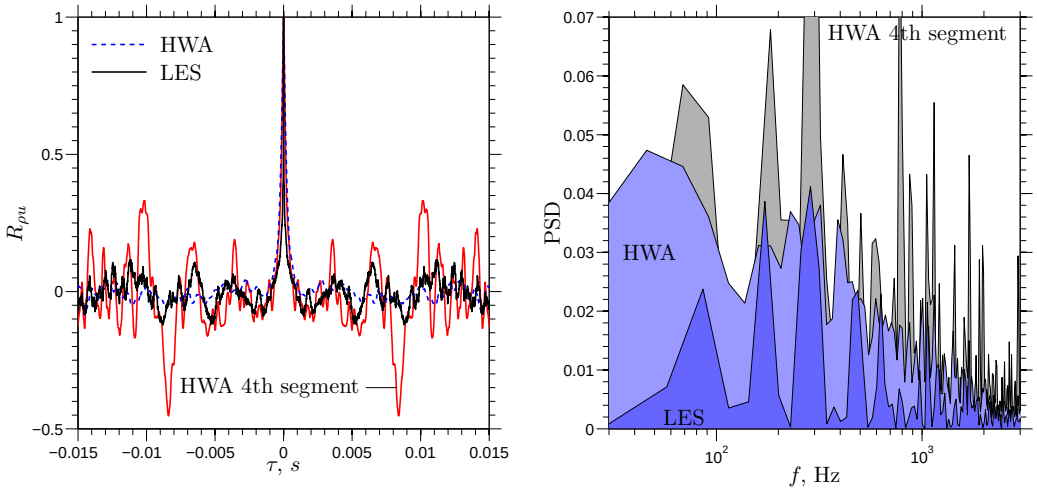

(a) (b)

FIGURE 6.14: LES and experimental correlation functions of the momentum fluctuations at a station crossed by the reflected shock (a) and associated spectra (b). The effect of the short LES signal is highlighted by cutting the experimental signal in segments spanning the same time as the one covered by the LES. The analysis of one particular segment (the 4^{th} one) is shown for comparison

this mismatch, it is of interest to check whether the low-frequency dynamics are similar. As discussed earlier, the low-frequency study is challenging for LES due to the fact that the most energetic low frequencies are found to be two orders of magnitude smaller than the characteristic frequency of the incoming boundary layer ($\bar{u}_1/\delta_0$). In addition, those low frequencies are broadband in nature and it is necessary to cover several cycles (ideally more than 50 from the earlier discussion) to achieve a proper convergence of the spectral analysis. Consequently, in order to resolve both the turbulence and the broadband low-frequency motions, the LES must span times of the order of $10^4\delta_0/\bar{u}_1$ with a time resolution of about $10^{-3}\delta_0/\bar{u}_1$, leading to an impressive frequency range of 7 decades. In practice, the LES of the ITAM signal covers about $20\,ms$ (at a rate of 47 MHz) whereas the HWA measurements span about $350\,ms$ (at a rate of 0.75 MHz). Thus, the LES signal is about 17 times shorter than its experimental counterpart and can only cover about 10 periods of a wave beating at 500 Hz. Therefore, the low-frequency spectral analysis of the LES is not fully converged and comparisons with the HWA results should be undertaken with care. Nevertheless, the signals are sufficiently long to provide reasonable trends.

Figure 6.14(a) compares the auto-correlation functions computed from the momentum time series obtained by a hot wire probe and the numerical equivalent at a fixed point along the reflected shock wave ($R_{\rho u} = \overline{[\rho u]'(t_0)\,[\rho u]'(t_0+\tau)}/\overline{[\rho u]'(t_0)\,[\rho u]'(t_0)}$), upstream of the shock-crossing point in the experiment and downstream of the shock-crossing point in the LES. As mentioned in the previous paragraph, the hot-wire signal

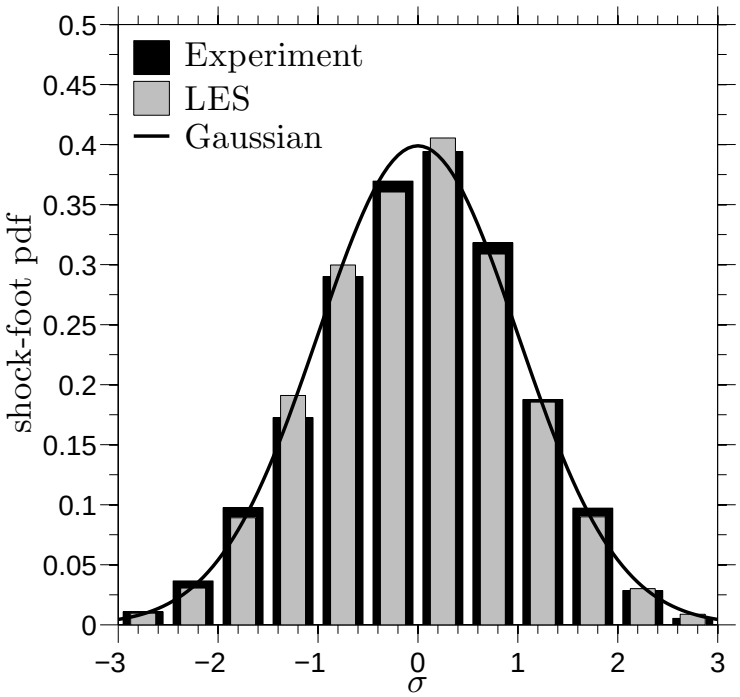

FIGURE 6.15: Shock-foot probability density function

is about 17 times longer than the LES one. To see the short-signal effect on the interpretation of the LES data, the experimental signal was cut into segments the same length as in the LES. One particular segment (the 4^{th} one) is provided in the figure for illustration purposes. It shows that for the frequencies of interest here, the LES signal, and to some extent the experimental signal, are too short to consider the statistics to be fully converged. Nevertheless, it is possible to infer that the experimental and LES signals both exhibit similar low-frequency content.

Figure 6.14(b) is the Fourier transform of the auto-correlation functions shown in figure 6.14(a). By definition, this corresponds to the power spectral distribution. It is clear that both the LES and the experiment are experiencing significant low-frequency "tones". As the time spanned by the signals is increased, the spiky aspect of the spectra will be reduced (as shown ealier) and the spectra will become more and more broadband. In figure 6.14(b), significant oscillations are found around 0.3 kHz, consistent between experiment and LES. Finally, the PSD levels below 0.1 kHz suggest there might be significant very low-frequency oscillations but, given the relatively poor convergence for that end of the spectrum, it is premature to draw any conclusion.

One additional quantity made available by ITAM is the post-treatment of high-speed Schlieren images, allowing tracking of the reflected-shock motions. From the Schlieren

snapshots, the shock was extracted using an algorithm based on the color intensity and then the shock foot was determined by a best-fit line. A similar procedure was applied to the LES data, using the divergence of the velocity as the basis for the shock detection (more details will be provided in the last section of this chapter). The resulting shock-foot time series were then analysed to compute the shock-foot probability-density functions, shown in figure 6.15. The probability-density functions of both the experimental and numerical shock-foot motions are found to agree remarkably well (despite the poor agreement in the time-averaged fields). Interestingly, they both seem to match the normal distribution (although one could argue that a slight skewness may be perceptible). Unfortunately, the time resolution of the Schlieren images does not allow a comparison based on the spectral content of the shock-foot motions.

Despite the limited direct comparisons with the experimental results and the discrepancies due to the presence of the wind-tunnel side walls which are not included in the LES, the numerical results share similar low-frequency dynamics with the experiments. Together with the success in reproducing the IUSTI data, LES are found capable of accurately reproducing the key mechanism responsible for the low-frequency shock motions.

6.2.2 Probability of separation

In chapter 4, it was shown that the separation bubbles in the IUSTI, ITAM and TUD cases differed significantly with span- and time-averaged maximum reversed flow of $0.27\bar{u}_1$, $0.007\bar{u}_1$ and $0.0007\bar{u}_1$, respectively. However, it was noted that despite those differences, all bubbles are intermittent with recorded instantaneous negative velocities of $\mathcal{O}(\bar{u}_1/2)$, independently of the size of the mean separation. Using the LES database, it is possible to compute the probability of separation, a result which is also accessible to PIV data. The probability of finding a negative u velocity is provided in figure 6.16. Unfortunately, the TUD case is the only case for which we have the required PIV data to perform a comparison. Note that all distances are normalised using δ_0^{imp}.

Although the IUSTI case exhibits occurences of reversed flow further away from the wall ($\mathcal{O}(\delta_0^{\text{imp}}/3)$) than the ITAM ($\mathcal{O}(\delta_0^{\text{imp}}/5)$), which in turn reaches further away from the wall than the TUD case ($\mathcal{O}(\delta_0^{\text{imp}}/10)$), the overall maps appear as rescaled versions of each other, suggesting the possible existence of a similarity law. The PIV data should be considered with care, given the increasing uncertainties as one approaches the wall region but if we focus on the peak of the 10% and 20% contours, the shape and lengthscales are not found to be significantly different from the LES (despite the large difference in Reynolds numbers). Finally, it is worth noting that the contour of $\bar{u} = 0$ is found in regions where the velocity is negative approximately 50% of the time. This

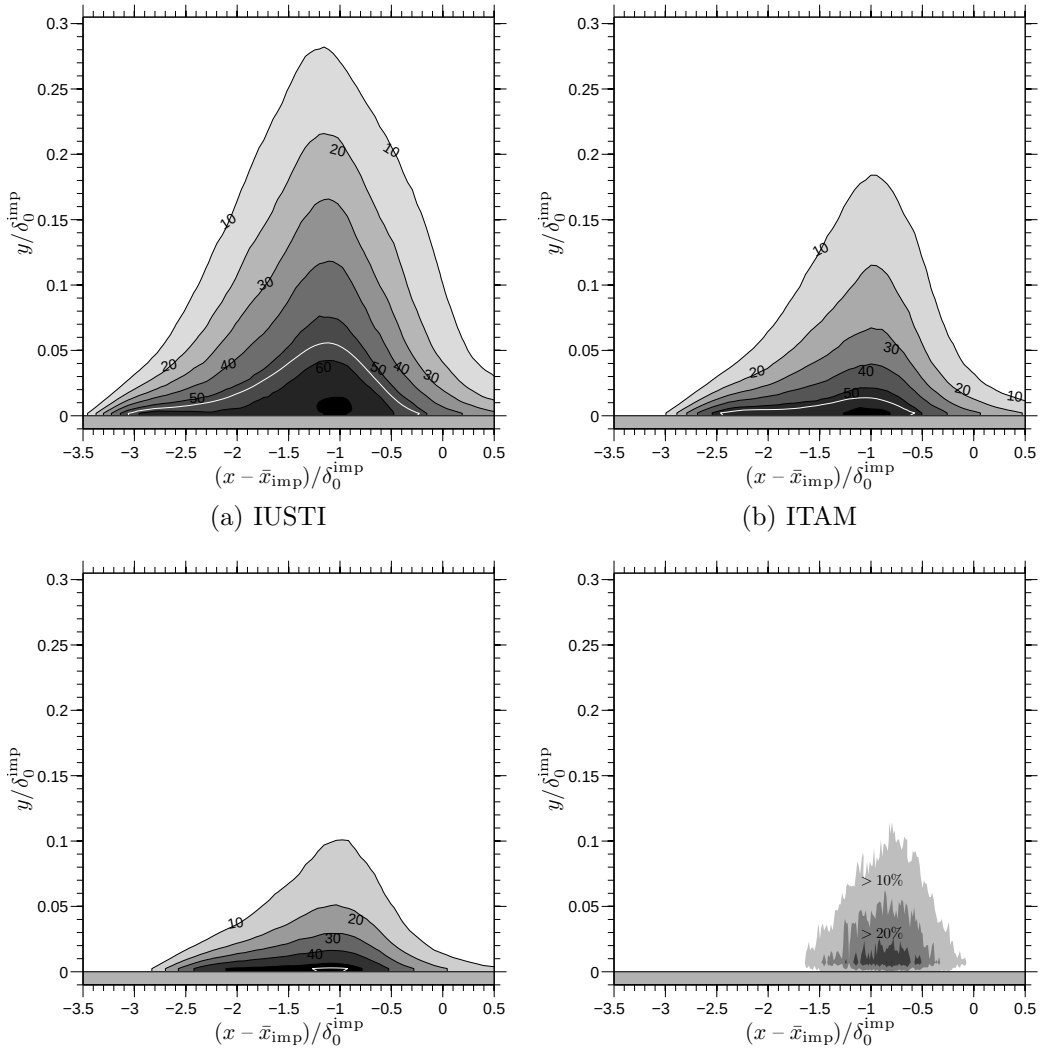

FIGURE 6.16: Side view of the probability of finding a reversed flow. The *probability isolines* are shown by increments of 10% for all three LES cases and the PIV data of TUD. The *white solid lines* correspond to the $\bar{u} = 0$ contour

may reflect the observed symmetry in the shock-foot PDF of the shock motions shown in the ITAM case.

So far, the results reported in this chapter did not consider three-dimensional effects. The next two sections will focus on the effect of the spanwise domain extent using the large- and narrow-span LES of the IUSTI case.

6.2.3 Narrow-span *vs* large-span LES

In this section, the wall-pressure fluctuations from the narrow- and large-span LES of the IUSTI case (see table 6.1) are compared. Using a complex set of windowing operations, it was shown in figure 6.2 that the narrow-span LES results are in good agreement with the

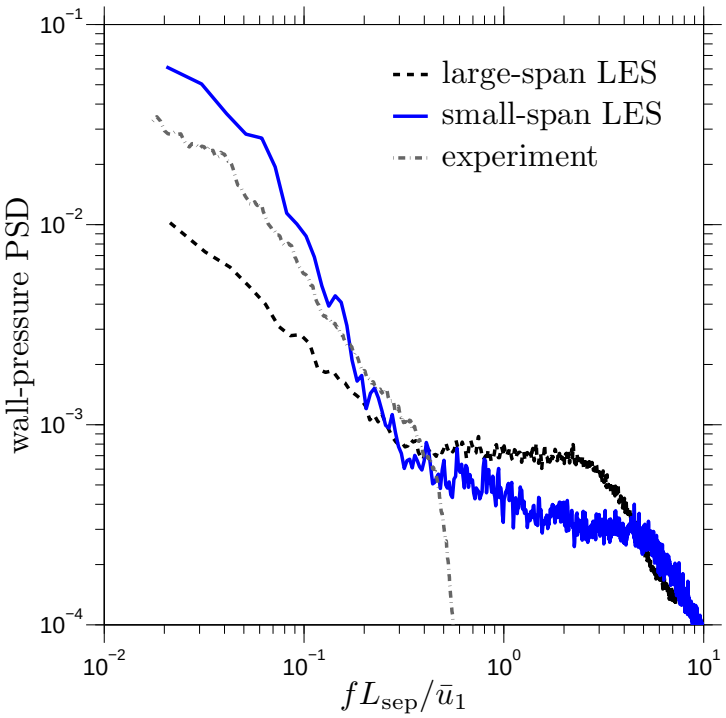

FIGURE 6.17: Narrow-span (*solid line*) *vs* large-span (*dashed line*) wall-pressure spectra near the reflected-shock foot. The experimental results are also provided (*grey dash-dotted line*)

experimental results. In the following comparison, we also make use of Welch's method (50% overlaps and Hanning windows) but the window size is kept fixed at $50L_{\mathrm{sep}}/\bar{u}_1$ for all the signals presented.

The wall-pressure power-spectral density in the vicinity of the reflected-shock foot is presented in figure 6.17. Two main differences can be seen: for $fL_{\mathrm{sep}}/\bar{u}_1 > 0.5$, the large-span LES exhibits more energetic fluctuations than the narrow-span case whereas the converse can be observed for $fL_{\mathrm{sep}}/\bar{u}_1 < 0.5$. The more energetic high-frequency content of the large-span case can be explained by the differences in the inlet conditions. As discussed in chapter 4, the digital-filter settings in the large-span LES were modified such that the energy of the fluctuations in the outer region of the boundary layer was increased to overcome their observed underestimation in the narrow-span LES upstream of interaction, when compared to the experimental results. However, the significant reduction by almost one decade of the PSD levels of the large-span LES low-frequency fluctuations is not easily explained. Nevertheless, some tentative explanations will be suggested in both this section and the following one.

In order to try to explain the significant damping of the low-frequency motions in the large-span LES, it is interesting to look at the one-dimensional weighted spectra

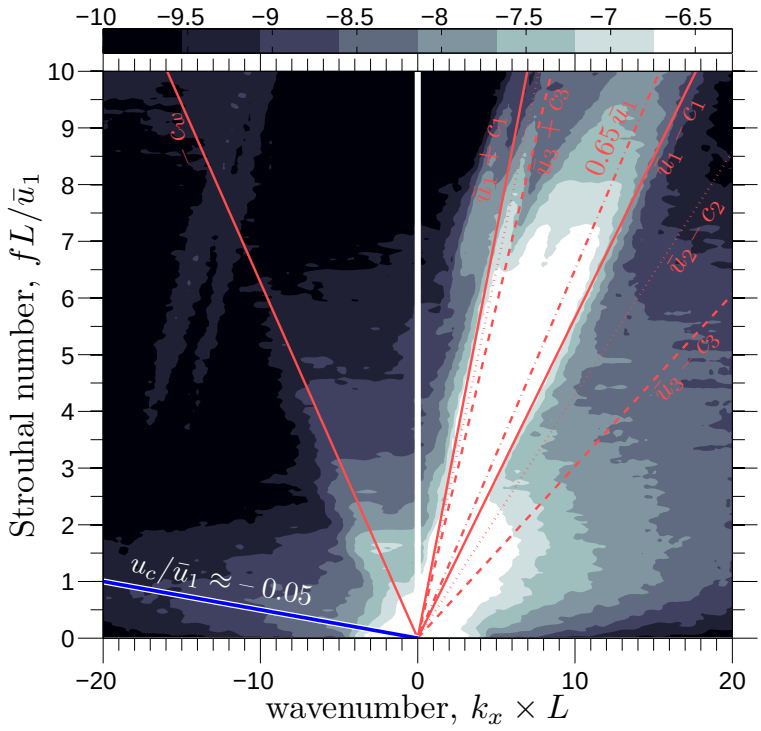

(a) narrow span

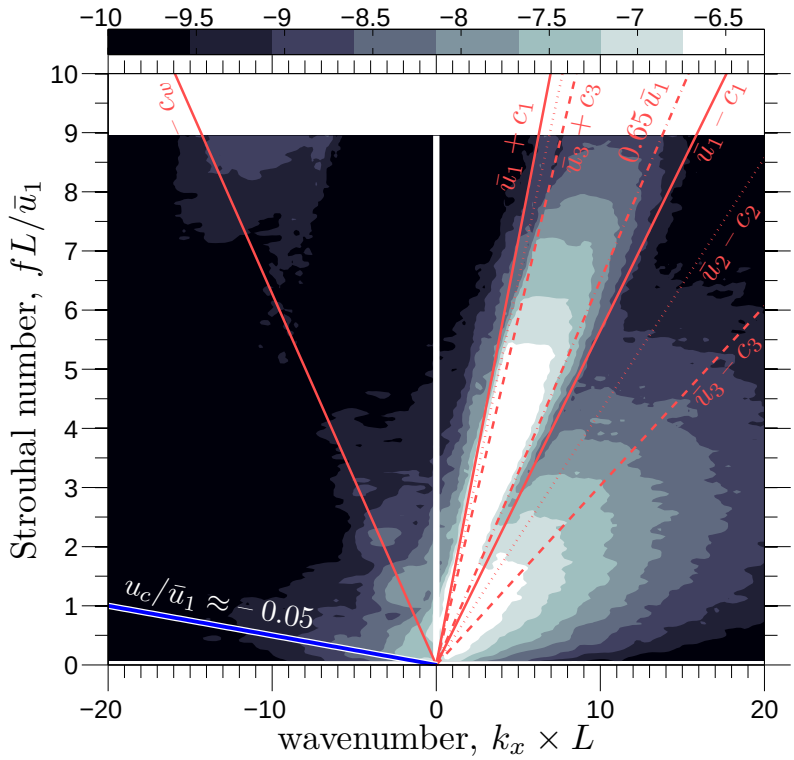

(b) large span

FIGURE 6.18: Wall-pressure dispersion relations: narrow-span *vs* large-span LES. The above maps were obtained similarly to figure 6.13 and the labelled dispersion relations are the same as the ones described in the caption of figure 6.13. Note that the *contours* are based on a logarithmic scale and shown at exactly the same levels in both the narrow-span and large-span cases to facilitate the comparison

of the spanwise autocorrelation function (computed on the streamwise-velocity component) as a function of the streamwise position, as was shown in figure 4.13. While all the relevant scales of the incoming turbulent boundary layer are correctly resolved in both simulations, it is clear that the narrow-span configuration does not capture all the energetically significant spanwise wavelengths within the interaction. This artificially forces the separation region to be mostly of a two-dimensional nature. The narrow-span time-averaged flow properties were analysed in chapter 5 and the flow topology was found to be globally unstable. Moreover, the global mode was shown to act on timescales two orders of magnitude longer than the characteristic timescale of the upstream boundary layer. By confining the separation bubble so that it remains mostly two-dimensional, one forces the flow to be closer to the one studied in the stability analysis. Therefore, the narrow-span LES could have greatly enhanced the possibility for the global mode to exist. Since the most unstable global-mode structure was found to be two dimensional with a tendency to enhance or reduce the separation, it could have made the narrow-span bubble follow more significant expansion/compression motions, leading to more pronounced low-frequency oscillations and enhanced separation. Although the large-span time-averaged flow field is found to be globally unstable, the growth rate is about an order of magnitude smaller than that found in the narrow-span case. This picture is consistent with the aforementioned explanation and the observed drop in the PSD levels at low frequencies, although it does not explain why the experimental results are closer to the narrow-span results than the large-span ones, despite the ample spanwise extent of the wind tunnel, unless the experimental bubble also suffers from confinement effects such as strong corner flows or the presence of coherent spanwise structures originating either from the upstream concave walls (Görtler-like vortices) or the way the flow is seeded from the wall, or a combination of both[5].

Figure 6.18 gives a comparison of the dispersion relations of the wall-pressure fluctuations of the two LES. The reference point to build the correlation function was taken at $(x - \bar{x}_{\text{sep}})/L_{\text{sep}} \approx 0.3$ in both cases. Both dispersion maps are plotted on a logarithmic scale using the same contours to allow a direct comparison between the two cases. Although a similar structure emerges in both cases, one can see a few differences. First, the shear-layer vortical footprint, responsible for the dominant elongated ridge (in white), is more pronounced in the narrow-span case. This is believed to be related to the enhanced two-dimensionality of the flow due to the spanwise confinement which can lead to more coherent and more energetic vortical structures inside the mixing layer.

[5]Although not shown here, the IUSTI group has looked at the spanwise auto-correlation function upstream of the interaction, which was seen to exhibit high levels of correlations at wavelengths shorter than the wind-tunnel width, providing clear evidence of significant levels of inhomogeneity in the spanwise direction. At the time, the IUSTI team suggested that those coherent spanwise structures were due to the use of periodic V-shaped Dynmo-tape roughness elements placed just upstream of the sonic neck (see Dussauge and Piponniau, 2008).

Similarly, both the downstream- and upstream-propagating acoustic waves are more clearly identified in the narrow-span case. Additionally, although still present in the large-span case, the ridge corresponding to slow upstream-propagating pressure fluctuations is more noticeable in the narrow-span case. Those observations confirm the more two-dimensional behaviour of the narrow domain. Despite the ability of the narrow-span case to reproduce the experimental low-frequency unsteadiness, it is of interest to look at the three dimensionality of the flow from the point of view of the large-span case. This is the focus of the next section.

6.2.4 Formation of large cells within the interaction

The three-dimensionality of the interaction is studied through the reversed mass flow rate per unit with $\dot{m}$, defined by:

$$\dot{m}(x,z,t) = \int_0^\infty \rho u^-(x,z,z,t)\mathrm{d}y, \text{ where: } u^- = \begin{cases} u \text{ if } u < 0, \\ 0 \text{ otherwise.} \end{cases} \tag{6.1}$$

This quantity was recorded during the large-span LES for all x and z grid points at a high frequency rate of once every twenty time steps. This can allow a well-resolved study of the evolution in time of pockets of reversed flow. Figure 6.19 was obtained by following the time variation of the $\dot{m}$ records from a fixed streamwise position located half the way down the mean separation bubble. Regions of strongest reversed mass flow rates are shown in yellow. It is found that large regions of reversed flows can form, some of which are highlighted in the subfigures (b) and (c). Such pockets of reversed flow can survive for more than $30L_{\mathrm{sep}}/\bar{u}_1$ and grow in the spanwise direction by as much as one separation-bubble length L_{sep}. In addition, they are often seen to meander in the spanwise direction[6]. Occasionaly, two of these structures can merge and form an even larger structure. It is clear that the narrow-span LES cannot capture the aforementioned dynamics, as is for example illustrated in subfigure (d) where the size of the narrow-span domain is highlighted. It is also of importance to note that the structures described here are generated inside the interaction itself and do not correspond to the long structures described by Ganapathisubramani et al. (2007b) in the upstream supersonic turbulent boundary layer.

Due to the meandering of the above long-lived cells of reversed flow, it is legitimate to question the meaning of single-point spectra such as the ones shown in figure 6.17. Indeed, if one such structure moves about a fixed probe, its footprint on the resulting spectra will be one of a higher frequency than that associated with the structure lifespan. In the narrow-span LES, it was shown that the flow topology inside the interaction

[6]This is more clearly seen in the animations of the LES fields.

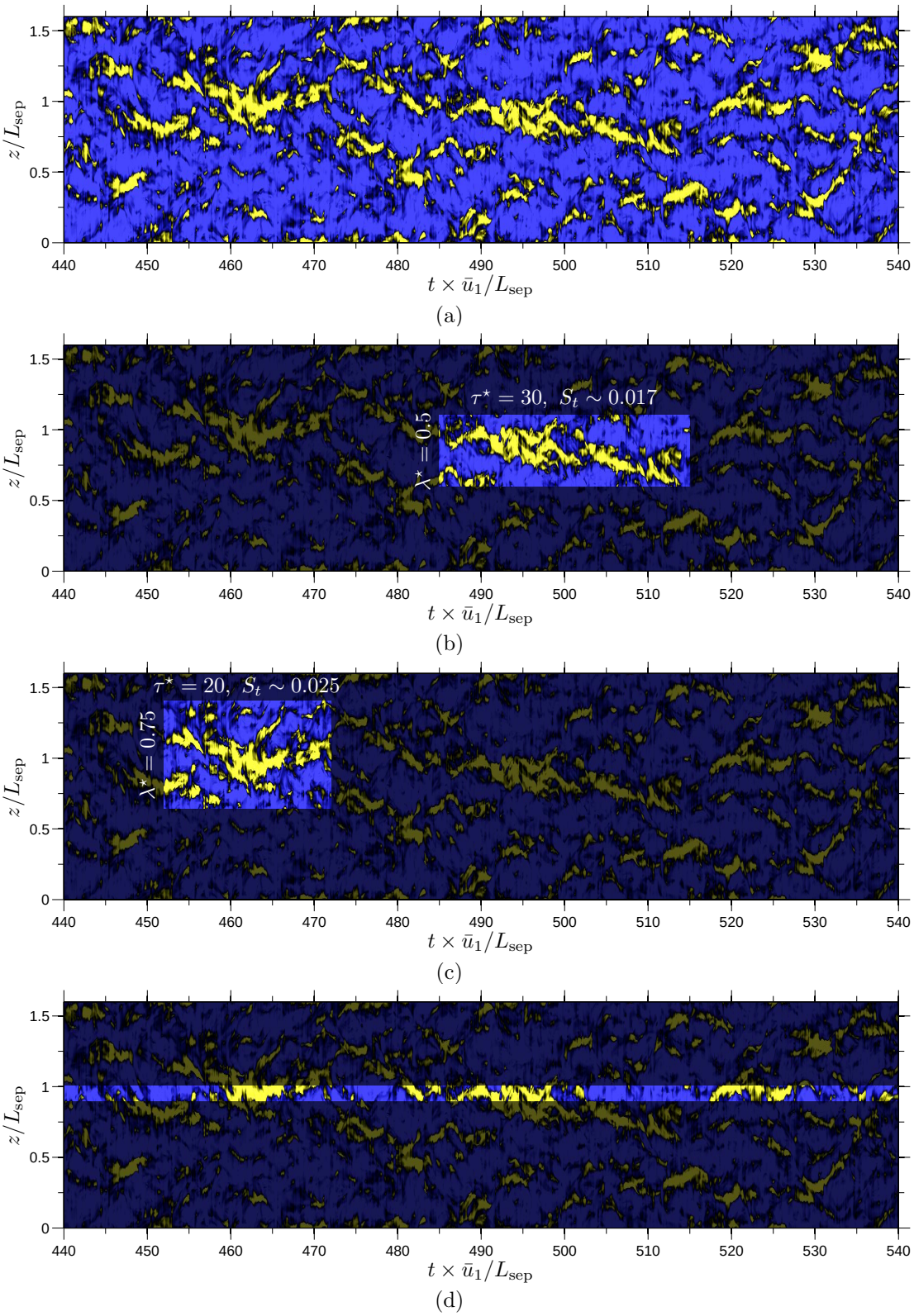

FIGURE 6.19: Time series of the reversed mass flow rate per unit width $\dot{m}$ at $(x - \bar{x}_{\text{sep}})/L_{\text{sep}} \approx 0.5$. The *yellow regions* correspond to $\dot{m}/(\bar{\rho}_1 \bar{u}_1 L) \leq -0.4$. The embedded quantities $\lambda^\star \equiv \lambda/L_{\text{sep}}$, $\tau^\star \equiv \tau \bar{u}_1/L_{\text{sep}}$ and $S_t \equiv 1/\tau^\star$ provide indications on the length- and time-scales associated with the highlighted coherent structures. The bottom figure (d) illustrates the spanwise extent covered by the narrow-span case

is nearly two dimensional because of the domain-confinement effect. In this case, the spanwise homogeneity of the flow allows the fixed-point observations to be relatively unbiased. Conversely, one can question the level of bias in the spectrum obtained from a fixed position in the large-span LES. To estimate this bias, we have tried to capture the meandering of the cells and have recorded the time series as seen by the moving probe. The tracking algorithm was based on a simple gradient method where the probe followed the valley formed by the function $\sqrt{[\partial\dot{m}/\partial x]^2 + [\partial\dot{m}/\partial z]^2}/|\dot{m}|^\alpha$ with $\alpha = 0.4$. The choice for α was made on heuristic grounds by visualy investigating the effect of its value on the resulting path. This is not necessarily an optimal choice but it gives satisfactory results, as shown in figure 6.20.

Using this tracking algorithm, time series of $\dot{m}$ obtained by a fixed probe, coincinding with the initial position of the tracking probe, and the one obtained by the moving station were recorded and compared. The resulting spectra are shown in figure 6.21. One can see that low frequencies contain more energy when the probe accounts for the meandering effects than when it is fixed. This confirms the idea that the narrow-span LES results are similar to the case of a moving probe due to the artificial confinement and thus, that the weaker low-frequency oscillations found by the large-span LES (see figure 6.17) can be partially explained by the fact that the large-span results did not include the meandering effects. However, from figure 6.21, it appears that the correction can hardly explain the difference of one decade in the PSD levels (see figure 6.17). Thus, the meandering corrections are not likely to be the unique explanation for the PSD differences between the large- and narrow-span LES and the earlier discussion about the possible global-mode effects is still relevant.

The mechanisms responsible for the formation and destruction of the coherent structures described in this section are not known. However, looking at animations based on the LES data, a tentative description may be briefly given. Indeed, it appears that the mixing layer, in addition to the adverse pressure gradient imposed by the shockwave system, may be playing an important role in the birth and growth of such structures. Some recognisable and repeatable patterns may be seen when looking at flow animations from the LES data and an attempt to describe them is shown in figure 6.22.

First, consider the shock system, the mean mixing-layer centreline (discussed in chapter 4) and a region of reversed flow (see figure 6.22(a)). Then consider one coherent vortex developing along the mixing-layer centreline[7]. As the vortex is convected, it grows until it reaches a sufficient size to interact with the reversed flow. As a result of this interaction, an eruption of the recirculation bubble occurs (see figure 6.22(b)), similar to the vortex-induced eruptions described in Peridier et al. (1991a,b) and Doligalski et al. (1994). This eruption is followed by an enhancement of the separation bubble. In some instances, while the initial coherent vortex is convected away and no longer influences

[7]We assume the vortex to be sufficiently coherent in the spanwise direction.

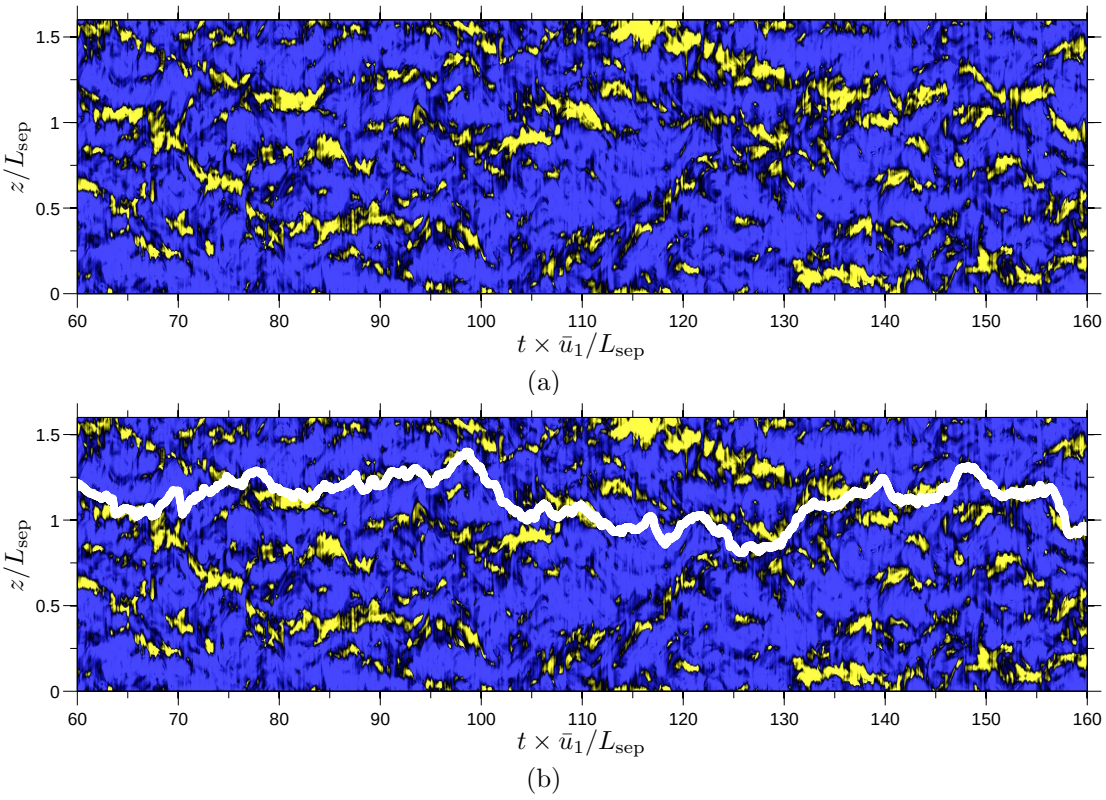

FIGURE 6.20: Tracking pockets of reversed flow. The coherent structures are tracked in time using a gradient-based algorithm. For each new time step, the selected path is one that minimises the function $\sqrt{[\partial\dot{m}/\partial x]^2 + [\partial\dot{m}/\partial z]^2}/|\dot{m}|^\alpha$ where $\alpha = 0.4$. The *white line* gives the resulting path

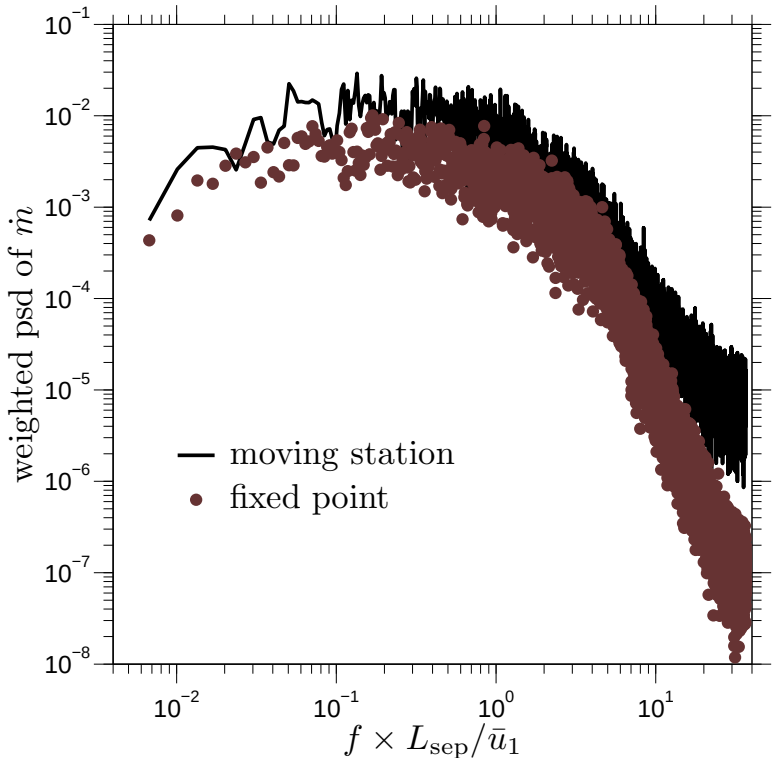

FIGURE 6.21: Meandering effect on the $\dot{m}$ spectrum

the separation bubble, a second coherent vortex starts interacting with the enlarged bubble, in a similar way as the previous one (figure 6.22(c)). Depending on the time separating the two vortex-induced eruptions, a favourable (dynamical) enhancement of the bubble can take place, leading to a separation bubble which has grown significantly larger than its initial state (figure 6.22(d)). This would translate into events of significant reversed mass-flow rates (see figure 6.19). To validate this idea, one should first study the statistical validity and significance of the vortex-induced eruptions, and then check whether the width of the structures shown in figure 6.19 can be correlated to the typical spanwise extent of the mixing-layer coherent vortices.

While the previous paragraph described a possible mechanism that can lead to a build up of the recirculation bubble, it is equally important to consider an opposing mechanism, which is also based on noticeable patterns in the flow animations. A built-up bubble can reach a size where a significant downwash occurs on its backside. This downwash can then deviate the shear-layer coherent vortices toward the wall, as shown in figure 6.22(e)[8]. As the vortex is forced to impinge on the wall, it can split the bubble into two sections. The upstream section is no longer fed from the back and progressively weakens, while the second section is lifted up by the vortex and transported into the faster stream, which rapidly destroys it (figure 6.22(f)). At this stage, the separation bubble can be nonexistant or severely damped and the whole process can repeat itself. The aforementioned mechanism is solely descriptive and its quantitative relevance should be examined in the future. It is possible that the associated timescales are of the same order of magnitude as the most significant low frequencies, or are comparable to the timescale from the model by Piponniau et al. (2009). Nevertheless, the coherent structures described in this section are found to be correlated with the reflected-shock motions.

One important consequence of the presence of long-lived and wide recirculation cells is the constraint such flow features put on the numerics. Indeed, because of the presence of energetically-significant large spanwise wavelengths evolving on timescales more than two orders of magnitude longer than the typical timescales of the upstream turbulence, it is sometimes difficult to achieve spanwise-homogeneous flow statistics, as one would expect given the flow configuration and the use of periodic boundary conditions. Figure 6.23 illustrates this issue by comparing the mean velocity field obtained by averaging over the full runtime and the one obtained by averaging over a timescale of the order of the most energetic low-frequency motions[9] ($35L_{\text{sep}}/\bar{u}_1$). It is found that the two averages can differ by $\mathcal{O}(0.1\bar{u}_1)$. The regions of largest differences form streaky and cell-like patterns. For example, in figure 6.23(a), two large cells of width $0.5L_{\text{sep}}$ are clearly visible. This is consistent with the presence of the long-lived structures discussed in this

[8]This is also seen in the flow animations.

[9]Note that this is longer than the time covered by Garnier et al. (2002).

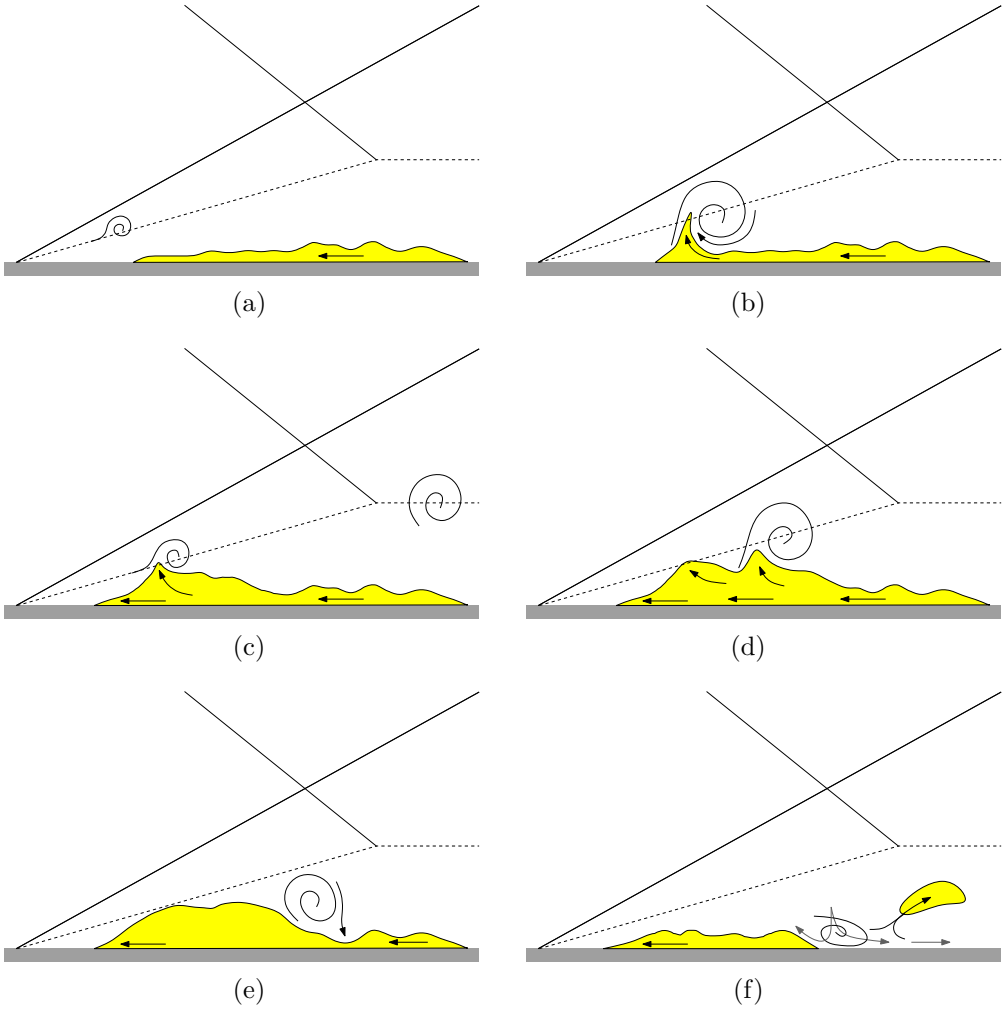

FIGURE 6.22: Descriptive sketch of some recognisable patterns in flow animations. The two *solid lines* represent the incident and reflected shocks, the *dashed line* represents the time-averaged mixing-layer centreline as shown in figure 4.32. The *filled yellow area* represents the region of negative streamwise velocity u. All events (a) to (f) are described in the text

section. Moreover, long streaky structures extending long before the interaction are also noticeable (see figure 6.23(b)) with magnitudes not exceeding a couple of percent. A correlation between a low-speed upstream streaky structure and the presence of a large recirculation cell may be seen, although one can also find counter examples. This is similar to the arguments of Ganapathisubramani et al. (2007b) and more data analysis would be needed to quantify the level of such correlation.

Irrespective of the mechanisms responsible for the formation of the long-lived structures, they will interact with the reflected shock. From flow animations, the reflected-shock is found to experience large spanwise-wavelength wrinkles that are correlated with the patterns of the recirculation region. This leads us to focus on the reflected shock itself, a study which will then be the starting point for a deeper analysis to be presented in chapter 7.

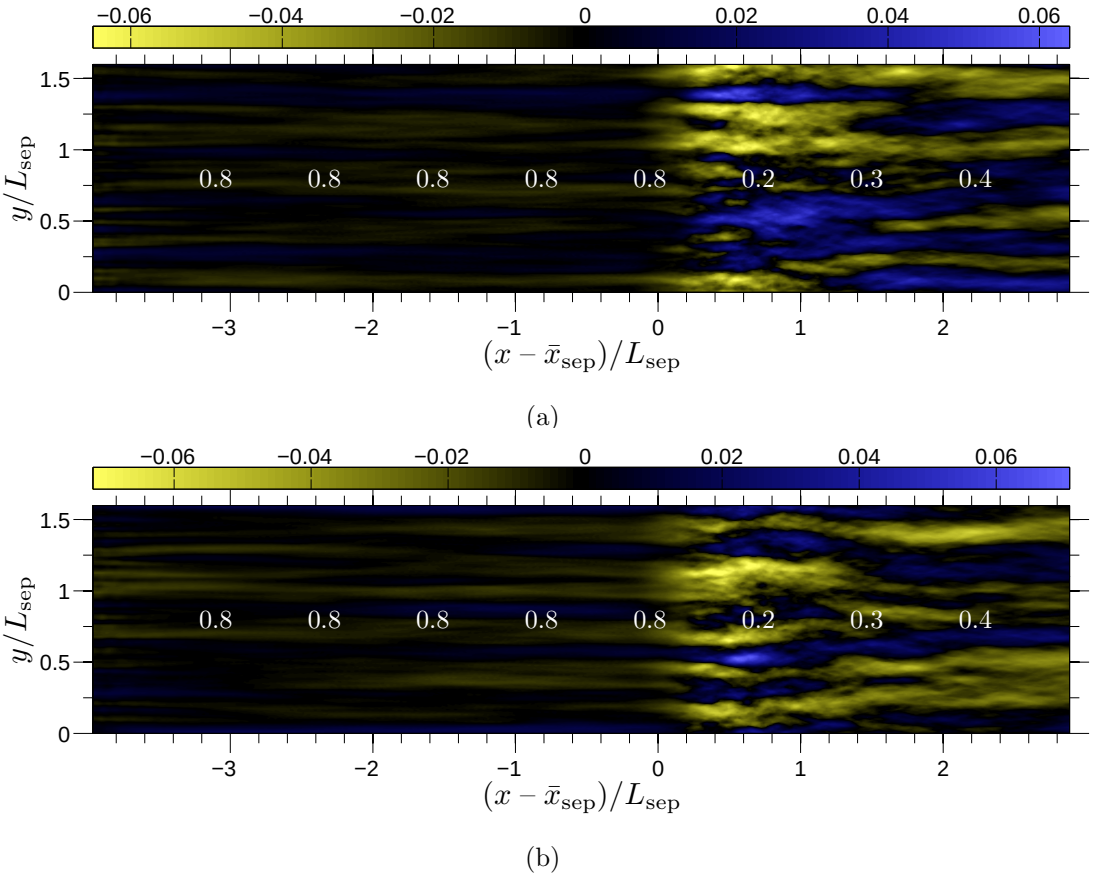

FIGURE 6.23: Large-cell effects on the flow-statistic convergence. Top views of $\langle u\rangle_T - \bar{u}$ where $\langle u\rangle_T$ is the time-average of u during a time T, with T being $35L_{\mathrm{sep}}/\bar{u}_1$ (about five FTT). The planar views are taken at $y/\delta_0^{\mathrm{imp}} \approx 0.27$. The white marks 0.8 to 0.4 indicate the local mean velocity $\bar{u}/\bar{u}_1$. Cases (a) and (b) are two different time intervals

6.3 Shock motions and conditional averages

6.3.1 Detection of the shock location

In order to study the shock-system position in time, one first needs to extract its position from the LES database using an automatic algorithm. This section briefly describes the algorithm used for that purpose, a copy of which is provided in appendix D.

First, the shock system is identified using a carefully chosen threshold value of the dilatation rate. While this approach is robust in the potential flow, it becomes less and less reliable as one penetrates in the boundary layer, where the shock is significantly weaker and compressible turbulence structures may match the selected threshold value. Nevertheless, spurious data points can be kept to a minimum. Furthermore, the choice of dilatation rate was found to produce smoother results than specific sensors such as the one from Ducros et al. (1999), which gave step-like results in the potential flow due to the high level of grid stretching.

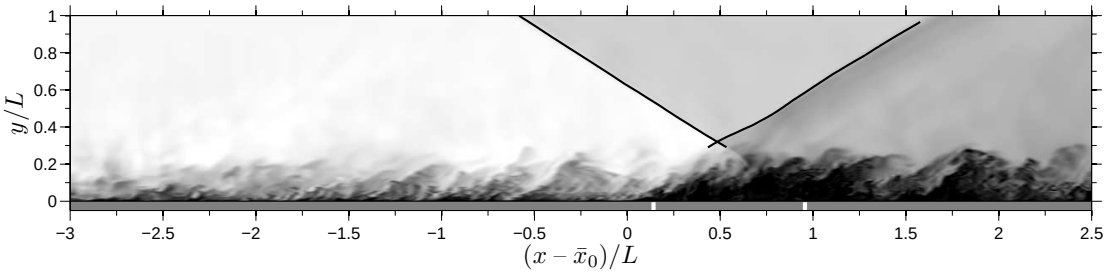

FIGURE 6.24: Instantaneous side view of the large-span-simulation interaction with the detected shock-system. The *grey colour scheme* linearly maps the temperature field ranging from hot (*black*) to cold (*white*) with $T_w/\bar{T}_1 \approx 2.06$. The *black lines* indicate the shock system which was captured using the detection algorithm. The *thick white ticks* incorporated in the wall show the time-averaged separation and reattachment positions

Then, the extracted instantaneous shock positions are averaged to estimate the streamwise extent along which the shock extraction can be deemed successful. This choice is manual and rather subjective but it aims at selecting a range of streamwise positions which occur a significant number of times. Therefore, extreme but rare shock positions are not considered. Following this choice, the raw data are then clipped to the selected domain and we are left with the final step, consisting of removing most of the remaining spurious points. The last step is performed automatically, where the decision is based on how far a data point is from the mean value. It was decided to remove points departing by more than four times the local standard deviation and to replace them using a linear interpolation from the closest instants where the position is reliably known.

A snapshot of the end-result is provided in figure 6.24, where one can see the detected shock system and the ability of the method to capture the oscillatory nature of the reflected shock.

6.3.2 Some characteristics of the shock motions

The aforedescribed shock-detection algorithm was applied to the IUSTI narrow- and large-span LES as well as to the ITAM and TUD cases. Given the instantaneous reflected-shock position, it is straightforward to compute the reflected-shock foot position variation in time by means of a best-line fit to its position which is then extended all the way to the wall. From there, the shock-foot probability-density function can be derived, as shown in figure 6.25. Interestingly, none of the cases is found to depart significantly from the normal-law distribution, perhaps with the exception of the ITAM case, where a slight asymmetry was already mentioned in this chapter (figure 6.15). Therefore, the reflected-shock motions can be said to be symmetrically distributed around

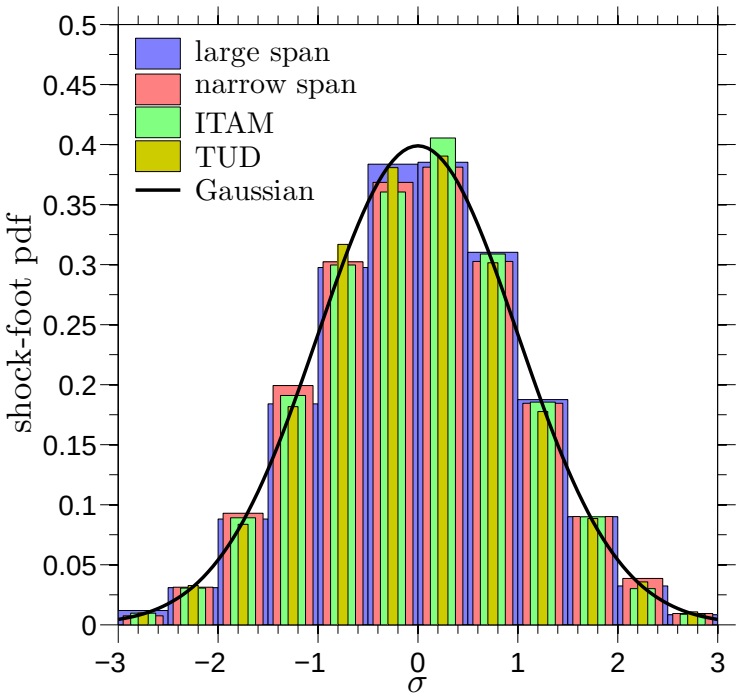

FIGURE 6.25: Shock-foot probability density function

the mean position. Any proposed mechanism responsible for the low-frequency shock motions should be able to reproduce this symmetry in the shock-foot PDF.

Looking at animations from the LES, one can notice that the reflected shock is subject to both spanwise wrinkles and traveling longitudinal waves. The extracted shock positions can be used to help characterise the traveling waves. In particular, their dispersion properties are of interest. Of course, it must be kept in mind that due to the oblique nature of the shock, the transverse waves are traveling on a non-uniform grid and the effect of inevitable numerical errors needs to be considered when looking at the obtained dispersion relations and amplitude evolutions. In addition, the use of periodic boundary conditions significantly affects the wave pattern on the shock surface since any spanwise-component into the propagation front is forced to come back in the computational domain to eventually form interference patterns. With these numerical constraints in mind, we proceed (with care) with analysing the large-span LES data of the IUSTI case.

First, let us use the time-averaged reflected shock to define a curvilinear system associated with the shock. The longitudinal position along the shock is denoted ξ_r with $\vec{t}$ and $\vec{n}$ respectively the associated tangential and normal unit-vector components. Fortuitously, the resulting curvilinear system is nearly a straight line and will be approximated

as such for convenience in the wavenumber/frequency analysis. Once the aforementioned reflected-shock axis is defined, for each instantaneous reflected-shock position one can compute the shock-normal displacement $\eta_r(\xi_r, t)$. From there, the η_r time series for each position along the shock is used to compute the shock-displacement PSD as a function of the distance along the shock, as shown in figure 6.26(a).

From figure 6.26(a), one can see that high-frequency oscillations (i.e. $fL/\bar{u}_1 > \mathcal{O}(1)$) are rapidly damped (for $\xi_r < L/5$) whereas low-frequency oscillations (i.e. $fL/\bar{u}_1 < \mathcal{O}(10^{-1})$) are almost not damped. Therefore, the reflected shock acts as a low-pass filter, a feature which is in agreement with earlier works (see Robinet and Casalis, 2001; Dussauge et al., 2006, and references therein). Of course, some of the high-frequency damping may be related to the grid stretching.

Furthermore, $\eta_r(\xi_r, t)$ can be used to evaluate the dispersion relations in the direction of the shock, the result of which is given in figure 6.26(b). Because of the fast decay of high-wavenumber components it is difficult to extend the dispersion-relation maps to high values of wavenumbers k_{ξ_r}. Nevetheless, favoured convective speeds may be seen. If one denotes by ϖ_2 and ς_2 the tangential (to the shock) components of the region-two freestream velocity $\bar{u}_2$ and speed of sound c_2, respectively, and by ϑ_2 the shock-normal component of $\bar{u}_2$, one can identify travelling waves at $\varpi_2 \pm \varsigma_2$ and $\varpi_2 \pm \sqrt{|\vartheta_2^2 - \varsigma_2^2|}$. While convective speeds of $\varpi_2 \pm \varsigma_2$ may be reasonably expected, the second family of convective speeds ($\varpi_2 \pm \sqrt{|\vartheta_2^2 - \varsigma_2^2|}$) is less intuitive. However, it can be explained in light of the work by Robinet and Casalis (2001) on the receptivity of a normal shock to the downstream acoustic field, based on classical linear-stability theory. They showed that there exists a critical angle at which the incindent acoustic waves are completely reflected in the form of transverse waves (i.e. along the shock) and that if an acoustic source emitting waves in all directions exists in the flow, the shock will preferentially respond to incident waves close to that critical angle. In the case of a normal shock, the resulting transverse waves are shown to follow a dispersion relation in $k_{\xi_r} = 2\pi f/\sqrt{|\vartheta_2^2 - \varsigma_2^2|}$. Naturally, in the case of an oblique shock, the contribution of the tangential-velocity component ϖ_2 must be added.

Therefore, the transverse waves along the shocks appear to have two main origins. First, from direct perturbation of the reflected shock by the acoustic field coming from region 2. Second, as a result of the impingement from the bottom side of the shock by acoustic waves at the critical angle at which they are completely reflected in the form of transverse waves along the shock.

Although the aforementioned transverse waves are an interesting feature of the shock dynamics, they occur on timescales that cannot be directly related to the low-frequency shock oscillations. In an attempt to understand the mechanism responsible for the low frequencies, we propose to make use of conditionaly averaged fields. The following section will thus describe the procedure and the conditionally averaged fields while chapter

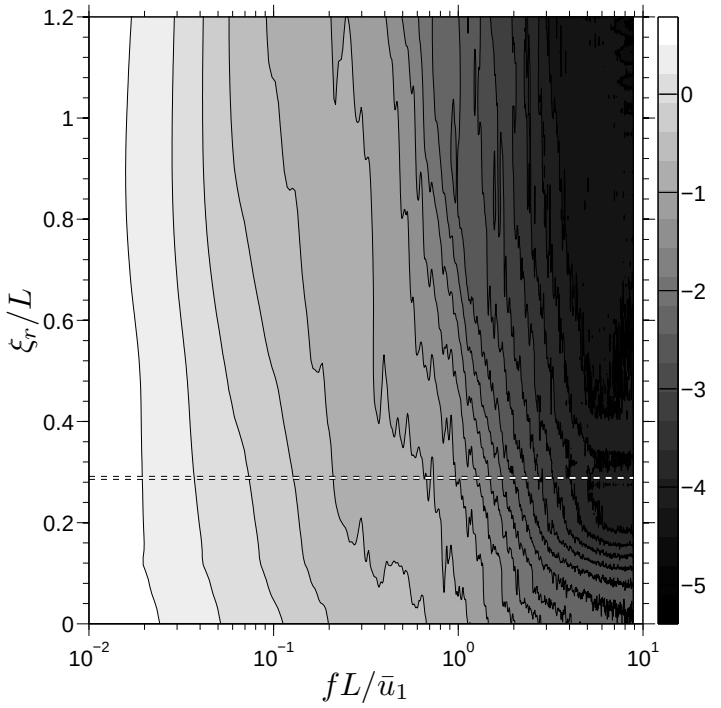

(a) power-spectral density map

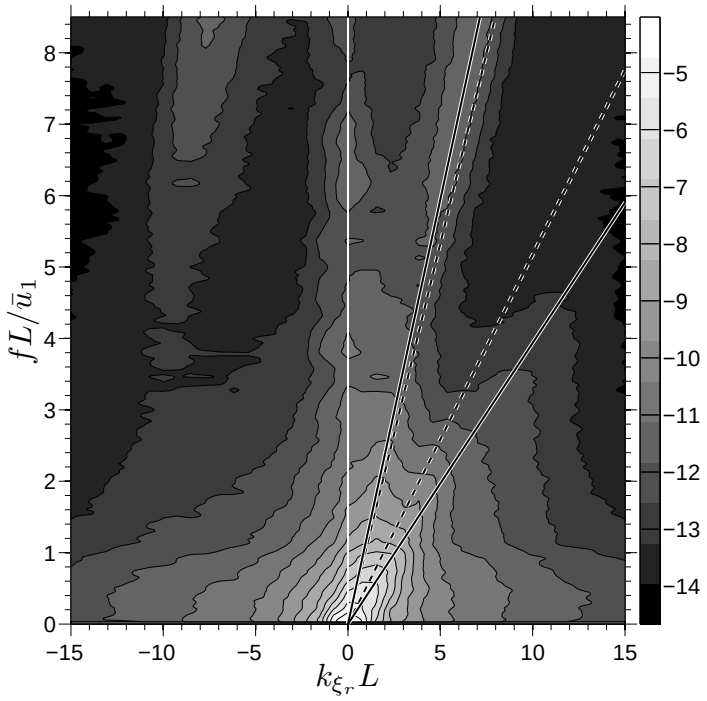

(b) dispersion-relation map

FIGURE 6.26: Power-spectral density and dispersion-relation maps of the shock displacements with respect to the mean reflected-shock axis system (based on the IUSTI large-span LES case). Both maps are shown on a logarithmic scale. The *thick dashed line* in (a) indicates the location along the shock where the incident shock crosses. In (b) the spectrum is premultiplied by the frequency and computed from the 2D Fourier transform of the two-point correlation function. The *thick solid lines* indicate the $\varpi_2 \pm \varsigma_2$ dispersion relations whereas the *dashed lines* indicate the $\varpi_2 \pm \sqrt{|\vartheta_2^2 - \varsigma_2^2|}$ dispersion relations

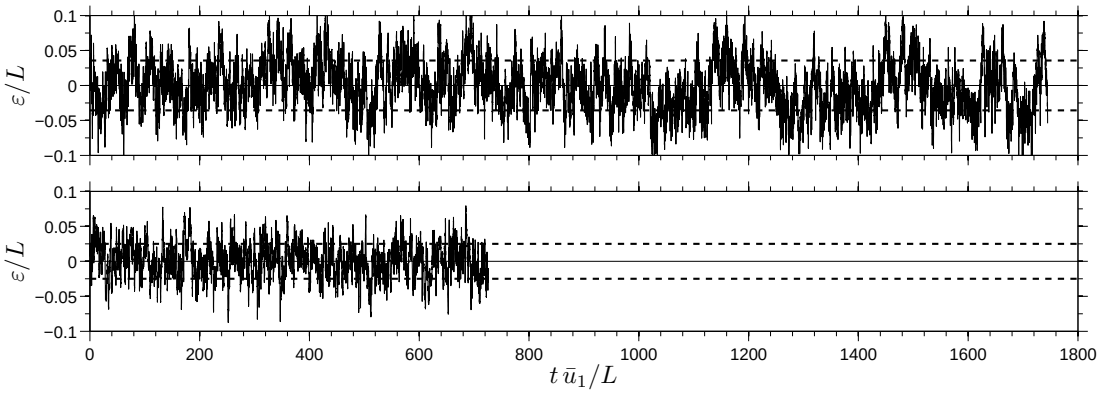

FIGURE 6.27: Shock-foot-displacement time series from the narrow-span (*top*) and large-span (*bottom*) simulations. The *dashed lines* indicate the location of the variance $\pm\sigma/L$ ($\bar{\varepsilon} = 0$, $\sigma^2 = \overline{\varepsilon\varepsilon}$)

7 will refer to these conditional averages in order to guide a more theoretical approach to the issue of the low-frequency shock oscillations.

6.3.3 Conditional averages

The conditional averages that will be extensively used in the remainder of this work are based on the shock-foot motions. As described earlier, the time-dependent reflected-shock position was extracted from the LES data allowing for a straightforward derivation of the time series of the reflected-shock foot displacement with respect to its mean position, denoted $\varepsilon(t)$, as shown in figure 6.27. The time spanned by the large-span LES is shorter than that covered by the narrow-span LES, due to the computational overhead in the large-span configuration.

Nevertheless, the mean and standard deviation (σ) of both raw time series can be computed. The standard deviation is then used as a selection criterion. First, the space spanned by the possible shock-foot positions is split into 12 equally-sized bins between -3σ and $+3\sigma$. Then, for each available instant in the LES database, the flow fields are averaged according to which bin they belong to.

Let $\mathcal{A}_{\varepsilon_0,\Delta\sigma}$ be the set of all the instants $t \in [0,T]$ such that the shock-foot displacement is located between ε_0 and $\varepsilon_0+\Delta\sigma$, where T, ε_0 and $\Delta\sigma$ are some predefined values. Let $\mathcal{N}(\mathcal{A}_{\varepsilon_0,\Delta\sigma})$ be a measure associated with this set, consisting of the time spanned by $\mathcal{A}_{\varepsilon_0,\Delta\sigma}$. This can be written:

$$\mathcal{A}_{\varepsilon_0,\Delta\sigma} = \{t \in [0,T] : \varepsilon(t) \in [\varepsilon_0, \varepsilon_0 + \Delta\sigma]\}, \tag{6.2a}$$

$$\mathcal{N}(\mathcal{A}_{\varepsilon_0,\Delta\sigma}) = \int_{\mathcal{A}_{\varepsilon_0,\Delta\sigma}} 1\,\mathrm{d}t. \tag{6.2b}$$

The set $\mathcal{A}_{\varepsilon_0,\Delta\sigma}$ and its associated measure $\mathcal{N}$ being specified, it is possible to define the conditional-average operator $\langle\cdot\rangle_{\varepsilon_0,\Delta\sigma}$:

$$\langle u_i\rangle_{\varepsilon_0,\Delta\sigma} = \frac{1}{\mathcal{N}(\mathcal{A}_{\varepsilon_0,\Delta\sigma})}\int_{\mathcal{A}_{\varepsilon_0,\Delta\sigma}} u_i(t)\,\mathrm{d}t. \tag{6.2c}$$

It is straightforward to see that this operator is linear and conserves constants. Note that in the definition of $\mathcal{A}_{\varepsilon_0,\Delta\sigma}$, no distinction about the sign of $\mathrm{d}\varepsilon/\mathrm{d}t$ is made, but this could easily be specified to separate the cases where the shock is moving in the upstream direction from the cases where it is moving in the downstream direction.

Idealy, the LES data could provide $\langle u_i\rangle_{\varepsilon_0,\Delta\sigma}$ for any given values of ε_0 and $\Delta\sigma$. In practice, this is impossible due to the finite and short time spanned by the LES; and ε_0, $\Delta\sigma$ are chosen such that the range $[-3\sigma, 3\sigma]$ can be split into 12 segments. Figure 6.28 is a plot of the resulting conditionally-averaged data. It features the different shock positions (expect for the extreme bins), the respective positions of the sonic line as well as the contours where the streamwise velocity is $-0.02\bar{u}_1$. To ease the reading of the figure the upstream displacements are in dashed lines. Note that in the case of figure 6.28 no effort is made to distinguish the positive $\mathrm{d}\varepsilon/\mathrm{d}t$ events from their negative counterparts. The most interesting aspects of both figures 6.28(a) and 6.28(b) are: (i) the clear correlation between a stronger separation and an upstream position of the reflected shock and (ii) the fact that the reflected-shock angle does not stay constant between upstream and downstream positions. Note that in both cases, the conditionally-averaged shocks are nearly linear and therefore it was decided to approximate them by their best-fit lines. Some differences between the narrow-span and large-span cases may be seen, namely, the smaller shock excursions and separation bubbles in the large-span LES (discussed earlier) and the behaviour of the sonic line which seems to rotate around a different fixed point. The correlation between the size of the separation and the shock position is a well-established result (see Piponniau et al., 2009). Moreover, the reduction of the streamwise excursions of the shock as one moves further away from the wall was also documented by Dupont et al. (2006). The LES results thus confirm those experimental observations.

From this point onward, we wish to associate the conditional averages with the notion of phase averaging, although we stress that the shock motions are not harmonic so that the notion of phase is different from its usual meaning. At any given position, the velocity-vector time series $u_i(t)$ can be decomposed in its time-averaged value $\bar{u}_i$ and a time-dependent component $u_i'(t)$. This is the classical Reynolds decomposition. Now suppose that the time dependency of u_i' occurs on two distinct timescales, a fast one denoted t_f and a slow one denoted t_s such that $t_f/t_s \ll 1$. In the present case, t_f is associated with the timescales of turbulent structures in the upstream boundary layer whereas t_s is associated with the timescales of the low-frequency shock motions. This

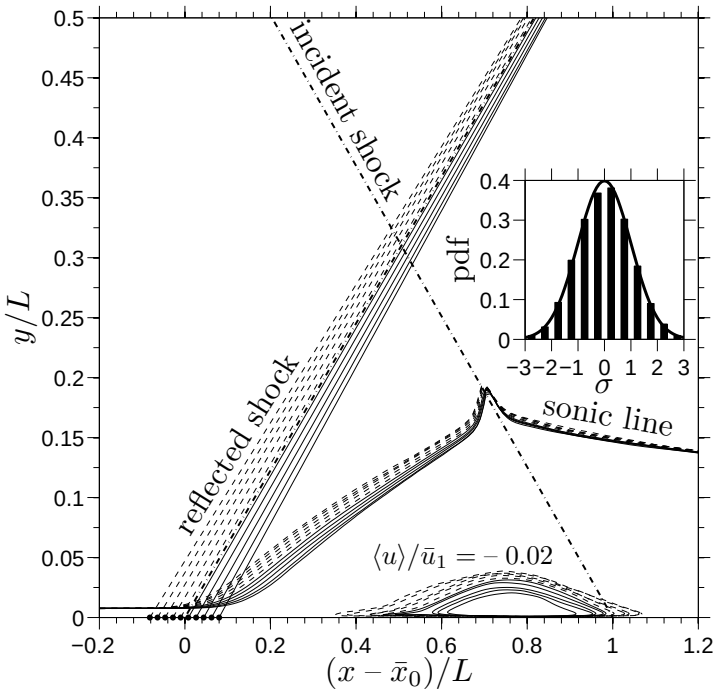

(a) narrow span

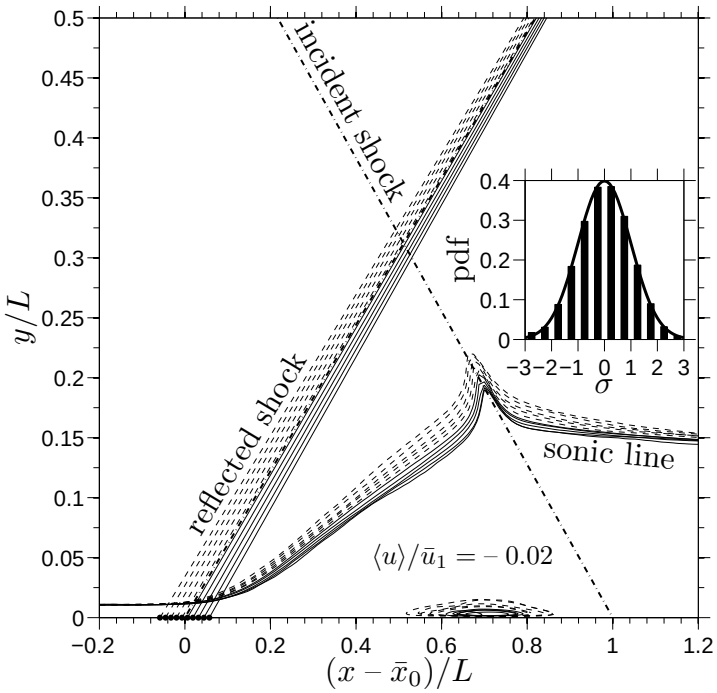

(b) large span

FIGURE 6.28: Conditional averages of the SBLI based on the probability density function of the shock-foot position, which is split into 12 bins in the range $\pm 3\sigma$. The conditionally-averaged shocks are nearly linear but only the best-fit lines are shown in this figure for clarity. Furthermore, the best-line fits are extended to the wall but in reality the shocks do not penetrate the subsonic region, which is also indicated in the figure. The total number of samples are $160,000$ and $64,990$ in the narrow-span and large-span cases, respectively. The normal-law PDF is shown on top of the black histograms

can be made more formal by setting:

$$\begin{cases} t_f \equiv \delta_0/\bar{u}_1, \\ t_s \equiv t_f/r_0, \text{ with } r_0 \ll 1. \end{cases} \tag{6.3}$$

From this chapter, it is known that for the shock-reflection case considered in this work, $r_0 \sim 10^{-2}$. Thus, the time-dependent component u_i' is decomposed into the low-frequency ($\tilde{u}_i$) and high-frequency (u_i'') contributions:

$$u_i(t) \equiv \bar{u}_i + \tilde{u}_i(t_s) + u_i''(t_f). \tag{6.4a}$$

By definition, the time average of all fluctuations is zero, i.e. $\overline{u_i'} = 0$. This implies that $\overline{u_i''} = -\overline{\tilde{u}_i}$, which is still too general for the present purposes. Thus, it is also required that each mean contribution vanishes:

$$\overline{\tilde{u}_i} = 0, \tag{6.4b}$$

$$\overline{u_i''} = 0. \tag{6.4c}$$

At this stage, it is tempting to try to relate $\tilde{u}_i$ with the conditionally-averaged fields $\langle u_i \rangle_{\varepsilon_0,\Delta\sigma}$, but this is not trivial. The main difficulty in reconciling the two resides in the temporal dependence of $\tilde{u}_i$, as opposed to the dependence of $\langle u_i \rangle_{\varepsilon_0,\Delta\sigma}$ on the selected shock-foot position. To remove this difficulty, the following (strong) hypothesis will be used:

Hypothesis 6.1. *For a given reflected-shock-foot position taken from a low-pass filtered signal (with cutoff frequency $\mathcal{O}(0.1\bar{u}_1/\delta_0)$), the associated flow field $\tilde{u}_i$ is uniquely defined:*

$$\tilde{u}_i(t_s) = \tilde{u}_i(\varepsilon(t_s)). \tag{6.5}$$

The validity of the above hypothesis is debatable but it may be justified in the light of the LES results. While it is clear that there exists an infinite number of different flow fields u_i yielding the same shock-foot position x_0 (when for example considering the transverse waves along the shock and the turbulence), it is argued that when only the low-frequency motions are retained, the picture may become uniquely defined. One supporting observation is that the conditionally-averaged LES data, where the distinction between upstream and downstream shock motion was made, do not show any significant level of hysteresis. In other words, for a given shock position, the fact that the shock-foot was moving upstream or downstram does not matter, giving one example where hypothesis 6.1 is satisfied. Once again, it is believed that the above arguments strongly depend on the observed scale separation between the low-frequency shock motions and the turbulence-related fluctuations.

If hypothesis 6.1 is satisfied, and assuming that the turbulence fluctuations do not correlate with the shock-foot motions, making the conditional-averaging operation similar to a time integration (i.e. $\langle u_i'' \rangle_{\varepsilon_0,\Delta\sigma} = \overline{u_i''} = 0$), the following two corollaries may be written (the details of which are provided in appendix E):

Corollary 6.1.

$$\langle u_i \rangle_{\varepsilon_0,\Delta\sigma} - \bar{u}_i \quad = \quad \tilde{u}_i(\varepsilon_0) + \mathcal{O}(\Delta\sigma). \tag{6.6a}$$

Corollary 6.2.

$$\int_{\mathcal{A}_{\varepsilon_0,\Delta\sigma}} \tilde{u}_i(\varepsilon(t_s))\tilde{u}_j(\varepsilon(t_s))\,\mathrm{d}t_s \quad = \quad [\tilde{u}_i(\varepsilon_0)\tilde{u}_j(\varepsilon_0) + \mathcal{O}(\Delta\sigma)]\,\mathcal{N}(\mathcal{A}_{\varepsilon_0,\Delta\sigma}). \tag{6.6b}$$

As mentioned earlier, the term *phase average* will be used here to refer to $\tilde{u}_i(t_s)$. To quantify the spatial and energetic relevance of the phase fluctuations, it is of interest to compute the phase-fluctuation stress tensor $\overline{\tilde{u}_i\tilde{u}_j}$. By invoking the previous corollaries, one can easily show that the phase-fluctuation stress tensor may be evaluated from the following sum (see appendix E):

$$\overline{\tilde{u}_i\tilde{u}_j} \approx \frac{1}{T}\sum_{k=0}^{N-1} \left[\langle u_i \rangle_{\varepsilon_{\min}+k\Delta\sigma,\Delta\sigma} - \bar{u}_i\right]\left[\langle u_j \rangle_{\varepsilon_{\min}+k\Delta\sigma,\Delta\sigma} - \bar{u}_j\right]\mathcal{N}(\mathcal{A}_{\varepsilon_{\min}+k\Delta\sigma,\Delta\sigma}), \tag{6.7}$$

where $N = (\varepsilon_{\max} - \varepsilon_{\min})/\Delta\sigma$ with $\varepsilon_{\max} = \max(\varepsilon(t))$, $\varepsilon_{\min} = \min(\varepsilon(t))$, $t \in [0, T]$.

Figure 6.29 compares the distribution of the kinetic energy associated with the phase fluctuations alone with the kinectic energy associated with all fluctuations. In the narrow-span case, the contribution of the phase fluctuations to the total energy represents about 30% whereas in the large-span case, where the low-frequency motions were found to be less energetic (see earlier section), the contribution of the phase fluctuation is less than 10%. In both cases, the contribution of the phase fluctuations is restricted around the mean reflected-shock position and in the vicinity of the first section of the mixing layer, as one would expect.

Similarly to figure 6.29, the shear stress is provided in figure 6.30, where the contribution of the phase fluctuations is of the order of 50% and 25% in the narrow-span and large-span cases, respectively. As for the kinetic energy, the significance of the phase fluctuations in the total shear stress is restricted to the reflected-shock region and the first section of the mixing layer. Of particular interest is the change of sign: the shear stress near the shock is negative for the total field whereas it is positive for the phase fluctuations. The positive contribution of the phase fluctuations is expected if one considers an oblique shock moving about a fixed point, due to shock-jump relations.

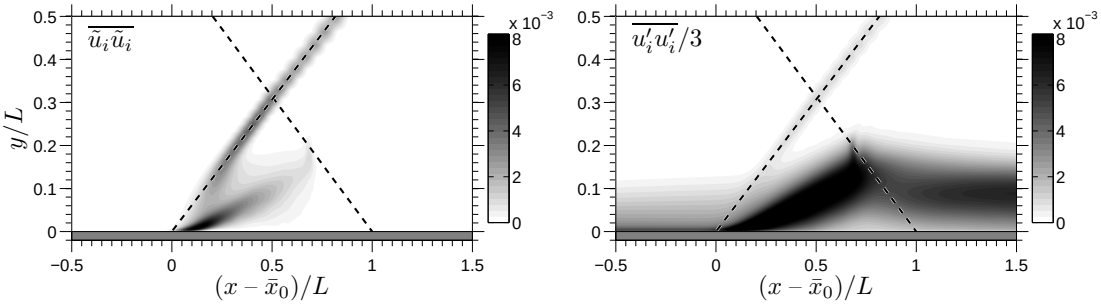

(a) narrow-span case (note the factor 1/3 on the right figure)

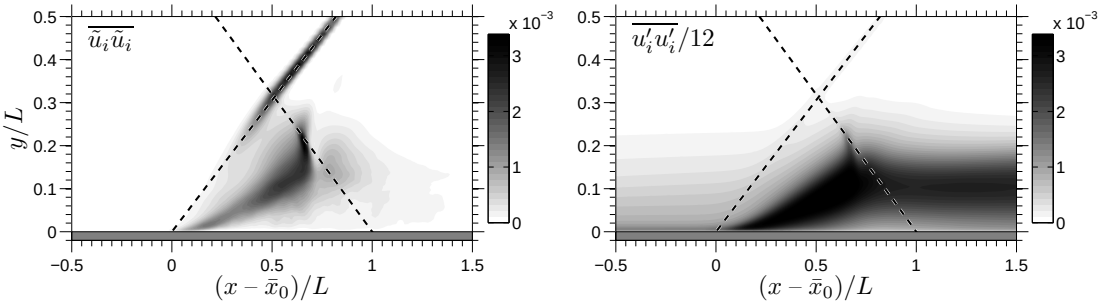

(b) large-span case (note the factor 1/12 on the right figure)

FIGURE 6.29: Kinetic-energy fields from all fluctuations (*right*) and from the phase fluctuations only (*left*)

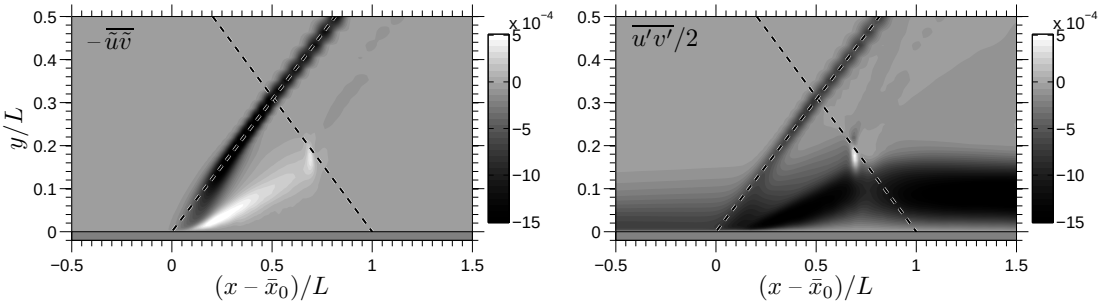

(a) narrow-span case (note the minus sign on the left and the factor 1/2 on the right figure)

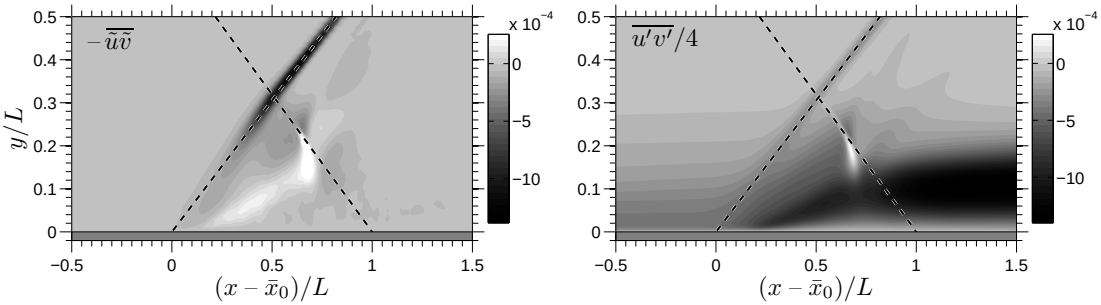

(b) large-span case (note the minus sign on the left and the factor 1/4 on the right figure)

FIGURE 6.30: Shear-stress fields from all fluctuations (*right*) and from the phase fluctuations only (*left*)

6.4 Summary

In summary, this chapter first established the ability of LES to properly reproduce the observed low-frequency shock motions. It is therefore assumed that the simulations capture the underlying key mechanisms at the origin of the low-frequency shock motions. Moreover, the good agreement with the wall-pressure experimental spectra suggests that the observed motions are unlikely to be solely caused by experimental artifacts. The region under the reflected shock exhibits the most significant low-frequency fluctuations. These are found to be broadband and to cover at least one decade of frequencies (around $St = 0.03$) about two orders of magnitude below the turbulence-related fluctuations. The choice of L and $\bar{u}_1$ for the definition of the Strouhal number appears justified in the light of the three flow cases considered in this chapter. The wall-pressure fluctuations attributed to the low frequency shock motions and to the turbulence are both significantly contributing to the signal variance, making the distinction between the two difficult. In all cases considered the most energetic low-frequency wall-pressure fluctuations were localised in the first part of the interaction whereas the energy was more evenly distributed between the low frequencies and the higher turbulence-related frequencies in the second section.

The dispersion relation of the wall-pressure fluctuations was characterised by organised convective structures such as shear-layer vortical structures and acoustic-wave propagation on top of more broadband dispersions which are characteristic of the turbulence. Upstream convecting pressure waves could be detected in the first third of the interaction with wavelengths exceeding the interaction length. Of particular interest was the phase evolution of such low-frequency pressure waves where a phase jump about one third down the interaction region could be detected, potentially indicating the source point of these waves. Following Hudy et al. (2003), the observed phase structure may be related to a global mode such as the one described in chapter 5.

Although the mean separation bubbles of the flow cases considered in this chapter were shallow (with heights not exceeding the beginning of the log-law region), the probability of encountering locally reversed flow could still be around 10% at $y/\delta_0 \sim 1/3$. One main challenge in performing time-resolved simulations of SBLI is the significant dynamical range required to resolve both the turbulence and the broadband low-frequency. One direct consequence is that achieving well-converged spectra for the low frequencies is still prohibitive in terms of computational cost. The short-signal effects were considered in this chapter and it was shown that at least an order of fifty low-frequency cycles are needed to achieve acceptable levels of convergence. An additional constraint is the choice of computational spanwise extent which can affect both the time-averaged flow fields (see chapter 4) and the amplitude of the low-frequency dynamics. It was argued that the computational domain should at least be wider than the interaction length itself, greatly

adding to the computational cost of resolving the low-frequency motions.

In cases where the computational domain was sufficiently wide, cells of reversed flow with preferential dimensions could form. These cells were found to be capable of persisting for more than $10^2\delta_0/\bar{u}_1$ with spanwise extents of the order of the interaction length. They were seen to meander in the spanwise direction which can occasionally lead to the merging of two cells. The presence of such structures and their spanwise motions has direct consequences on the interpretation of fixed-point wall-pressure spectra, for example where the low-frequency end of the spectrum can be artificially underestimated while the high-frequency end is artificially enhanced. This can account for some but not all the differences between the large- and wide-span wall-pressure spectra.

This chapter was also concerned with the choice of the digital-filter approach described in chapter 2 to generate the inflow turbulence. It was shown that this approach could prevent long coherent structures from developing at the inflow plane. Consequently, the length of the coherent structures approaching the interaction region was mainly governed by the computational extent available upstream of interaction. In the present work this was set to be about $10\delta_0$. The main idea behind such a choice was to prevent long coherent structures such those described in Ganapathisubramani et al. (2007b) from interfering with the interaction. The present chapter provides evidence of a flow deprived of upstream long coherent structures, but still exhibiting low-frequency shock motions. This leads us to suggest that although long-coherent upstream structures are likely to enhance the low-frequency shock motions they are not necessary to the existence of the aforementioned shock motions.

Finally, the motions of the reflected shock were extracted from the simulation data. It was shown that the observed transverse waves along the shock have two main origins: direct perturbations by the upstream acoustic field and reflections in the form of transverse waves by the acoustic field from the bottom side of the shock, impinging at the critical angle studied in Robinet and Casalis (2001). Moreover, the spectral analysis of the shock motions confirmed that the oblique shock acts like a low-pass filter with the oscillations at the lowest frequencies propagating along the shock more easily than at the highest frequencies. Based on the shock-foot displacement, conditionally-averaged fields could be computed and phase-averaged flow fields could be defined. These phase averages were used to estimate the kinetic energy of the low-frequency motions. In the case of the narrow-span LES of the IUSTI case, we found that the low-frequency motions could account for up to 30% of the total energy of the fluctuations, which is in agreement with the findings from the wall-pressure data analysis.

Guided by the aforementioned LES data, the following chapter will propose an analytic approach to the problem of the reflected-shock low-frequency motions. As we shall see, the derivations will lead to a stochastic ordinary differential equation which will then be discussed in light of the presented numerical and experimental observations.

7. Low-order stochastic model

The variety of mechanisms proposed in the literature as being potentially responsible for the low-frequency shock motions, together with the subsequent debate about the merits of one approach relative to another is symptomatic of the difficulty one has in identifying and then separating individual events from a (supposedly) non-linear (chaotic) system, where actual causal events may well be impossible to detect. Instead of attempting to check the relevance of one assumed mechanism against numerical/experimental data with the inherent complexity of extracting this from fully turbulent flow, it could be more useful to identify the properties of the dynamical system arising from the coupling between the shock and the boundary layer. To some extent, this is the approach followed by Plotkin (1975), who postulated that the shock displacement was obeying a first-order stochastic Ordinary Differential Equation (ODE) with an associated characteristic timescale. Plotkin shows that such a mathematical model is capable of reproducing the wall-pressure low-frequency spectrum. This interesting point has been verified in two subsequent papers by Poggie and Smits (2001, 2005). Two main reasons why Plotkin's model has not been widely adopted are: (i) it is a postulate and therefore lacks a physical basis for its ability to reproduce experimental wall-pressure spectra; (ii) it is impractical since the key parameter, the characteristic timescale of the ODE, needs to be determined *a posteriori* from existing data.

Nevertheless, it is intriguing that a relatively simple ODE is capable of reproducing the low-frequency spectra. The mathematical implications of this observation have been considered only at a superficial level. For example, one can read that Plotkin's model is a mathematical explanation of how relatively broadband perturbations, caused by the incoming turbulence, can lead to relatively low-frequency motions; or that it assumes that the restoring mechanism ensuring the shock stability is linear. But there are more subtle implications. First, the analytical expression given by Plotkin for the spectrum is based on the response to white noise, meaning that the model does not assume as an input a turbulent signal but instead one which is equally composed of high and low frequencies. Second, while it is true that the postulated governing equation is linear, it is possible that the time constant associated with the restoring mechanism already incorporates non-linear interactions between a velocity fluctuation and the coupled shock/boundary-layer system. This latter point is clearly indicated by Poggie and Smits (2001).

This chapter aims at deriving an equation describing the shock low-frequency motions, in the spirit of Plotkin's pioneering work, but from a completely different approach. The same case of a shock-impingement configuration as described in the previous chapters is chosen but this work could be extended to compression-ramp flows in the future. A combined LES/analytical approach is used, where the LES results are extensively employed to support and guide each step of the derivations. The chapter is organised as follows. The first section presents the derivations of the shock-foot dynamical equation, the constituents of which are then modelled in the subsequent section. The closed form of the model is then summarised and its solutions to particular forcing examined. Finally, the last section discusses the low-frequency shock motions in the light of the model.

7.1 Derivation of model equations

7.1.1 Initial form of the momentum integral equation

To derive the model, the streamwise component of the unsteady momentum equation is first integrated in the wall-normal direction. After some algebraic manipulations (provided in appendix F), one can obtain the following exact form of the momentum integral equation:

$$\begin{aligned}\rho_h\left(h-\delta_1\right)\left[\frac{\partial u_h}{\partial t}+u_h\frac{\partial u_h}{\partial x}\right]+u_h\frac{\partial}{\partial t}\left[\rho_h(\delta_\rho-\delta_1)\right]-\frac{\partial}{\partial x}\left[\rho_h u_h^2\delta_2\right]+\frac{\partial}{\partial z}\left[\int_0^h\rho uw\,\mathrm{d}y\right]\\ -u_h\frac{\partial}{\partial z}\left[\int_0^h\rho w\,\mathrm{d}y\right]=\frac{\partial}{\partial x}\left[p_h\left(\delta_p-h\right)\right]+\frac{\mu_h}{\mathrm{Re}}\left[\left.\frac{\partial v}{\partial x}\right|_{y=h}+\left.\frac{\partial u}{\partial y}\right|_{y=h}\right]-\frac{1}{2}C_f\rho_h u_h^2\\ +\frac{1}{\mathrm{Re}}\frac{\partial}{\partial x}\left[\int_0^h\tau_{xx}\,\mathrm{d}y\right]+\frac{1}{\mathrm{Re}}\left(\frac{\partial}{\partial z}\left[\int_0^h\tau_{xz}\,\mathrm{d}y\right]-\left.\tau_{xz}\right|_{y=h}\frac{\partial h}{\partial z}\right),\end{aligned}\tag{7.1}$$

where the following thicknesses are defined (displacement, momentum, pressure and density thicknesses, respectively):

$$\delta_1 = \int_0^h\left(1-\frac{\rho u}{\rho_h u_h}\right)\mathrm{d}y,\tag{7.2a}$$

$$\delta_2 = \int_0^h\frac{\rho u}{\rho_h u_h}\left(1-\frac{u}{u_h}\right)\mathrm{d}y,\tag{7.2b}$$

$$\delta_p = \int_0^h\left(1-\frac{p}{p_h}\right)\mathrm{d}y,\tag{7.2c}$$

$$\delta_\rho = \int_0^h\left(1-\frac{\rho}{\rho_h}\right)\mathrm{d}y,\tag{7.2d}$$

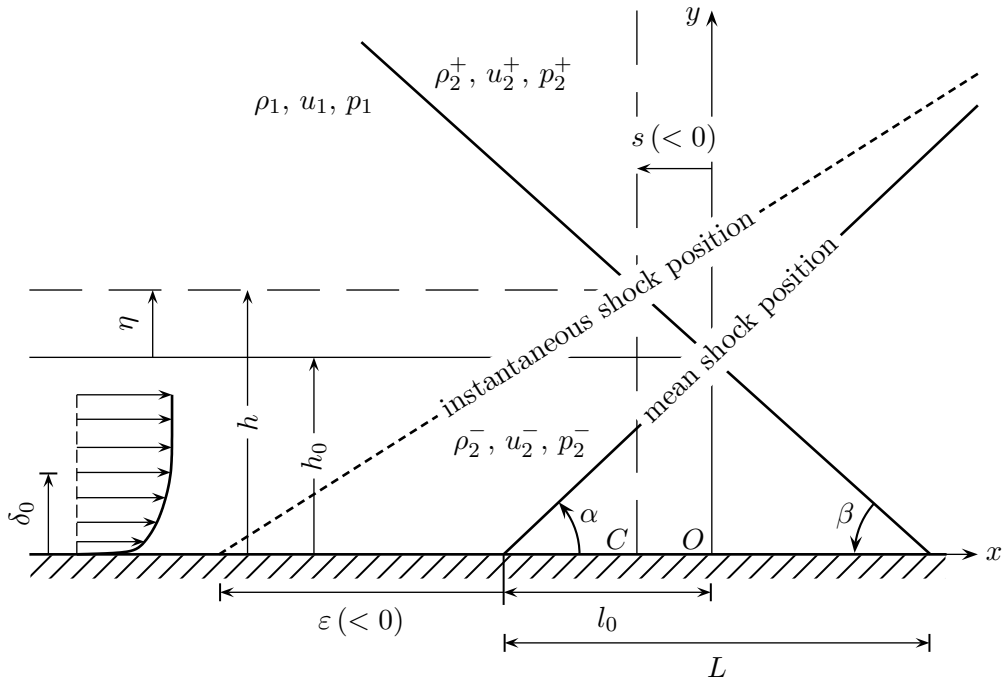

FIGURE 7.1: Sketch of the interaction with the definition of the notations in use

and:

$$C_f = \frac{2\mu_w}{\rho_h u_h^2 \mathrm{Re}} \left.\frac{\partial u}{\partial y}\right|_w , \tag{7.3}$$

where the subscripts h and w denote that variables are evaluated at $y = h$ and at the wall, respectively.

7.1.2 Change of variable

It is convenient to introduce a new coordinate system by moving the origin of the streamwise x axis to the instantaneous shock-foot position and then normalising with the distance covered from the instantaneous shock-foot to the instantaneous shock-crossing point (denoted C in figure 7.1). Note that l_0 is the absolute distance between the mean shock-foot position and the mean streamwise cross-point position whereas x, s and ε can be either positive or negative distances. With the upstream movement of the shock foot sketched in figure 7.1, s and ε are negative. The distance from the origin of the axis system O to the instantaneous shock-foot location is $l_0 - \varepsilon$ and the distance separating the instantaneous shock foot from the instantaneous crossing point is $l_0 - \varepsilon + s$. Therefore, the new coordinate system, denoted ξ, is:

$$\xi \equiv \frac{x + l_0 - \varepsilon}{l_0 - \varepsilon + s} \text{ or equivalently, } x \equiv (l_0 - \varepsilon)(\xi - 1) + s\xi. \tag{7.4}$$

Hence, in the following sections, $\xi = 0$ will be the instantaneous shock-foot position, ε the shock-foot displacement with respect to its mean position and $\xi = 1$ the instantaneous location of the shock crossing.

Because of the integration in the wall-normal directions, the terms in (7.1) are only functions of x, z and t. This can be expressed in a generic way by writing that the terms in (7.1) are of the type $f(x, z, t)$. Equation (7.4) will transform $f(x, z, t)$ into $f(\xi(z, t))$. From the chain rule:

$$\frac{\partial f}{\partial t} = \frac{\partial f}{\partial \xi}\frac{\partial \xi}{\partial t}, \tag{7.5a}$$

$$\frac{\partial f}{\partial x} = \frac{\partial f}{\partial \xi}\frac{\partial \xi}{\partial x}, \tag{7.5b}$$

$$\frac{\partial f}{\partial z} = \frac{\partial f}{\partial \xi}\frac{\partial \xi}{\partial z}. \tag{7.5c}$$

From (7.4), it is straightforward to compute the following derivatives:

$$\frac{\partial \xi}{\partial t} = \frac{1}{l_0 - \varepsilon + s}\left[(\xi - 1)\frac{\partial \varepsilon}{\partial t} - \xi\frac{\partial s}{\partial t}\right], \tag{7.6a}$$

$$\frac{\partial \xi}{\partial x} = \frac{1}{l_0 - \varepsilon + s}, \tag{7.6b}$$

$$\frac{\partial \xi}{\partial z} = \frac{1}{l_0 - \varepsilon + s}\left[(\xi - 1)\frac{\partial \varepsilon}{\partial z} - \xi\frac{\partial s}{\partial z}\right]. \tag{7.6c}$$

Using (7.5 *a–c*) and (7.6 *a–c*), one can express (7.1) in the new coordinate system:

$$\begin{aligned}
&\frac{\rho_h\,(h-\delta_1)}{l_0-\varepsilon+s}\left[(\xi-1)\,\frac{\partial\varepsilon}{\partial t} - \xi\frac{\partial s}{\partial t} + u_h\right]\frac{\partial u_h}{\partial \xi} \\
&\qquad + \frac{1}{l_0-\varepsilon+s}\left[u_h\left((\xi-1)\,\frac{\partial\varepsilon}{\partial t} - \xi\frac{\partial s}{\partial t}\right)\frac{\partial}{\partial\xi}\left[\rho_h(\delta_\rho-\delta_1)\right] - \frac{\partial}{\partial\xi}\left[\rho_h u_h^2\delta_2\right]\right] \\
&\qquad + \frac{1}{l_0-\varepsilon+s}\left[(\xi-1)\,\frac{\partial\varepsilon}{\partial z} - \xi\frac{\partial s}{\partial z}\right]\left\{\frac{\partial}{\partial\xi}\left[\int_0^h \rho u w\,\mathrm{d}y\right] - u_h\frac{\partial}{\partial\xi}\left[\int_0^h \rho w\,\mathrm{d}y\right]\right\} \\
&= \frac{1}{l_0-\varepsilon+s}\frac{\partial}{\partial\xi}\left[p_h\,(\delta_p - h)\right] + \frac{\mu_h}{\mathrm{Re}}\left[\frac{1}{l_0-\varepsilon+s}\,\frac{\partial v}{\partial\xi}\bigg|_{y=h} + \frac{\partial u}{\partial y}\bigg|_{y=h}\right] - \frac{1}{2}C_f\rho_h u_h^2 \\
&\qquad\qquad + \frac{1}{\mathrm{Re}}\frac{1}{l_0-\varepsilon+s}\frac{\partial}{\partial\xi}\left[\int_0^h \tau_{xx}\,\mathrm{d}y\right] \\
&\qquad + \frac{1}{\mathrm{Re}}\frac{1}{l_0-\varepsilon+s}\left[(\xi-1)\,\frac{\partial\varepsilon}{\partial z} - \xi\frac{\partial s}{\partial z}\right]\left\{\frac{\partial}{\partial\xi}\left[\int_0^h \tau_{xz}\,\mathrm{d}y\right] - \tau_{xz}|_{y=h}\,\frac{\partial h}{\partial\xi}\right\}.
\end{aligned} \tag{7.7}$$

The form of (7.7) will prove to be convenient in deriving an approximate form of the momentum integral equation for the shock-reflection problem.

7.1.3 Approximate form of the momentum integral equation

In principle, if one could find all the appropriate necessary closure terms, (7.7) would be used to resolve the shock dynamics. However, in its current state, (7.7) is unpractical and one needs to make further assumptions in order to simply it. Some reasonable assumptions are:

1. the study shall be restricted to $\xi < 1$
2. the potential flow is assumed constant (e.g. the acoustic field is neglected) so that u_1, ρ_1, and p_1 are true constants ($\rho_1 = \bar{\rho}_1$, $u_1 = \bar{u}_1$, $p_1 = \bar{p}_1$)
3. the top boundary (delimited by h in figure 7.1) is assumed to be always inside the potential flow, i.e. $h > \delta_0$ at all times
4. the shock system is considered two-dimensional (i.e. spanwise variations are not considered) so that $h = h(t)$, $s = s(t)$, $\varepsilon = \varepsilon(t)$ (three-dimensional effects could be considered in a future study)

With the above assumptions, the subscripts h can be replaced by 1 (e.g. $u_h = u_1$) since h is inside the potential flow (assumption 3) and the study restricted to the section upstream of the shock-crossing point (assumption 1). Furthermore, for a constant potential flow (assumption 2), one can write $\partial u_h/\partial\xi = \partial u_1/\partial\xi = 0$. For similar reasons, multiplicative terms like ρ_h, u_h or p_h can be pulled out of derivatives. The 2D assumption (assumption 4) is used to zero out terms with $\partial/\partial z$. Finally, the shear-stress term $\tau_{xz}|_{y=h}$ vanishes under assumptions 2 and 3. Implementing the above simplifications to (7.7) eventually leads to the following approximate form of the momentum integral equation (MIE):

$$\underbrace{\frac{1}{u_1 l_0}\left[(1-\xi)\frac{\mathrm{d}\varepsilon}{\mathrm{d}t} + \xi\frac{\mathrm{d}s}{\mathrm{d}t}\right]\frac{\partial}{\partial\xi}\left[\delta_\rho - \delta_1\right]}_{\text{(i)}} + \underbrace{\frac{1}{l_0}\frac{\partial\delta_2}{\partial\xi}}_{\text{(ii)}} + \underbrace{\frac{p_1}{\rho_1 u_1^2 l_0}\frac{\partial\delta_p}{\partial\xi}}_{\text{(iii)}}$$
$$= \underbrace{\frac{1}{2}\left(1 - \frac{\varepsilon}{l_0} + \frac{s}{l_0}\right)C_f}_{\text{(iv)}} - \underbrace{\frac{1}{\rho_1 u_1^2 l_0 \mathrm{Re}}\frac{\partial}{\partial\xi}\left[\int_0^h \tau_{xx}\mathrm{d}y\right]}_{\text{(v)}}. \quad (7.8)$$

In a canonical boundary layer, term (v) would be neglected and it is worth checking if this would also hold for the current SBLI configuration. Each term in (7.8) is therefore evaluated using the LES data and the magnitudes are shown in figure 7.2(a). It can be seen that upstream of interaction, (v) is $\mathcal{O}(10^{-7})$ whereas all the other terms are greater than $\mathcal{O}(10^{-5})$, justifying the common assumption made in canonical boundary

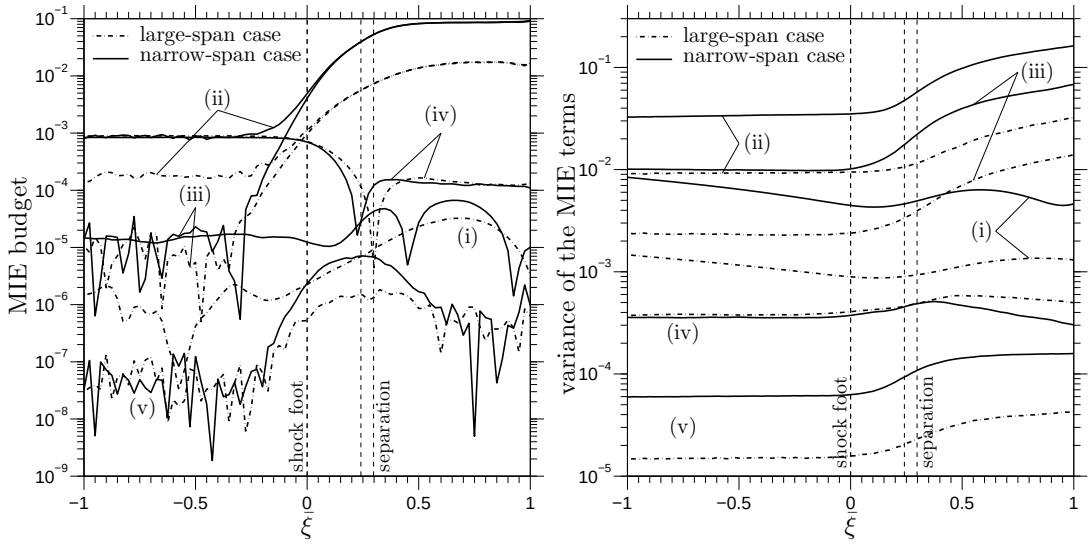

(a) magnitude of the MIE terms (b) variance of the MIE terms

FIGURE 7.2: Evaluation of the contribution from each term in (7.8) to the time-averaged balance (a) and their relative importance to the energy of the fluctuations (b). Note that most of the data smaller than $\mathcal{O}(10^{-5})$ are subject to noise

layers. Upon entering the interaction region, the amplitude of (v) rises, as one would expect, to reach a maximum (for the region considered here) near separation. However, it may be argued that this maximum remains small compared to the other terms, with the exception of the skin-friction term (iv) right at separation, where it is strictly zero. Because the analysis of the time-averaged data is not sufficient to judge the relevance of (v) in the unsteady context, the relative importance of the variance of each terms in (7.8) is also considered in figure 7.2(b). It is found that term (v) only makes a marginal contribution to the energy of the fluctuations and it appears justified, as a leading-order approximation, to neglect (v) from (7.8) and use the following approximate form of the momentum integral equation as the starting point for the shock-motion model:

$$\underbrace{\frac{1}{u_1 l_0}\left[(1-\xi)\frac{\mathrm{d}\varepsilon}{\mathrm{d}t}+\xi\frac{\mathrm{d}s}{\mathrm{d}t}\right]\frac{\partial}{\partial\xi}\left[\delta_\rho-\delta_1\right]}_{\text{(i)}}+\underbrace{\frac{1}{l_0}\frac{\partial\delta_2}{\partial\xi}}_{\text{(ii)}}+\underbrace{\frac{p_1}{\rho_1 u_1^2 l_0}\frac{\partial\delta_p}{\partial\xi}}_{\text{(iii)}}\approx\underbrace{\frac{1}{2}\left(1-\frac{\varepsilon}{l_0}+\frac{s}{l_0}\right)C_f}_{\text{(iv)}}. \tag{7.9}$$

In figure 7.2(a), it is also interesting to note that on average within the interaction, there is an approximate balance between the rate of changes of momentum and pressure thicknesses (terms (ii) and (iii)). At leading order, those two terms control the interaction length by setting the necessary equilibrium between the adverse pressure gradient and the rate of change of momentum thickness. We shall come back to this point later.

7.1.4 Hypothesis of the existence of a similarity solution

Equation (7.9) is not yet in a closed form but some interesting features are already emerging. The final dynamical equation which is sought is the governing equation for ε and, looking at (7.9), some terms in ε can already be identified amongst terms involving the streamwise evolutions of the various thicknesses. One common approach to transform a partial differential equation into an ordinary one is to seek similarity solutions. In this particular case, one can attempt to map terms in $\partial/\partial\xi$ into a family of functions playing the role of coefficients in the final governing equation for the shock motions. Such families can indeed arise if the following hypothesis is invoked.

Hypothesis 7.1. *There exists a similarity function (F) that describes the streamwise evolution of the various boundary-layer thicknesses independent of the time variable, i.e.*

$$\begin{cases} F(\xi) \equiv \dfrac{\delta_i(\xi) - \delta_i(\xi = 0)}{\Delta_i}, \\ \Delta_i(t) \equiv \delta_i(\xi = 1) - \delta_i(\xi = 0), \end{cases} \tag{7.10}$$

where the subscript i is any of the following: 1, 2, ρ, p.

Mathematically, hypothesis 7.1 corresponds to the supposed existence of a separation of variables. From (7.10):

$$\delta_i(\xi) = F(\xi)\Delta_i(t) + \delta_i(\xi = 0), \ \frac{\partial \delta_i}{\partial \xi} = \frac{\mathrm{d}F}{\mathrm{d}\xi}\Delta_i \equiv F'\Delta_i, \tag{7.11}$$

so that the MIE becomes:

$$\frac{1}{u_1 l_0}\left[(1-\xi)\frac{\mathrm{d}\varepsilon}{\mathrm{d}t} + \xi\frac{\mathrm{d}s}{\mathrm{d}t}\right]\left(F'\Delta_\rho - F'\Delta_1\right) + \frac{1}{l_0}F'\Delta_2 + \frac{p_1}{\rho_1 u_1^2 l_0}F'\Delta_p = \frac{1}{2}\left(1 - \frac{\varepsilon}{l_0} + \frac{s}{l_0}\right)C_f. \tag{7.12}$$

The validity of hypothesis 7.1 can be tested using conditionally-averaged LES data, as shown in figure 7.3. In subfigure (a), the δ_i functions are shown from the stationary axis $\bar{\xi}$. The same functions are then plotted in the moving coordinate system ξ (see subfigure (b)), making the local extrema in the δ_i distributions centred at $\xi = 1$. Finally, the δ_i functions are shifted by $\delta_i(\xi = 0)$ and normalised by their respective amplitudes Δ_i to give the F functions shown in subfigure (c). It is argued that the thirty curves represented in subfigure (c) collapse reasonably well onto the hypothesised universal function F. However, evaluating the thicknesses from the LES fields, and in particular at the shock-crossing point streamwise station $\xi = 1$, is difficult due to the shock-smearing and grid-stretching effects, reducing the accuracy of these quantities at this particular station. The plots in figure 7.3 should thus be regarded as indicative only.

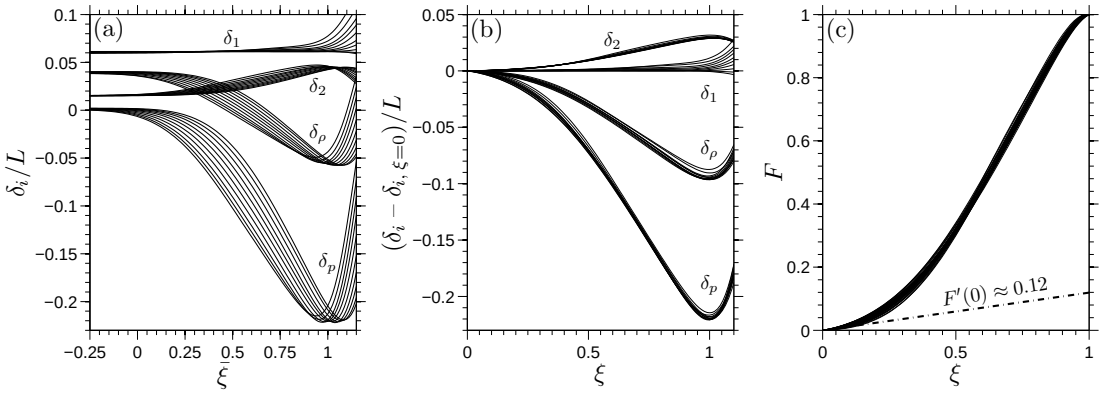

FIGURE 7.3: Validity of hypothesis 7.1 from the conditionally-averaged LES data, see text for details

Furthermore, one can see in figure 7.3 that the time-averaged displacement thickness does not increase much between $\xi = 0$ and $\xi = 1$, compared to the other thicknesses, making the division by Δ_1 in (7.10) sensitive to numerical errors. Therefore, the case of the δ_1 distributions was not included in subfigure (c).

Despite the issues outlined above, the LES data provide good support for hypothesis 7.1. Looking at (7.12), one also needs to consider the Δ_i functions and these quantities are also difficult to obtain numerically. Nevertheless, figure 7.4(a) gives an idea of how the Δ_i functions depend on the shock-system position. The numerical results suggest that, as a first approximation, the overall changes of the different thicknesses considered here may be approximated by the mean value plus a linear dependence on η, defined as the shock-crossing point wall-normal displacement (see figure 7.1):

$$\Delta_i = \Theta_i + \kappa_i \, \eta(t). \tag{7.13}$$

The above approximation will be further discussed in section 7.2. Next, it is easily seen from geometrical considerations (see figure 7.1) that:

$$\eta(t) = -s(t) \tan \beta. \tag{7.14}$$

From equations (7.12) and (7.14), it is clear that a relationship between the shock-foot displacement ε and the shock-crossing-point streamwise displacement s is needed. This relation is reported in figure 7.4(b) using the LES data sets. Again, a linear relation seems appropriate and reflects the earlier impressions on the conditionally-averaged data in figure 6.28:

$$s(t) = k \, \varepsilon(t). \tag{7.15}$$

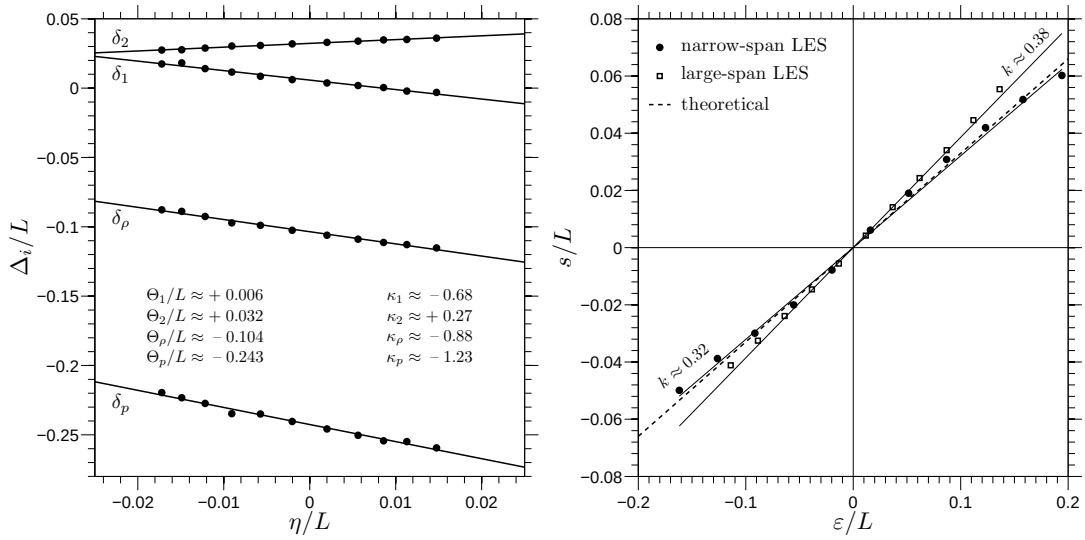

(a) dependency of Δ_i on η (b) Shock-foot/shock-crossing-point relation

FIGURE 7.4: Thicknesses-amplification dependency on the shock-system position (a) and relationship between the shock-foot motions and the shock-cross point motions (b). The theoretical line in (b) will be described in section 7.2

The rationale behind (7.15) will be further discussed in section 7.2 and the theoretical line in figure 7.4(b) will be explained.

Using (7.13), (7.14) and (7.15) in (7.12), one can write:

$$\begin{aligned}\frac{1}{u_1}\underbrace{k\tan\beta\,(\kappa_1-\kappa_\rho)\,F'(\xi)\,[1+\xi\,(k-1)]}_{c_1(\xi)}\frac{\mathrm{d}\varepsilon}{\mathrm{d}t}\varepsilon+\frac{L}{u_1}\underbrace{\left(\frac{\Theta_\rho}{L}-\frac{\Theta_1}{L}\right)F'(\xi)\,[1+\xi\,(k-1)]}_{c_2(\xi)}\frac{\mathrm{d}\varepsilon}{\mathrm{d}t}\\ +\underbrace{\left[\frac{1}{2}C_f\,(1-k)-k\tan\beta\left(\kappa_2+\frac{p_1}{\rho_1 u_1^2}\kappa_p\right)F'(\xi)\right]}_{c_3(\xi)}\varepsilon\\ =\underbrace{L\left(\frac{1}{2}\frac{l_0}{L}C_f-\frac{\Theta_2}{L}F'(\xi)-\frac{p_1}{\rho_1 u_1^2}\frac{\Theta_p}{L}F'(\xi)\right)}_{c_4(\xi)}.\end{aligned}\tag{7.16}$$

If one introduces the following non-dimensional variables:

$$\begin{cases}\zeta\equiv\varepsilon/L,\\ t^\star\equiv tu_1/L,\\ \dot{\zeta}\equiv\mathrm{d}\zeta/\mathrm{d}t^\star,\end{cases}\tag{7.17}$$

equation (7.16) becomes:

$$(c_1\zeta+c_2)\,\dot{\zeta}+c_3\zeta=c_4.\tag{7.18}$$

Equation (7.18) constitutes the governing equation for the unforced reflected-shock-foot motions, where the coefficients c_1 to c_4 are defined in (7.16) and are functions of the choice of ξ station. Since the location of interest in this study is the shock foot, the coefficients should be evaluated at $\xi = 0$. Allowing for $F'(0)$ being non-zero (figure 7.3), one can write:

$$k \tan\beta \left(\kappa_1 - \kappa_\rho\right) \zeta\dot{\zeta} + \left(\frac{\Theta_\rho}{L} - \frac{\Theta_1}{L}\right)\dot{\zeta} + \left[\frac{C_f(0)}{2F'(0)}\left(1-k\right) - k\tan\beta\left(\kappa_2 + \frac{p_1}{\rho_1 u_1^2}\kappa_p\right)\right]\zeta = \frac{l_0 C_f(0)}{2LF'(0)} - \frac{\Theta_2}{L} - \frac{p_1}{\rho_1 u_1^2}\frac{\Theta_p}{L}. \quad (7.19)$$

Equation (7.19) is a first-order non-linear ordinary differential equation representing the shock-foot motions in the presence of the forcing term $C_f(\xi = 0)$[1]. For particular cases the constants could be computed from the LES, but for more general applications we need to model them. Prior to discussing some tentative modelling efforts, it is of interest to use the LES data to perform a leading-order analysis.

7.1.5 Leading-order equations

To further simplify the equation for the shock-foot motions, it is convenient to apply the triple decomposition approach introduced earlier (see (6.4a)) to decompose the skin-friction time-series at the shock foot:

$$C_f(\xi = 0) = \bar{C}_{f_0} + \tilde{C}_{f_0}(t_s) + C''_{f_0}(t_f). \quad (7.20)$$

Terms $\tilde{C}_{f_0}$ and C''_{f_0} correspond to the skin-friction fluctuations at the shock foot associated with the low-frequency motions and the high-frequency fluctuations due to the turbulence, respectively. From the LES time series, it is found that both $\tilde{C}_{f_0}$ and C''_{f_0} contribute to the skin-friction fluctuations and therefore one cannot neglect C''_{f_0} in (7.20). Furthermore, using the LES conditional averages and invoking corollary 6.1, it is possible to evaluate the correlation between $\bar{C}_{f_0} + \tilde{C}_{f_0}$ and the shock displacement ζ, as shown in figure 7.5. Although there is some departure at larger ε, it is argued that, as a first approximation, the variations in $\tilde{C}_{f_0}$ are linearly correlated with the shock-foot displacement:

$$\tilde{C}_{f_0} \approx \Lambda\zeta, \quad (7.21)$$

[1]Note that separation occurs for $\xi > 0$ (figure 7.2(a)) so that $C_f(\xi = 0) > 0$.

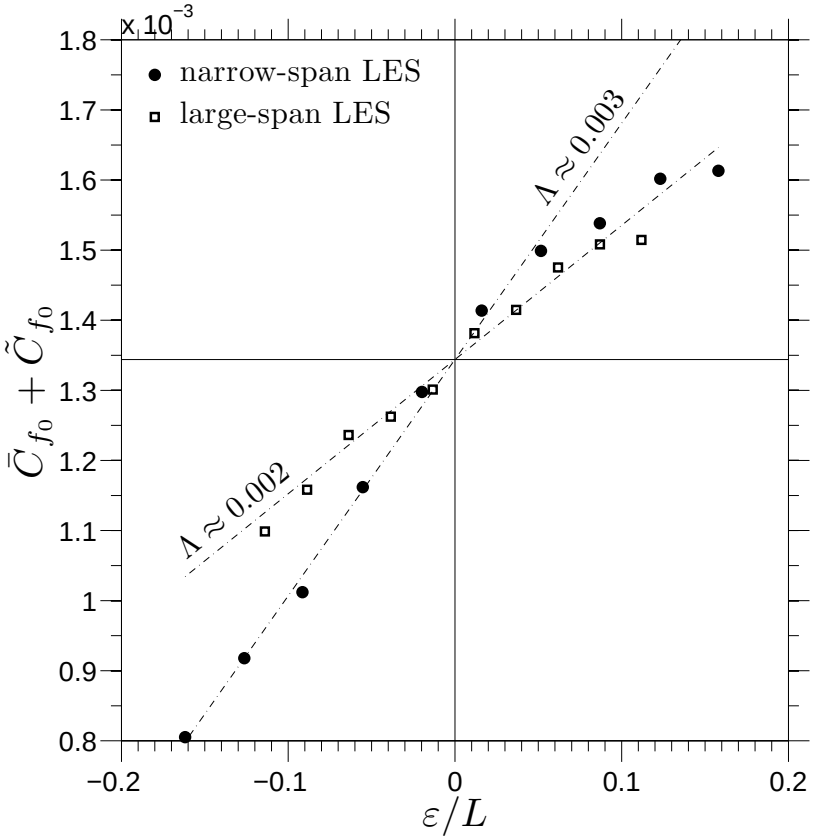

FIGURE 7.5: Relationship between $\bar{C}_{f_0} + \tilde{C}_{f_0}$ and $\zeta = \varepsilon/L$

with Λ in the range 2×10^{-3} to 3×10^{-3} for the case considered. Using (7.20) and (7.21) in (7.19) gives:

$$k \tan\beta \left(\kappa_1 - \kappa_\rho\right) \zeta\dot{\zeta} + \left(\frac{\Theta_\rho}{L} - \frac{\Theta_1}{L}\right)\dot{\zeta} + \left[\frac{1-k}{2F'(0)}\left(\bar{C}_{f_0} + \Lambda\zeta + C''_{f_0}\right) - k\tan\beta\left(\kappa_2 + \frac{p_1}{\rho_1 u_1^2}\kappa_p\right)\right]\zeta = \frac{l_0}{2LF'(0)}\left(\bar{C}_{f_0} + \Lambda\zeta + C''_{f_0}\right) - \frac{\Theta_2}{L} - \frac{p_1}{\rho_1 u_1^2}\frac{\Theta_p}{L}. \quad (7.22)$$

Each term in (7.22) can now be quantified. This is performed in the case of an upstream Mach number $\mathrm{M}_1 = 2.3$ and a wedge angle θ set to 8°, which gives $\alpha \approx 29°$ and $\beta \approx 32°$ from inviscid theory. The orders of magnitude of all the constituents in (7.22) are provided in table 7.1 and the governing equation is:

$$\underbrace{k\tan\beta}_{\mathcal{O}(10^{-1})}\left(\underbrace{\kappa_1}_{\mathcal{O}(1)}-\underbrace{\kappa_\rho}_{\mathcal{O}(1)}\right)\underbrace{\zeta\dot{\zeta}}_{\mathcal{O}(10^{-4})}+\left(\underbrace{\left[\frac{\Theta_\rho}{L}\right]}_{\mathcal{O}(10^{-1})}-\underbrace{\left[\frac{\Theta_1}{L}\right]}_{\mathcal{O}(10^{-2})}\right)\underbrace{\dot{\zeta}}_{\mathcal{O}(10^{-3})}$$
$$+\left[\left(\underbrace{\bar{C}_{f_0}}_{\mathcal{O}(10^{-3})}+\underbrace{\Lambda\zeta}_{\mathcal{O}(10^{-4})}+\underbrace{C'_{f_0}}_{\mathcal{O}(10^{-4})}\right)\underbrace{\left[\frac{1-k}{2F'(0)}\right]}_{\mathcal{O}(1)}\right.$$
$$\left.-\underbrace{k\tan\beta}_{\mathcal{O}(10^{-1})}\left(\underbrace{\kappa_2}_{\mathcal{O}(10^{-1})}+\underbrace{\left[\frac{p_1}{\rho_1u_1^2}\kappa_p\right]}_{\mathcal{O}(10^{-1})}\right)\right]\underbrace{\zeta}_{\mathcal{O}(10^{-1})}$$
$$=\underbrace{\left[\frac{l_0}{2LF'(0)}\right]}_{\mathcal{O}(1)}\left(\underbrace{\bar{C}_{f_0}}_{\mathcal{O}(10^{-3})}+\underbrace{\Lambda\zeta}_{\mathcal{O}(10^{-4})}+\underbrace{C'_{f_0}}_{\mathcal{O}(10^{-4})}\right)-\underbrace{\left[\frac{\Theta_2}{L}\right]}_{\mathcal{O}(10^{-2})}-\underbrace{\left[\frac{p_1}{\rho_1u_1^2}\frac{\Theta_p}{L}\right]}_{\mathcal{O}(10^{-2})}. \quad (7.23)$$

Neglecting all the $\mathcal{O}(10^{-5})$ terms, (7.23) reduces to:

$$\frac{\Theta_\rho}{L}\dot{\zeta}+\left[\frac{1}{2F'(0)}\underbrace{\left(\bar{C}_{f_0}(1-k)-\frac{l_0}{L}\Lambda\right)}_{\Sigma}-k\tan\beta\left(\kappa_2+\frac{p_1}{\rho_1u_1^2}\kappa_p\right)\right]\zeta$$
$$=\frac{l_0C''_{f_0}}{2LF'(0)}+\underbrace{\frac{l_0\bar{C}_{f_0}}{2LF'(0)}-\frac{\Theta_2}{L}-\frac{p_1}{\rho_1u_1^2}\frac{\Theta_p}{L}}_{\Upsilon}. \quad (7.24)$$

Equation (7.24) is now a linear first-order ODE with both a forcing term C''_{f_0} and a steady term Υ on the right-hand side. It is well known from the LES and from the experiments that the reflected shock oscillates about a mean position (in a non-harmonic manner). In other words, the reflected-shock foot motions must be governed by a stable dynamical system and in the absence of any external forcing, the shock must remain at its equilibrium position. In the current coordinate system, this means that we must have $\zeta=0$ in the absence of any forcing (i.e. $C''_{f_0}=0$). Applying this condition to (7.24) leads to $\Upsilon=0$. Hence the system is governed by:

$$\frac{l_0\bar{C}_{f_0}}{2LF'(0)}-\frac{\Theta_2}{L}-\frac{p_1}{\rho_1u_1^2}\frac{\Theta_p}{L} = 0, \quad (7.25a)$$

Variable	Amplitude	Justification
ζ	$\mathcal{O}(10^{-1})$	figure 6.27
$\dot{\zeta}^{\mathrm{a}}$	$\mathcal{O}(10^{-3})$	(6.3), (7.17) with $t \equiv t_s$
k, $k\tan\beta$	$\mathcal{O}(10^{-1})$	figure 7.4(b), $\beta \approx 32^\circ$
$\bar{C}_{f_0}$	$\mathcal{O}(10^{-3})$	configuration input, figure 7.5
C''_{f_0}	$\mathcal{O}(10^{-4})$	from LES data
Λ	$\mathcal{O}(10^{-3})$	figure 7.5
$F'(0)$	$\mathcal{O}(10^{-1})$	figure 7.3
$p_1/(\rho_1 u_1^2)^{\mathrm{b}}$	$\mathcal{O}(10^{-1})$	for $\gamma = 1.4$ and $\mathrm{M}_1 = 2.3$
$l_0/(2L)^{\mathrm{c}}$	$\mathcal{O}(10^{-1})$	by geometry with $\alpha \approx 29^\circ$, $\beta \approx 32^\circ$
κ_1, κ_ρ, κ_p	$\mathcal{O}(10^{+0})$	figure 7.4(a)
κ_2	$\mathcal{O}(10^{-1})$	figure 7.4(a)
Θ_1/L, Θ_2/L	$\mathcal{O}(10^{-2})$	figure 7.4(a)
Θ_ρ/L, Θ_p/L	$\mathcal{O}(10^{-1})$	figure 7.4(a)

[a] $\dot{\zeta} = \mathrm{d}\zeta/\mathrm{d}t^\star \sim L\zeta/(u_1 t_s) = \zeta r_0 L/\delta_0$ with $r_0 \sim 10^{-2}$, $L/\delta_0 \approx 4$ (Dupont et al., 2006)
[b] $p_1/(\rho_1 u_1^2) = 1/(\gamma \mathrm{M}_1^2)$ from ideal-gas law
[c] $l_0/(2L) = \tan\beta/\left[2(\tan\alpha + \tan\beta)\right]$ by construction (see figure 7.1)

TABLE 7.1: Amplitudes of all the constituents found in (7.23) for $\mathrm{M}_1 = 2.3$ and $\theta = 8^\circ$

and

$$\frac{\Theta_\rho}{L}\dot{\zeta} + \left[\frac{\Sigma}{2F'(0)} - k\tan\beta\left(\kappa_2 + \frac{p_1}{\rho_1 u_1^2}\kappa_p\right)\right]\zeta \;=\; \frac{l_0 C''_{f_0}}{2LF'(0)}. \tag{7.25b}$$

Equation (7.25a) is the reflected-shock foot steady state equation whereas (7.25b) is its dynamical equation in the presence of fluctuations. Equation (7.25a) shows that, on average, the most significant balance is the balance between the rate of changes of momentum and pressure thicknesses (as previously noted in connection with figure 7.2(a)). As one could have anticipated, the error in this statement scales with the mean skin friction and is of the order of 10^{-3} in the present case. Equation (7.25b) is the main equation of interest (although we shall use (7.25a) later) and can be written in the following more generic way:

$$\dot{\zeta} + \phi\zeta = \psi(t), \tag{7.26a}$$

where:

$$\phi \;=\; \frac{L}{\Theta_\rho}\left[\frac{1}{2F'(0)}\left(\bar{C}_{f_0}(1-k) - \frac{l_0}{L}\Lambda\right) - k\tan\beta\left(\kappa_2 + \frac{p_1}{\rho_1 u_1^2}\kappa_p\right)\right], \tag{7.26b}$$

$$\psi(t) \;=\; \frac{l_0 C''_{f_0}(t)}{2LF'(0)}. \tag{7.26c}$$

Quite remarkably, equation (7.26a) is similar to the model proposed by Plotkin (1975) and the above may be viewed as a derivation of his model. This is discussed in more

detail later. Generally speaking, equation (7.26a) is a stochastic differential equation resembling a Langevin equation for Brownian motions (see chapter 3 of Risken, 1989), where ϕ is the damping coefficient and $\psi(t)$ the Langevin force, with zero mean (i.e. $\overline{\psi(t)} = 0$). However, the main difference with the classical Langevin equation resides in the time-correlation properties of the forcing, which is not proportional to a Dirac function, at least for time scales of the order of $\delta_0/\bar{u}_1{}^2$. One interesting property of (7.26a) is that it is sufficient to know the two-time correlation of the forcing (i.e. $\overline{C''_{f_0}(t)C''_{f_0}(t+\tau)}$) to calculate the correlation function of ζ (i.e. $\overline{\zeta(t)\zeta(t+\tau)}$), which is our ultimate goal. Therefore, if the time-correlation function of the skin-friction turbulence-related fluctuations is known, and provided that one can calculate the damping factor ϕ, the derived governing equation (7.26a) is sufficient to predict the low-frequency shock-motion spectrum.

In the present case, the aforementioned results (i.e. $\Theta_\rho/L = -0.104$, $F'(0) = 0.12$, $\bar{C}_{f_0} = 1.35 \times 10^{-4}$, $k = 0.32$, $l_0/L = \tan\beta/(\tan\alpha + \tan\beta) = 0.55$, $\Lambda = 3 \times 10^{-3}$, $k\tan\beta = 0.2$, $\kappa_2 = 0.27$, $\kappa_p = -1.23$ and $p_1/(\rho_1 u_1^2) = 0.134$) can be used to find that the damping factor ϕ is roughly 0.23. It will be shown later that the premultiplied spectrum of ζ when subject to a white-noise forcing is broadband with a peak at $\phi/(2\pi)$. For $\phi \approx 0.23$, one finds $\phi/(2\pi) \approx 0.037$, which is reminiscent of the Strouhal-number value observed in the LES weighted spectrum (see figure 6.2(b)). However, before discussing this encouraging result further, it is of importance to try to model the coefficients Θ_ρ, k, κ_2 and κ_p to overcome the need for some prior LES results.

7.2 Modelling the ODE coefficients

7.2.1 The k coefficient

If the shock maintains its inclination angle at all times, one could write $s = \varepsilon\tan\alpha/(\tan\alpha + \tan\beta)$. However, this is not the case. For example, Dupont et al. (2006) note that "the reflected shock appears as a low-frequency unsteady sheet with a length of excursion vanishing far from the wall". This implies that the reflected-shock angle with respect to the wall changes as the shock moves back and forth. This picture may also be observed in the conditional averages, as shown in figure 6.28 and also in side-view animations of the LES. At high frequencies, the shock cannot be considered to be a straight line (or sheet) because of transverse travelling waves (analysed in figure 6.26) and defining an inclination angle may be difficult and not meaningful. However, at sufficiently low frequencies, the reflected shock appears to move as a whole and may be thought of a

[2] We shall see that for the timescales considered in the present problem (i.e. $\mathcal{O}(10^2\delta_0/\bar{u}_1)$), the forcing may be considered similar to a white noise.

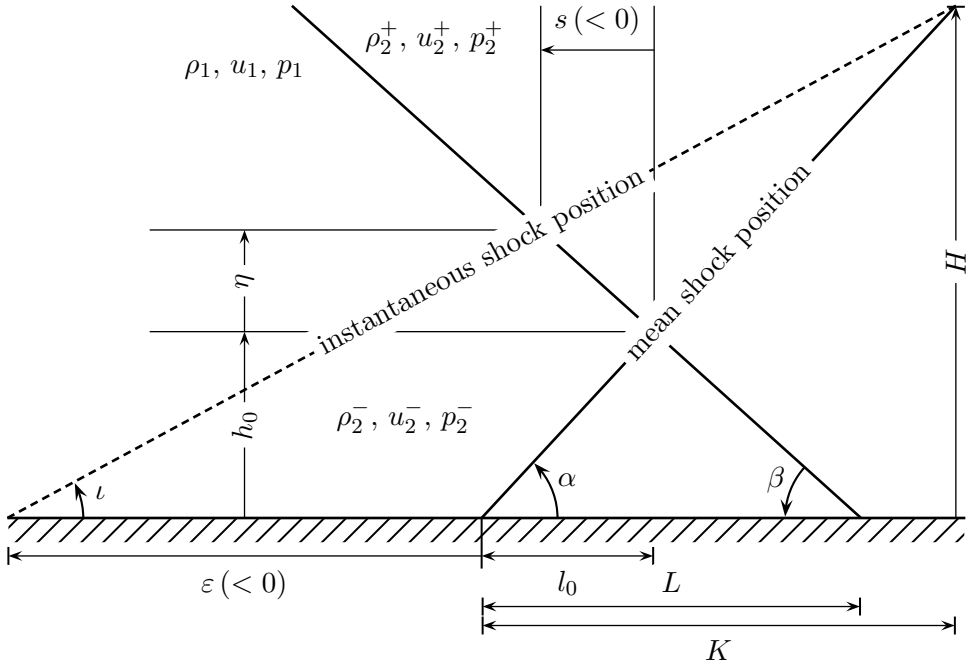

FIGURE 7.6: Sketch of the interaction with the notations used to compute k

straight line (or sheet) with a given foot position and inclination angle. The quantitative relationship between s and ε seen in figure 7.4(b) can be combined with the aforementioned comments to justify relating s and ε as in (7.15), if the study is restricted to the low-frequency motions. An analytical expression for k in (7.15) is derived in the following paragraph.

From the notation defined in figure 7.6, one can write the following geometric relations:

$$\begin{cases} K = H/\tan\alpha, \\ K - \varepsilon = H/\tan\iota, \\ \tan\iota = (h_0 + \eta)\,/\,(l_0 - \varepsilon + s)\,, \\ \eta = -s\tan\beta, \end{cases} \tag{7.27}$$

to find that:

$$\varepsilon \;=\; H\left(\frac{1}{\tan\alpha} - \frac{l_0 - \varepsilon + s}{h_0 - s\tan\beta}\right), \tag{7.28a}$$

which is re-arranged:

$$\varepsilon\,(h_0 - H) + H\left(l_0 - \frac{h_0}{\tan\alpha}\right) \;=\; s\left[\varepsilon\tan\beta - H\left(1 + \frac{\tan\beta}{\tan\alpha}\right)\right]. \tag{7.28b}$$

Noting that $\tan\alpha = h_0/l_0$, the second term on the left-hand side of (7.28b) vanishes and the equation can be re-written:

$$s = \frac{(\varepsilon/h_0)\,(h_0 - H)}{(\varepsilon/h_0)\tan\beta - (H/h_0)\left(1 + \dfrac{\tan\beta}{\tan\alpha}\right)}. \tag{7.29}$$

Assuming $\varepsilon/h_0 \ll 1$, one can expand the above equation in series of ε/h_0 to find:

$$s = \frac{H/h_0 - 1}{(H/h_0)\left(1 + \dfrac{\tan\beta}{\tan\alpha}\right)}\varepsilon + \mathcal{O}(\varepsilon^2/h_0), \tag{7.30a}$$

Following the aforementioned remark by Dupont et al. (2006), which is supported by figure 6.28, one can say that H is significantly larger than the incoming boundary-layer height δ_0. One way to look at H is to see it as a penetration lengthscale corresponding to the wall-normal distance a perturbation associated with a shock-foot displacement can travel along the shock during half of a low-frequency cycle. If V is the propagation speed and T the typical period of a low-frequency cycle, one could write $H = (T/2)V\sin\alpha$. Roughly, the propagation speed can be thought to scale with $u_1\cos\alpha$ and the characteristic frequency of the system with u_1/L so that $H \sim \pi L\sin\alpha\cos\alpha = L\pi\sin(2\alpha)/2$. Considering that $\pi\sin(2\alpha)/2 \sim 1$, one finds that $H \sim L$. Therefore, one could replace H with L in (7.30a) and write:

$$s \approx \frac{L/h_0 - 1}{(L/h_0)\left(1 + \dfrac{\tan\beta}{\tan\alpha}\right)}\varepsilon. \tag{7.30b}$$

Noting the geometrical relation $h_0/L = \tan\alpha\tan\beta/(\tan\alpha + \tan\beta)$, one finds that the theoretical value for k is:

$$k = \frac{1 - \tan\alpha\tan\beta/\left(\tan\alpha + \tan\beta\right)}{1 + \tan\beta/\tan\alpha}. \tag{7.31}$$

For $\mathrm{M}_1 = 2.3$ and a wedge angle of 8°, inviscid theory gives that $\beta \approx 32.4^\circ$ and $\alpha \approx 29.4^\circ$ so that the theoretical k value is about 0.33, to compare with 0.38 in the large-span LES and 0.32 in the narrow-span LES (see figure 7.4(b)). The average error is less than 6% and therefore (7.31) is considered a good first-order approximation.

7.2.2 The Θ_i coefficients

The Θ coefficients represent the mean changes of thicknesses (i.e. δ_1, δ_2, δ_ρ, δ_p) between the shock foot $\xi = 0$ and the shock crossing point[3] $\xi = 1$. Although such quantities are not generally known, this section will introduce a model to estimate Θ_p and show how it can be related to Θ_ρ and Θ_2 in a useful way.

In canonical boundary layers, the pressure is considered constant in the wall-normal direction. In the presence of the oblique shock, this approximation is obviously inadequate. However, upstream of the interaction, the boundary layer is a typical turbulent boundary layer and one can write:

$$\bar{p}(\xi < 0, y) \approx p_1, \tag{7.32}$$

which is easily verified from figure 7.7. Inside the interaction, the picture is more complex. At $\xi = 1$ and $y = h_0$, the pressure is discontinuous, jumping from p_1 to $\bar{p}_3$ (where $\bar{p}_3$ refers to the mean pressure downstream of the interaction) whereas at the wall, the pressure continuously increases from p_1 to $\bar{p}_3$ over a streamwise distance ranging from $\xi \approx 0$ to well beyond the reattachement point. However, based on figure 7.7, we argue that the isobar in the vicinity of $\xi = 1$ can be modelled as a straight line given its actual "S" shape in the figure (see white dots), with the straight line chosen such that it averages the S. From the data, this idealised isobar would take a value between p_2^+ and $\bar{p}_3$ (see the dash-dotted isobar corresponding to p_2^+), hence:

$$\bar{p}(\xi = 1, y) \approx (1 - r)\, p_2^+ + r\, \bar{p}_3, \tag{7.33}$$

with r a weighting factor. In the present case, $r \approx 0.2$ gives satisfactory results. Assuming the distributions (7.32) and (7.33), one finds:

$$\begin{aligned}\frac{\Theta_p}{L} \equiv \frac{1}{L}\left[\int_0^{h_0}\left(1 - \frac{\bar{p}(\xi = 1^-, y)}{p_1}\right)\mathrm{d}y - \int_0^{h_0}\left(1 - \frac{\bar{p}(\xi = 0, y)}{p_1}\right)\mathrm{d}y\right] \\ \approx \left\{1 - (1 - r)\,\frac{p_2^+}{p_1} - r\,\frac{\bar{p}_3}{p_1}\right\}\frac{\tan\alpha\tan\beta}{\tan\alpha + \tan\beta},\end{aligned} \tag{7.34}$$

noting from geometrical considerations in figure 7.6 that:

$$\frac{h_0}{L} = \frac{\tan\alpha\tan\beta}{\tan\alpha + \tan\beta}. \tag{7.35}$$

Applying (7.34) to the $\mathrm{M}_1 = 2.3$ and 8°-wedge-angle case gives $\Theta_p/L = -0.233$ (with $r = 0.2$) to compare with the LES value of -0.243 from figure 7.4(a). Of course, the

[3]Note that rigorously, we should write $\xi = 1^-$ owing to the discontinuity at this station. However, the thicknesses being integral quantities, the presence of the discontinuity is in fact irrelevant and we can write $\xi = 1$.

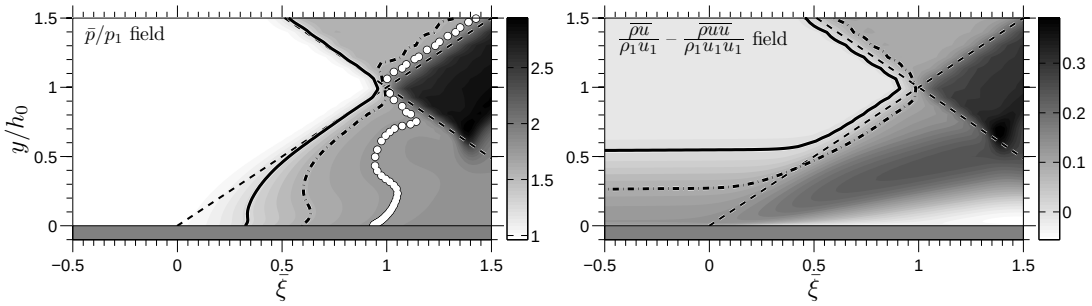

(a) narrow-span LES

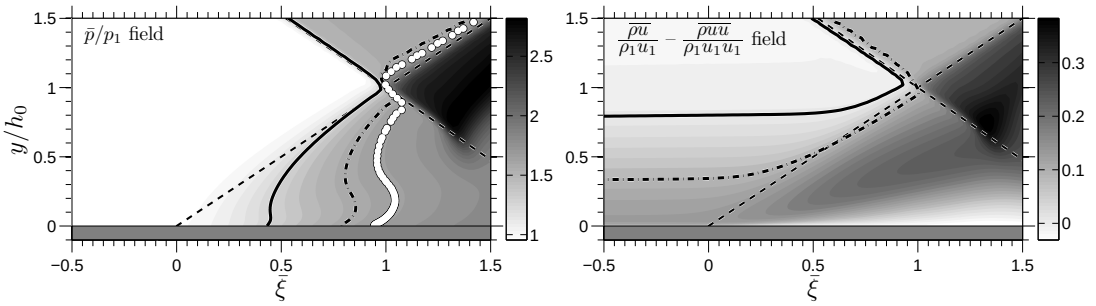

(b) large-span LES

FIGURE 7.7: Mean pressure field $\bar{p}/p_1$ *(left-hand side)* and mean momentum-thickness-integrand field $[\overline{\rho u}/(\rho_1 u_1) - \overline{\rho u u}/(\rho_1 u_1 u_1)]$ *(right-hand side)*. Both the narrow-span (a) and large-span (b) LES data are shown. The *thick solid* and *dash-dotted lines* indicate the contours equal to the inviscid-theory results, using the upper-region values (e.g. p_2^+, ρ_2^+, u_2^+) for the dash-dotted lines and the bottom-region values (e.g. p_2^-, ρ_2^-, u_2^-) for the solid lines. The shock-system location is indicated by the set of *dashed lines*. The *white dots* in the pressure fields show the contours $(1-r)\,p_2^+/p1 + r\,\bar{p}_3/p_1$ with $r = 0.2$ and 0.1 for (a) and (b) respectively

choice of r was based on the LES data whereas generally one has no prior knowledge of this value. However, note that the existence of a similarity function (see figure 7.3(c)) suggests that the weighting factor r does not change during the shock motions and can thus be treated as a true constant.

In the previous section it was shown that, on average, the changes of pressure and momentum thicknesses between $\xi = 0$ and $\xi = 1$ are close to equilibrium with an error scaling on the skin friction (see (7.25a)). Therefore, as a first approximation:

$$\Theta_2 \approx -\frac{p_1}{\rho_1 u_1^2}\Theta_p, \text{ or equivalently: } \frac{\Theta_2}{\Theta_p} \approx -\frac{1}{\gamma \mathrm{M}_1^2}, \tag{7.36}$$

where the ideal-gas law was used to transform $p_1/(\rho_1 u_1^2)$ in $1/(\gamma \mathrm{M}_1^2)$. Using (7.36) with $\mathrm{M}_1 = 2.3$ and $\gamma = 1.4$, one finds $\Theta_2/\Theta_p = -0.135$ whereas from figure 7.4(a), the LES gives -0.132, which is a satisfactory agreement. This result confirms that the error in (7.36) scales with $l_0 \bar{C}_{f_0}/(2LF'(0)) \approx 3 \times 10^{-3}$, providing an encouraging consistency check.

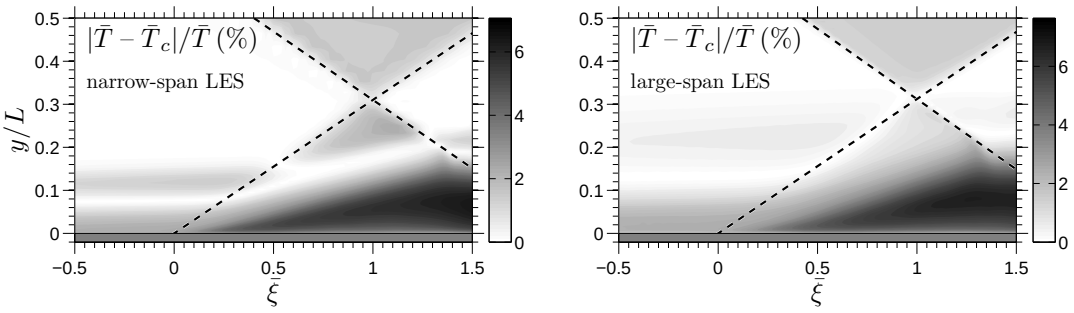

FIGURE 7.8: Percentage error between the temperature field computed from the velocity field using the Crocco–Busemann equation and the actual LES temperature field for the narrow-span *(left)* and large-span *(right)* simulations

Finally, to relate Θ_ρ to Θ_p, the Crocco–Busemann relation will be used (see White, 1991). The temperature field computed using the Crocco–Busemann relation is labelled T_c and defined as:

$$\frac{T_c}{T_1} = 1 + \frac{\gamma-1}{2}\mathrm{M}_1^2\left(\frac{u}{u_1}\right)^2, \tag{7.37}$$

assuming the wall to be isothermal and equal to the upstream adiabatic-wall condition (as in the current LES settings). The validity of (7.37) is tested using the LES results and the error contour levels are shown in figure 7.8. Overall, the use of (7.37) is remarkably accurate with errors not exceeding 7%.

Starting from the definition of the pressure thickness and using the ideal-gas law, one finds:

$$\delta_p = \int_0^h \left(1-\frac{p}{p_1}\right)\mathrm{d}y = \int_0^h \left(1-\frac{\rho T}{\rho_1 T_1}\right)\mathrm{d}y, \tag{7.38a}$$

which with (7.37) may be approximated by:

$$\delta_p \approx \int_0^h \left\{1-\frac{\rho}{\rho_1}\left[1+\frac{\gamma-1}{2}\mathrm{M}_1^2\left(1-\frac{u^2}{u_1^2}\right)\right]\right\}\mathrm{d}y, \tag{7.38b}$$

which can be expressed in terms of the density, displacement and momentum thickness definitions:

$$\delta_p \;\approx\; \delta_\rho\left(1+\frac{\gamma-1}{2}\mathrm{M}_1^2\right) - \frac{\gamma-1}{2}\mathrm{M}_1^2\left(\delta_1+\delta_2\right). \tag{7.38c}$$

Using (7.38c) in the definition of Δ_i (see (7.10)) and time-averaging, one finds:

$$\Theta_p \approx \Theta_\rho\left(1+\frac{\gamma-1}{2}\mathrm{M}_1^2\right) - \frac{\gamma-1}{2}\mathrm{M}_1^2\left(\Theta_1+\Theta_2\right). \tag{7.39a}$$

Using (7.36), (7.39a) becomes:

$$\Theta_p \approx \Theta_\rho \left(1 + \frac{\gamma-1}{2}\mathrm{M}_1^2\right) - \frac{\gamma-1}{2}\mathrm{M}_1^2 \left(\Theta_1 - \frac{1}{\gamma \mathrm{M}_1^2}\Theta_p\right). \tag{7.39b}$$

From figure 7.4(a), it is found that for the configuration studied here $|\Theta_p/(\gamma L \mathrm{M}_1^2)| \approx 3 \times 10^{-2}$ whereas $\Theta_1/L \approx 6 \times 10^{-3}$. Therefore, as a leading-order approximation, the term in Θ_1 in (7.39b) may be neglected:

$$\Theta_p \approx \Theta_\rho \left(1 + \frac{\gamma-1}{2}\mathrm{M}_1^2\right) + \frac{\gamma-1}{2\gamma}\Theta_p. \tag{7.39c}$$

Equation (7.39c) is re-arranged:

$$\Theta_p \approx \chi \Theta_\rho, \text{ with: } \chi = \frac{2\gamma + \gamma\left(\gamma-1\right)\mathrm{M}_1^2}{\gamma+1}. \tag{7.39d}$$

For $\mathrm{M}_1 = 2.3$, (7.39d) gives $\chi = 2.40$ while the LES data in figure 7.4(a) give $\chi = 2.34$. It should be stressed that the Crocco–Busemann equation used to derive (7.39d) was assumed to be applicable to the unsteady velocity field, the displacement-thickness contribution was neglected and the momentum-thickness contribution was related to the pressure-thickness using (7.36). Despite those gross assumptions, only a 3% difference with the LES can be found for the present configuration.

7.2.3 The κ_p and κ_2 coefficients

By definition, the κ_p and κ_2 coefficients in (7.13) correspond to the rate of change of the pressure and momentum thickness between $\xi = 1$ and $\xi = 0$ as the shock moves back and forth (i.e. $\kappa_p = \mathrm{d}\Delta_p/\mathrm{d}\eta$, $\kappa_2 = \mathrm{d}\Delta_2/\mathrm{d}\eta$). Although not explicitly written in (7.13) the shock motions of interest for this study are the low-frequency ones. Therefore, the reflected shock is considered to remain straight and to rotate around its foot as it oscillates. One direct consequence of such a motion is a modification of the pressure field in the region 2^- as well as in region 3 (i.e. p_2^- and p_3 in figure 7.6), whereas p_2^+ remains unchanged. We wish to express those changes in terms of the variable η, which is made possible by developing a series expansion of the classical oblique-shock jump relations, considering that η/h_0 is sufficiently small. The details of such expansions are provided in appendix G and only the final result is reported here. For the pressure in region 3, we find:

$$\frac{p_3}{p_1} = \frac{\bar{p}_3}{p_1} + \frac{p_2^+}{p_1}\frac{\gamma \mathrm{M}_2^2 \varkappa}{1+\gamma}\frac{\eta}{h_0} + \mathcal{O}\left(\frac{\eta^2}{h_0^2}\right), \tag{7.40}$$

where $\varkappa = \left(\tan\alpha + \tan\beta\right)\sin\left(2\alpha\right)\sin\left[2\left(\alpha+\theta\right)\right] / \left(\tan\beta\left(1 - 1/\tan\alpha\right) - 1\right)$. Assuming that the distributions (7.32) and (7.33) can be extented to the low-frequency oscillations,

it is possible to write:

$$\Delta_p = \left[1 - (1-r)\frac{p_2^+}{p1} - r\frac{p_3}{p_1}\right](h_0 + \eta)\,. \tag{7.41a}$$

Using the series expansion (7.40) and (7.34), the above equation becomes:

$$\Delta_p = \Theta_p + \left\{1 - r\frac{\bar{p}_3}{p_1} - \frac{p_2^+}{p_1}\left[1 - r\left(1 + \frac{\gamma \mathrm{M}_2^2 \varkappa}{1+\gamma}\right)\right]\right\}\eta + \mathcal{O}\left(\frac{\eta^2}{h_0}\right). \tag{7.41b}$$

Thus,

$$\kappa_p \approx 1 - r\frac{\bar{p}_3}{p_1} - \frac{p_2^+}{p_1}\left[1 - r\left(1 + \frac{\gamma \mathrm{M}_2^2 \varkappa}{1+\gamma}\right)\right],$$
$$\text{with } \varkappa = \frac{\tan\alpha + \tan\beta}{\tan\beta\,(1 - 1/\tan\alpha) - 1}\sin(2\alpha)\sin\left[2\,(\alpha+\theta)\right],\ r = 0.2. \tag{7.42}$$

For $\mathrm{M}_1 = 2.3$ and $\theta = 8°$, the modelled κ_p using (7.42) gives -1.21 whereas the measured value on the narrow-span LES data is -1.23. The difference is thus less than 2% for the particular choice of weighting factor $r = 0.2$. As mentioned earlier, the weighting factor is based on time-averaged LES data and its use here is justified based on the similarity hypothesis, combined with (7.33) and the above series expansion.

The case of κ_2 is more complex than κ_p mainly because the quantity $\mathcal{M} \equiv \rho u(1 - u/u_1)/(\rho_1 u_1)$ at $\xi = 0$ and $\xi = 1$ is not constant along the wall-normal direction, even approximatively, as shown in figures 7.7 and 7.9(b). From the definition of the momentum thickness (7.2b), we have:

$$\frac{\Delta_2}{h} = \underbrace{\frac{1}{h}\int_0^h \mathcal{M}|_{\xi=1}\,\mathrm{d}y}_{\delta_{2,\xi=1}/h} - \underbrace{\frac{1}{h}\int_0^h \mathcal{M}|_{\xi=0}\,\mathrm{d}y}_{\delta_{2,\xi=0}/h}. \tag{7.43}$$

Decomposing $\mathcal{M}(\xi = 1, y)$ in its steady ($\overline{\mathcal{M}}(\xi = 1, y)$) and time-dependent ($\mathcal{M}'(\xi = 1, y)$) component, one can write:

$$\frac{\delta_{2,\xi=1}}{h} = \frac{1}{h}\int_0^h \overline{\mathcal{M}}\big|_{\xi=1}\,\mathrm{d}y + \frac{1}{h}\int_0^h \mathcal{M}'\big|_{\xi=1}\,\mathrm{d}y. \tag{7.44}$$

Since $\overline{\mathcal{M}}(\xi = 1, y)$ is a continuous function on $y \in [0, h[$, the mean-value theorem states that there exists a positive real number R such that:

$$\frac{1}{h}\int_0^h \overline{\mathcal{M}}\big|_{\xi=1}\,\mathrm{d}y = (1-R)\min_{0\le y<h}\left[\overline{\mathcal{M}}\big|_{\xi=1}\right] + R\max_{0\le y<h}\left[\overline{\mathcal{M}}\big|_{\xi=1}\right],\ R > 0. \tag{7.45}$$

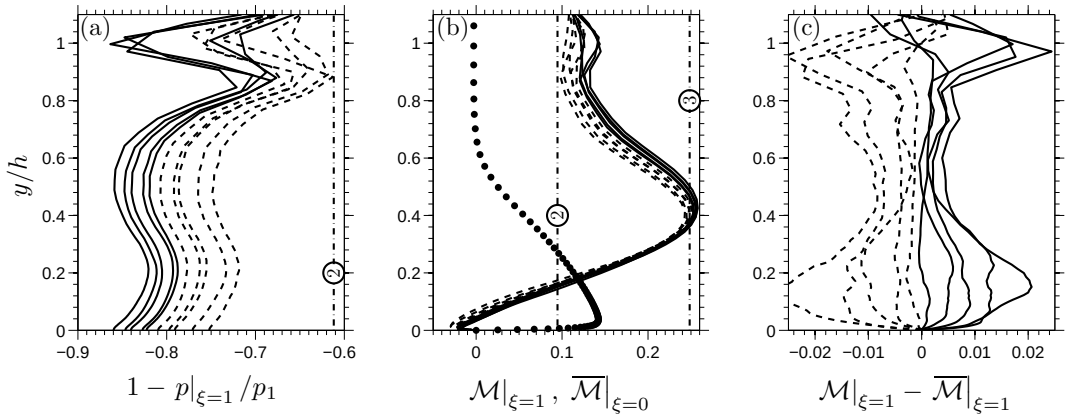

FIGURE 7.9: Integrands of δ_p and δ_2 at $\xi = 1$. The *solid lines* indicate cases where $\eta > 0$ whereas *dashed lines* indicate cases where $\eta < 0$. In (b), the *dotted line* corresponds to $\overline{\mathcal{M}}$ at $\xi = 0$. The numbers 2 and 3 embedded in black circles indicate the potential-flow values in regions 2 and 3, respectively

Let us denote by $\mathcal{M}_3$ and $\overline{\mathcal{M}}_3$ the following quantities:

$$\mathcal{M}_3 \equiv \frac{\rho_3 u_3}{\rho_1 u_1}\left(1 - \frac{u_3}{u_1}\right), \; \overline{\mathcal{M}}_3 \equiv \frac{\bar{\rho}_3 \bar{u}_3}{\rho_1 u_1}\left(1 - \frac{\bar{u}_3}{u_1}\right). \tag{7.46}$$

From figure 7.9(b) one can see that $\overline{\mathcal{M}}\big|_{\xi=1}$ does not exceed $\overline{\mathcal{M}}_3$ whereas inside the separation bubble, it is possible that it becomes negative. Recalling that the separation bubble height is very small compared to h (see chapter 4), it is argued that the possible negative contribution of $\overline{\mathcal{M}}$ in (7.45) remains small so that (7.45) becomes:

$$\frac{1}{h}\int_0^h \overline{\mathcal{M}}\big|_{\xi=1}\,\mathrm{d}y = R\overline{\mathcal{M}}_3. \tag{7.47a}$$

Similarly, the fluctuating component $\mathcal{M}'\big|_{\xi=1}$ (shown in figure 7.9(c)) is related to $\mathcal{M}'_3$ by invoking the mean-value theorem:

$$\frac{1}{h}\int_0^h \mathcal{M}'\big|_{\xi=1}\,\mathrm{d}y = r'\left(\mathcal{M}_3 - \overline{\mathcal{M}}_3\right), \tag{7.47b}$$

where r' is a real number. As for the pressure p_3, when the reflected shock moves back and forth, $\mathcal{M}_3$ will fluctuate and those changes can be expressed in terms of a series expansion in η/h_0:

$$\mathcal{M}_3 = \overline{\mathcal{M}}_3 + D\frac{\eta}{h_0} + \mathcal{O}\left(\frac{\eta^2}{h_0^2}\right), \tag{7.48}$$

where D is a constant defined in (G.18) in appendix G. Using (7.44), (7.47) and (7.48) in (7.43) gives:

$$\Delta_2 = \underbrace{R\overline{\mathcal{M}}_3 h_0 - \bar{\delta}_{2,\xi=0}}_{\Theta_2} + \underbrace{\left(R\overline{\mathcal{M}}_3 + r'D\right)}_{\kappa_2}\eta + \mathcal{O}\left(\frac{\eta^2}{h_0}\right), \tag{7.49}$$

assuming that the fluctuations of the momentum thickness at $\xi = 0$ are negligible compared to the variations at $\xi = 1$ (i.e. $\tilde{\delta}_{2,\xi=0} \approx 0$) and where terms Θ_2 and κ_2 are identified according to (7.13). To be consistent with (7.36), we must take R such that:

$$R = \frac{1}{\overline{\mathcal{M}}_3}\left(\frac{\bar{\delta}_{2,\xi=0}}{h_0} - \frac{1}{\gamma \mathrm{M}_1^2}\frac{\Theta_p}{h_0}\right). \tag{7.50}$$

The term in $\bar{\delta}_{2,\xi=0}$ is problematic since the momentum thickness at the shock foot is different from that of the incoming boundary layer and therefore needs to be modelled. The noticeable linear relationship between L/δ_0 and $(p_2^+ - p_1)/(2\tau_w)$ in figure 4.31 suggests that the momentum thickness at the shock foot may be related to the pressure jump $p_2^+ - p_1$ as follows:

$$\frac{\bar{\delta}_{2,\xi=0}}{h_0} = r''\frac{2\tau_w}{p_2^+ - p_1}\frac{L}{h_0}, \tag{7.51a}$$

where the ratio $\bar{\delta}_{2,\xi=0}/\delta_0$ was considered constant and r'' is a positive real number to determine from the LES data. Noting that $2\tau_w = \bar{C}_{f_0} p_1 \gamma \mathrm{M}_1^2$ and $h_0/L = \tan\alpha\tan\beta/(\tan\alpha + \tan\beta)$, one finds:

$$\frac{\bar{\delta}_{2,\xi=0}}{h_0} = r''\frac{\gamma \mathrm{M}_1^2 \bar{C}_{f_0}}{p_2^+/p_1 - 1}\frac{\tan\alpha + \tan\beta}{\tan\alpha\tan\beta}. \tag{7.51b}$$

Hence the following expression for κ_2:

$$\kappa_2 = r''\frac{\gamma \mathrm{M}_1^2 \bar{C}_{f_0}}{p_2^+/p_1 - 1}\frac{\tan\alpha + \tan\beta}{\tan\alpha\tan\beta} - \frac{1}{\gamma \mathrm{M}_1^2}\frac{\Theta_p}{h_0} + r'D. \tag{7.52}$$

The factors r' and r'' are computed from the LES. Using the narrow-span LES results, one finds $r' = -0.14$ and $r'' = 0.2$ (giving $\kappa_2 \approx 0.27$). Similarly to r in (7.34), r' is assumed to remain constant in time. This completes the modelling of the unknowns k, Θ_ρ, κ_2 and κ_1 in (7.26).

7.3 Final form of the model

Upon substituting (7.31), (7.34), (7.39d), (7.42) and (7.52) into (7.26), one can write the following closed form of the model:

$$\frac{1}{\bar{u}_1}\frac{\mathrm{d}\varepsilon}{\mathrm{d}t} + \phi\frac{\varepsilon}{L} = \Pi C''_{f_0}(t), \tag{7.53a}$$

with:

$$\Pi = \frac{\tan\beta}{2F'(0)\,(\tan\alpha + \tan\beta)}, \tag{7.53b}$$

$$\phi = \frac{2\gamma+\gamma(\gamma-1)\,\mathrm{M}_1^2}{(\gamma+1)\left[1+(1-r)\,P_2-rP_3\right]}\left\{\Pi\left[\left(\frac{1}{\tan\alpha}+\frac{1}{\tan\beta}\right)\left(\bar{C}_{f_0}-\Lambda\right)+\bar{C}_{f_0}\frac{\tan\alpha}{\tan\beta}\right]+\left(1-\frac{\tan\alpha\tan\beta}{\tan\alpha+\tan\beta}\right)\left[r''\frac{\gamma\mathrm{M}_1^2\bar{C}_{f_0}}{P_2-1}-r'D-r\frac{P_2\varkappa}{\gamma+1}\left(\frac{\mathrm{M}_2}{\mathrm{M}_1}\right)^2\right]\right\}, \tag{7.53b}$$

$$\varkappa = \frac{\tan\alpha+\tan\beta}{\tan\beta\,(1-1/\tan\alpha)-1}\sin(2\alpha)\sin\left[2\,(\alpha+\theta)\right], \tag{7.53c}$$

$$D = \frac{\overline{\mathrm{M}}_3}{\mathrm{M}_1}\left\{\left(\frac{1}{2}\sqrt{\frac{R_3}{P_3}}-\frac{\overline{\mathrm{M}}_3}{\mathrm{M}_1}\right)A+\frac{1}{2}\sqrt{\frac{P_3}{R_3}}\,B+\left(\frac{\mathrm{M}_1}{\overline{\mathrm{M}}_3}\sqrt{R_3P_3}-2P_3\right)C\right\} \tag{7.53d}$$

$$A = \frac{\gamma\varkappa\mathrm{M}_2^2}{1+\gamma}P_2 \tag{7.53e}$$

$$B = \varkappa\left[\frac{1}{2\sin^2(\alpha+\theta)}-\frac{(\gamma-1)\,\mathrm{M}_2^2}{4+2\,(\gamma-1)\,\mathrm{M}_2^2\sin^2(\alpha+\theta)}\right]R_3 \tag{7.53f}$$

$$C = \frac{\overline{\mathrm{M}}_3}{\mathrm{M}_1}\left\{\varkappa\left[\frac{(\gamma-1)\,\mathrm{M}_2^2}{8+4\,(\gamma-1)\,\mathrm{M}_2^2\sin^2(\alpha+\theta)}-\frac{\gamma\mathrm{M}_2^2}{2\,(1-\gamma)+4\gamma\mathrm{M}_2^2\sin^2(\alpha+\theta)}\right]-\frac{(\tan\alpha+\tan\beta)\cos^2\alpha}{\tan\beta\,(1-1/\tan\alpha)-1}\right\}, \tag{7.53g}$$

where α, β, $P_2 \equiv p_2^+/p_1$, $P_3 \equiv \bar{p}_3/p_1$, $R_3 \equiv \bar{\rho}_3/\rho_1$, M_2 and $\overline{\mathrm{M}}_3$ are computed from the inviscid shock reflection problem for a given pair of wedge angle θ and upstream Mach number M_1. Factors $F'(0)$, r, r' and r'' are assumed to take the values of 0.12, 0.2, -0.14 and 0.2, respectively. Term $\bar{C}_{f_0}$ is an input parameter, together with the upstream Mach number M_1 and wedge angle θ. The coefficient Λ, although of the same order as $\bar{C}_{f_0}$, is not an input parameter and is not generally known. In this work, it is taken to be 3×10^{-3} (from the LES). The term C''_{f_0} corresponds to the skin-friction turbulence-related variations at the reflected-shock foot and therefore constitutes the dynamical-system input signal.

7.4 Solutions to the derived stochastic model

7.4.1 Solution to white noise: shock-foot and pressure spectra

As mentioned earlier, the model system (7.53 *a–h*) is a first-order linear stochastic differential equation resembling the Langevin equation for Brownian motion, written:

$$\dot{\varepsilon}+\Phi\varepsilon=\Gamma(t), \tag{7.54a}$$

where in the present case $\Phi = \bar{u}_1\phi/L$ and $\Gamma = \bar{u}_1 \Pi C''_{f_0}$. If Γ is taken to be a Langevin force with zero mean and a correlation function proportional to a Dirac function (δ),

$$\overline{\Gamma(t)} = 0, \text{ and } \overline{\Gamma(t)\Gamma(t')} = q\delta(t - t'), \tag{7.54b}$$

with q the proportionality coefficient, then (7.54a) is equivalent to equation (3.1) in Risken (1989) and the system (7.54 a,b) can be solved with the correlation function of the shock-displacement ε given by (see (3.9) in Risken, 1989):

$$\overline{\varepsilon(t_0)\varepsilon(t_0+\tau)} = \varepsilon^2(t_0)\mathrm{e}^{-\Phi(2t_0+\tau)} + \frac{q}{2\Phi}\left[\mathrm{e}^{-\Phi|\tau|} - \mathrm{e}^{-\Phi(2t_0+\tau)}\right], \tag{7.55a}$$

where t_0 is a chosen time and τ the time lag separating the actual time from t_0. To remain general, τ can be taken both positive and negative. If t_0 is taken such that $\varepsilon(t_0) = 0$, (7.55a) becomes:

$$\overline{\varepsilon(t_0)\varepsilon(t_0+\tau)} = \frac{q}{2\Phi}\mathrm{e}^{-\Phi|\tau|}\left[1 - \mathrm{e}^{-2\Phi t_0}\right]. \tag{7.55b}$$

Note that, dimensionally speaking, the damping coefficient $\Phi \equiv 1/\tau_s$ is the inverse of a time so that Φt_0 is the ratio between t_0 and the system characteristic timescale τ_s. If t_0 is chosen long after the initial transients from starting up the flow, t_0 will be significantly larger than τ_s so that $\Phi t_0 \gg 1$. The autocorrelation function of the shock-foot motions in response to a white-noise forcing with amplitude $2q$ will therefore become:

$$\overline{\varepsilon(t_0)\varepsilon(t_0+\tau)} = \frac{q}{2\Phi}\mathrm{e}^{-\Phi|\tau|}. \tag{7.55c}$$

By definition, the power spectral density (denoted $\mathcal{S}$) is the Fourier transform of the autocorrelation function, hence:

$$\mathcal{S}(f) = \frac{q/\Phi^2}{1 + (2\pi f/\Phi)^2} = \frac{A_0}{1 + (S_t/\phi_{\max})^2}, \tag{7.56}$$

where $A_0 \equiv q\left[L/(\bar{u}_1\phi)\right]^2$, $\phi_{\max} \equiv \phi/(2\pi)$ and S_t is the previously defined Strouhal number $S_t = fL/\bar{u}_1$.

In general, one is interested in the wall-pressure PSD near the mean shock-foot position rather than the PSD of the shock-foot position itself. Let us assume that the instantaneous pressure at the mean shock-foot position $\bar{x}_0$ may be approximated by the mean pressure at $\bar{x}_0 - \varepsilon$:

$$p_w(\bar{x}_0, t_s) \approx \bar{p}_w(\bar{x}_0 - \varepsilon). \tag{7.57a}$$

The above equation is not expected to be correct on fast timescales, hence the use of t_s which was defined in (6.3). Since the shock motions in this study are considered small

compared to the interaction length, one can expand (7.57a) using the first term in ε:

$$p_w(\bar{x}_0, t_s) \approx \bar{p}_w(\bar{x}_0) - \left.\frac{\mathrm{d}\bar{p}}{\mathrm{d}x}\right|_{\bar{x}_0} \varepsilon. \tag{7.57b}$$

For the slow timescales considered here, we have $p(t_s) - \bar{p} \approx \tilde{p}$, hence:

$$\tilde{p}_w(\bar{x}_0, t_s) \approx - \left.\frac{\mathrm{d}\bar{p}_w}{\mathrm{d}x}\right|_{\bar{x}_0} \varepsilon. \tag{7.57c}$$

Therefore, the autocorrelation of the pressure fluctuations near the mean shock-foot position can be approximated by the shock-foot autocorrelation function using:

$$\overline{\tilde{p}_w(\bar{x}_0, t_0)\tilde{p}_w(\bar{x}_0, t_0 + \tau)} \approx \left(\left.\frac{\mathrm{d}\bar{p}_w}{\mathrm{d}x}\right|_{\bar{x}_0} \right)^2 \overline{\varepsilon(t_0)\varepsilon(t_0 + \tau)}, \tag{7.58}$$

for sufficiently large time lags τ. Then, the wall-pressure PSD near the mean shock-foot position, denoted $\mathcal{S}_p$ is:

$$\mathcal{S}_p(S_t) \approx \frac{A_0 \left(\mathrm{d}\bar{p}_w/\mathrm{d}x|_{\bar{x}_0} \right)^2}{1 + \left(S_t/\phi_{\max}\right)^2}. \tag{7.59}$$

7.4.2 Solution for forcing by synthetic turbulence

It is emphasised that (7.59) is the response of the model to white-noise forcing and that the solution is only valid for sufficiently low frequencies (typically, $S_t < 1$). As an alternative, in the event that the forcing term C''_{f_0} is known, one can numerically integrate (7.54a). In practice, this may not be needed and (7.59) may be sufficiently accurate. To convince ourselves, we will use an artificial signal for C''_{f_0}, representative of the incoming turbulence. To do so, one can employ a digital-filter approach, similar to the one used to generate the inflow conditions for the LES. In this case, the problem is one-dimensional and starting from N normally-distributed random numbers $\{a_n\}_{0 \leq n \leq N-1}$ with zero mean and unit variance (i.e. $\overline{a_n} = 0$, $\overline{a_n a_n} = 1$ and $\overline{a_n a_m} = 0$ if $n \neq m$), the following synthetic turbulence series is produced:

$$C''_{f_0}(t_0 + n\Delta t) = C''_{f_0}(t_0 + (n-1)\Delta t) \exp\left(-\frac{\pi \Delta t}{2\tau_c}\right) + a_n \sqrt{q\left(1 - \exp\left(-\frac{\pi \Delta t}{\tau_c}\right)\right)},$$
$$C''_{f_0}(t_0) = a_0 \sqrt{q} \text{ and, } n \in \{1, \ldots, N-1\}, \tag{7.60}$$

where q is the imposed variance of C''_{f_0} (i.e. $q = \overline{C''_{f_0} C''_{f_0}}$) and τ_c is the characteristic timescale of the correlation. In the present case, we take $q \approx 7 \times 10^{-4}$, $\tau_c = 5 \times 10^{-2} \bar{u}_1/L$, $\Delta t = 5 \times 10^{-3} \bar{u}_1/L$ and $N = 5 \times 10^8$.

Once the synthetic signal C''_{f_0} is obtained using (7.60), (7.53a) is integrated numerically using a fourth-order Runge–Kutta method, giving $\varepsilon(t)$, which is then used to compute $\mathcal{S}(f)$. If the wall-pressure PSD near the mean shock-foot position is of interest, the pressure-gradient conversion factor may be applied (see (7.58)). Note that for the weighted spectra, the correction is not necessary since the pressure-gradient factor term will appear in both the numerator and denominator. This equivalence between the shock-displacement and wall-pressure weighted spectra will be used to directly compare the model predictions with the experimental and numerical results which are based on the pressure rather than the shock-displacement itself.

7.5 Model performances and discussion

7.5.1 Model results compared with LES and experimental findings

Before comparing the predicted spectrum with experiment and LES, it is important to consider the effect of the choice of forcing as this may have implications for the discussion. First, the analytical solution to white noise (see section 7.4.1) is considered. Second, the synthetic turbulence signal described in section 7.4.2 is used to integrate the governing equation (7.53a). Finally, a high-pass filtered version of the same synthetic turbulence signal is examined. In all cases, the flow conditions correspond to the IUSTI 8° case. Results are reported in figure 7.10.

First of all, it is seen that in the case of the white-noise and synthetic-turbulence forcing, the resulting shock motions exhibit significantly amplified low-frequency motions whereas the contributions of the higher frequencies are weaker than in the forcing itself. Moreover, it is found that at low frequencies the analytical solution to white noise is identical to the response to the synthetic-turbulence forcing. This is due to the particular synthetic-turbulence spectrum resembling that of white noise at low frequencies (see figure 7.10(a)). These results suggest that the model is not sensitive to the high-frequency content of the forcing, but to whether or not a level of noise is present at low frequencies. To test this idea, the synthetic turbulence was high-pass filtered to remove the low-frequency noise. As a consequence, the low-frequency motions disappear and the high-frequency content is reduced compared to the level of the forcing. Therefore, one important property of the system is that it acts as a low-pass filter. As such, it does not transfer energy from the higher to the lower frequencies but simply damps any fluctuations greater than a cutoff frequency while it amplifies any fluctuations smaller than this cutoff frequency. In fact, this is clear from (7.56) and figure 7.10 simply provides numerical evidence of the low-pass filtering property of (7.53a).

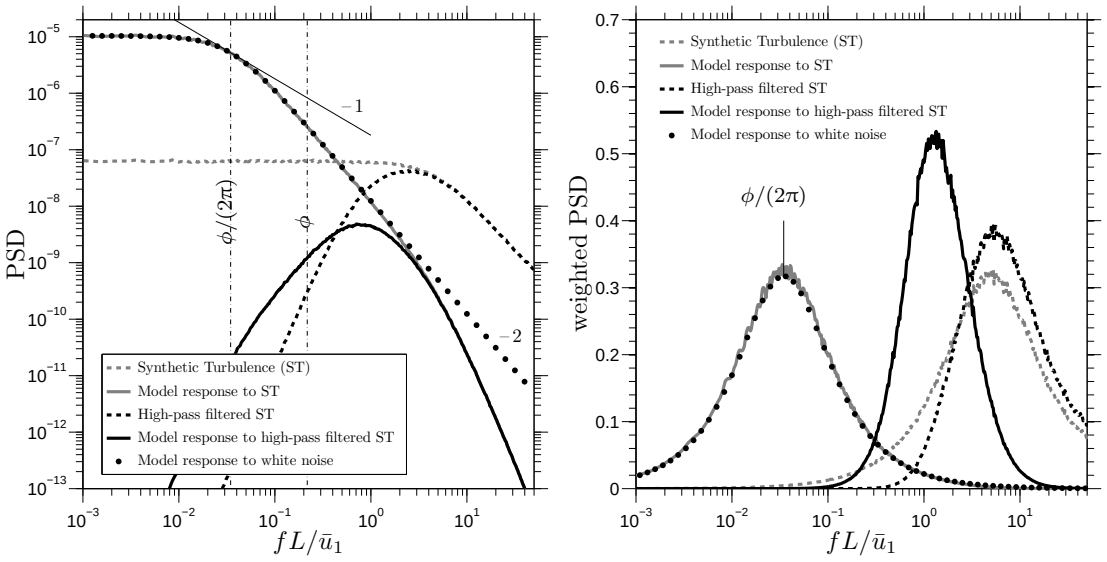

(a) PSD (b) weighted PSD

FIGURE 7.10: Spectra from the stochastic ODE using different forcing: a synthetic turbulence signal based on a one-dimensional digital-filter approach (see section 7.4.2), the same synthetic turbulence signal but high-pass filtered with cutoff frequency $f_c = 5\bar{u}_1/L$, and white noise (see section 7.4.1)

From (7.56) or (7.59), it is straightforward to see that the system is a first-order low-pass filter with cutoff Strouhal number $\phi/(2\pi)$. The power spectral density of the shock motions or wall-pressure fluctuations near the mean shock foot rolls off as S_t^{-2}. Moreover, considering the premultiplied spectra (i.e. $f \times \mathcal{S}(f)$), one can show that there exists a maximum at $\phi/(2\pi)$ which will be denoted $\phi_{\max}$. Note that it coincides with the frequency (i.e. Strouhal number here) where the PSD is tangent to S_t^{-1}, as indicated in figure 7.10. This is the frequency typically quoted when characterising the property of the low-frequency oscillations (see Dupont et al., 2006, for example). Incidentally, it corresponds to the cutoff frequency of the dynamical system (7.53).

Based on the above results, it appears justified to simply use a white-noise forcing to predict the wall-pressure weighted spectra and directly compare the result with the low-frequency motions observed both numerically and experimentally. Such a comparison is provided in figure 7.11, where the model is seen to be capable of not only predicting reasonably well the frequency of the most energetic low-frequency motion but also the broadband nature of the dynamics, which is an important aspect of the problem. This encouraging result and the implications for understanding the underlying source of the low-frequency motions will be discussed in section 7.5.3. Before doing so, we would like to take advantage of the model to describe the map of $\phi_{\max}$ for any given combination of upstream Mach number and wedge angle and discuss the sensitivity of the model to the choice of the constant values.

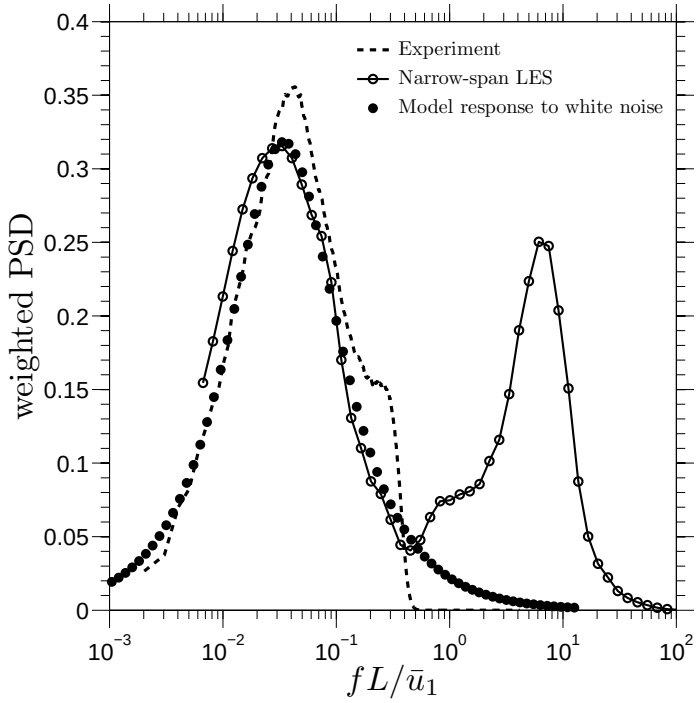

FIGURE 7.11: Weighted spectra from the model compared with the LES and experimental results. The LES spectrum is taken from figure 6.2 and the experimental data from Dupont et al. (2006). Both the LES and experimental data are from wall-pressure probes near the mean shock-foot position. The experimental signal was low-pass filtered with cutoff frequency $f_c = 2.5\bar{u}_1/L$. The premultiplied spectra were normalised using the power available at low-frequencies only (i.e. for the LES signal, the peak at higher frequencies is not included in the normalisation)

7.5.2 Cutoff-frequency map and sensitivity to the model constants

One great advantage of the present model is the possibility to use it for any given values of M_1 and θ. Figure 7.12(a) shows the map of $\phi_{\max}$ for M_1 ranging from 1 to 6 and θ from 2° to 30°, whenever a regular reflection exists. The first remark is that most values are within the range 10^{-2} to 10^{-1}, which is consistent with the experimental observations of SBLI (see Dussauge et al., 2006, for example). Additionally, it is found that for a constant wedge angle, $\phi_{\max}$ increases with increasing Mach number and for a constant upstream Mach number, $\phi_{\max}$ decreases with increasing wedge angle. The latter trend can be tested against the experimental results of Dupont et al. (2006)[4], as shown in figure 7.12(b). The agreement is well within the model and measurement uncertainties.

One should point out that $\phi_{\max}$ is expected to depend on the boundary-layer properties. Indeed, ϕ is explicitly related to the boundary-layer skin friction in (7.53b) and this could affect the results presented in figure 7.12(a), where $\bar{C}_{f_0} = 1.35 \times 10^{-3}$. In addition, the modelling constants $F'(0)$, r, r', r'' and Λ may all have significant impacts

[4]Note that those are to the author's knowledge the only data available to date on reflected-shock unsteadiness with sufficiently long sample size.

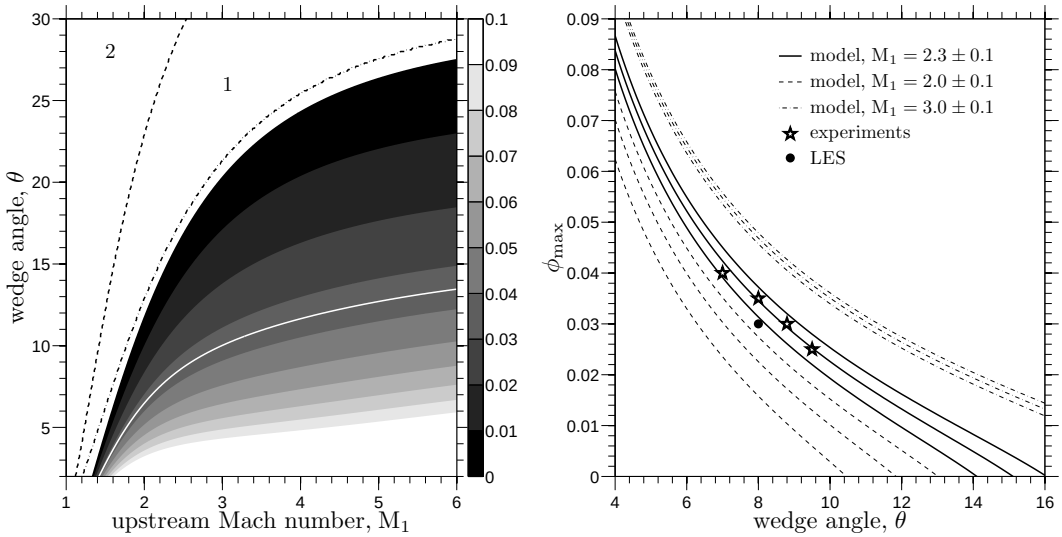

(a) map of $\phi/(2\pi)$ (b) IUSTI case

FIGURE 7.12: Predicted most energetic low frequency $\phi_{\max}$ for different (M_1, θ) pairs. In (a), the *solid white line* gives the $\phi_{\max} = 0.035$ contour. The *dashed line* and *dash-dotted line* delimit two regions, labelled 1 and 2. Region 1 corresponds to Mach reflection cases and region 2 to cases where no oblique incident shock is formed. In (b), the Mach 2.3 case of IUSTI is described for a wide range of wedge angles. The cases where $M_1 = 2$ and $M_1 = 3$ are also provided. For all cases, a variation of ± 0.1 in the upstream Mach number value is applied to look at the sensitivity of the result to M_1. The narrow-span LES result is also indicated together with the experimental results of Dupont et al. (2006). In both (a) and (b), the boundary-layer skin-friction properties were those of the IUSTI flow case

on the map of $\phi_{\max}$. To estimate the relative sensitivity to each of those constants, one can introduce an error with respect to their chosen values and look at the modifications of figure 7.12(a).

The results of such sensitivity study are presented in figure 7.13, where each constant is successively doubled and halved. Overall, the aforedescribed monotonic trends are preserved with steeper/more gradual slopes and/or increased/reduced levels of $\phi_{\max}$. To go into this in more detail, let us first note that the contour-plot is split into 10 equally-spaced levels between 0 and 0.1. In addition, both the original and new $\phi_{\max} = 0.035$ contours are displayed. By looking by how much the new contour is displaced relative to the original one, it is possible to provide a qualitative judgement on the sensitivity of $\phi_{\max}$ to a significant error in each individual model parameters. If a change by a factor two or one half of the parameter value introduces less than a 5% change in the $\phi_{\max} = 0.035$ contour, the model is deemed *not sensitive* to this particular parameter. If the effect is between 5% to 20%, the model is qualified *weakly sensitive* to the parameter in question; from 20% to 50% it is said to be *sensitive* and if beyond 50% *strongly sensitive*. The characterisation of each model parameter is reported in table 7.2.

Variable	Response of $\phi_{\max}$ to a:		characteristisation
	100% increase in	50% decrease in	
r''	$< 5\%$	$< 5\%$	not sensitive
$\bar{C}_{f_0}$, Λ	$< 15\%$	$< 15\%$	weakly sensitive
$F'(0)$	$< 15\%$	$< 15\%$	weakly sensitive
r	$< 40\%$	$< 40\%$	sensitive
r'	$< 40\%$	$< 70\%$	strongly sensitive

TABLE 7.2: Gross estimate of the sensitivity of the model to significant individual errors in the choice of the model parameters

Two important results arose from the sensitivity study. First, the sensitivity of the model to the mean boundary-layer properties is weak for $\bar{C}_{f_0}$ and insignificant for r'', suggesting that the map in figure 7.12(a) is a good estimate for other mean boundary-layer properties (as long as the hypotheses used to derive the model hold). The mean boundary-layer properties thus play a major role in setting the interaction length (see the steady-state equation (7.25a)) but their effect on the final dynamical equation is only weak. Second, the accuracy of the model for κ_2 and to a lesser extent for κ_p is crucial. While r can be easily determined to a relatively good accuracy (see section 7.2), r' is the most critical aspect of the present model and further improvements could be sought in the future. Nevertheless, the overall monotonicity of the map of $\phi_{\max}$ and the order of magnitude of the predicted $\phi_{\max}$ are maintained even for these sensitive cases. This demonstrates that the Strouhal-number value for the most energetic low-frequency shock motions is robust with values remaining below 0.1 for a wide range of configurations, as argued by Dussauge et al. (2006).

Finally, it is important to bear in mind that the model is based on an approximate form of the momentum integral equation which itself relies on four assumptions (see section 7.1.3), among which two are of primary importance. First, the interaction must be sufficiently large for the shock-crossing point to be above the incoming boundary layer. Therefore, one does not expect the model to be correct for weak interactions (i.e. for the smallest $(p_2^+ - p_1)/\tau_w$ values). Second, the interaction was considered to be two dimensional. Thus, any large spanwise wrinkling of the shock is not considered. In both cases, it would be possible to extend the model and release those constraints but this is left for future work. We now proceed to a more general discussion about the contribution of the model to the understanding of the low-frequency shock motions.

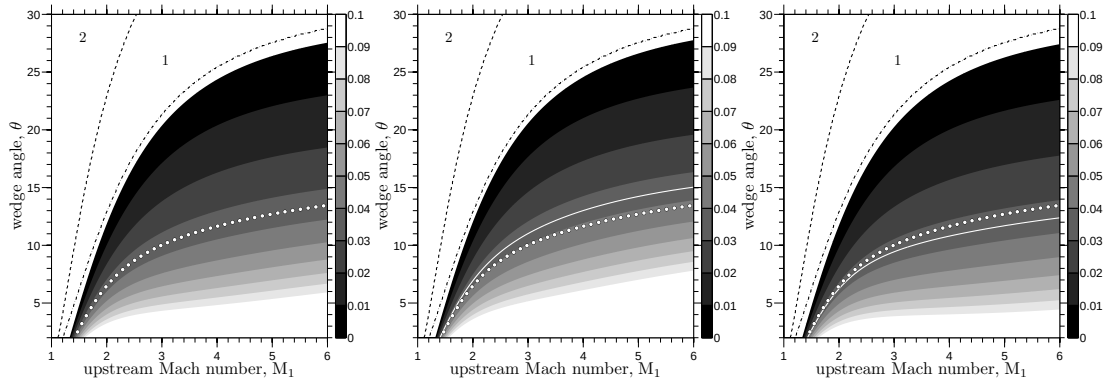

(a) original (b) $F'(0)/2$ (c) $2F'(0)$

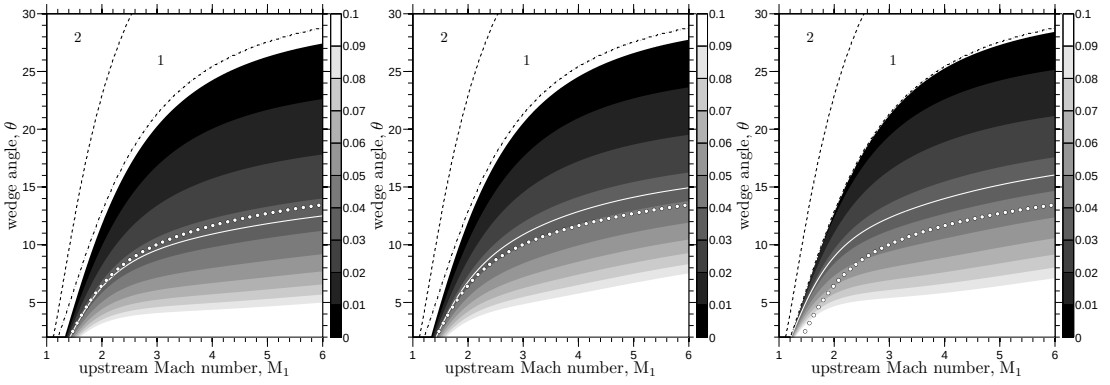

(d) $\bar{C}_{f_0}/2$, $\Lambda/2$ (e) $2\bar{C}_{f_0}$, 2Λ (f) $r/2$

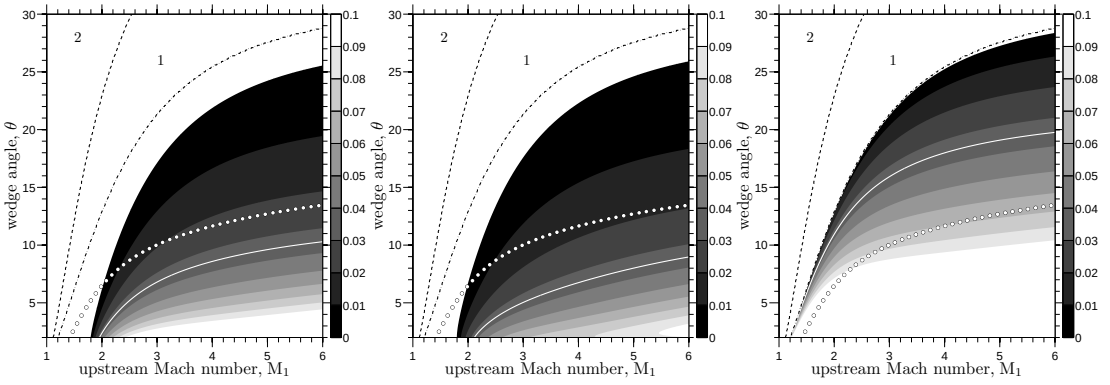

(g) $2r$ (h) $r'/2$ (i) $2r'$

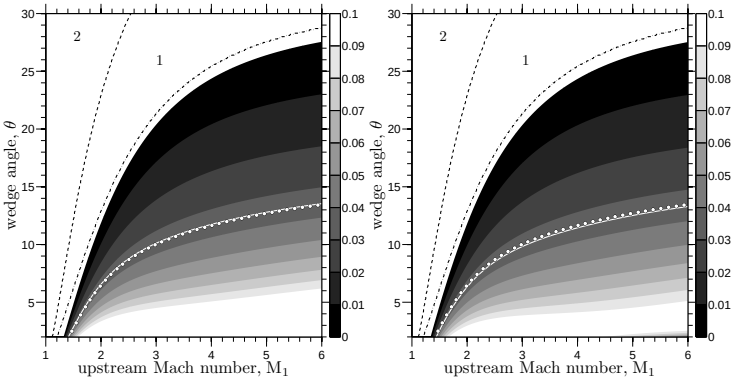

(j) $r''/2$ (k) $2r''$

FIGURE 7.13: Sensitivity of the predicted $\phi_{\max}$ map to variations in the model constants. Same legend as in figure 7.12(a) at the difference that the additional *white dots* indicate the position of the $\phi_{\max} = 0.035$ contour when using the reference values

7.5.3 Discussion and implications with respect to the low-frequency unsteadiness

Plotkin (1975) first postulated that the reflected-shock could obey a stochastically forced first-order ordinary equation which is mathematically identical to the one derived here (see (7.53a))[5]. The fact that the above lengthy derivations lead to the same governing equation as the one proposed by Plotkin (1975) is comforting given the completely different approaches undertaken. In the present approach the final governing equation is derived from the Navier–Stokes equations. To some extent, it may be seen as a proof of Plotkin's postulate (although this was not our original intention), with two distinct advantages that the underlying assumptions may be more clearly identified and that the timescale of the restoring mechanism is formally expressed as a function of the problem input parameters. In Plotkin (1975), one needs to determine this constant experimentally, resulting in a lack of applicability of the model, despite its mathematically appealing form. To the best of the author's knowledge, since the original publication of Plotkin (1975), only the two papers by Poggie and Smits (2001, 2005) offer careful comparisons between Plotkin's model and experimental data, in each case with success.

Poggie and Smits (2001) argue that, although the final model is described by a linear equation, it does not mean that the non-linearities of the system are not accounted for. Their argument is that if one had considered a linearised theory (i.e. linearised Euler equations), the shock-motion spectrum would be the same as that of the incoming turbulence, which is not the case in the model. In the present derivation, one can see that, while the governing equation for the shock motions was clearly linearised (see steps between (7.22) and (7.24)) on the basis of sufficiently small shock displacements relatively to the interaction size, other significant non-linear effects are mechanically embedded in the timescale ϕ^{-1}. Indeed, looking at the constituents of ϕ, one can see that although the model is expressed in the form of point-particle dynamics (i.e. the shock foot position), it does not convey a direct relation between a given velocity fluctuation and the shock response to it, as linearised Euler would do, but instead it accounts for integrated effects by means of the different thicknesses (see (7.2 *a*–*d*)) which are non-linear functions of the velocity perturbations. In other words, the model accounts for the non-linear coupling between the shock-system and the boundary layer.

As mentioned in the previous section, the model describes this coupled shock/boundary-layer system as a low-pass filter with characteristic timescale ϕ^{-1}. One remarkable result is that this timescale is significantly larger than any characteristic timescales of the incoming boundary layer ($\phi/(2\pi)$ is in the 10^{-2} to 10^{-1} range giving $t_s \sim 10$ to $100L/\bar{u}_1$ to compare with $t_f = \delta_0/\bar{u}_1 \sim L/\bar{u}_1$ assuming that the interaction length scales with δ_0). This conforms to experimental observations (Dupont et al., 2006), and the known issue

[5]Note that Plotkin (1975) developed his model in the context of the compression-corner configuration.

in numerical simulations that such flows have long initial transients, even for laminar cases (indeed, in the absence of forcing, the convergence to the steady solution would be as $\exp(-t/t_s)$).

The low-pass filtering property of the system indicates that, strictly speaking no transfer of energy from the higher to the lower frequencies is occurring. Instead, any high frequency is damped and any low frequency is amplified, with the frontier between high and low being determined by ϕ. This was shown mathematically through the model response to white-noise forcing and numerically through direct integration of the response to synthetic turbulence signals. Therefore, the system itself is simply amplifying *existing* low-frequency fluctuations, even if energetically insignificant, while it filters out the high-frequency fluctuations, even if energetically significant. Moreover, the resulting broadband spectrum about a particular Strouhal number is not a property of the forcing but a characteristic of the shock/boundary-layer system itself.

Based on the preceding discussion, it is inferred that the origin of the low-frequency oscillations is not in the forcing but in the dynamics of the system formed by the shock/boundary-layer interaction. Of course, if one applies any specific forcing below the natural frequency of the system, such forcing will be picked up and magnified. A specific forcing could be any significantly-long upstream coherent structures (see Ganapathisubramani et al., 2007b, 2009, and references therein) or particular flow features within the interaction itself (see Dussauge and Piponniau, 2008; Piponniau et al., 2009; Pirozzoli and Grasso, 2006, and references therein). However, we stress that, mathematically speaking, these are not necessary and the low-frequency motions can simply arise from a background (white) noise, as successfully demonstrated in figure 7.11. This leads to the final question of flow control.

In the light of the current discussion, there are no reasons to believe that a periodic oscillation could be of any help in order to inhibit the low-frequency motions. From the dynamical-system point of view, there are two possible approaches: remove any low-frequency forcing or modify in some ways the natural frequency of the system. The first option seems rather impracticable and it is better to focus on the second option. Obviously, one cannot modify the Navier–Stokes equations and the only alternative in practical applications is to modify the boundary conditions. Thus, one would need to implement wall-boundary conditions such that the net effect on the coupled shock/boundary-layer system may be written in the form of a first-order linear ODE for ε so that (7.53a) becomes:

$$\frac{1}{\bar{u}_1}\frac{\mathrm{d}\varepsilon}{\mathrm{d}t} + (\phi - \Xi)\frac{\varepsilon}{L} = \Pi C''_{f_0}(t), \tag{7.61}$$

with ideally $\Xi = \phi$. One possible solution is through blowing/sucking upstream and downstream of the mean shock-foot position with a decision based on the shock-foot

motion, if of course this is technically feasible. Supposing that such an algorithm could be implemented, (7.61) would lead to $\varepsilon(t) = \bar{u}_1 \Pi \int_0^t C''_{f_0}(t')\mathrm{d}t'$ and the shock-foot weighted PSD would be that of C''_{f_0}. The key point is that such an actuation would need to be based on the instantaneous (low-pass filtered) shock-foot motion and would therefore be occurring on timescales of the order of ϕ^{-1}, which is typically $\mathcal{O}(10\delta_0/\bar{u}_1)$. Failing to be out-of-phase with the low-frequency shock motions would be catastrophic as one would then potentially be exciting the system natural frequency.

A stochastic ODE for the reflected-shock foot motions has been derived in this chapter, starting from the Navier–Stokes equations and based on some assumptions that were checked using LES data. The general form (7.19) of the governing equation relies on the assumed existence of a separation of variables (7.10), which is well supported by the LES data, allowing a transformation of what was initially a partial differential equation into an ordinary one. The derivation assumes two-dimensional motions (i.e. the spanwise wrinkling of the shock was not considered) with the shock crossing point located above the incoming boundary-layer height δ_0. Under such conditions, (7.19) was derived and then linearised on the basis of sufficiently small shock displacements and the analysis of LES data. This final form of the governing equation was found to be mathematically identical to the one postulated by Plotkin (1975) and capable of reproducing the wall-pressure low-frequency spectrum in the vicinity of the mean shock-foot position.

Upon modelling the constituents of the derived governing equation, the dynamical system could be closed and expressed in terms of its input parameters: the upstream Mach number M_1, the wedge angle θ and the upstream boundary-layer properties (i.e. skin friction and momentum thickness). Although the upstream boundary-layer properties are found to be important at setting up the interaction length, the dynamical system was shown to be mainly controlled by M_1 and θ. A wide range of input (M_1, θ) pairs was tested and the predicted most energetically significant low-frequency motions, expressed in the form of the Strouhal number $S_t = fL/\bar{u}_1$, were shown to remain in the range 0.01 to 0.1, confirming the experimental evidence collected in Dussauge et al. (2006). The most energetic Strouhal number was found to increase with increasing M_1 for a constant wedge angle θ, whereas it decreased with increasing wedge angle for constant M_1.

Mathematically speaking, the derived governing equation was shown to correspond to a first-order low-pass filter and the analytical spectrum derived from forcing the system with white noise was shown to be in excellent agreement with the available experimental and numerical spectra. This result is consistent with the findings of Plotkin (1975) and Poggie and Smits (2001, 2005) and leads to the suggestion that the low-frequency motions observed in SBLI need not be a characteristic of the forcing but simply the result of the low-pass filtering property of the dynamical system formed by the coupling between the boundary layer and the reflected shock, as demonstrated by the white-noise

forcing. This does not mean that specific forcing from upstream (see Ganapathisubramani et al., 2007b, amongst others) or downstream (see Pirozzoli and Grasso, 2006; Piponniau et al., 2009; Robinet, 2007, and chapters 5 and 6) does not play a role, but that they are not necessary. Obviously, if present and acting below the system cutoff frequency, they will inevitably be picked up by the system.

Finally, one obvious possible application of the closed form of the low-order model presented in this chapter is in the field of aerodynamic design where shockwaves interact with turbulent boundary layers. In this case, designers may be concerned with the fatigue induced by the shock low-frequency motions. This model can potentially predict the frequency of the most energetic low-frequency motions as well as the amplitude of the shock motions, given the magnitude of the forcing.

8. Conclusion

A major concern in practical high-speed aerospace applications is the occurrence of energetically-significant low-frequency shock motions when shock waves interact with turbulent boundary layers, potentially leading to undesirable unsteady pressure loads on the airframe. Understanding the origin of such low-frequency motions was the principal motivation of this dissertation.

When this project started, and to the best of the author's knowledge, no numerical evidence on the existence of low-frequency shock motions in shock-reflection configurations was available and all initial efforts were therefore aimed at establishing whether the experimental observations could be confirmed using large-eddy simulations. To this end, an inflow-turbulence generator that could cover integration times of the order of $10^4\delta_0/\bar{u}_1$ was needed, with the principal constraint that it would not introduce any particular mode into the computational domain which were susceptible of interacting with the shock/boundary-layer system. Thus, a modified version of the digital filter was introduced in the SBLI code (see chapter 2). The ability of this approach to produce statistical results in good agreement with earlier results was demonstrated in chapters 3 and 4 via grid-, domain- and subgrid-scale-model-sensitivity studies. It was established that, given the chosen final grid resolution, results were only marginally affected by the choice of eddy-viscosity model and that the most critical parameter for the prediction of the interaction length was the choice of the domain spanwise extent.

In the process of establishing whether one could reproduce the low-frequency dynamics observed in experiments, three different flow cases were used with a particular focus on the experiments of the IUSTI group in Marseille, for which two simulations covering long integration times were run. In particular, the first one was performed on a narrow domain to allow for the longest integration time possible, covering about sixty cycles of the most energetic low-frequency motions. Despite the artificial confinement due to the short spanwise extent used, this first LES clearly established that numerical simulations could exhibit low-frequency motions that are similar to the experimental findings. These motions were found to be most prominent in the vicinity of the reflected-shock foot and characterised by a broadband spectrum covering more than one decade of frequencies with a peak in the weighted spectrum located about two orders of magnitude below the peak associated with the upstream boundary-layer turbulence.

Upon studying the unsteady wall-pressure distributions of all (four) LES, it was confirmed that using L and $\bar{u}_1$ as reference scales for the Strouhal number gave values of

about 0.03 for the most energetic oscillations. Moreover, looking at dispersion maps, all cases were characterised by broadband contours typical of the turbulence but also by linear dispersion relations due to the organised shedding of shear-layer vortical structures and propagation of acoustic waves (in both upstream and downstream directions). Of particular interest was the detection of upstream-propagating pressure waves with wavelengths exceeding the interaction length and confined within the first third of the interaction.

The phase-evolution of the pressure fluctuations at different frequencies was studied in the case of the narrow-span IUSTI case. For sufficiently low Strouhal numbers (near 0.05), a phase jump of π was found about one third of the way down the interaction. Following Hudy et al. (2003), it was argued that this jump could be an indication of the existence of a global mode, similar to the one found in chapter 5 where the stability of the time-averaged flow was studied. Although the validity of such a stability analysis is debatable, the highest global-mode growth rate was for the 2D mode (i.e. for zero spanwise wavenumber) with a linear regime which could scale on timescales similar to the timescale of the most significant low-frequency shock motions. It was argued on the basis of a decoupling between the global-mode characteristic timescale and the timescales associated with the incoming turbulence that the turbulent nature of the flow may only be required to produce the base-flow profiles and that it is not playing a significant role in the development of the large-scale motions.

It is manifest from looking at the LES flow fields that the interaction region is the place of high levels of intermittency. Of particular interest is the separation bubble which in fact is better viewed as a mixture of reversed and non reversed flow forming what were called cells or pockets of reversed flow. These cells were found capable of persisting for more than $10^2\delta_0/\bar{u}_1$ with spanwise extents of the order of the interaction length, setting important constraints on the simulation cost to capture them. They were seen to meander in the spanwise direction, followed occasionally by the merging of two of such cells. The presence of such structures and their spanwise motions has direct consequences on the interpretation of fixed-point wall-pressure spectra where, for example, the low-frequency end of the spectrum can be artificially underestimated while the high-frequency end is artificially enhanced. This can account for some of the differences between the wall-pressure spectra obtained from a computational domain that is sufficiently wide to resolve such structures and from a computational domain that is too narrow to capture such patterns.

The choice of the computational-box spanwise extent can be critical to the accuracy of the predicted flow fields. In the course of this work this difficulty was combined with other pitfalls arising from attempts to compare simulation data with experimental data. While the occurrence of low-frequency shock motions appeared to be a relatively robust feature, the topology of the interaction was seen to be rather sensitive to both

experimental and numerical artifacts such as the presence of the wind-tunnel side walls, spanwise-confinement effects and inflow conditions to name a few. Fundamental studies on the origin of the low-frequency motions are therefore difficult. However, the digital-filter approach used in this study allowed the manipulation of the incoming boundary layer and a numerical exercise, consisting in restricting the size of the upstream coherent structures, led to the conclusion that independently of the existence of long coherent structures the low-frequency motions would persist. Therefore, although the structures described in Ganapathisubramani et al. (2007b, 2009) are likely to enhance the low-frequency shock motions, they are not found essential to the low-frequency dynamics of shock-reflection configurations. In the author's view, this may be an illustration of an artifact obscuring the actual mechanism sought. Unfortunately, the need to cover a significant dynamical range to resolve both the turbulence and the broadband low frequencies at satisfying levels of convergence makes sensitivity studies unrealistic due to the associated prohibitive computational cost. Finally, to add to the complexity of the problem, it has been illustrated that both the turbulence and the low-frequency fluctuations significantly contribute to the total energy of the fluctuations. Decoupling events related to low-frequency motions from purely turbulence-related events, as perhaps pointed out by the stability-analysis results, is not achievable in a purely dynamical framework. This led us to look at conditional averages, which were then used for a more theoretical study.

As exposed in the beginning of this study, the physical mechanisms at the origin of the low-frequency shock motions are not understood. A number of tentative explanations were considered in chapter 1 and usually fall into one of two categories. The first relates the low-frequency motions to specific events or flow structures from the upstream turbulent boundary layer, whereas the second looks for causal mechanisms within the interaction itself (i.e. downstream of the shock). In both cases, the difficulty resides in identifying a mechanism that can span timescales of the order of $10^1\delta_0/\bar{u}_1$ to $10^2\delta_0/\bar{u}_1$. In the author's view, the variety of the mechanisms proposed in the literature, together with the subsequent debate about the merits of one approach relative to another is symptomatic of the difficulty one has in identifying and then separating individual events from a (supposedly) non-linear (chaotic) system, where actual causal events may well be impossible to detect. Instead of attempting to check the relevance of one assumed mechanism against numerical/experimental data with the inherent complexity of extracting this from fully turbulent flow, an attempt to characterise in a useful way the properties of the dynamical system arising from the coupling between the shock and the boundary layer was offered.

This led to the development of a stochastic ODE for the reflected-shock foot motions, starting from the Navier–Stokes equations and based on assumptions that were all supported by the LES data. The most simplified form of the derived ODE was found to be

mathematically identical to the one postulated by Plotkin (1975) and capable of reproducing the wall-pressure low-frequency spectrum in the vicinity of the mean shock-foot position. All the constituents of the final ODE were modelled and the closed system could be solved. It was found that although the upstream boundary-layer properties are important at setting up the interaction length, the dynamical system is mainly controlled by M_1 and θ. A wide range of input (M_1, θ) pairs was tested and the predicted most energetically significant low-frequency motions, expressed in the form of the Strouhal number $S_t = fL/\bar{u}_1$, were shown to remain in the range 0.01 to 0.1, confirming the experimental evidence collected in Dussauge et al. (2006) and the present LES results. The Strouhal number was found to increase with increasing M_1 for a constant wedge angle θ, whereas it decreased with increasing wedge angle for constant M_1.

Mathematically speaking, the derived governing equation was shown to correspond to a first-order low-pass filter and the analytical spectrum derived from forcing the system with white noise was shown to be in excellent agreement with the available experimental and numerical spectra. This result leads to the suggestion that the low-frequency motions observed in SBLI need not be a characteristic of the forcing but can simply be the result of the low-pass filtering property of the dynamical system formed by the coupling between the boundary layer and the reflected shock. Of course, this does not mean that a specific forcing either from upstream or downstream does not play a role, but that it is not necessary.

In summary, the principal results and conclusions of this study are:

- large-eddy simulation is capable of reproducing the observed reflected-shock low-frequency motions at a lower cost than direct numerical simulation and is therefore a good tool to investigate the key mechanisms involved in SBLI
- the digital filter is an effective approach to control the size of the incoming turbulence structures
- low-frequency motions appear near the shock foot even when the inflow is carefully controlled to exclude upstream forcing at these frequencies
- the occurrence of broadband low-frequency shock motions is a robust feature of SBLI despite their sensitivity to small variations in the configuration
- great care must be taken to minimise possible numerical and experimental artifacts (side-wall effects, inflow turbulence, meandering effect of coherent structure on the interpretation of the spectrum obtained from a static probe, short-signal effects...)
- the time-averaged flow field in the interaction is globally unstable with growth rates compatible with timescales characteristic of the low-frequency motions

- the LES results support the idea that the interaction length L/δ_0 may be linearly related to the ratio $(p_2 - p_1)/\tau_w$, in connection with the approximate balance between the rates of change of momentum and pressure thicknesses in the initial part of the interaction
- a phase jump of π is observed in the propagation of wall-pressure fluctuations at low frequencies with a spatial distribution in agreement with that of the global mode
- the low-frequency shock motions can be modelled by a first-order stochastic ODE which is derived from the Navier–Stokes equations
- the closed form of the proposed model supports the experimental finding that the Strouhal number of the most energetic fluctuations is similar over a wide range of Mach numbers and wedge angles
- the low-frequency shock motions need not be a characteristic of the forcing and can simply be the result of the coupled shock/boundary-layer system acting as a low-pass filter

In future work it would be of particular interest to improve and extend the model proposed in this dissertation. More specifically, the 2D assumption could be relaxed to allow for the shock to have spanwise wrinkles. More LES results could be acquired at higher Mach numbers and different wedge angles to improve some of the crude modelling approaches (e.g. κ_2). The model could also be extended to compression-ramp configurations. In addition, wall-boundary conditions for the temperature could be modified to include cold- or hot-wall configurations. The model may also be used to look at active-control approaches. As a byproduct of the model derivations, we have also obtained a steady-state equation which can in principle be closed to obtain a useful predictive tool for the interaction length, in connection with the suggested linear trend between L/δ_0 and $(p_2 - p_1)/(2\tau_w)$ in chapter 4. In the course of this study, the question of wind-tunnel side-wall effects was raised and it would be of interest to run simulations which account for the presence of the side walls as this would also be relevant for practical applications (e.g. engine intakes). Finally, one immediate possible work would consist in further analysis of the present LES database to investigate the dynamics of the reversed-flow pockets in relation with the low-frequency motions (see figure 6.22).

A. Filtering the Navier–Stokes equations

One can apply the grid-filter operator defined in section 2.1.2.1 to (2.1 a–c). For example, the filtered continuity equation is

$$\frac{\partial \bar{\rho}}{\partial t} + \frac{\partial \overline{\rho u_i}}{\partial x_i} = 0, \tag{A.1}$$

following the linearity and commutativity properties of the filter (see 2.1.2.1). Furthermore, using the Favre-filter notation (defined page 24), (A.1) can be written

$$\frac{\partial \bar{\rho}}{\partial t} + \frac{\partial \bar{\rho}\tilde{u}_i}{\partial x_i} = 0. \tag{A.2}$$

Similarly, the momentum equation becomes:

$$\frac{\partial \bar{\rho}\tilde{u}_i}{\partial t} + \frac{\partial \bar{\rho}\widetilde{u_i u_j}}{\partial x_j} = -\frac{\partial \bar{p}}{\partial x_i} + \frac{1}{\mathrm{Re}}\frac{\partial \bar{\tau}_{ij}}{\partial x_j}. \tag{A.3}$$

Notice that the second term in (A.3) cannot be known (this is a direct consequence of the application of the filter operator onto non-linear terms). The stress tensor σ_{ij} is thus introduced (defined below) and will have to be modelled and related to the resolved fields. Similarly, the viscous stress tensor (see (2.1f)) is composed of non-linear terms that cannot be computed explicitly so that the following tensor d_{ij} is also introduced.

$$\sigma_{ij} = \bar{\rho}\left(\widetilde{u_i u_j} - \tilde{u}_i \tilde{u}_j\right), \tag{A.4}$$

$$d_{ij} = \bar{\tau}_{ij} - \underbrace{\tilde{\mu}\left(\frac{\partial \tilde{u}_j}{\partial x_i} + \frac{\partial \tilde{u}_i}{\partial x_j} - \frac{2}{3}\delta_{ij}\frac{\partial \tilde{u}_k}{\partial x_k}\right)}_{\breve{\tau}_{ij}}. \tag{A.5}$$

With those notations, the Favre-filtered momentum equation is:

$$\frac{\partial \bar{\rho}\tilde{u}_i}{\partial t} + \frac{\partial \bar{\rho}\tilde{u}_i\tilde{u}_j}{\partial x_j} + \frac{\partial \bar{p}}{\partial x_i} - \frac{1}{\mathrm{Re}}\frac{\partial \breve{\tau}_{ij}}{\partial x_j} = -\frac{\partial \sigma_{ij}}{\partial x_j} + \frac{1}{\mathrm{Re}}\frac{\partial d_{ij}}{\partial x_j}, \tag{A.6}$$

where the right-hand side cannot be computed solely from the resolved fields and thus must be modelled. Following the approach used for the momentum equation, the following scalar and vectors are defined:

$$\breve{E}_t = \frac{\bar{p}}{\gamma-1} + \frac{1}{2}\bar{\rho}\tilde{u}_i\tilde{u}_i, \tag{A.7a}$$

$$\alpha_j^{\mathrm{i}} = \overline{E_t u_j} - \breve{E}_t\tilde{u}_j, \tag{A.7b}$$

$$\alpha_j^{\mathrm{ii}} = \overline{p u_j} - \bar{p}\tilde{u}_j, \tag{A.7c}$$

$$\alpha_j^{\mathrm{iii}} = \frac{1}{\mathrm{Re}}\left(\overline{\tau_{ij}u_i} - \breve{\tau}_{ij}\tilde{u}_i\right), \tag{A.7d}$$

$$\alpha_j^{\mathrm{iv}} = \overline{\mu\frac{\partial T}{\partial x_j}} - \tilde{\mu}\frac{\partial\tilde{T}}{\partial x_j}. \tag{A.7e}$$

Notice the relation:

$$\bar{E}_t = \breve{E}_t + \frac{1}{2}\sigma_{ii}. \tag{A.8}$$

The Favre-filtered energy equation can then be expressed as:

$$\begin{aligned}\frac{\partial\breve{E}_t}{\partial t} + \frac{\partial(\breve{E}_t+\bar{p})\tilde{u}_j}{\partial x_j} - \frac{1}{\mathrm{Re}}\frac{\partial\breve{\tau}_{ij}\tilde{u}_i}{\partial x_j} + \frac{1}{(\gamma-1)\,\mathrm{Re}\,\mathrm{Pr}\,\mathrm{M}^2}\frac{\partial}{\partial x_j}\left[\tilde{\mu}\frac{\partial\tilde{T}}{\partial x_j}\right] \\ = -\frac{1}{2}\frac{\partial\sigma_{ii}}{\partial t} - \frac{\partial}{\partial x_j}\left[\alpha_j^{\mathrm{i}} + \alpha_j^{\mathrm{ii}} - \alpha_j^{\mathrm{iii}}\right] - \underbrace{\frac{1}{(\gamma-1)\,\mathrm{Re}\,\mathrm{Pr}\,\mathrm{M}^2}\frac{\partial\alpha_j^{\mathrm{iv}}}{\partial x_j}}_{B_7}\end{aligned} \tag{A.9}$$

In theory, the entire right-hand side of the above equation should be modelled. In practice, this is difficult and the smallest terms are neglected. To do so, (A.9) is written in a different way to give more physical meaning to each subgrid scale terms. First, the divergence of equations (A.7b) and (A.7c) is rearranged:

$$\frac{\partial\alpha_j^{\mathrm{i}}}{\partial x_j} = \underbrace{\frac{1}{\gamma-1}\frac{\partial}{\partial x_j}\left[\overline{pu_j} - \bar{p}\tilde{u}_j\right]}_{B_1} + \frac{1}{2}\frac{\partial}{\partial x_j}\left[\overline{\rho u_i u_i u_j} - \bar{\rho}\tilde{u}_i\tilde{u}_i\tilde{u}_j\right], \tag{A.10}$$

$$\frac{\partial\alpha_j^{\mathrm{ii}}}{\partial x_j} = \underbrace{\overline{p\frac{\partial u_j}{\partial x_j}} - \bar{p}\frac{\partial\tilde{u}_j}{\partial x_j}}_{B_2} + \overline{u_j\frac{\partial p}{\partial x_j}} - \tilde{u}_j\frac{\partial\bar{p}}{\partial x_j}. \tag{A.11}$$

Upon multiplication of the momentum equation by u_i, one obtains the kinetic energy equation:

$$\frac{1}{2}\frac{\partial\rho u_i u_i}{\partial t} + \frac{1}{2}\frac{\partial\rho u_i u_i u_j}{\partial x_j} = -u_i\frac{\partial p}{\partial x_i} + \frac{1}{\mathrm{Re}}u_i\frac{\partial\tau_{ij}}{\partial x_j}. \tag{A.12}$$

Filtering (A.12) yields:

$$\frac{1}{2}\frac{\partial\bar{\rho}\widetilde{u_i u_i}}{\partial t} + \frac{1}{2}\frac{\partial\overline{\rho u_i u_i u_j}}{\partial x_j} = -\overline{u_i\frac{\partial p}{\partial x_i}} + \frac{1}{\mathrm{Re}}\overline{u_i\frac{\partial\tau_{ij}}{\partial x_j}}. \tag{A.13}$$

Similarly, multiplying the filtered momentum equation (A.6) by $\tilde{u}_i$ gives:

$$\frac{1}{2}\frac{\partial\bar{\rho}\tilde{u}_i\tilde{u}_i}{\partial t}+\frac{1}{2}\frac{\partial\bar{\rho}\tilde{u}_i\tilde{u}_i\tilde{u}_j}{\partial x_j}+\tilde{u}_i\frac{\partial\bar{p}}{\partial x_i}-\frac{1}{\mathrm{Re}}\tilde{u}_i\frac{\partial\breve{\tau}_{ij}}{\partial x_j}=-\tilde{u}_i\frac{\partial\sigma_{ij}}{\partial x_j}+\frac{1}{\mathrm{Re}}\tilde{u}_i\frac{\partial d_{ij}}{\partial x_j}. \tag{A.14}$$

Subtracting (A.14) to (A.13) and using the definitions (A.4) and (A.5), one finds:

$$\begin{aligned}\frac{1}{2}\frac{\partial}{\partial t}\underbrace{\left[\bar{\rho}\widetilde{u_iu_i}-\bar{\rho}\tilde{u}_i\tilde{u}_i\right]}_{\sigma_{ii}}+\frac{1}{2}\frac{\partial}{\partial x_j}\left[\overline{\rho u_iu_iu_j}-\bar{\rho}\tilde{u}_i\tilde{u}_i\tilde{u}_j\right]&\\ =\tilde{u}_i\frac{\partial\bar{p}}{\partial x_i}-\overline{u_i\frac{\partial p}{\partial x_i}}+\frac{1}{\mathrm{Re}}\left(\overline{u_i\frac{\partial\tau_{ij}}{\partial x_j}}\underbrace{-\tilde{u}_i\frac{\partial\breve{\tau}_{ij}}{\partial x_j}-\tilde{u}_i\frac{\partial d_{ij}}{\partial x_j}}_{-\tilde{u}_i\partial\bar{\tau}_{ij}/\partial x_j}\right)+\tilde{u}_i\frac{\partial\sigma_{ij}}{\partial x_j}&\end{aligned} \tag{A.15}$$

The quadruple product in (A.10), which is not convenient and certainly difficult to model, can be replaced using (A.15) so that the sum of (A.10) and (A.11) may be written:

$$\frac{\partial\alpha_j^{\mathrm{i}}}{\partial x_j}+\frac{\partial\alpha_j^{\mathrm{ii}}}{\partial x_j}=B_1+B_2-\frac{1}{2}\frac{\partial\sigma_{ii}}{\partial t}+\frac{1}{\mathrm{Re}}\left\{\overline{u_i\frac{\partial\tau_{ij}}{\partial x_j}}-\tilde{u}_i\frac{\partial\bar{\tau}_{ij}}{\partial x_j}\right\}+\tilde{u}_i\frac{\partial\sigma_{ij}}{\partial x_j}. \tag{A.16}$$

Using the chain rule, (A.16) is rearranged:

$$\begin{aligned}\frac{\partial\alpha_j^{\mathrm{i}}}{\partial x_j}+\frac{\partial\alpha_j^{\mathrm{ii}}}{\partial x_j}=B_1+B_2-\frac{1}{2}\frac{\partial\sigma_{ii}}{\partial t}&\\ +\frac{1}{\mathrm{Re}}\left\{\frac{\partial\overline{u_i\tau_{ij}}}{\partial x_j}-\overline{\tau_{ij}\frac{\partial u_i}{\partial x_j}}-\frac{\partial\tilde{u}_i\bar{\tau}_{ij}}{\partial x_j}+\bar{\tau}_{ij}\frac{\partial\tilde{u}_i}{\partial x_j}\right\}+\underbrace{\frac{\partial\sigma_{ij}\tilde{u}_i}{\partial x_j}}_{B_3}-\underbrace{\sigma_{ij}\frac{\partial\tilde{u}_i}{\partial x_j}}_{B_4},&\end{aligned} \tag{A.17}$$

and then injected into (A.9), together with (A.7d), to give:

$$\begin{aligned}\frac{\partial\breve{E}_t}{\partial t}+\frac{\partial\left(\breve{E}_t+\bar{p}\right)\tilde{u}_j}{\partial x_j}-\frac{1}{\mathrm{Re}}\frac{\partial\breve{\tau}_{ij}\tilde{u}_i}{\partial x_j}+\frac{1}{(\gamma-1)\,\mathrm{Re}\,\mathrm{Pr}\,\mathrm{M}^2}\frac{\partial}{\partial x_j}\left[\tilde{\mu}\frac{\partial\tilde{T}}{\partial x_j}\right]&\\ =-B_1-B_2-B_3+B_4+\underbrace{\frac{1}{\mathrm{Re}}\left(\overline{\tau_{ij}\frac{\partial u_i}{\partial x_j}}-\bar{\tau}_{ij}\frac{\partial\tilde{u}_i}{\partial x_j}\right)}_{B_5}&\\ +\underbrace{\frac{1}{\mathrm{Re}}\left(\frac{\partial\tilde{u}_i\bar{\tau}_{ij}}{\partial x_j}-\frac{\partial\breve{\tau}_{ij}\tilde{u}_i}{\partial x_j}\right)}_{B_6}-B_7.&\end{aligned} \tag{A.18}$$

This completes the Favre-filtered energy equation. The terms B_1 to B_7 are consistent with the findings of Vreman et al. (1995).

B. Fortran routine to generate the mean inflow profiles

```
! ************************************************************************
!  This program generates the semi-analytic mean inflow profiles for the
!  turbulent compressible boundary layer.
!
!                                                        Emile :: January 2007
! ************************************************************************

 PROGRAM main

   IMPLICIT NONE

! ========================================================================
! Declaration section
! ========================================================================

! --- parameters ---

   integer, PARAMETER :: DBL=8 !SELECTED_REAL_KIND(15) ! Double precision parameter
   integer, PARAMETER :: Ny=81 ! Number of points to use
   real(DBL), PARAMETER :: gamma=1.4 ! Specific heats ratio
   real(DBL), PARAMETER :: kapa=0.41 ! V--K constant
   real(DBL), PARAMETER :: b=5.17
   real(DBL), PARAMETER :: omega=0.67 ! power law coeff. for dynamic visco.
   real(DBL), PARAMETER :: Csuth=0.76 ! S/Tref. ratio for Sutherland law
   real(DBL), PARAMETER :: eps=0.25 ! distance between the two x-planes

! --- global variables ---

   real(DBL) :: Uchk_eplus ! edge velocity+ in Van Driest space
   real(DBL) :: Uchk_eplus2 ! edge velocity+ in Van Driest space
   real(DBL) :: U_eplus ! edge velocity+ in Normal space
   real(DBL) :: U_eplus2 ! edge velocity+ in Normal space
   real(DBL) :: xi_eplus ! xi_edge+ value
   real(DBL) :: xi_eplus2 ! xi_edge+ value

   real(DBL) :: delta0 ! BL thickness
   real(DBL) :: delta1vd ! BL VD disp. thickness
   real(DBL) :: delta1 ! BL disp. thickness
   real(DBL) :: Taw, Tw ! Adiabatic wall & wall temperature

   real(DBL), DIMENSION(1:Ny) :: Uchk_plus ! velocity+ in Van Driest space
   real(DBL), DIMENSION(1:Ny) :: xi_plus ! xi+ coord.
   real(DBL), DIMENSION(1:Ny) :: y_plus ! y+ coord. (same in both spaces)
   real(DBL), DIMENSION(1:Ny) :: yCHK ! y coord. in Van Driest space
   real(DBL), DIMENSION(1:Ny) :: y ! y coord.
   real(DBL), DIMENSION(1:Ny) :: Uchk ! Van Driest velocity profile
   real(DBL), DIMENSION(1:Ny) :: U ! u-velocity profile
   real(DBL), DIMENSION(1:Ny) :: rho ! density profile
   real(DBL), DIMENSION(1:Ny) :: T ! temperature profile
! --- for second x-plane ---
   real(DBL), DIMENSION(1:Ny) :: Uchk_plus2 ! velocity+ in Van Driest space
   real(DBL), DIMENSION(1:Ny) :: xi_plus2 ! xi+ coord.
   real(DBL), DIMENSION(1:Ny) :: y_plus2 ! y+ coord. (same in both spaces)
   real(DBL), DIMENSION(1:Ny) :: yCHK2 ! y coord. in Van Driest space
   real(DBL), DIMENSION(1:Ny) :: y2 ! y coord.
   real(DBL), DIMENSION(1:Ny) :: Uchk2 ! Van Driest velocity profile
   real(DBL), DIMENSION(1:Ny) :: U2,Uint ! u-velocity profile
   real(DBL), DIMENSION(1:Ny) :: T2, Tint ! temperature profile
! ------
   real(DBL), DIMENSION(1:Ny) :: V ! v-velocity profile
   real(DBL), DIMENSION(1:Ny) :: dudx ! dU/dx

! --- dummy variables ---

   integer j, kk, n
   real(DBL) :: alpha, eta, f, a1, b1, c1, K, Cf1, Re1, ReX1, X1, ReX2, ReVD2
   real(DBL) :: Re2, Cf2, level, dif1, dif2, dist

! --- specific to user ---

   real(DBL), PARAMETER :: ReVD=2950.0 ! Reynolds # based on VD disp. thickness
```

```
   real(DBL), PARAMETER :: M=2.3 ! Mach number


! ================================================================================
! Main program
! ================================================================================

! --- guess for veplus ---

   WRITE(*,*) 'Guessed edge velocity+ (Re=2950, Uchk_eplus=23.64254613498937):'
   READ(*,*) Uchk_eplus

! --- generate uniform grid (in terms of velocity!) ---

   DO j=1,Ny
      Uchk_plus(j)=Uchk_eplus*REAL(j-1)/REAL(Ny-1)
   END DO

! --- compute xi-coord ---

   DO j=1,Ny
      f=Uchk_plus(j)
      xi_plus(j)=f+EXP(-kapa*b)*(EXP(kapa*f)-1.-kapa*f-0.5*((kapa*f)**2)- &
           ((kapa*f)**3)/6.)
   END DO
   xi_eplus=xi_plus(Ny)

! --- transform to y+ units ---

   DO j=1,Ny-1
      y_plus(j)=xi_plus(j)*xi_eplus/(xi_eplus-xi_plus(j))
   END DO
   y_plus(Ny)=1.e6 ! a big number to represent infinity

! --- transform to yCHK units ---

   DO j=1,Ny
      yCHK(j)=y_plus(j)*Uchk_eplus/ReVD
   END DO

! --- compute delta0 ---

   alpha=EXP(2.*ReVD/(690.+1.5*ReVD))-1.
   delta0=Uchk_eplus*xi_eplus/(alpha*ReVD)

! --- compute VD velocity profile ---

   Uchk(1)=0_DBL
   DO j=2,Ny
      eta=yCHK(j)/delta0
      f=EXP(-3.*(EXP(eta**(1./kapa))-1.))
      Uchk(j)=1.-f+(Uchk_plus(j)/Uchk_eplus)*f
   END DO

! --- compute VD disp. thickness ---

   delta1vd=0_DBL

   DO j=1,Ny-1
      delta1vd=delta1vd+0.5*(2.-Uchk(j)-Uchk(j+1))*(yCHK(j+1)-yCHK(j))
   END DO

   WRITE(*,*) 'The Van Driest displacement thickness is: ',delta1vd

! --- compute the adiabatic wall & wall temperatures ---
! we assume that the wall is adiabatic so Taw=Tw

   Taw=1.+0.5*(gamma-1.)*(M**2)
   Tw=Taw
   a1=Tw
   b1=1.+0.5*(gamma-1.)*(M**2)-Tw ! b1=0 (Taw=Tw) but in future modification...
   c1=-0.5*(gamma-1.)*(M**2)

! --- compute u, rho, T profiles ---

   K=SQRT(-Tw/c1)*(ASIN(b1/SQRT(b1**2-4.*a1*c1))- &
        ASIN((2.*c1+b1)/SQRT(b1**2-4.*a1*c1)))

   U_eplus=Uchk_eplus/K

   WRITE(*,*) 'ueplus=',U_eplus

   DO j=1,Ny
      f=Uchk(j)*Uchk_eplus/U_eplus
      K=ASIN(b1/SQRT(b1**2-4.*a1*c1))-f*SQRT(-c1/Tw)
      U(j)=(SQRT(b1**2-4.*a1*c1)*SIN(K)-b1)/(2.*c1)
      T(j)=a1+b1*U(j)+c1*(U(j)**2)
      rho(j)=1./T(j)
   END DO
```

```
! --- go from yCHK to y coord. ---

   DO j=1,Ny
     ! power law version
     ! y(j)=U_eplus*(T(1)**(omega+1.))*yCHK(j)/Uchk_eplus
     ! Sutherland law version
      y(j)=U_eplus*((T(1)**(5./2.))*((1.+Csuth)/(T(1)+Csuth))) &
           *yCHK(j)/Uchk_eplus
   END DO

! --- compute disp. thickness ---

   delta1=0_DBL

   DO j=1,Ny-1
      delta1=delta1+0.5*(2.-rho(j)*U(j)-rho(j+1)*U(j+1))*(y(j+1)-y(j))
   END DO

   WRITE(*,*) 'The displacement thickness is: ',delta1
   WRITE(*,*) 'Re_delta1=',delta1*ReVD

! ************************************************************************
! --- compute mean V(y) profile! ---
! ************************************************************************

! *** move downstream ***

!> skin friction:
   Cf1=2./(Uchk_eplus**2)
!> Re_delta99 (White - eqn (6.68) page 430):
   Re1=(Cf1/0.020)**(-6)
!> Re_x (White - eqn (6.70) page 430):
   ReX1=(Re1/0.16)**(7./6.)
!> Get position from plate egde
   X1=ReX1/ReVD
!> Move slightly downstream...
   ReX2=ReX1*(1.+eps/X1)
!> Get new Re_delta99
   Re2=0.16*(ReX2**(6./7.))
!> Get new Cf
   Cf2=0.02*(Re2**(-1./6.))
!> Get new Uchk_eplus
   Uchk_eplus2=SQRT(2./Cf2)
!> Get new ReVD
   ReVD2=ReX2/(X1+eps)

! *** generate new U(y) ***

! --- generate uniform grid (in terms of velocity!) ---

   DO j=1,Ny
      Uchk_plus2(j)=Uchk_eplus2*REAL(j-1)/REAL(Ny-1)
   END DO

! --- compute xi-coord ---

   DO j=1,Ny
      f=Uchk_plus2(j)
      xi_plus2(j)=f+EXP(-kapa*b)*(EXP(kapa*f)-1.-kapa*f-0.5*((kapa*f)**2)- &
           ((kapa*f)**3)/6.)
   END DO
   xi_eplus2=xi_plus2(Ny)

! --- transform to y+ units ---

   DO j=1,Ny-1
      y_plus2(j)=xi_plus2(j)*xi_eplus2/(xi_eplus2-xi_plus2(j))
   END DO
   y_plus2(Ny)=1.e6 ! a big number to represent infinity

! --- transform to yCHK units ---

   DO j=1,Ny
      yCHK2(j)=y_plus2(j)*Uchk_eplus2/ReVD2
   END DO

! --- compute delta0 ---

   alpha=EXP(2.*ReVD2/(690.+1.5*ReVD2))-1.
   delta0=Uchk_eplus2*xi_eplus2/(alpha*ReVD2)

! --- compute VD velocity profile ---

   Uchk2(1)=0_DBL
   DO j=2,Ny
      eta=yCHK2(j)/delta0
      f=EXP(-3.*(EXP(eta**(1./kapa))-1.))
      Uchk2(j)=1.-f+(Uchk_plus2(j)/Uchk_eplus2)*f
```

```
   END DO

! --- compute u, rho, T profiles ---

   K=SQRT(-Tw/c1)*(ASIN(b1/SQRT(b1**2-4.*a1*c1))- &
        ASIN((2.*c1+b1)/SQRT(b1**2-4.*a1*c1)))

   U_eplus2=Uchk_eplus2/K

   DO j=1,Ny
      f=Uchk2(j)*Uchk_eplus2/U_eplus2
      K=ASIN(b1/SQRT(b1**2-4.*a1*c1))-f*SQRT(-c1/Tw)
      U2(j)=(SQRT(b1**2-4.*a1*c1)*SIN(K)-b1)/(2.*c1)
      T2(j)=a1+b1*U2(j)+c1*(U2(j)**2)
   END DO

! --- go from yCHK to y coord. ---

   DO j=1,Ny
      ! power law version
      !y2(j)=U_eplus2*(T2(1)**(omega+1.))*yCHK2(j)/Uchk_eplus2
      ! Sutherland law version
      y2(j)=U_eplus2*((T2(1)**(5./2.))*((1.+Csuth)/(T2(1)+Csuth))) &
           *yCHK2(j)/Uchk_eplus2
   END DO

! *** Interpolate U2(y2) on U2(y) ***

   Uint(1)=0.0
   Tint(1)=T2(1)
   DO j=2,Ny
! --- find two nearest y2's of y_j ---
      level=y(j)
      n=0
      DO kk=1,Ny-1
         dif1=level-y2(kk)
         dif2=level-y2(kk+1)
         IF (dif1*dif2.LT.0.0) n=kk
      END DO
! --- linear interpolation
      dif1=level-y2(n)
      dif2=y2(n+1)-level
      dist=dif1+dif2
      Uint(j)=U2(n)*(dif2/dist)+U2(n+1)*(dif1/dist)
      Tint(j)=T2(n)*(dif2/dist)+T2(n+1)*(dif1/dist)
   END DO

! *** Integrate continuity to get V(y) ***

! --- compute d(rho*U)/dx ---

   DO j=1,Ny
      dudx(j)=(Uint(j)/Tint(j)-U(j)/T(j))/eps
   END DO

! --- integrate ---

   V(1)=0.0
   DO j=2,Ny
      V(j)=V(j-1)-0.5*T(j)*(dudx(j)+dudx(j-1))*(y(j)-y(j-1))
   END DO

! ******************************************************************************


! --- write profiles in ASCII files ---

   OPEN(UNIT=10,FILE='4matlab.txt',STATUS='REPLACE',ACTION='WRITE')
   REWIND(10)

   DO j=1,Ny
      WRITE(10,900) y(j),U(j),T(j),yCHK(j),Uchk(j),y_plus(j),Uchk_plus(j),V(j)
   END DO

   CLOSE(10)

   OPEN(UNIT=10,FILE='inflow.txt',STATUS='REPLACE',ACTION='WRITE')
   REWIND(10)

   DO j=1,Ny
      WRITE(10,901) y(j),U(j),T(j),V(j)
   END DO

   CLOSE(10)

900  FORMAT(8f22.14)
901  FORMAT(4f22.14)

 END PROGRAM main
```

C. Digital-filter Fortran routines

This appendix reproduces parts of the code used to generate the inflow turbulence. Although it is not shown in complete form for conciseness, it ought to be sufficiently accurate to see how the digital-filter approach described in chapter 2 was implemented in the in-house code and how one could use it in a future code.

C.1 Main digital-filter routine

```
! -------1---------2---------3---------4---------5---------6---------7--
! ++++++++++++++++++++++++++++++++++++++++++++++++++++++++++++++++++++++
!  This subroutine generates the inflow conditions for a (compressible)
!  turbulent boundary layer based on the technique of Klein in JCP 186,
!  (2003).
!
!                                                    Emile :: March 07'
!                  Modified in Sep. 07': MPI-friendly in all directions
! ++++++++++++++++++++++++++++++++++++++++++++++++++++++++++++++++++++++

      SUBROUTINE digi_filt(l,lstr)

      USE incl3d            ! common array/parameter declarations
      USE stdtypes          ! definitions of common & standard integer &
                            ! real types used in 32/64-bit architectures
      USE mersenne_twister  ! pseudo-random number generator
      USE mppvars           ! MPI common declarations

      IMPLICIT NONE

! ***********************************************************************
! - oOo - :: Declaration section :: - oOo -
! ***********************************************************************

      real*8 randx(1-yhalo:nyp_m+yhalo,1:nzp_m-1)
      real*8 randy(1-yhalo:nyp_m+yhalo,1:nzp_m-1)
      real*8 randz(1-yhalo:nyp_m+yhalo,1:nzp_m-1)

      real*8, DIMENSION(1:3,1:3) :: lund
      real*8 :: R11, R12, R22, R33

      real*8 :: Txu, Txv, Txw

      real*8 :: rnd1, rnd2
      real*8 :: sumz, sumyi, sumyo
      real*8 :: delta99, tmp1, tmp2, tmp3

      integer :: j, k, l, lstr, jj, kk, qz, qy, tst
      integer :: tsti, tsts, jjinf, jjsup

      type(mtprng_state) :: state

! ***********************************************************************
! - oOo - :: Program section :: - oOo -
! ***********************************************************************

! Re-seed the random number generator

      IF (l.EQ.1) THEN

         CALL mtprng_init(1,state)

      ELSE

         CALL restart_gen(iseed,iarray,state)

      END IF
```

```
! Initialize random fields

      DO k=1,nzp_m-1
         DO j=1-yhalo,nyp_m+yhalo
            randx(j,k)=0.0
            randy(j,k)=0.0
            randz(j,k)=0.0
         END DO
      END DO

! Harvest random numbers (normal distribution)
! 0-mean and unit-variance (checked)

! Collect two numbers from a uniform distribution
! Add them as follows to get a normal distribution
! Cf. Box-Muller theorem

      DO k=1,nzp_m-1
         DO j=1-yhalo,nyp_m+yhalo

            rnd1=mtprng_rand_real3(state)
            rnd2=mtprng_rand_real3(state)

            randx(j,k)=SQRT(-2.*LOG(rnd1))*COS(2*pi*rnd2)

            rnd1=mtprng_rand_real3(state)
            rnd2=mtprng_rand_real3(state)

            randy(j,k)=SQRT(-2.*LOG(rnd1))*COS(2*pi*rnd2)

            rnd1=mtprng_rand_real3(state)
            rnd2=mtprng_rand_real3(state)

            randz(j,k)=SQRT(-2.*LOG(rnd1))*COS(2*pi*rnd2)

         END DO
      END DO

! Save generator's state

      CALL save_gen(iseed,iarray,state)

!   CALL randstat(randx)
!   CALL randstat(randy)
!   CALL randstat(randz)

! ********************************************************************
! |-------------------- ::  Filters' coeff. :: ----------------------|
! ********************************************************************

! No need to compute the coeff. at each iteration, only the first time

! Compute the convolution coeff.

      IF (l.eq.lstr+1) THEN

! Z-dir.

         sumz=0.0
         kk=(NfzU/2.)
         DO k=-NfzU,NfzU
            sumz=sumz+EXP(-2.*pi*REAL(ABS(k))/REAL(kk))
         END DO
         sumz=SQRT(sumz)
         DO k=-NfzU,NfzU
            buz(k)=EXP(-pi*REAL(ABS(k))/REAL(kk))/sumz
         END DO

         sumz=0.0
         kk=(NfzV/2.)
         DO k=-NfzV,NfzV
            sumz=sumz+EXP(-2.*pi*REAL(ABS(k))/REAL(kk))
         END DO
         sumz=SQRT(sumz)
         DO k=-NfzV,NfzV
            bvz(k)=EXP(-pi*REAL(ABS(k))/REAL(kk))/sumz
         END DO

         sumz=0.0
         kk=(NfzW/2.)
         DO k=-NfzW,NfzW
            sumz=sumz+EXP(-2.*pi*REAL(ABS(k))/REAL(kk))
         END DO
         sumz=SQRT(sumz)
         DO k=-NfzW,NfzW
            bwz(k)=EXP(-pi*REAL(ABS(k))/REAL(kk))/sumz
         END DO

! Y-dir
```

```
! -- zone 1 (inner) --

         sumyi=0.0
         kk=(NfyUi/2.)
         DO k=-NfyUi,NfyUi
            sumyi=sumyi+EXP(-2.*pi*REAL(ABS(k))/REAL(kk))
         END DO
         sumyi=SQRT(sumyi)
         DO k=-NfyUi,NfyUi
            buyi(k)=EXP(-pi*REAL(ABS(k))/REAL(kk))/sumyi
         END DO

         sumyi=0.0
         kk=(NfyVi/2.)
         DO k=-NfyVi,NfyVi
            sumyi=sumyi+EXP(-2.*pi*REAL(ABS(k))/REAL(kk))
         END DO
         sumyi=SQRT(sumyi)
         DO k=-NfyVi,NfyVi
            bvyi(k)=EXP(-pi*REAL(ABS(k))/REAL(kk))/sumyi
         END DO

         sumyi=0.0
         kk=(NfyWi/2.)
         DO k=-NfyWi,NfyWi
            sumyi=sumyi+EXP(-2.*pi*REAL(ABS(k))/REAL(kk))
         END DO
         sumyi=SQRT(sumyi)
         DO k=-NfyWi,NfyWi
            bwyi(k)=EXP(-pi*REAL(ABS(k))/REAL(kk))/sumyi
         END DO

! -- zone 2 (outer) --

         sumyo=0.0
         kk=(NfyUo/2.)
         DO k=-NfyUo,NfyUo
            sumyo=sumyo+EXP(-2.*pi*REAL(ABS(k))/REAL(kk))
         END DO
         sumyo=SQRT(sumyo)
         DO k=-NfyUo,NfyUo
            buyo(k)=EXP(-pi*REAL(ABS(k))/REAL(kk))/sumyo
         END DO

         sumyo=0.0
         kk=(NfyVo/2.)
         DO k=-NfyVo,NfyVo
            sumyo=sumyo+EXP(-2.*pi*REAL(ABS(k))/REAL(kk))
         END DO
         sumyo=SQRT(sumyo)
         DO k=-NfyVo,NfyVo
            bvyo(k)=EXP(-pi*REAL(ABS(k))/REAL(kk))/sumyo
         END DO

         sumyo=0.0
         kk=(NfyWo/2.)
         DO k=-NfyWo,NfyWo
            sumyo=sumyo+EXP(-2.*pi*REAL(ABS(k))/REAL(kk))
         END DO
         sumyo=SQRT(sumyo)
         DO k=-NfyWo,NfyWo
            bwyo(k)=EXP(-pi*REAL(ABS(k))/REAL(kk))/sumyo
         END DO


! Build the 2D filter

! --- zone 1 ---

         DO j=-NfyUi,NfyUi
            DO k=-NfzU,NfzU
               buyzi(j,k)=buz(k)*buyi(j)
            END DO
         END DO

         DO j=-NfyVi,NfyVi
            DO k=-NfzV,NfzV
               bvyzi(j,k)=bvz(k)*bvyi(j)
            END DO
         END DO

         DO j=-NfyWi,NfyWi
            DO k=-NfzW,NfzW
               bwyzi(j,k)=bwz(k)*bwyi(j)
            END DO
         END DO

! --- zone 2 ---
```

```
         DO j=-NfyUo,NfyUo
            DO k=-NfzU,NfzU
               buyzo(j,k)=buz(k)*buyo(j)
            END DO
         END DO

         DO j=-NfyVo,NfyVo
            DO k=-NfzV,NfzV
               bvyzo(j,k)=bvz(k)*bvyo(j)
            END DO
         END DO

         DO j=-NfyWo,NfyWo
            DO k=-NfzW,NfzW
               bwyzo(j,k)=bwz(k)*bwyo(j)
            END DO
         END DO

      END IF

! --------------- :: filters' coeff. are computed :: -------------------

! ********************************************************************
! |------------------- ::  Filter random data :: ----------------------|
! ********************************************************************

! Initialize the new filtered data planes

      DO k=1-zhalo,nzp+zhalo
         DO j=1-yhalo,nyp+yhalo
            urn(j,k)=0.0
            vrn(j,k)=0.0
            wrn(j,k)=0.0
         END DO
      END DO

! ::::::::::::::::::::::::::: Filter u ::::::::::::::::::::::::::::::

      DO j=1-yhalo,nyp+yhalo

         IF (y(1,j,1).LT.ylzone) THEN

! --- Zone 1 (inner) ---

! Check if filter is out of bound
            jjinf=-NfyUi
            jjsup=NfyUi
            jj=j+(jbegin(sy)-1) ! global jj, local j
            tsti=jj-(1-yhalo+NfyUi)
            tsts=jj+NfyUi-(nyp_m+yhalo)
            IF (tsti.LT.0) jjinf=-NfyUi-tsti
            IF (tsts.GT.0) jjsup=NfyUi-tsts
! End of check
            DO k=1-zhalo,nzp+zhalo
               DO kk=-NfzU,NfzU
                  qz=k+kk+(kbegin(sz)-1)
! periodic in z
                  IF (qz.lt.1) qz=qz-1+nzp_m
                  IF (qz.gt.(nzp_m-1)) qz=qz-nzp_m+1

                  DO jj=jjinf,jjsup
                     qy=j+jj+(jbegin(sy)-1)
                     urn(j,k)=urn(j,k)+buyzi(jj,kk)*randx(qy,qz)
                  END DO
               END DO
            END DO

         ELSE

! --- Zone 2 (outer) ---

! Check if filter is out of bound
            jjinf=-NfyUo
            jjsup=NfyUo
            jj=j+(jbegin(sy)-1) ! global jj, local j
            tsti=jj-(1-yhalo+NfyUo)
            tsts=jj+NfyUo-(nyp_m+yhalo)
            IF (tsti.LT.0) jjinf=-NfyUo-tsti
            IF (tsts.GT.0) jjsup=NfyUo-tsts
! End of check
            DO k=1-zhalo,nzp+zhalo
               DO kk=-NfzU,NfzU
                  qz=k+kk+(kbegin(sz)-1)
! periodic in z
                  IF (qz.lt.1) qz=qz-1+nzp_m
                  IF (qz.gt.(nzp_m-1)) qz=qz-nzp_m+1

                  DO jj=jjinf,jjsup
```

```
                  qy=j+jj+(jbegin(sy)-1)
                  urn(j,k)=urn(j,k)+buyzo(jj,kk)*randx(qy,qz)
               END DO
            END DO
         END DO

      END IF

   END DO

! :::::::::::::::::::::::::::: Filter v ::::::::::::::::::::::::::::::

   DO j=1-yhalo,nyp+yhalo

      IF (y(1,j,1).LT.ylzone) THEN

! --- Zone 1 (inner) ---

! Check if filter is out of bound
         jjinf=-NfyVi
         jjsup=NfyVi
         jj=j+(jbegin(sy)-1) ! global jj, local j
         tsti=jj-(1-yhalo+NfyVi)
         tsts=jj+NfyVi-(nyp_m+yhalo)
         IF (tsti.LT.0) jjinf=-NfyVi-tsti
         IF (tsts.GT.0) jjsup=NfyVi-tsts
! End of check
         DO k=1-zhalo,nzp+zhalo
            DO kk=-NfzV,NfzV
               qz=k+kk+(kbegin(sz)-1)
! periodic in z
               IF (qz.lt.1) qz=qz-1+nzp_m
               IF (qz.gt.(nzp_m-1)) qz=qz-nzp_m+1

               DO jj=jjinf,jjsup
                  qy=j+jj+(jbegin(sy)-1)
                  vrn(j,k)=vrn(j,k)+bvyzi(jj,kk)*randy(qy,qz)
               END DO
            END DO
         END DO

      ELSE

! --- Zone 2 (outer) ---

! Check if filter is out of bound
         jjinf=-NfyVo
         jjsup=NfyVo
         jj=j+(jbegin(sy)-1) ! global jj, local j
         tsti=jj-(1-yhalo+NfyVo)
         tsts=jj+NfyVo-(nyp_m+yhalo)
         IF (tsti.LT.0) jjinf=-NfyVo-tsti
         IF (tsts.GT.0) jjsup=NfyVo-tsts
! End of check
         DO k=1-zhalo,nzp+zhalo
            DO kk=-NfzV,NfzV
               qz=k+kk+(kbegin(sz)-1)
! periodic in z
               IF (qz.lt.1) qz=qz-1+nzp_m
               IF (qz.gt.(nzp_m-1)) qz=qz-nzp_m+1

               DO jj=jjinf,jjsup
                  qy=j+jj+(jbegin(sy)-1)
                  vrn(j,k)=vrn(j,k)+bvyzo(jj,kk)*randy(qy,qz)
               END DO
            END DO
         END DO

      END IF

   END DO

! :::::::::::::::::::::::::::: Filter w ::::::::::::::::::::::::::::::

   DO j=1-yhalo,nyp+yhalo

      IF (y(1,j,1).LT.ylzone) THEN

! --- Zone 1 (inner) ---

! Check if filter is out of bound in y
         jjinf=-NfyWi
         jjsup=NfyWi
         jj=j+(jbegin(sy)-1) ! global jj, local j
         tsti=jj-(1-yhalo+NfyWi)
         tsts=jj+NfyWi-(nyp_m+yhalo)
         IF (tsti.LT.0) jjinf=-NfyWi-tsti
         IF (tsts.GT.0) jjsup=NfyWi-tsts
! End of check
```

```
            DO k=1-zhalo,nzp+zhalo
               DO kk=-NfzW,NfzW
                  qz=k+kk+(kbegin(sz)-1)
! periodic in z
                  IF (qz.lt.1) qz=qz-1+nzp_m
                  IF (qz.gt.(nzp_m-1)) qz=qz-nzp_m+1

                  DO jj=jjinf,jjsup
                     qy=j+jj+(jbegin(sy)-1)
                     wrn(j,k)=wrn(j,k)+bwyzi(jj,kk)*randz(qy,qz)
                  END DO
               END DO
            END DO

         ELSE

! --- Zone 2 (outer) ---

! Check if filter is out of bound
            jjinf=-NfyWo
            jjsup=NfyWo
            jj=j+(jbegin(sy)-1) ! global jj, local j
            tsti=jj-(1-yhalo+NfyWo)
            tsts=jj+NfyWo-(nyp_m+yhalo)
            IF (tsti.LT.0) jjinf=-NfyWo-tsti
            IF (tsts.GT.0) jjsup=NfyWo-tsts
! End of check
            DO k=1-zhalo,nzp+zhalo
               DO kk=-NfzW,NfzW
                  qz=k+kk+(kbegin(sz)-1)
! periodic in z
                  IF (qz.lt.1) qz=qz-1+nzp_m
                  IF (qz.gt.(nzp_m-1)) qz=qz-nzp_m+1

                  DO jj=jjinf,jjsup
                     qy=j+jj+(jbegin(sy)-1)
                     wrn(j,k)=wrn(j,k)+bwyzo(jj,kk)*randz(qy,qz)
                  END DO
               END DO
            END DO

         END IF

      END DO

! --------------- :: random fields are now filtered :: -----------------

! ************************************************************************
! |---------- ::  Apply streamwise two-point correlation :: ----------|
! ************************************************************************

! Use previous filtered field

      IF (1.GT.1) THEN

         DO j=1-yhalo,nyp+yhalo

! Get mean velocity (stored in sv(j,k,1=rho,2=u,3=v,...)=u(y))
            IF(sv(j,1,2).eq.0.) THEN
               tmp1=0.000000000001
            ELSE
               tmp1=sv(j,1,2)/sv(j,1,1)
            END IF
! Get Lagrangian time scale
            Txu=Lxu/tmp1
            Txv=Lxv/tmp1
            Txw=Lxw/tmp1

            DO k=1-zhalo,nzp+zhalo
               urn(j,k)=uro(j,k)*EXP(-pi*dt/(2.*Txu))+urn(j,k)*SQRT(1-
     +              EXP(-pi*dt/Txu))
               vrn(j,k)=vro(j,k)*EXP(-pi*dt/(2.*Txv))+vrn(j,k)*SQRT(1-
     +              EXP(-pi*dt/Txv))
               wrn(j,k)=wro(j,k)*EXP(-pi*dt/(2.*Txw))+wrn(j,k)*SQRT(1-
     +              EXP(-pi*dt/Txw))
            END DO

         END DO

      END IF

! Save current filtered field

      DO k=1-zhalo,nzp+zhalo
         DO j=1-yhalo,nyp+yhalo
            uro(j,k)=urn(j,k)
            vro(j,k)=vrn(j,k)
            wro(j,k)=wrn(j,k)
         END DO
```

```
      END DO

! -------------- :: new filtered fields are now ready :: ---------------

! ************************************************************************
! |----------- ::  Apply Lund's transfo. to filtered data :: ----------|
! ************************************************************************


      DO j=1,3
         DO k=1,3
            lund(j,k)=0.0
         END DO
      END DO

! Loop starts here ...

      DO j=1-yhalo,nyp+yhalo

! Load the Reynold's stress

         R11=RStress(j,1)
         R22=RStress(j,2)
         R33=RStress(j,3)
         R12=RStress(j,4)

c         END IF

! Prepare Lund's transformation array

         lund(1,1)=R11
         IF (R12.NE.0.0) THEN
            lund(2,1)=(ABS(R12)/R12)*(R12**2)/R11
         ELSE
            lund(2,1)=0.0
         END IF
         tmp1=(R22**2)-(lund(2,1)**2)
         IF (tmp1.GE.0.0) THEN
            lund(2,2)=SQRT(tmp1)
         ELSE
            lund(2,2)=0.0
         END IF
         lund(3,3)=R33

! Get the synthetic fluctuations

         DO k=1-zhalo,nzp+zhalo

            upp(j,k)=urn(j,k)*lund(1,1)
            vpp(j,k)=urn(j,k)*lund(2,1)+vrn(j,k)*lund(2,2)
            wpp(j,k)=wrn(j,k)*lund(3,3)

         END DO

      END DO

! -------------- :: disturbances from DF method ready :: ---------------

! ************************************************************************
! |-------------- ::  Get thermodynamic fluctuations :: ---------------|
! ************************************************************************

! We make use here of the Strong Reynolds Analogy (SRA) and assume that
! pressure fluctuations are small compared to density and temperature
! fluctuations. For a discussion about the validity of the SRA, see
! Guarini et al.'s JFM paper vol. 414 pp. 1-33.

      DO j=1-yhalo,nyp+yhalo

         tmp3=sv(j,1,1)
         tmp1=tmp3*((xm*sv(j,1,2)/tmp3)**2)

         DO k=1-zhalo,nzp+zhalo

            tmp2=-(gamma-1)*tmp1*upp(j,k)*tmp3/sv(j,1,2)

            rpp(j,k)=-tmp2*tmp3

            IF (rpp(j,k).LT.-tmp3) rpp(j,k)=-0.99*tmp3

         END DO
      END DO

      IF(ym_bound) then
         DO k=1-zhalo,nzp+zhalo
            DO j=1-yhalo,1
               rpp(j,k)=0.
            END DO
         END DO
```

```
      END IF

      RETURN

! :::::::::::::::::::::::::::: The End! ::::::::::::::::::::::::::::::

      END SUBROUTINE digi_filt
```

C.2 Some of the common arrays and parameters used

```
module incl3d
c
      ...
c
      integer nx_m, ny_m, nz_m
      integer nxp_m, nyp_m, nzp_m
      integer nprocx, nprocy, nprocz
      integer, parameter :: nhalo=2
      integer, parameter :: xhalo=nhalo, yhalo=nhalo, zhalo=nhalo
      integer nxp, nyp, nzp

      parameter(nx_m=450 , ny_m=150, nz_m=280)
      parameter ( nxp_m = nx_m+1, nyp_m = ny_m+1, nzp_m = nz_m+1 )
      parameter ( nprocx=8, nprocy=4, nprocz=8 )
c
      real*8 gamma,pi
c
      ...
c
! Inflow generator parameters

! :: Filter width || Z-direction ::
! ------------------------------------------------------------------------
! dz=zl/nz, Nfz=2*Lz/dz
! ------------------------------------------------------------------------
!                 --> Lz(u,v,w)= 0.75 | 0.5 | 1.5 <--
! ------------------------------------------------------------------------

      integer, PARAMETER :: NfzU=20, NfzV=20, NfzW=30

! :: Filter width || Y-direction ::
! ------------------------------------------------------------------------
! dy=0.15, Nfy=2*Ly/dy
! ------------------------------------------------------------------------
!                 --> Ly(u,v,w)= 1.5 | 1.75 | 0.5 <--
! ------------------------------------------------------------------------

      integer, PARAMETER :: NfyUi=20, NfyVi=25, NfyWi=15
      integer, PARAMETER :: NfyUo=35, NfyVo=45, NfyWo=20
      real*8, PARAMETER :: ylzone=1.0

! :: Filter width || X-direction ::
! ------------------------------------------------------------------------

      real*8, PARAMETER :: Lxu=10., Lxv=4., Lxw=4.

! :: Filtered random data, n=new & o=old ::
      real*8, DIMENSION(1-yhalo:nyd+yhalo,1-zhalo:nzd+zhalo) :: urn,
     +     vrn,wrn
      real*8, DIMENSION(1-yhalo:nyd+yhalo,1-zhalo:nzd+zhalo) :: uro,
     +     vro,wro
      real*8, DIMENSION(1-yhalo:nyd+yhalo,1-zhalo:nzd+zhalo) :: upp,
     +     vpp,wpp, rpp

! :: Filter coeff. ::

      real*8, DIMENSION(-NfzU:NfzU) :: buz
      real*8, DIMENSION(-NfzV:NfzV) :: bvz
      real*8, DIMENSION(-NfzW:NfzW) :: bwz

      real*8, DIMENSION(-NfyUi:NfyUi) :: buyi
      real*8, DIMENSION(-NfyVi:NfyVi) :: bvyi
      real*8, DIMENSION(-NfyWi:NfyWi) :: bwyi
      real*8, DIMENSION(-NfyUo:NfyUo) :: buyo
      real*8, DIMENSION(-NfyVo:NfyVo) :: bvyo
      real*8, DIMENSION(-NfyWo:NfyWo) :: bwyo

      real*8, DIMENSION(-NfyUi:NfyUi,-NfzU:NfzU) :: buyzi
      real*8, DIMENSION(-NfyVi:NfyVi,-NfzV:NfzV) :: bvyzi
      real*8, DIMENSION(-NfyWi:NfyWi,-NfzW:NfzW) :: bwyzi
      real*8, DIMENSION(-NfyUo:NfyUo,-NfzU:NfzU) :: buyzo
      real*8, DIMENSION(-NfyVo:NfyVo,-NfzV:NfzV) :: bvyzo
      real*8, DIMENSION(-NfyWo:NfyWo,-NfzW:NfzW) :: bwyzo
```

```
! :: Prescribed Reynolds stress ::

      integer, parameter :: nRS=81 ! number of lines in RStress.txt
      integer, parameter :: ninflow=81 ! number of lines in inflow.txt

      real*8, DIMENSION(1-yhalo:nyd+yhalo,4) :: RStress

! Random number generator

      integer, parameter :: INT64 = selected_int_kind(18)
      integer, parameter :: INT32 = selected_int_kind(9)

      integer(INT32), parameter :: Ngene = 624_INT32
      integer(INT32) :: iseed
      integer(INT64), dimension(0:Ngene-1) :: iarray
c
      ...
c
      end module incl3d

////////////////////////////////////////////////////////////////////////

      module stdtypes

!-----------------------------------------------------------------------
! From the Algorithmic Conjurings of Scott Robert Ladd comes...
!-----------------------------------------------------------------------
!
!   stdtypes.f90 (a Fortran 95 module)
!
!   Definitions of common and standard integer and real types used in
!   32- and 64-bit architectures.
!-----------------------------------------------------------------------
!
!  COPYRIGHT NOTICE, DISCLAIMER, and LICENSE:
!
!  This notice applies *only* to this specific expression of this
!  algorithm, and does not imply ownership or invention of the
!  implemented algorithm.
!
!  If you modify this file, you may insert additional notices
!  immediately following this sentence.
!
!  Copyright 2001, 2002, 2004 Scott Robert Ladd.
!  All rights reserved, except as noted herein.
!
!  This computer program source file is supplied "AS IS". Scott Robert
!  Ladd (hereinafter referred to as "Author") disclaims all warranties,
!  expressed or implied, including, without limitation, the warranties
!  of merchantability and of fitness for any purpose. The Author
!  assumes no liability for direct, indirect, incidental, special,
!  exemplary, or consequential damages, which may result from the use
!  of this software, even if advised of the possibility of such damage.
!
!  The Author hereby grants anyone permission to use, copy, modify, and
!  distribute this source code, or portions hereof, for any purpose,
!  without fee, subject to the following restrictions:
!
!       1. The origin of this source code must not be misrepresented.
!
!       2. Altered versions must be plainly marked as such and must not
!          be misrepresented as being the original source.
!
!       3. This Copyright notice may not be removed or altered from any
!          source or altered source distribution.
!
!  The Author specifically permits (without fee) and encourages the use
!  of this source code for entertainment, education, or decoration. If
!  you use this source code in a product, acknowledgment is not required
!  but would be appreciated.
!
!  Acknowledgement:
!       This license is based on the wonderful simple license that
!       accompanies libpng.
!
!-----------------------------------------------------------------------
!
!  For more information on this software package, please visit
!  Scott's web site, Coyote Gulch Productions, at:
!
!       http://www.coyotegulch.com
!
!-----------------------------------------------------------------------

    ! Kind types for 64-, 32-, 16-, and 8-bit signed integers
      integer, parameter :: INT64 = selected_int_kind(18)
      integer, parameter :: INT32 = selected_int_kind(9)
      integer, parameter :: INT16 = selected_int_kind(4)
```

```
      integer, parameter :: INT08 = selected_int_kind(2)

    ! Kind types for IEEE 754/IEC 60559 single- and double-precision reals
      integer, parameter :: IEEE32 = selected_real_kind(  6,  37 )
      integer, parameter :: IEEE64 = selected_real_kind( 15, 307 )

      end module stdtypes

////////////////////////////////////////////////////////////////////////

      module mersenne_twister

!--------------------------------------------------------------------
! From the Algorithmic Conjurings of Scott Robert Ladd comes...
!--------------------------------------------------------------------
!
!  mtprng.f90 (a Fortran 95 module)
!
!  An implementation of the Mersenne Twister algorithm for generating
!  psuedo-random sequences.
!
!  History
!  -------
!   1.0.0   Initial release
!
!   1.1.0   6 February 2002
!           Updated to support algorithm revisions posted
!           by Matsumoto and Nishimura on 26 January 2002
!
!   1.5.0   12 December 2003
!           Added to hypatia project
!           Minor style changes
!           Tightened code
!           Now state based; no static variables
!           Removed mtprng_rand_real53
!
!   2.0.0   4 January 2004
!           Corrected erroneous unsigned bit manipulations
!           Doubled resolution by using 64-bit math
!           Added mtprng_rand64
!
!  ORIGINAL ALGORITHM COPYRIGHT
!  ============================
!  Copyright (C) 1997,2002 Makoto Matsumoto and Takuji Nishimura.
!  Any feedback is very welcome. For any question, comments, see
!  http://www.math.keio.ac.jp/matumoto/emt.html or email
!  matumoto@math.keio.ac.jp
!--------------------------------------------------------------------
!
!  COPYRIGHT NOTICE, DISCLAIMER, and LICENSE:
!
!  This notice applies *only* to this specific expression of this
!  algorithm, and does not imply ownership or invention of the
!  implemented algorithm.
!
!  If you modify this file, you may insert additional notices
!  immediately following this sentence.
!
!  --> March 2007: This file was modified by Emile Touber to allow
!                  for stoping/restarting the generator
!
!  Copyright 2001, 2002, 2004 Scott Robert Ladd.
!  All rights reserved, except as noted herein.
!
!  This computer program source file is supplied "AS IS". Scott Robert
!  Ladd (hereinafter referred to as "Author") disclaims all warranties,
!  expressed or implied, including, without limitation, the warranties
!  of merchantability and of fitness for any purpose. The Author
!  assumes no liability for direct, indirect, incidental, special,
!  exemplary, or consequential damages, which may result from the use
!  of this software, even if advised of the possibility of such damage.
!
!  The Author hereby grants anyone permission to use, copy, modify, and
!  distribute this source code, or portions hereof, for any purpose,
!  without fee, subject to the following restrictions:
!
!      1. The origin of this source code must not be misrepresented.
!
!      2. Altered versions must be plainly marked as such and must not
!         be misrepresented as being the original source.
!
!      3. This Copyright notice may not be removed or altered from any
!         source or altered source distribution.
!
!  The Author specifically permits (without fee) and encourages the use
!  of this source code for entertainment, education, or decoration. If
!  you use this source code in a product, acknowledgment is not required
!  but would be appreciated.
!
```

```
!  Acknowledgement:
!      This license is based on the wonderful simple license that
!      accompanies libpng.
!
!--------------------------------------------------------------------
!
!  For more information on this software package, please visit
!  Scott's web site, Coyote Gulch Productions, at:
!
!      http://www.coyotegulch.com
!
!--------------------------------------------------------------------

      use stdtypes

      implicit none

    !--------------------------------------------------------------------
    ! Everything is private unless explicitly made public
      private

      public :: mtprng_state,
     +     mtprng_init, mtprng_init_by_array,
     +     mtprng_rand64, mtprng_rand, mtprng_rand_range,
     +     mtprng_rand_real1, mtprng_rand_real2, mtprng_rand_real3,
     +     save_gen, restart_gen

    !--------------------------------------------------------------------
    ! Constants
      integer(INT32), parameter :: N = 624_INT32
      integer(INT32), parameter :: M = 397_INT32

    !--------------------------------------------------------------------
    ! types
      type mtprng_state
      integer(INT32)                    :: mti = -1
      integer(INT64), dimension(0:N-1) :: mt
      end type

      contains
    !--------------------------------------------------------------------
    !  Initializes the generator with "seed"
      subroutine mtprng_init(seed, state)

        ! arguments
      integer(INT32),     intent(in)  :: seed
      type(mtprng_state), intent(out) :: state

        ! working storage
      integer :: i
      integer(INT64) :: s, b

        ! save seed
      state%mt(0) = seed

        ! Set the seed using values suggested by Matsumoto & Nishimura,
        ! using a generator by Knuth. See original source for details.
      do i = 1, N - 1
         state%mt(i) = iand(4294967295_INT64,1812433253_INT64 *
     +        ieor(state%mt(i-1),ishft(state%mt(i-1),-30_INT64)) + i)
      end do

      state%mti = N

      end subroutine mtprng_init

    !--------------------------------------------------------------------
    ! Initialize with an array of seeds
      subroutine mtprng_init_by_array(init_key, state)

        ! arguments
      integer(INT32), dimension(:), intent(in) :: init_key
      type(mtprng_state), intent(out) :: state

        ! working storage
      integer :: key_length
      integer :: i
      integer :: j
      integer :: k

      call mtprng_init(19650218_INT32,state)

      i = 1
      j = 0
      key_length = size(init_key)

      do k = max(N,key_length), 0, -1
         state%mt(i) = ieor(state%mt(i),(ieor(state%mt(i-
     +        1),ishft(state%mt(i-1),-30_INT64) * 1664525_INT64))) +
```

```
+        init_key(j) + j

     i = i + 1
     j = j + 1

     if (i >= N) then
        state%mt(0) = state%mt(N-1)
        i = 1
     end if

     if (j >= key_length) j = 0
  end do

  do k = N-1, 0, -1
     state%mt(i) = ieor(state%mt(i),(ieor(state%mt(i-
+        1),ishft(state%mt(i-1),-30_INT64) *
+        1566083941_INT64))) - i

     i = i + 1

     if (i>=N) then
        state%mt(0) = state%mt(N-1)
        i = 1
     end if
  end do

  state%mt(0) = 1073741824_INT64 ! 0x40000000, assuring non-zero initial array

  end subroutine mtprng_init_by_array

!----------------------------------------------------------------------
!   Obtain the next 32-bit integer in the psuedo-random sequence
  function mtprng_rand64(state) result(r)

    ! arguments
  type(mtprng_state), intent(inout) :: state

    !return type
  integer(INT64) :: r

    ! internal constants
  integer(INT64), dimension(0:1), parameter :: mag01 = (/ 0_INT64,
+     -1727483681_INT64 /)

    ! Period parameters
  integer(INT64), parameter :: UPPER_MASK =  2147483648_INT64
  integer(INT64), parameter :: LOWER_MASK =  2147483647_INT64

    ! Tempering parameters
  integer(INT64), parameter :: TEMPERING_B = -1658038656_INT64
  integer(INT64), parameter :: TEMPERING_C =  -272236544_INT64

    ! Note: variable names match those in original example
  integer(INT32) :: kk

    ! Generate N words at a time
  if (state%mti >= N) then
        ! The value -1 acts as a flag saying that the seed has not
        ! been set.
     if (state%mti == -1) call mtprng_init(4357_INT32,state)

        ! Fill the mt array
     do kk = 0, N - M - 1
        r = ior(iand(state%mt(kk),UPPER_MASK),
+            iand(state%mt(kk+1),LOWER_MASK))
        state%mt(kk) = ieor(ieor(state%mt(kk + M),ishft(r,
+            -1_INT64)),mag01(iand(r,1_INT64)))
     end do

     do kk = N - M, N - 2
        r = ior(iand(state%mt(kk),UPPER_MASK),iand(state%mt(kk+
+            1),LOWER_MASK))
        state%mt(kk) = ieor(ieor(state%mt(kk + (M - N)),ishft(r,
+            -1_INT64)),mag01(iand(r,1_INT64)))
     end do

     r = ior(iand(state%mt(N-1),UPPER_MASK),
+         iand(state%mt(0),LOWER_MASK))
     state%mt(N-1) = ieor(ieor(state%mt(M-1),ishft(r,-1)),
+         mag01(iand(r,1_INT64)))

        ! Start using the array from first element
     state%mti = 0
  end if

    ! Here is where we actually calculate the number with a series
    ! of transformations
  r = state%mt(state%mti)
  state%mti = state%mti + 1
```

```
  r = ieor(r,ishft(r,-11))
  r = iand(4294967295_INT64,ieor(r,iand(ishft(r, 7),TEMPERING_B)))
  r = iand(4294967295_INT64,ieor(r,iand(ishft(r,15),TEMPERING_C)))
  r = ieor(r,ishft(r,-18))

  end function mtprng_rand64

!-----------------------------------------------------------------------
!   Obtain the next 32-bit integer in the psuedo-random sequence
  function mtprng_rand(state) result(r)

    ! arguments
  type(mtprng_state), intent(inout) :: state

    !return type
  integer(INT32) :: r

    ! working storage
  integer(INT64) :: x

    ! done
  x = mtprng_rand64(state)

  if (x > 2147483647_INT64) then
     r = x - 4294967296_INT64
  else
     r = x
  end if

  end function mtprng_rand

!-----------------------------------------------------------------------
!   Obtain a psuedorandom integer in the range [lo,hi]
  function mtprng_rand_range(state, lo, hi) result(r)

    ! arguments
  type(mtprng_state), intent(inout) :: state
  integer, intent(in) :: lo
  integer, intent(in) :: hi

    ! return type
  integer(INT32) :: r

    ! Use real value to caluclate range
  r = lo + floor((hi - lo + 1.0_IEEE64) * mtprng_rand_real2(state))

  end function mtprng_rand_range

!-----------------------------------------------------------------------
!   Obtain a psuedorandom real number in the range [0,1], i.e., a
!   number greater than or equal to 0 and less than or equal to 1.
  function mtprng_rand_real1(state) result(r)

    ! arguments
  type(mtprng_state), intent(inout) :: state

    ! return type
  real(IEEE64) :: r

    ! Local constant; precalculated to avoid division below
  real(IEEE64), parameter :: factor = 1.0_IEEE64 /
 +     4294967295.0_IEEE64

    ! compute
  r = real(mtprng_rand64(state),IEEE64) * factor

  end function mtprng_rand_real1

!-----------------------------------------------------------------------
!   Obtain a psuedorandom real number in the range [0,1), i.e., a
!   number greater than or equal to 0 and less than 1.
  function mtprng_rand_real2(state) result(r)

    ! arguments
  type(mtprng_state), intent(inout) :: state

    ! return type
  real(IEEE64) :: r

    ! Local constant; precalculated to avoid division below
  real(IEEE64), parameter :: factor = 1.0_IEEE64 /
 +     4294967296.0_IEEE64

    ! compute
  r = real(mtprng_rand64(state),IEEE64) * factor

  end function mtprng_rand_real2
```

```
    !-----------------------------------------------------------------
    !   Obtain a psuedorandom real number in the range (0,1), i.e., a
    !   number greater than 0 and less than 1.
      function mtprng_rand_real3(state) result(r)

        ! arguments
      type(mtprng_state), intent(inout) :: state

        ! return type
      real(IEEE64) :: r

        ! Local constant; precalculated to avoid division below
      real(IEEE64), parameter :: factor = 1.0_IEEE64 /
     +     4294967296.0_IEEE64

      r = (real(mtprng_rand64(state),IEEE64) + 0.5_IEEE64) * factor

      end function mtprng_rand_real3

! Subroutine to save the current state of the generator

      subroutine save_gen(iseed,iarray,state)

      ! arguments
      integer(INT32),     intent(out)  :: iseed
      integer(INT64), dimension(0:N-1), intent(out) :: iarray
      type(mtprng_state), intent(inout) :: state

      ! working storage
      integer :: i

      iseed=state%mti

      do i=0,N-1
         iarray(i)=state%mt(i)
      end do

      return

      end subroutine save_gen

! Subroutine to load the saved state of the generator

      subroutine restart_gen(iseed,iarray,state)

      ! arguments
      integer(INT32),     intent(in)  :: iseed
      integer(INT64), dimension(0:N-1), intent(in) :: iarray
      type(mtprng_state), intent(inout) :: state

      ! working storage
      integer :: i

      state%mti=iseed

      do i=0,N-1
         state%mt(i) = iarray(i)
      end do

      return

      end subroutine restart_gen

      end module mersenne_twister
```

C.3 Dependent subroutines

```
program main
c
      use incl3d
      use mppvars
      use stdtypes
c
      ...
c
      integer j,k,l,lstr
c
      ...
c
      call bounds ! gives local/global index position conversion
c
      ...
c
```

```
      pi=4.*atan(1.)
c
      ...
c
      if(readfrom) then ! if restarting simulation
c
         ...
c
c load random number generator status from last time step
c load the last filtered random field and last field of fluctuations

         IF(xm_bound) CALL rand_load

      else
c
         lstr = 0
         l = 1
c
         ...
c
c set disturbances to zero
c
         IF (xm_bound) THEN
            DO j=1-yhalo,nyp+yhalo
               DO k=1-zhalo,nzp+zhalo
                  upp(j,k)=0.0
                  vpp(j,k)=0.0
                  wpp(j,k)=0.0
               END DO
            END DO
         END IF
c
         ...
c
      end if
c
c load the inflow prescribed Reynolds stress

      IF (xm_bound) call loadRS
c
      ...
c
c     iteration start
c
      do l = lstr+1 , lstr+nstep
c
         ...
c
c get the inflow disturbances --
c ** do NOT call digi_filt again in the same time step! **

         IF (xm_bound) CALL digi_filt(l,lstr)
c
         ...
c
c save state of the random number generator
c save last filtered random field

         if(mod(l,100).eq.0) then
            IF(xm_bound) CALL rand_dump(l)
         end if
c
        ...
c
      end do
c
      ...
c
c save state of the random number generator
c save last filtered random field

      IF(xm_bound) CALL rand_dump(l)
c
      ...
c
      end program main

////////////////////////////////////////////////////////////////////////

! -------1---------2---------3---------4---------5---------6---------7--
! ++++++++++++++++++++++++++++++++++++++++++++++++++++++++++++++++++++++
! This subroutine saves the current state of the random number generator
! That is: the seed and the last field of fluctuations
!
!                                                        Emile :: May 07'
! ++++++++++++++++++++++++++++++++++++++++++++++++++++++++++++++++++++++

      SUBROUTINE rand_load
```

```
      USE incl3d
      USE mppvars

      implicit none

! :: Variables ::::::::::::::::::::::::::::::::::::::::::::::::::::::::::

      real*8 t
      real*8 qtmp(1-zhalo:nzp_m+zhalo,1-yhalo:nyp_m+yhalo,7)

      integer jbeg, kbeg, nrec, j, k

      character*19 file

! :: Main part ::::::::::::::::::::::::::::::::::::::::::::::::::::::::::::

      file='Last_filtered.bin'

      nrec=(1+(nzp_m+2*zhalo)*(nyp_m+2*yhalo)*7)*8

      open(123,file=file, status='old',
     +     form='unformatted', access='direct',
     +     recl=nrec)
c     +     convert='BIG_ENDIAN',recl=nrec)

      read(123,rec=1) t,qtmp

      close(123)

      if (ioproc) then
        print*, 'Read from file ',file
        print*, 'saved at t=',t
      endif

      jbeg=jbegin(sy)-1
      kbeg=kbegin(sz)-1

      do k=1-zhalo,nzp+zhalo
         do j=1-yhalo,nyp+yhalo

            uro(j,k)=qtmp(k+kbeg,j+jbeg,1)
            vro(j,k)=qtmp(k+kbeg,j+jbeg,2)
            wro(j,k)=qtmp(k+kbeg,j+jbeg,3)
            upp(j,k)=qtmp(k+kbeg,j+jbeg,4)
            vpp(j,k)=qtmp(k+kbeg,j+jbeg,5)
            wpp(j,k)=qtmp(k+kbeg,j+jbeg,6)
            rpp(j,k)=qtmp(k+kbeg,j+jbeg,7)
            if (.not.(abs(rpp(j,k)).lt.1.5)) rpp(j,k)=0.

         end do
      end do

! ::::::::::::::::::::::::::::::::::::::::::::::::::::::::::::::::::::::::

c      if(ioproc) then

         OPEN(10,file='randstate.dat',status='old',
     +           action='read', form='formatted')

         READ(10,1111) iseed
         DO j=0,Ngene-1
            READ(10,1111) iarray(j)
         END DO

         CLOSE(10)

         print*, 'Mersenne Twister state loaded!'

c      end if

 1111 FORMAT(I20)

      RETURN

      END SUBROUTINE rand_load

//////////////////////////////////////////////////////////////////////////

! -------1---------2---------3---------4---------5---------6---------7--
! ++++++++++++++++++++++++++++++++++++++++++++++++++++++++++++++++++++++++
! This subroutine saves the current state of the random number generator
! That is: the seed and the last field of fluctuations
!
!                                                        Emile :: May 07'
! ++++++++++++++++++++++++++++++++++++++++++++++++++++++++++++++++++++++++

      SUBROUTINE rand_dump(l)

      USE incl3d
```

```
      USE mppvars

      implicit none

      integer l

! :: Variables ::::::::::::::::::::::::::::::::::::::::::::::::::::::::

      integer j,k
      real*8 qtmp(1-zhalo:nzp+zhalo,1-yhalo:nyp+yhalo,7)

      integer accmod, bufsize, contig, subarray, real_mp_size,ier
      integer hand, status(MPI_STATUS_SIZE), offset_r
      integer(kind=MPI_OFFSET_KIND) disp, ioff, size
      integer totaldims(3), blockdims(3), blockstart(3)
      character*50 file
      real*8 iobuf_r(2)

! :: Main part ::::::::::::::::::::::::::::::::::::::::::::::::::::::::::

      do k=1-zhalo,nzp+zhalo
         do j=1-yhalo,nyp+yhalo

            qtmp(k,j,1)=uro(j,k)
            qtmp(k,j,2)=vro(j,k)
            qtmp(k,j,3)=wro(j,k)
            qtmp(k,j,4)=upp(j,k)
            qtmp(k,j,5)=vpp(j,k)
            qtmp(k,j,6)=wpp(j,k)
            qtmp(k,j,7)=rpp(j,k)

         end do
      end do

      if(l.le.9) then
         write(file,'(''Last_filtered_'',i1)') l
      else if (l.le.99) then
         write(file,'(''Last_filtered_'',i2)') l
      else if (l.le.999) then
         write(file,'(''Last_filtered_'',i3)') l
      else if (l.le.9999) then
         write(file,'(''Last_filtered_'',i4)') l
      else if (l.le.99999) then
         write(file,'(''Last_filtered_'',i5)') l
      else if (l.le.999999) then
         write(file,'(''Last_filtered_'',i6)') l
      else
         write(file,'(''Last_filtered_'',i7)') l
      endif

      if (procid==0) then
         print*, 'writing to file ',file
      endif

      accmod = ior(MPI_MODE_WRONLY,MPI_MODE_CREATE)
      call MPI_FILE_OPEN(MPI_comm_self, file,
     +     accmod, MPI_info_null, hand, ier)
c
      bufsize = 1
      call MPI_TYPE_CONTIGUOUS(bufsize, real_mp_type, contig,ier)
      call MPI_TYPE_COMMIT(contig, ier)
c
      iobuf_r(1) = time

      offset_r = 1
c
      ioff = 0
      disp = 0
      call MPI_FILE_SET_VIEW(hand, ioff, real_mp_type,
     +     contig, 'native', MPI_INFO_NULL, ier)
      if(procid == 0) then
         call MPI_FILE_WRITE_AT(hand, disp, iobuf_r,
     +        bufsize, real_mp_type, status, ier)
      endif
      call MPI_TYPE_EXTENT(real_mp_type, real_mp_size, ier)
c
      ioff = offset_r*real_mp_size
      disp = 0
c
      totaldims(1)  = nzp_m+2*zhalo
      totaldims(2)  = nyp_m+2*yhalo
      totaldims(3)  = 7

      blockdims(1)  = nzp+2*zhalo
      blockdims(2)  = nyp+2*yhalo
      blockdims(3)  = 7

      blockstart(1) = kbegin(sz)-1
      blockstart(2) = jbegin(sy)-1
```

```
      blockstart(3) = 0

      bufsize = product(blockdims)
c
      call MPI_TYPE_CREATE_SUBARRAY(3,totaldims,blockdims,blockstart,
     +     MPI_ORDER_FORTRAN, real_mp_type, subarray, ier)
      call MPI_TYPE_COMMIT(subarray, ier)
      call MPI_FILE_SET_VIEW(hand, ioff, real_mp_type, subarray,
     +     'native', MPI_INFO_NULL, ier)
      call MPI_FILE_WRITE_AT_ALL(hand, disp,
     +     qtmp(1-zhalo:nzp+zhalo,1-yhalo:nyp+yhalo,1:7), bufsize,
     +     real_mp_type, status, ier)
      call MPI_FILE_CLOSE(hand,ier)
      if (procid==0) then
         print*, 'completed write, ier = ', ier
      endif

! ::::::::::::::::::::::::::::::::::::::::::::::::::::::::::::::::::::::::

      if(ioproc) then

         if(l.le.9) then
            write(file,'(''randstate_'',i1)') l
         else if (l.le.99) then
            write(file,'(''randstate_'',i2)') l
         else if (l.le.999) then
            write(file,'(''randstate_'',i3)') l
         else if (l.le.9999) then
            write(file,'(''randstate_'',i4)') l
         else if (l.le.99999) then
            write(file,'(''randstate_'',i5)') l
         else if (l.le.999999) then
            write(file,'(''randstate_'',i6)') l
         else
            write(file,'(''randstate_'',i7)') l
         endif

         print*, 'writing to file ',file

         OPEN(10,file=file,status='unknown',
     +        action='write', form='formatted')

         WRITE(10,1111) iseed
         DO j=0,Ngene-1
            WRITE(10,1111) iarray(j)
         END DO
         CLOSE(10)

         print*, 'Mersenne Twister state is saved!'

      end if

 1111 FORMAT(I20)

      RETURN

      END SUBROUTINE rand_dump

//////////////////////////////////////////////////////////////////////////

! -------1---------2---------3---------4---------5---------6---------7--
! ++++++++++++++++++++++++++++++++++++++++++++++++++++++++++++++++++++++++
!  This subroutine loads the prescribed Reynolds stresses
!
!                                                          Emile :: May 07'
! ++++++++++++++++++++++++++++++++++++++++++++++++++++++++++++++++++++++++

      subroutine loadRS

! ---
      use incl3d
      use mppvars
! ---

      implicit none

! :: Declaration section ::::::::::::::::::::::::::::::::::::::::::::::::

      integer j

      real*8, DIMENSION(nRS) :: rs1, rs2, rs3, rs4
      real*8, DIMENSION(nRS) :: yfile, yf1, yf2, yf3, yf4
      real*8 :: tmp1, tmp2, tmp3, tmp4

! :: Subroutine starts here... ::::::::::::::::::::::::::::::::::::::::::

! It is assumed that lengths in 'RStress.txt' are expressed in
! displacement thickness units
```

```
! Load data

      open(37,file='RStress.txt',status='old',form='formatted')

      do j=1,nRS
         read(37,*) yfile(j),rs1(j),rs2(j),rs3(j),rs4(j)
      end do

      close(37)

! Interpolate

      do j=1-yhalo,nyp+yhalo

         RStress(j,1)=0.
         RStress(j,2)=0.
         RStress(j,3)=0.
         RStress(j,4)=0.

      end do

      call spline(yfile,rs1,nRS-1,0.,0.,yf1)
      call spline(yfile,rs2,nRS-1,0.,0.,yf2)
      call spline(yfile,rs3,nRS-1,0.,0.,yf3)
      call spline(yfile,rs4,nRS-1,0.,0.,yf4)

      do j=1-yhalo,nyp+yhalo

         if((y(1,j,1).le.yfile(nRS)).and.(y(1,j,1).gt.0.)) then

            call splint(yfile,rs1,yf1,nRS-1,y(1,j,1),tmp1)
            call splint(yfile,rs2,yf2,nRS-1,y(1,j,1),tmp2)
            call splint(yfile,rs3,yf3,nRS-1,y(1,j,1),tmp3)
            call splint(yfile,rs4,yf4,nRS-1,y(1,j,1),tmp4)

            RStress(j,1)=tmp1
            RStress(j,2)=tmp2
            RStress(j,3)=tmp3
            RStress(j,4)=tmp4

         end if

      end do

      return

      end subroutine loadRS
```

D. Matlab/Fortran scripts to extract the shock system

D.1 Step 1. Extraction from the raw data

```
% +--------------------------------------------------------------+ %
% |                                                              | %
% |     This program extracts the location of the shock system   | %
% |                                                              | %
% |                                          emile :: 21/10/08   | %
% |                                                   05/03/09   | %
% +--------------------------------------------------------------+ %

% -- clear workspace -- ::::::::::::::::::::::::::::::::::::::::::::

close all
clear all

% -- load parameters -- ::::::::::::::::::::::::::::::::::::::::::::

% > manual stuff

nfirst=100100;
nlast=1400000;
nstep=100;

dir1='/mnt/HD1TB/XLES/Results/Inst/Planes/Reduced/';
dir2=['/home/emile/Soton/ControlCenter/IUSTI/XLES/MatScripts/',...
    'ShockSystem/binaries/'];

% > automatic stuff... enjoy! ... with care though

path=cellstr('../../BinTreat/Stats/toplot.bin');
filename=char(path);
fid=fopen(filename,'r');
read=fread(fid,11,'double');
nx=read(1);
ny=read(2);
nz=read(3);
clear read
ldata=nx;
x=fread(fid,ldata,'double');
clear ldata
ldata=ny;
y=fread(fid,ldata,'double');
clear ldata
ldata=nz;
z=fread(fid,ldata,'double');
clear ldata
fclose(fid);

% -- load buffer info -- ::::::::::::::::::::::::::::::::::::::::::::

path=cellstr([dir1,'Qplane_',num2str(100100)]);
filename=char(path);
fid=fopen(filename,'r');

nbuf=fread(fid,1,'single');
nbuf=nbuf+5*3;
read=fread(fid,nbuf-1,'single');
nvar=read(2);
t0=read(3);
xy=read(7:11);
clear read

fclose(fid);

% -- extract the shock system -- ::::::::::::::::::::::::::::::::::::

for n=nfirst:nstep:nlast                % -> loop over the data range
```

```
if rem(n,10000)==0
  n %#ok<NOPTS>
end

% > load data

path=cellstr([dir1,'Qplane_',num2str(n)]);
filename=char(path);
fid=fopen(filename,'r');

read=fread(fid,nbuf,'single');
t1=read(4);
clear read

ldata=nx*ny*nvar*5;
plan1=fread(fid,ldata,'single');
plan1=reshape(plan1,nx,ny,nvar,5);

clear ldata

fclose(fid);

div=zeros(ny,nx,5);

for i=1:nx
  for j=1:ny
    for nplane=1:5
      div(j,i,nplane)=plan1(i,j,3,nplane);
    end
  end
end

clear plan1

% > open binary file where the data are dumped

path=cellstr([dir2,'shocksys_',num2str(n)]);
filename=char(path);
fid=fopen(filename,'wb');

fwrite(fid,single(t1-t0),'single'); % write time

%fclose(fid); % temporary clean

% > loop over planes

for nplane=1:5

  % Find all contours where div(u)=-0.025
  figure(99)
  [C,h]=contour(x,y,div(:,:,nplane),-0.025*[1 1]);
  clear h
  close(99)

  % Keep the longest contour, which should be the shock system
  I=find(C(1,:)==-0.025);
  [ii,jj]=max(C(2,I));
  C(:,[1:I(jj),I(jj+1):end])=[];

  clear ii
  clear jj
  clear I

  % Retain only the points belonging to the y-axis
  IX=[];
  cp=0;
  for p=1:length(C(2,:))
    I=find(y==C(2,p));   %#ok<EFIND>
    if isempty(I)
      cp=cp+1;
      IX(cp)=p; %#ok<AGROW>
    end
    clear I
  end
  C(:,IX)=[];
  clear IX
  clear cp
  clear p

  % Keep only cases with 4 points per y value
  %Co=C;
  IX=[];
  for j=1:ny
    I=find(C(2,:)==y(j));
    if length(I)~=4
      IX=[IX,I]; %#ok<AGROW>
    end
  end
  C(:,IX)=[];
```

```
clear IX

% Sort C array by same y value
[C(2,:),IX]=sort(C(2,:));
C(1,:)=C(1,IX);
clear IX

% Weak compression waves may have been captured... let's remove
% occurences of points spaced by less than 1.5*dx to suppress them
IX=[];
k=1;
for j=1:length(C(1,:))/4
  tmpo=C(1,k:k+3);
  tmpo=sort(tmpo);
  dtmpo=zeros(3,1);
  for p=1:3
    dtmpo(p)=tmpo(p+1)-tmpo(p);
  end
  I=find(dtmpo<=1.5*(x(2)-x(1))); %#ok<EFIND>
  if ~isempty(I)
    IX=[IX,k:1:k+3]; %#ok<AGROW>
  end
  k=k+4;
  clear I
  clear dtmpo
  clear tmpo
end
clear k
clear p
C(:,IX)=[];
clear IX

% Split the obtained >< shape in the > and < side
left=zeros(2,length(C(1,:))/4);
right=zeros(2,length(C(1,:))/4);

k=1;
for i=1:length(C(1,:))/4
  tmpo=C(1,k:k+3);
  tmpo=sort(tmpo);

  left(1,i)=0.5*(tmpo(1)+tmpo(2));
  right(1,i)=0.5*(tmpo(3)+tmpo(4));

  left(2,i)=C(2,k);
  right(2,i)=C(2,k);

  k=k+4;
end
clear k
clear tmpo

clear C

% Transform > and < into / and \
% locate turn in > and <
[m,I1]=max(left(1,:));
[m,I2]=min(right(1,:));
clear m
incident=[left(:,I1+1:end),right(:,1:I2-1)];
reflected=[left(:,1:I1-1),right(:,I2+1:end)];

[incident(1,:),IX]=sort(incident(1,:));
incident(2,:)=incident(2,IX);
clear IX
[incident(2,:),IX]=sort(incident(2,:),'descend');
incident(1,:)=incident(1,IX);
clear IX

[reflected(1,:),IX]=sort(reflected(1,:));
reflected(2,:)=reflected(2,IX);
clear IX
[reflected(2,:),IX]=sort(reflected(2,:));
reflected(1,:)=reflected(1,IX);
clear IX

clear I1
clear I2

clear left
clear right

% shock lines must be surjective functions to avoid issues when
% interpolating... let's remove multi-valued x-positions

dx=zeros(length(incident(1,:))-1,1);
for j=1:length(incident(1,:))-1
  dx(j)=incident(1,j+1)-incident(1,j);
end
```

```
  I=find(dx<=0);
  if ~isempty(I)
    incident(:,I(1):end)=[];
  end
  clear I
  clear dx

  dx=zeros(length(reflected(1,:))-1,1);
  for j=1:length(reflected(1,:))-1
    dx(j)=reflected(1,end-j)-reflected(1,end-j+1);
  end
  I=find(dx>=0);
  if ~isempty(I)
    reflected(:,1:end-I(1))=[];
  end
  clear I
  clear dx

  % interpolate shock lines on x-axis values

  I=find(x>=min(reflected(1,:)));
  imin=I(1);
  clear I
  I=find(x>=max(reflected(1,:)));
  imax=I(1)-1;
  clear I
  xr=x(imin:imax);

  I=find(x>=min(incident(1,:)));
  imin=I(1);
  clear I
  I=find(x>=max(incident(1,:)));
  imax=I(1)-1;
  clear I
  xi=x(imin:imax);

  clear imin
  clear imax

  yi=interp1(incident(1,:),incident(2,:),xi,'cubic');
  yr=interp1(reflected(1,:),reflected(2,:),xr,'cubic');

  clear incident
  clear reflected

  if 1==2

    figure(1)
    hold on

    %plot(C(1,I(jj)+1:I(jj+1)-1),C(2,I(jj)+1:I(jj+1)-1),'b*')
    %plot(Co(1,:),Co(2,:),'r*')
    %plot(C(1,:),C(2,:),'b*')

    %plot(left(1,:),left(2,:),'ro-')
    %plot(right(1,:),right(2,:),'ko-')

    %plot(incident(1,:),incident(2,:),'m*')
    %plot(reflected(1,:),reflected(2,:),'y*')

    plot(xr,yr,'b','LineWidth',2)
    plot(xi,yi,'r','LineWidth',2)

    %plot([xr;xi],[yr;yi],'b.','LineWidth',2,'MarkerSize',14)

    %axis([230 330 0 70])

  end

  fwrite(fid,single(z(xy(nplane))),'single'); % write xy-p. loc.
  fwrite(fid,single(length(xi)),'single'); % write array size
  fwrite(fid,single(length(yi)),'single'); % write array size
  fwrite(fid,single(length(xr)),'single'); % write array size
  fwrite(fid,single(length(yr)),'single'); % write array size

  fwrite(fid,single(xi),'single');
  fwrite(fid,single(yi),'single');
  fwrite(fid,single(xr),'single');
  fwrite(fid,single(yr),'single');

  clear xr
  clear yr
  clear xi
  clear yi

end
  %pause(0.3)
  %close(1)
```

```
    fclose(fid); % close binary data where we dumped the shock position
end
```

D.2 Step 2. Compute mean position

```
! +++++++1+++++++++2+++++++++3+++++++++4+++++++++5+++++++++6+++++++++7++
!  This program computes the average location of the shock system
!
!                                                  Emile  -  Oct. 2008
!                                                            Mar. 2009
! ++++++++++++++++++++++++++++++++++++++++++++++++++++++++++++++++++++++

 PROGRAM main

   IMPLICIT NONE

! :: Declaration section ::::::::::::::::::::::::::::::::::::::::::::::

! parameters

   integer, PARAMETER :: sp=kind(0.0E0) ! single
   integer, PARAMETER :: dp=kind(0.0D0) ! double

   integer, PARAMETER :: nfirst=100100
   integer, PARAMETER :: nlast=1400000
   integer, PARAMETER :: nfreq=100

   integer, PARAMETER :: lbits=1

   integer, PARAMETER :: nx=451,ny=151,nz=281

   real(sp), PARAMETER :: eps=0.0001

! paths

   character(LEN=150) :: path1='/home/emile/Soton/ControlCenter/IUSTI/XLES/Grid/'
   character(LEN=150) :: path2='/home/emile/Soton/ControlCenter/IUSTI/XLES/
                                          MatScripts/ShockSystem/binaries/'

! dummy variables

   integer :: nrec,pos,ierror,nplane

   integer :: nxi,nyi,nxr,nyr

   integer :: n,i,ii

   integer, DIMENSION(1:nx) :: cpi,cpr

   real(sp) :: time,tmp

   real(dp), DIMENSION(1:nx) :: x
   real(sp), DIMENSION(1:nx) :: xg,yig,yrg

   real(sp), DIMENSION(:), ALLOCATABLE :: xi,yi,xr,yr

   character(LEN=200) file

! :: Main program ::::::::::::::::::::::::::::::::::::::::::::::::::::::

! :: Load global x-axis ::::::::::::::::::::::::::::::::::::::::::::::::

   file='axis'
   file=TRIM(path1)//TRIM(file)

   WRITE(*,*) 'Loading grid points...'

   OPEN(UNIT=10,FILE=file,STATUS='OLD',ACTION='READ', &
        FORM='UNFORMATTED',IOSTAT=ierror)
   IF (ierror>0) THEN
      WRITE(*,*) 'Error! -> could not open grid point data file', ierror
      STOP
   END IF

   REWIND(10)

   READ(10) (x(i),i=1,nx)

   CLOSE(10)

   xg=x

   WRITE(*,*) 'x(1)=', xg(1), 'x(nx)=',xg(nx)
```

```
! :: Initialise ::::::::::::::::::::::::::::::::::::::::::::::::::::::::::

   DO i=1,nx
      cpi(i)=0
      cpr(i)=0
      yig(i)=0.0
      yrg(i)=0.0
   END DO

! :: Average ::::::::::::::::::::::::::::::::::::::::::::::::::::::::::::::

   nrec=lbits

   DO n=nfirst,nlast,nfreq

      IF (mod(n,100000).eq.0) THEN
         WRITE(*,*) 'n=',n
      END IF

      if(n.le.9) then
         write(file,'(''shocksys_'',i1)') n
      else if (n.le.99) then
         write(file,'(''shocksys_'',i2)') n
      else if (n.le.999) then
         write(file,'(''shocksys_'',i3)') n
      else if (n.le.9999) then
         write(file,'(''shocksys_'',i4)') n
      else if (n.le.99999) then
         write(file,'(''shocksys_'',i5)') n
      else if (n.le.999999) then
         write(file,'(''shocksys_'',i6)') n
      else
         write(file,'(''shocksys_'',i7)') n
      endif

      file=TRIM(path2)//TRIM(file)

      pos=1

      OPEN(11,file=file, status='old',form='unformatted', &
           access='direct',recl=nrec)
      READ(11,rec=pos) time

      !WRITE(*,*) 'time =', time

      ! loop over planes

      DO nplane=1,5

         pos=pos+1
         READ(11,rec=pos) tmp
         !WRITE(*,*) 'z(plane) =', tmp

         pos=pos+1
         READ(11,rec=pos) tmp
         nxi=tmp
         !WRITE(*,*) 'nxi =', nxi

         pos=pos+1
         READ(11,rec=pos) tmp
         nyi=tmp
         !WRITE(*,*) 'nyi =', nyi

         pos=pos+1
         READ(11,rec=pos) tmp
         nxr=tmp
         !WRITE(*,*) 'nxr =', nxr

         pos=pos+1
         READ(11,rec=pos) tmp
         nyr=tmp
         !WRITE(*,*) 'nyr =', nyr

         ALLOCATE(xi(1:nxi),yi(1:nyi),xr(1:nxr),yr(1:nyr))

         DO i=1,nxi
            pos=pos+1
            READ(11,rec=pos) tmp
            xi(i)=tmp
         END DO
         DO i=1,nyi
            pos=pos+1
            READ(11,rec=pos) tmp
            yi(i)=tmp
            !WRITE(*,*) i,xi(i),yi(i)
         END DO
         DO i=1,nxr
            pos=pos+1
```

```
            READ(11,rec=pos) tmp
            xr(i)=tmp
         END DO
         DO i=1,nyr
            pos=pos+1
            READ(11,rec=pos) tmp
            yr(i)=tmp
         END DO

         ! Accumulate where possible...

         DO i=1,nx
            DO ii=1,nxi
               IF (abs(xi(ii)-x(i))<eps) THEN
                  yig(i)=yig(i)+yi(ii)
                  cpi(i)=cpi(i)+1
               END IF
            END DO
            DO ii=1,nxr
               IF (abs(xr(ii)-x(i))<eps) THEN
               !IF (xr(ii).eq.x(i)) THEN
                  yrg(i)=yrg(i)+yr(ii)
                  cpr(i)=cpr(i)+1
               END IF
            END DO
         END DO

         DEALLOCATE(xi,yi,xr,yr)

      END DO

      CLOSE(11)

   END DO

   ! average

   DO i=1,nx
      IF (cpi(i).ne.0) THEN
         yig(i)=yig(i)/real(cpi(i))
      END IF
      IF (cpr(i).ne.0) THEN
         yrg(i)=yrg(i)/real(cpr(i))
      END IF
   END DO

   file='shock_avg.bin'

   file=TRIM(path2)//TRIM(file)

   print*, 'writing single precision file:',file

   nrec=(nx*5)*lbits

   OPEN(11,file=file, status='unknown',form='unformatted', &
        access='direct',recl=nrec)
   WRITE(11,rec=1) xg,yig,yrg,real(cpi),real(cpr)
   CLOSE(11)

   WRITE(*,*) 'Done!'

 END PROGRAM main
```

D.3 Step 3. Select the data range to clip

```
% +-------------------------------------------------------------+ %
% |                                                             | %
% |   Use the computed mean shock system to pick the best common    | %
% |                     x-range for the shocks                  | %
% |                                                             | %
% |                                          emile :: 06/03/09  | %
% +-------------------------------------------------------------+ %

% -- clear workspace -- ::::::::::::::::::::::::::::::::::::::::::::

close all
clear all

% -- parameters -- ::::::::::::::::::::::::::::::::::::::::::::::::::

nx=451;

dir1=['/home/emile/Soton/ControlCenter/IUSTI/XLES/MatScripts/',...
```

```
    'ShockSystem/binaries/'];

Inc1=194;
Inc2=293;

Ref1=285;
Ref2=377;

% -- load mean position of the shock system -- ::::::::::::::::::::::::

path=cellstr([dir1,'shock_avg.bin']);
filename=char(path);
fid=fopen(filename,'rb');
xg=fread(fid,nx,'single');
yig=fread(fid,nx,'single');
yrg=fread(fid,nx,'single');
cpi=fread(fid,nx,'single');
cpr=fread(fid,nx,'single');
fclose(fid);

figure(1)
% ------------
subplot(1,2,1)
hold on
plot(xg,yig,'r')
plot(xg,yrg,'b')

plot(xg(Inc1),yig(Inc1),'m*')
plot(xg(Inc2),yig(Inc2),'m*')
plot(xg(Ref1),yrg(Ref1),'k*')
plot(xg(Ref2),yrg(Ref2),'k*')

% ------------
subplot(1,2,2)
hold on
plot(xg,cpi,'r')
plot(xg,cpr,'b')

plot(xg(Inc1),cpi(Inc1),'m*')
plot(xg(Inc2),cpi(Inc2),'m*')
plot(xg(Ref1),cpr(Ref1),'k*')
plot(xg(Ref2),cpr(Ref2),'k*')
```

D.4 Step 4. Clip the extracted data

```
! +++++++1+++++++++2+++++++++3+++++++++4+++++++++5+++++++++6+++++++++7++
!  This program writes the shock system positions in the preselected
!  x-range
!
!                                                    Emile  -  Mar. 2009
! ++++++++++++++++++++++++++++++++++++++++++++++++++++++++++++++++++++++

 PROGRAM main

   IMPLICIT NONE

! :: Declaration section ::::::::::::::::::::::::::::::::::::::::::::::

! parameters

   integer, PARAMETER :: sp=kind(0.0E0)
   integer, PARAMETER :: dp=kind(0.0D0)
   integer, PARAMETER :: wp=sp

   integer, PARAMETER :: lbits=1
   integer, PARAMETER :: lbitd=2

   integer, PARAMETER :: nfirst=100100 ! first restart file available

   integer, PARAMETER :: nt=12999      ! number of files to load
   integer, PARAMETER :: nfreq=100     ! number of time steps between
                                       ! each snapshots

   integer, PARAMETER :: nx=451 ! full x-axis size
   integer, PARAMETER :: nxi1=194,nxi2=293 ! extraction region
   integer, PARAMETER :: nxr1=285,nxr2=377 ! extraction region

!   real(sp), PARAMETER :: eps=0.1

! paths

   character(LEN=150) :: path1='/home/emile/Soton/ControlCenter/IUSTI/XLES/Grid/'
   character(LEN=150) :: path2='/home/emile/Soton/ControlCenter/IUSTI/XLES/
```

```
                                                MatScripts/ShockSystem/binaries/'
   character(LEN=150) :: path3='/home/emile/Soton/ControlCenter/IUSTI/XLES/
                                                MatScripts/ShockSystem/incident/'
   character(LEN=150) :: path4='/home/emile/Soton/ControlCenter/IUSTI/XLES/
                                               MatScripts/ShockSystem/reflected/'

! output arrays

   real(sp), DIMENSION(1:nxi2-nxi1+1,1:nt) :: inc1,inc2,inc3,inc4,inc5
   real(sp), DIMENSION(1:nxr2-nxr1+1,1:nt) :: ref1,ref2,ref3,ref4,ref5

   real(sp), DIMENSION(1:nxi2-nxi1+1) :: xinc
   real(sp), DIMENSION(1:nxr2-nxr1+1) :: xref

   real(sp), DIMENSION(1:nt) :: t

! dummy variables

   integer :: ierror,pos,nplane,nrec

   integer :: nxi,nyi,nxr,nyr

   integer :: step,n,i,ii

   real(sp) :: time,tmp

   real(dp), DIMENSION(1:nx) :: x

   real(sp), DIMENSION(:), ALLOCATABLE :: xi,yi,xr,yr

   character(LEN=200) file

! :: Main program ::::::::::::::::::::::::::::::::::::::::::::::::::::::

! :: Load x-axis ::::::::::::::::::::::::::::::::::::::::::::::::::::::

   file='axis'
   file=TRIM(path1)//TRIM(file)

   WRITE(*,*) 'Loading grid points...'

   OPEN(UNIT=10,FILE=file,STATUS='OLD',ACTION='READ', &
        FORM='UNFORMATTED',IOSTAT=ierror)
   IF (ierror>0) THEN
      WRITE(*,*) 'Error! -> could not open grid point data file', ierror
      STOP
   END IF

   REWIND(10)

   READ(10) (x(i),i=1,nx)

   CLOSE(10)

   WRITE(*,*) 'x(1)=', x(1), 'x(nx)=',x(nx)

   DO i=nxi1,nxi2
      xinc(i-nxi1+1)=x(i)
   END DO
   DO i=nxr1,nxr2
      xref(i-nxr1+1)=x(i)
   END DO

! :: Initialise ::::::::::::::::::::::::::::::::::::::::::::::::::::::::

   ! step number to load
   step=nfirst-nfreq

   nrec=lbits

! :: Extract data ::::::::::::::::::::::::::::::::::::::::::::::::::::::

   DO n=1,nt

      step=step+nfreq

      IF(step.LE.9) THEN
         WRITE(file,'(''shocksys_'',i1)') step
      ELSE IF (step.LE.99) THEN
         WRITE(file,'(''shocksys_'',i2)') step
      ELSE IF (step.LE.999) THEN
         WRITE(file,'(''shocksys_'',i3)') step
      ELSE IF (step.LE.9999) THEN
         WRITE(file,'(''shocksys_'',i4)') step
      ELSE IF (step.LE.99999) THEN
         WRITE(file,'(''shocksys_'',i5)') step
      ELSE IF (step.LE.999999) THEN
         WRITE(file,'(''shocksys_'',i6)') step
      ELSE IF (step.LE.9999999) THEN
```

```
   WRITE(file,'(''shocksys_'',i7)') step
END IF

file=TRIM(path2)//TRIM(file)

pos=1

OPEN(11,file=file, status='old',form='unformatted', &
     access='direct',recl=nrec)
READ(11,rec=pos) time

t(n)=time

! loop over planes

DO nplane=1,5

   pos=pos+1
   READ(11,rec=pos) tmp
   !WRITE(*,*) 'z(plane) =', tmp

   pos=pos+1
   READ(11,rec=pos) tmp
   nxi=tmp
   !WRITE(*,*) 'nxi =', nxi

   pos=pos+1
   READ(11,rec=pos) tmp
   nyi=tmp
   !WRITE(*,*) 'nyi =', nyi

   pos=pos+1
   READ(11,rec=pos) tmp
   nxr=tmp
   !WRITE(*,*) 'nxr =', nxr

   pos=pos+1
   READ(11,rec=pos) tmp
   nyr=tmp
   !WRITE(*,*) 'nyr =', nyr

   ALLOCATE(xi(1:nxi),yi(1:nyi),xr(1:nxr),yr(1:nyr))

   DO i=1,nxi
      pos=pos+1
      READ(11,rec=pos) tmp
      xi(i)=tmp
   END DO
   DO i=1,nyi
      pos=pos+1
      READ(11,rec=pos) tmp
      yi(i)=tmp
   END DO
   DO i=1,nxr
      pos=pos+1
      READ(11,rec=pos) tmp
      xr(i)=tmp
   END DO
   DO i=1,nyr
      pos=pos+1
      READ(11,rec=pos) tmp
      yr(i)=tmp
   END DO

   ! store in output arrays if data is available
   ! if not, set y to 0
   IF (nplane==1) THEN
      DO i=1,nxi2-nxi1+1
         DO ii=1,nxi
            IF (xi(ii)==xinc(i)) inc1(i,n)=yi(ii)
         END DO
      END DO
      DO i=1,nxr2-nxr1+1
         DO ii=1,nxr
            IF (xr(ii)==xref(i)) ref1(i,n)=yr(ii)
         END DO
      END DO
   END IF

   IF (nplane==2) THEN
      DO i=1,nxi2-nxi1+1
         DO ii=1,nxi
            IF (xi(ii)==xinc(i)) inc2(i,n)=yi(ii)
         END DO
      END DO
      DO i=1,nxr2-nxr1+1
         DO ii=1,nxr
            IF (xr(ii)==xref(i)) ref2(i,n)=yr(ii)
         END DO
```

```
         END DO
       END IF

       IF (nplane==3) THEN
          DO i=1,nxi2-nxi1+1
             DO ii=1,nxi
                IF (xi(ii)==xinc(i)) inc3(i,n)=yi(ii)
             END DO
          END DO
          DO i=1,nxr2-nxr1+1
             DO ii=1,nxr
                IF (xr(ii)==xref(i)) ref3(i,n)=yr(ii)
             END DO
          END DO
       END IF

      IF (nplane==4) THEN
          DO i=1,nxi2-nxi1+1
             DO ii=1,nxi
                IF (xi(ii)==xinc(i)) inc4(i,n)=yi(ii)
             END DO
          END DO
          DO i=1,nxr2-nxr1+1
             DO ii=1,nxr
                IF (xr(ii)==xref(i)) ref4(i,n)=yr(ii)
             END DO
          END DO
       END IF

       IF (nplane==5) THEN
          DO i=1,nxi2-nxi1+1
             DO ii=1,nxi
                IF (xi(ii)==xinc(i)) inc5(i,n)=yi(ii)
             END DO
          END DO
          DO i=1,nxr2-nxr1+1
             DO ii=1,nxr
                IF (xr(ii)==xref(i)) ref5(i,n)=yr(ii)
             END DO
          END DO
       END IF

       DEALLOCATE(xi,yi,xr,yr)

    END DO

    CLOSE(11)

END DO

!DO n=1,nt
!   write(*,*), t(n),inc1(1,n)
!END DO

! Write data to files

file='buffer.bin'
file=TRIM(path3)//TRIM(file)
print*, 'writing single precision file:',file
nrec=(3+(nxi2-nxi1+1)+nt)*lbits
OPEN(11,file=file, status='unknown',form='unformatted', &
     access='direct',recl=nrec)
WRITE(11,rec=1) real(nxi1),real(nxi2),real(nt),xinc,t
CLOSE(11)

file='inc1.bin'
file=TRIM(path3)//TRIM(file)
print*, 'writing single precision file:',file
nrec=((nxi2-nxi1+1)*nt)*lbits
OPEN(11,file=file, status='unknown',form='unformatted', &
     access='direct',recl=nrec)
WRITE(11,rec=1) inc1
CLOSE(11)

file='inc2.bin'
file=TRIM(path3)//TRIM(file)
print*, 'writing single precision file:',file
nrec=((nxi2-nxi1+1)*nt)*lbits
OPEN(11,file=file, status='unknown',form='unformatted', &
     access='direct',recl=nrec)
WRITE(11,rec=1) inc2
CLOSE(11)

file='inc3.bin'
file=TRIM(path3)//TRIM(file)
print*, 'writing single precision file:',file
nrec=((nxi2-nxi1+1)*nt)*lbits
OPEN(11,file=file, status='unknown',form='unformatted', &
     access='direct',recl=nrec)
```

```
  WRITE(11,rec=1) inc3
  CLOSE(11)

  file='inc4.bin'
  file=TRIM(path3)//TRIM(file)
  print*, 'writing single precision file:',file
  nrec=((nxi2-nxi1+1)*nt)*lbits
  OPEN(11,file=file, status='unknown',form='unformatted', &
       access='direct',recl=nrec)
  WRITE(11,rec=1) inc4
  CLOSE(11)

  file='inc5.bin'
  file=TRIM(path3)//TRIM(file)
  print*, 'writing single precision file:',file
  nrec=((nxi2-nxi1+1)*nt)*lbits
  OPEN(11,file=file, status='unknown',form='unformatted', &
       access='direct',recl=nrec)
  WRITE(11,rec=1) inc5
  CLOSE(11)



  file='buffer.bin'
  file=TRIM(path4)//TRIM(file)
  print*, 'writing single precision file:',file
  nrec=(3+(nxr2-nxr1+1)+nt)*lbits
  OPEN(11,file=file, status='unknown',form='unformatted', &
       access='direct',recl=nrec)
  WRITE(11,rec=1) real(nxr1),real(nxr2),real(nt),xref,t
  CLOSE(11)

  file='ref1.bin'
  file=TRIM(path4)//TRIM(file)
  print*, 'writing single precision file:',file
  nrec=((nxr2-nxr1+1)*nt)*lbits
  OPEN(11,file=file, status='unknown',form='unformatted', &
       access='direct',recl=nrec)
  WRITE(11,rec=1) ref1
  CLOSE(11)

  file='ref2.bin'
  file=TRIM(path4)//TRIM(file)
  print*, 'writing single precision file:',file
  nrec=((nxr2-nxr1+1)*nt)*lbits
  OPEN(11,file=file, status='unknown',form='unformatted', &
       access='direct',recl=nrec)
  WRITE(11,rec=1) ref2
  CLOSE(11)

  file='ref3.bin'
  file=TRIM(path4)//TRIM(file)
  print*, 'writing single precision file:',file
  nrec=((nxr2-nxr1+1)*nt)*lbits
  OPEN(11,file=file, status='unknown',form='unformatted', &
       access='direct',recl=nrec)
  WRITE(11,rec=1) ref3
  CLOSE(11)

  file='ref4.bin'
  file=TRIM(path4)//TRIM(file)
  print*, 'writing single precision file:',file
  nrec=((nxr2-nxr1+1)*nt)*lbits
  OPEN(11,file=file, status='unknown',form='unformatted', &
       access='direct',recl=nrec)
  WRITE(11,rec=1) ref4
  CLOSE(11)

  file='ref5.bin'
  file=TRIM(path4)//TRIM(file)
  print*, 'writing single precision file:',file
  nrec=((nxr2-nxr1+1)*nt)*lbits
  OPEN(11,file=file, status='unknown',form='unformatted', &
       access='direct',recl=nrec)
  WRITE(11,rec=1) ref5
  CLOSE(11)

  WRITE(*,*) 'Done!'

END PROGRAM main
```

D.5 Step 5. Remove most of the spurious points

```
% +--------------------------------------------------------------------+ %
% |                                                                    | %
% |                Remove spurious shock position data                 | %
% |                                                                    | %
% |                                              emile :: 06/03/09     | %
% +--------------------------------------------------------------------+ %

% -- clear workspace -- ::::::::::::::::::::::::::::::::::::::::::::::

close all
clear all

% -- parameters -- ::::::::::::::::::::::::::::::::::::::::::::::::::::

dirI=['/home/emile/Soton/ControlCenter/IUSTI/XLES/MatScripts/',...
    'ShockSystem/incident/'];
dirR=['/home/emile/Soton/ControlCenter/IUSTI/XLES/MatScripts/',...
    'ShockSystem/reflected/'];

% -- load data -- ::::::::::::::::::::::::::::::::::::::::::::::::::::

path=cellstr([dirI,'buffer.bin']);
filename=char(path);
fid=fopen(filename,'rb');
nxi1=fread(fid,1,'single');
nxi2=fread(fid,1,'single');
fread(fid,1,'single');
xi=fread(fid,nxi2-nxi1+1,'single');
fclose(fid);

path=cellstr([dirR,'buffer.bin']);
filename=char(path);
fid=fopen(filename,'rb');
nxr1=fread(fid,1,'single');
nxr2=fread(fid,1,'single');
nt=fread(fid,1,'single');
xr=fread(fid,nxr2-nxr1+1,'single');
t=fread(fid,nt,'single');
fclose(fid);

t2=t(1):t(2)-t(1):t(end);
clear t
t=t2;
%clear t2

for nplane=1:5

  t=t2;

  path=cellstr([dirI,'inc',num2str(nplane),'.bin']);
  filename=char(path);
  fid=fopen(filename,'rb');
  inc=fread(fid,(nxi2-nxi1+1)*nt,'single');
  fclose(fid);
  inc=reshape(inc,nxi2-nxi1+1,nt);

  path=cellstr([dirR,'ref',num2str(nplane),'.bin']);
  filename=char(path);
  fid=fopen(filename,'rb');
  ref=fread(fid,(nxr2-nxr1+1)*nt,'single');
  fclose(fid);
  ref=reshape(ref,nxr2-nxr1+1,nt);

  if 1==1


    icut1i=0;
    icut2i=length(t)+1;

    for i=1:length(inc(:,1))

      % detect unusual points and set them to zero
      % get unbiased mean by removing the zeros
      sig=inc(i,:);
      I=find(sig==0);
      sig(I)=[]; %#ok<FNDSB>
      clear I
      moy=mean(sig);
      sigma=std(sig,1);

      sig=inc(i,:);

      % detect data points beyond the avg +/- 4*std
      I=find(sig>=moy+4*sigma);
      inc(i,I)=zeros(size(I));
```

```
    clear I

    I=find(sig<=moy-4*sigma);
    inc(i,I)=zeros(size(I));
    clear I

    % locate bad data points
    I=find(inc(i,:)==0);
    tmpo1=inc(i,:);
    tmpo1(I)=[];
    tmpo=t;
    tmpo(I)=[];
    clear I

    % replace bad points using a linear interpolation
    inc(i,:)=interp1(tmpo,tmpo1,t,'linear');

    % t support starts earlier than tmpo... interpolation failed!
    if tmpo(1)>t(1)
      I=find(t<tmpo(1));
      icut1i=max([icut1i,I(end)]);
      clear I
    end

    % t support finishes after tmpo... interpolation failed!
    if t(end)>tmpo(end)
      I=find(t>tmpo(end));
      icut2i=min([icut2i,I(1)]);
      clear I
    end

    if 1==2
      figure(1)
      hold on
      plot(t,sig,'b')
      plot(t,inc(i,:),'r')
    end

    clear tmpo
    clear tmpo1

  end

end

if 1==1

  icut1r=0;
  icut2r=length(t)+1;

  for i=1:length(ref(:,1))

    % detect unusual points and set them to zero
    % get unbiased mean by removing the zeros
    sig=ref(i,:);
    I=find(sig==0);
    sig(I)=[]; %#ok<FNDSB>
    clear I
    moy=mean(sig);
    sigma=std(sig,1);

    sig=ref(i,:);

    % detect data points beyond the avg +/- 4*std
    I=find(sig>=moy+4*sigma);
    ref(i,I)=zeros(size(I));
    clear I

    I=find(sig<=moy-4*sigma);
    ref(i,I)=zeros(size(I));
    clear I

    % locate bad data points
    I=find(ref(i,:)==0);
    tmpo1=ref(i,:);
    tmpo1(I)=[];
    tmpo=t;
    tmpo(I)=[];
    clear I

    % replace bad points using a linear interpolation
    ref(i,:)=interp1(tmpo,tmpo1,t,'linear');

    % t support starts earlier than tmpo... interpolation failed!
    if tmpo(1)>t(1)
      I=find(t<tmpo(1));
      icut1r=max([icut1r,I(end)]);
      clear I
    end
```

```
      % t support finishes after tmpo... interpolation failed!
      if t(end)>tmpo(end)
        I=find(t>tmpo(end));
        icut2r=min([icut2r,I(1)]);
        clear I
      end

      if 1==2
        figure(1)
        hold on
        plot(t,sig,'b')
        plot(t,ref(i,:),'r')
      end

      clear tmpo
      clear tmpo1

    end

  end

  cut=[1:max([icut1i,icut1r]),min([icut2i,icut2r]):length(t)];

  t(cut)=[];
  inc(:,cut)=[];
  ref(:,cut)=[];

  %clear cut
  clear icut1i
  clear icut2i
  clear icut1r
  clear icut2r

  path=cellstr(['./matfiles/incident_shock_plane_',...
  num2str(nplane),'.mat']);
  filename=char(path);
  save(filename,'t','inc','xi');

  path=cellstr(['./matfiles/reflected_shock_plane_',...
  num2str(nplane),'.mat']);
  filename=char(path);
  save(filename,'t','ref','xr');


end

%figure(1)
%plot(xi,inc(:,:))

%figure(2)
%plot(t,inc(:,:))

figure(99)
plot(t,ref(1:5:end,:))
```

E. Proof of the phase- and conditional-average relationships inherited from hypothesis 6.1

E.1 Proof of corollary 6.1

Starting from the triple decomposition (6.4a), invoking the linear and scalar-conserving properties of the conditional-averaging operator and assuming that $\langle u_i'' \rangle_{\varepsilon_0,\Delta\sigma} = 0$, it is straightforward to write:

$$\langle u_i \rangle_{\varepsilon_0,\Delta\sigma} = \frac{1}{\mathcal{N}(\mathcal{A}_{\varepsilon_0,\Delta\sigma})} \int_{\mathcal{A}_{\varepsilon_0,\Delta\sigma}} \left(\bar{u}_i + \tilde{u}_i + u_i'' \right) \, \mathrm{d}t = \langle \tilde{u}_i \rangle_{\varepsilon_0,\Delta\sigma} + \bar{u}_i. \tag{E.1}$$

By introducing hypothesis 6.1 (see (6.5)) into the above equation, one finds:

$$\langle u_i \rangle_{\varepsilon_0,\Delta\sigma} - \bar{u}_i = \frac{1}{\mathcal{N}(\mathcal{A}_{\varepsilon_0,\Delta\sigma})} \int_{\mathcal{A}_{\varepsilon_0,\Delta\sigma}} \tilde{u}_i(t_s) \, \mathrm{d}t_s = \frac{1}{\mathcal{N}(\mathcal{A}_{\varepsilon_0,\Delta\sigma})} \int_{\mathcal{A}_{\varepsilon_0,\Delta\sigma}} \tilde{u}_i(\varepsilon(t_s)) \, \mathrm{d}t_s \tag{E.2}$$

Noting that the above integration is performed on the set $\mathcal{A}_{\varepsilon_0,\Delta\sigma}$, by definition of $\mathcal{A}_{\varepsilon_0,\Delta\sigma}$ one can write that:

$$\varepsilon(t_s) = \varepsilon_0 + \varphi(t_s)\Delta\sigma, \tag{E.3}$$

where φ is a bounded function in $[0, 1]$. If the phase-fluctuation velocity field $\tilde{u}_i(\varepsilon)$ is continuously differentiable on $[\varepsilon_0, \varepsilon_0 + \Delta\sigma]$, Taylor's theorem with the Lagrange form of the remainder may be written:

$$\begin{aligned} &\tilde{u}_i(\varepsilon(t_s)) = \tilde{u}_i(\varepsilon_0) + \Delta\sigma \, q_0(t_s), \\ &\qquad \text{with } |q_0(t_s)| \leq \varphi(t_s) \sup_{\varepsilon\in[\varepsilon_0,\varepsilon_0+\Delta\sigma]} \left| \frac{\partial \tilde{u}_i}{\partial \varepsilon} \right| \leq \sup_{\varepsilon\in[\varepsilon_0,\varepsilon_0+\Delta\sigma]} \left| \frac{\partial \tilde{u}_i}{\partial \varepsilon} \right|. \end{aligned} \tag{E.4}$$

The condition that $\tilde{u}_i(\varepsilon)$ be continuously differentiable is questionable due to the presence of shocks, but this is purely a mathematical concern here, since the numerical velocity fields are differentiated across shockwaves in the process of solving the Navier–Stokes equations. Thus, we argue that in practice the remainder is well defined and

bounded. Next, (E.4) is used in the integral (E.2):

$$\langle u_i \rangle_{\varepsilon_0,\Delta\sigma} - \bar{u}_i = \frac{1}{\mathcal{N}(\mathcal{A}_{\varepsilon_0,\Delta\sigma})} \left[\int_{\mathcal{A}_{\varepsilon_0,\Delta\sigma}} \tilde{u}_i(\varepsilon_0)\,\mathrm{d}t_s + \int_{\mathcal{A}_{\varepsilon_0,\Delta\sigma}} \Delta\sigma\, q_0(t_s)\,\mathrm{d}t_s \right] \tag{E.5}$$

The first integral is trivial since the integrand does not depend on t_s. Moreover, given the definition of $\mathcal{N}(\mathcal{A}_{\varepsilon_0,\Delta\sigma})$ in (6.2b), the first term is simply $\tilde{u}_i(\varepsilon_0)$. The second integral concerns a bounded function of $t_s \in \mathcal{A}_{\varepsilon_0,\Delta\sigma}$ and is therefore controlled by the supremum of the function times the integral range. Hence:

$$\langle u_i \rangle_{\varepsilon_0,\Delta\sigma} - \bar{u}_i = \tilde{u}_i(\varepsilon_0) + \Delta\sigma Q_0(\mathcal{A}_{\varepsilon_0,\Delta\sigma}), \text{ with } |Q_0(\mathcal{A}_{\varepsilon_0,\Delta\sigma})| \leq \sup_{\varepsilon\in[\varepsilon_0,\varepsilon_0+\Delta\sigma]} \left| \frac{\partial \tilde{u}_i}{\partial \varepsilon} \right|. \tag{E.6}$$

For simplicity, (E.6) can be expressed in the Landau notation by noting that the remainder is of the order of $\Delta\sigma$:

$$\langle u_i \rangle_{\varepsilon_0,\Delta\sigma} - \bar{u}_i = \tilde{u}_i(\varepsilon_0) + \mathcal{O}(\Delta\sigma). \tag{E.7}$$

In words, (E.7) simply expresses the idea that on $\mathcal{A}_{\varepsilon_0,\Delta\sigma}$, the phase-fluctuation field $\tilde{u}_i$ may be approximated by $\langle u_i \rangle_{\varepsilon_0,\Delta\sigma} - \bar{u}_i$ with an error of the order of $\Delta\sigma$, provided that hypothesis 6.1 is satisfied.

E.2 Proof of corollary 6.2

For the second corollary, we still consider that the phase-fluctuation velocity field is continuously differentiable on $[\varepsilon_0, \varepsilon_0 + \Delta\sigma]$ and therefore start from (E.4) to write that for $t_s \in \mathcal{A}_{\varepsilon_0,\Delta\sigma}$:

$$\begin{aligned} \tilde{u}_i(\varepsilon(t_s))\tilde{u}_j(\varepsilon(t_s)) &= \left[\tilde{u}_i(\varepsilon_0) + \Delta\sigma\, q_0(t_s)\right]\left[\tilde{u}_j(\varepsilon_0) + \Delta\sigma\, s_0(t_s)\right], \\ &\text{with } |q_0(t_s)| \leq \sup_{\varepsilon\in[\varepsilon_0,\varepsilon_0+\Delta\sigma]} \left| \frac{\partial \tilde{u}_i}{\partial \varepsilon} \right|, |s_0(t_s)| \leq \sup_{\varepsilon\in[\varepsilon_0,\varepsilon_0+\Delta\sigma]} \left| \frac{\partial \tilde{u}_j}{\partial \varepsilon} \right|. \end{aligned} \tag{E.8}$$

Equation (E.8) can then be integrated over $\mathcal{A}_{\varepsilon_0,\Delta\sigma}$:

$$\int_{\mathcal{A}_{\varepsilon_0,\Delta\sigma}} \tilde{u}_i(\varepsilon(t_s))\tilde{u}_j(\varepsilon(t_s))\,\mathrm{d}t_s = \int_{\mathcal{A}_{\varepsilon_0,\Delta\sigma}} \left[\tilde{u}_i(\varepsilon_0) + \Delta\sigma\, q_0(t_s)\right]\left[\tilde{u}_j(\varepsilon_0) + \Delta\sigma\, s_0(t_s)\right]\mathrm{d}t_s \tag{E.9}$$

Terms $\tilde{u}_i(\varepsilon_0),\ \tilde{u}_j(\varepsilon_0)$ being independent of t_s, and $q_0(t_s),\ s_0(t_s)$ being bounded functions on $\mathcal{A}_{\varepsilon_0,\Delta\sigma}$, (E.9) becomes:

$$\begin{aligned}\int_{\mathcal{A}_{\varepsilon_0,\Delta\sigma}} \tilde{u}_i(\varepsilon(t_s))\tilde{u}_j(\varepsilon(t_s))\,\mathrm{d}t_s = [\tilde{u}_i(\varepsilon_0)\tilde{u}_j(\varepsilon_0) + \Delta\sigma\,\{Q_0(\mathcal{A}_{\varepsilon_0,\Delta\sigma})\tilde{u}_j(\varepsilon_0) \\ +S_0(\mathcal{A}_{\varepsilon_0,\Delta\sigma})\tilde{u}_i(\varepsilon_0)\} + \Delta\sigma^2 M_0]\,\mathcal{N}(\mathcal{A}_{\varepsilon_0,\Delta\sigma}), \\ \text{with } |Q_0(\mathcal{A}_{\varepsilon_0,\Delta\sigma})| \leq \sup_{\varepsilon\in[\varepsilon_0,\varepsilon_0+\Delta\sigma]}\left|\frac{\partial\tilde{u}_i}{\partial\varepsilon}\right|,\ |S_0(\mathcal{A}_{\varepsilon_0,\Delta\sigma})| \leq \sup_{\varepsilon\in[\varepsilon_0,\varepsilon_0+\Delta\sigma]}\left|\frac{\partial\tilde{u}_j}{\partial\varepsilon}\right| \\ \text{and } |M_0| \leq \sup_{\varepsilon\in[\varepsilon_0,\varepsilon_0+\Delta\sigma]}\left|\frac{\partial\tilde{u}_i}{\partial\varepsilon}\right| \sup_{\varepsilon\in[\varepsilon_0,\varepsilon_0+\Delta\sigma]}\left|\frac{\partial\tilde{u}_j}{\partial\varepsilon}\right|. \quad \text{(E.10)}\end{aligned}$$

Using Landau's notation, the second corollary can be expressed:

$$\int_{\mathcal{A}_{\varepsilon_0,\Delta\sigma}} \tilde{u}_i(\varepsilon(t_s))\tilde{u}_j(\varepsilon(t_s))\,\mathrm{d}t_s = [\tilde{u}_i(\varepsilon_0)\tilde{u}_j(\varepsilon_0) + \mathcal{O}(\Delta\sigma)]\,\mathcal{N}(\mathcal{A}_{\varepsilon_0,\Delta\sigma}). \quad \text{(E.11)}$$

E.3 Estimation of the phase-fluctuation stress tensor

Starting with the stress tensor computed from the conditionally-averaged fields,

$$I = \frac{1}{T}\sum_{k=0}^{N-1} [\langle u_i\rangle_{\varepsilon_{\min}+k\Delta\sigma,\Delta\sigma} - \bar{u}_i]\,[\langle u_j\rangle_{\varepsilon_{\min}+k\Delta\sigma,\Delta\sigma} - \bar{u}_j]\,\mathcal{N}(\mathcal{A}_{\varepsilon_{\min}+k\Delta\sigma,\Delta\sigma}), \quad \text{(E.12)}$$

where $N = (\varepsilon_{\max} - \varepsilon_{\min})/\Delta\sigma$ with $\varepsilon_{\max} = \max(\varepsilon(t))$, $\varepsilon_{\min} = \min(\varepsilon(t))$, $t \in [0,T]$; it is possible to use corollary 6.1 to write:

$$\begin{aligned}I = \frac{1}{T}\sum_{k=0}^{N-1} [\tilde{u}_i(\varepsilon_{\min}+k\Delta\sigma) + \Delta\sigma Q_0(\mathcal{A}_{\varepsilon_{\min}+k\Delta\sigma,\Delta\sigma})]\,[\tilde{u}_j(\varepsilon_{\min}+k\Delta\sigma) \\ +\Delta\sigma S_0(\mathcal{A}_{\varepsilon_{\min}+k\Delta\sigma,\Delta\sigma})]\,\mathcal{N}(\mathcal{A}_{\varepsilon_{\min}+k\Delta\sigma,\Delta\sigma}), \quad \text{(E.13)}\end{aligned}$$

and re-arrange to:

$$\begin{aligned}I = \frac{1}{T}\sum_{k=0}^{N-1} [\tilde{u}_i(\varepsilon_{\min}+k\Delta\sigma)\tilde{u}_j(\varepsilon_{\min}+k\Delta\sigma) + \Delta\sigma\,\{Q_0(\mathcal{A}_{\varepsilon_{\min}+k\Delta\sigma,\Delta\sigma})\tilde{u}_j(\varepsilon_{\min}+k\Delta\sigma) \\ +S_0(\mathcal{A}_{\varepsilon_{\min}+k\Delta\sigma,\Delta\sigma})\tilde{u}_i(\varepsilon_{\min}+k\Delta\sigma)\} \\ +\Delta\sigma^2 Q_0(\mathcal{A}_{\varepsilon_{\min}+k\Delta\sigma,\Delta\sigma})S_0(\mathcal{A}_{\varepsilon_{\min}+k\Delta\sigma,\Delta\sigma})]\,\mathcal{N}(\mathcal{A}_{\varepsilon_{\min}+k\Delta\sigma,\Delta\sigma}), \quad \text{(E.14)}\end{aligned}$$

The form (E.10) of corollary 6.2 is introduced in (E.14) to find:

$$I = \frac{1}{T}\sum_{k=0}^{N-1}\int_{\mathcal{A}_{\varepsilon_{\min}+k\Delta\sigma,\Delta\sigma}} \tilde{u}_i(\varepsilon(t_s))\tilde{u}_j(\varepsilon(t_s))\,\mathrm{d}t_s + J, \quad \text{(E.15)}$$

where:

$$J = \frac{1}{T}\sum_{k=0}^{N-1} \Delta\sigma^2 \left\{ Q_0(\mathcal{A}_{\varepsilon_{\min}+k\Delta\sigma,\Delta\sigma}) S_0(\mathcal{A}_{\varepsilon_{\min}+k\Delta\sigma,\Delta\sigma}) \right. \\ \left. - M_0(\mathcal{A}_{\varepsilon_{\min}+k\Delta\sigma,\Delta\sigma}) \right\} \mathcal{N}(\mathcal{A}_{\varepsilon_{\min}+k\Delta\sigma,\Delta\sigma}). \quad \text{(E.16)}$$

Since the functions $Q_0,\ S_0,\ M_0$ are all bounded, the sum J can be crudely bounded by:

$$J \leq \frac{\Delta\sigma^2}{T} M \sum_{k=0}^{N-1} \mathcal{N}(\mathcal{A}_{\varepsilon_{\min}+k\Delta\sigma,\Delta\sigma}), \quad \text{(E.17)}$$

with M a constant taken to be:

$$M = \max_{k\in\{0,\dots,N-1\}} \left[\sup_{\mathcal{A}_{\varepsilon_{\min}+k\Delta\sigma,\Delta\sigma}} |Q_0(\mathcal{A}_{\varepsilon_{\min}+k\Delta\sigma,\Delta\sigma}) S_0(\mathcal{A}_{\varepsilon_{\min}+k\Delta\sigma,\Delta\sigma})| \right. \\ \left. + \sup_{\mathcal{A}_{\varepsilon_{\min}+k\Delta\sigma,\Delta\sigma}} |M_0(\mathcal{A}_{\varepsilon_{\min}+k\Delta\sigma,\Delta\sigma})| \right]. \quad \text{(E.18)}$$

By definition of $\mathcal{N}$, the sum on all $\mathcal{N}(\mathcal{A}_{\varepsilon_{\min}+k\Delta\sigma,\Delta\sigma})$ is simply equal to T so that:

$$I = \frac{1}{T}\sum_{k=0}^{N-1} \int_{\mathcal{A}_{\varepsilon_{\min}+k\Delta\sigma,\Delta\sigma}} \tilde{u}_i(\varepsilon(t_s))\tilde{u}_j(\varepsilon(t_s))\,\mathrm{d}t_s + K\Delta\sigma^2, \text{ with } K \leq M. \quad \text{(E.19)}$$

Invoking the additivity properties of the integral, the sum over all the subsets $\mathcal{A}_{\varepsilon_{\min}+k\Delta\sigma,\Delta\sigma}$ of $[0,T]$ can be changed into the integral over their union:

$$I = \frac{1}{T}\int_{\bigcup_{k=0}^{N-1} \mathcal{A}_{\varepsilon_{\min}+k\Delta\sigma,\Delta\sigma}} \tilde{u}_i(\varepsilon(t_s))\tilde{u}_j(\varepsilon(t_s))\,\mathrm{d}t_s + K\Delta\sigma^2. \quad \text{(E.20)}$$

Given the definition of N, the union of the subsets $\mathcal{A}_{\varepsilon_{\min}+k\Delta\sigma,\Delta\sigma}$ spans the full time interval $[0,T]$ only once, so that (E.20) becomes, using Landau's notation:

$$I = \underbrace{\frac{1}{T}\int_T \tilde{u}_i(\varepsilon(t_s))\tilde{u}_j(\varepsilon(t_s))\,\mathrm{d}t_s}_{\overline{\tilde{u}_i\tilde{u}_j}} + \mathcal{O}(\Delta\sigma^2). \quad \text{(E.21)}$$

Therefore, to second order in $\Delta\sigma$, we have:

$$\overline{\tilde{u}_i\tilde{u}_j} \approx \frac{1}{T}\sum_{k=0}^{N-1} \left[\langle u_i\rangle_{\varepsilon_{\min}+k\Delta\sigma,\Delta\sigma} - \bar{u}_i\right] \left[\langle u_j\rangle_{\varepsilon_{\min}+k\Delta\sigma,\Delta\sigma} - \bar{u}_j\right] \mathcal{N}(\mathcal{A}_{\varepsilon_{\min}+k\Delta\sigma,\Delta\sigma}). \quad \text{(E.22)}$$

F. Derivation of the momentum integral equation

Let us start from the continuity equation and the streamwise component of the momentum equation:

$$\frac{\partial \rho}{\partial t} + \frac{\partial \rho u}{\partial x} + \frac{\partial \rho v}{\partial y} + \frac{\partial \rho w}{\partial z} = 0, \tag{F.1a}$$

$$\rho\frac{\partial u}{\partial t} + \rho u\frac{\partial u}{\partial x} + \rho v\frac{\partial u}{\partial y} + \rho w\frac{\partial u}{\partial z} = -\frac{\partial p}{\partial x} + \frac{1}{\mathrm{Re}}\left[\frac{\partial \tau_{xx}}{\partial x} + \frac{\partial \tau_{xy}}{\partial y} + \frac{\partial \tau_{xz}}{\partial z}\right], \tag{F.1b}$$

$$\tau_{ij} = \mu\left(\frac{\partial u_j}{\partial x_i} + \frac{\partial u_i}{\partial x_j} - \frac{2}{3}\delta_{ij}\frac{\partial u_k}{\partial x_k}\right). \tag{F.1c}$$

Equation (F.1b) can be integrated in the wall normal direction up to h (see figure 7.1 for the notations):

$$\int_0^h \left(\rho\frac{\partial u}{\partial t} + \rho u\frac{\partial u}{\partial x} + \rho w\frac{\partial u}{\partial z}\right)\mathrm{d}y + \underbrace{\int_0^h \rho v\frac{\partial u}{\partial y}\,\mathrm{d}y}_{A} = \int_0^h \left(-\frac{\partial p}{\partial x} + \frac{1}{\mathrm{Re}}\left[\frac{\partial \tau_{xx}}{\partial x} + \frac{\partial \tau_{xy}}{\partial y} + \frac{\partial \tau_{xz}}{\partial z}\right]\right)\mathrm{d}y. \tag{F.2}$$

Term A can be integrated by parts and together with (F.1a) gives:

$$A = [\rho u v]_0^h - \int_0^h u\frac{\partial \rho v}{\partial y}\,\mathrm{d}y = -u_h\int_0^h \left(\frac{\partial \rho}{\partial t} + \frac{\partial \rho u}{\partial x} + \frac{\partial \rho w}{\partial z}\right)\mathrm{d}y + \int_0^h u\left(\frac{\partial \rho}{\partial t} + \frac{\partial \rho u}{\partial x} + \frac{\partial \rho w}{\partial z}\right)\mathrm{d}y, \tag{F.3}$$

where the no-slip boundary condition at $y = 0$ was used to eliminate $\rho uv|_{y=0}$. Equation (F.2) can be re-written, using (F.3):

$$\begin{aligned}
&\underbrace{\int_0^h \rho\frac{\partial u}{\partial t}\,\mathrm{d}y - u_h\int_0^h \frac{\partial \rho}{\partial t}\,\mathrm{d}y + \int_0^h u\frac{\partial \rho}{\partial t}\,\mathrm{d}y}_{a} + \underbrace{\int_0^h \rho u\frac{\partial u}{\partial x}\,\mathrm{d}y - u_h\int_0^h \frac{\partial \rho u}{\partial x}\,\mathrm{d}y + \int_0^h u\frac{\partial \rho u}{\partial x}\,\mathrm{d}y}_{b} \\
&\qquad + \underbrace{\int_0^h \rho w\frac{\partial u}{\partial z}\,\mathrm{d}y - u_h\int_0^h \frac{\partial \rho w}{\partial z}\,\mathrm{d}y + \int_0^h u\frac{\partial \rho w}{\partial z}\,\mathrm{d}y}_{c} \\
&= \underbrace{\int_0^h -\frac{\partial p}{\partial x}\,\mathrm{d}y}_{d} + \underbrace{\frac{1}{\mathrm{Re}}\int_0^h \frac{\partial \tau_{xy}}{\partial y}\,\mathrm{d}y}_{e} + \underbrace{\frac{1}{\mathrm{Re}}\int_0^h \frac{\partial \tau_{xx}}{\partial x}\,\mathrm{d}y}_{f} + \underbrace{\frac{1}{\mathrm{Re}}\int_0^h \frac{\partial \tau_{xz}}{\partial z}\,\mathrm{d}y}_{g}. \quad \text{(F.4)}
\end{aligned}$$

To re-arrange terms a to g, we have to commute the integration and derivation operators. To do so, Leibnitz's rule is recalled:

$$\frac{\partial}{\partial \alpha}\left[\int_0^h f\,\mathrm{d}y\right] = \int_0^h \frac{\partial f}{\partial \alpha}\,\mathrm{d}y + f(y=h)\frac{\partial h}{\partial \alpha} - f(y=0)\underbrace{\frac{\partial 0}{\partial \alpha}}_{=0}. \quad \text{(F.5)}$$

Term a can be re-arranged using Leibnitz's rule:

$$\begin{aligned}
a = \int_0^h \frac{\partial \rho u}{\partial t}\,\mathrm{d}y - u_h\int_0^h \frac{\partial \rho}{\partial y}\,\mathrm{d}y &= \frac{\partial}{\partial t}\left[\int_0^h \rho u\,\mathrm{d}y\right] - \rho_h u_h\frac{\partial h}{\partial t} \\
&\quad - u_h\left(\frac{\partial}{\partial t}\left[\int_0^h \rho\,\mathrm{d}y\right] - \rho_h\frac{\partial h}{\partial t}\right) \\
&= \frac{\partial}{\partial t}\left[\int_0^h \rho u\,\mathrm{d}y\right] - u_h\frac{\partial}{\partial t}\left[\int_0^h \rho\,\mathrm{d}y\right].
\end{aligned}$$

Equation (7.2a) can be re-arranged:

$$\rho_h u_h\delta_1 = \rho_h u_h\int_0^h \left(1 - \frac{\rho u}{\rho_h u_h}\right)\mathrm{d}y = \int_0^h \rho_h u_h\left(1 - \frac{\rho u}{\rho_h u_h}\right)\mathrm{d}y = \rho_h u_h h - \int_0^h \rho u\,\mathrm{d}y,$$

where the independence of ρ_h and u_h on y ($u_h = u_h(x,z,t)$) was used. The same manipulation can be performed with (7.2d) and term a becomes:

$$a = \rho_h\left(h - \delta_1\right)\frac{\partial u_h}{\partial t} + u_h\frac{\partial}{\partial t}\left[\rho_h(\delta_\rho - \delta_1)\right]. \quad \text{(F.6)}$$

Similarly, term b is re-arranged using Leibnitz's rule:

$$\begin{aligned} b = \int_0^h \frac{\partial \rho u u}{\partial x}\,\mathrm{d}y - u_h \int_0^h \frac{\partial \rho u}{\partial x}\,\mathrm{d}y &= \frac{\partial}{\partial x}\left[\int_0^h \rho u u\,\mathrm{d}y\right] - \rho_h u_h u_h \frac{\partial h}{\partial x} \\ &\quad - u_h\left(\frac{\partial}{\partial x}\left[\int_0^h \rho u\,\mathrm{d}y\right] - \rho_h u_h \frac{\partial h}{\partial x}\right) \\ &= \frac{\partial}{\partial x}\left[\int_0^h \rho u u\,\mathrm{d}y\right] - u_h \frac{\partial}{\partial x}\left[\int_0^h \rho u\,\mathrm{d}y\right]. \end{aligned}$$

From (7.2b), one finds:

$$\begin{aligned} \rho_h u_h^2 \delta_2 = \rho_h u_h^2 \int_0^h \frac{\rho u}{\rho_h u_h}\left(1 - \frac{u}{u_h}\right)\mathrm{d}y = u_h \int_0^h \rho u\,\mathrm{d}y - \int_0^h \rho u u\,\mathrm{d}y \\ = \rho_h u_h^2 (h - \delta_1) - \int_0^h \rho u u\,\mathrm{d}y, \end{aligned}$$

so that b becomes:

$$b = \rho_h u_h (h - \delta_1)\frac{\partial u_h}{\partial x} - \frac{\partial}{\partial x}\left[\rho_h u_h^2 \delta_2\right]. \tag{F.7}$$

Invoking Leibnitz's rule again, c is rearranged:

$$\begin{aligned} c = \int_0^h \frac{\partial \rho u w}{\partial z}\,\mathrm{d}y - u_h \int_0^h \frac{\partial \rho w}{\partial z}\,\mathrm{d}y &= \frac{\partial}{\partial z}\left[\int_0^h \rho u w\,\mathrm{d}y\right] - \rho_h u_h w_h \frac{\partial h}{\partial z} \\ &\quad - u_h\left(\frac{\partial}{\partial z}\left[\int_0^h \rho w\,\mathrm{d}y\right] - \rho_h w_h \frac{\partial h}{\partial z}\right) \\ &= \frac{\partial}{\partial z}\left[\int_0^h \rho u w\,\mathrm{d}y\right] - u_h \frac{\partial}{\partial z}\left[\int_0^h \rho w\,\mathrm{d}y\right]. \end{aligned} \tag{F.8}$$

Note that h is, by construction, allowed to depend on z but is independent of x, so that term d becomes:

$$d = -\left(\frac{\partial}{\partial x}\left[\int_0^h p\,\mathrm{d}y\right] - p_h \frac{\partial h}{\partial x}\right) = -\frac{\partial}{\partial x}\left[\int_0^h p\,\mathrm{d}y\right].$$

From (7.2c), noting that p_h does not depend on y, one finds:

$$p_h \delta_p = p_h \int_0^h \left(1 - \frac{p}{p_h}\right)\mathrm{d}y = p_h h - \int_0^h p\,\mathrm{d}y,$$

so that:

$$d = \frac{\partial}{\partial x}\left[p_h (\delta_p - h)\right]. \tag{F.9}$$

Term e can be easily integrated to give (using the definition (7.3)):

$$e = \frac{1}{\mathrm{Re}}\left\{\left[\mu\left(\frac{\partial v}{\partial x}+\frac{\partial u}{\partial y}\right)\right]_{y=h} - \left[\mu\frac{\partial u}{\partial y}\right]_{y=0}\right\} = \frac{\mu_h}{\mathrm{Re}}\left(\left.\frac{\partial v}{\partial x}\right|_{y=h} + \left.\frac{\partial u}{\partial y}\right|_{y=h}\right) - \frac{1}{2}C_f\rho_h u_h^2. \quad \text{(F.10)}$$

Terms f and g are rearranged, using Leibnitz's rule and the independence of h on x:

$$f = \frac{1}{\mathrm{Re}}\left(\frac{\partial}{\partial x}\left[\int_0^h \tau_{xx}\,\mathrm{d}y\right] - \tau_{xx}|_{y=h}\frac{\partial h}{\partial x}\right) = \frac{1}{\mathrm{Re}}\frac{\partial}{\partial x}\left[\int_0^h \tau_{xx}\,\mathrm{d}y\right], \quad \text{(F.11)}$$

$$g = \frac{1}{\mathrm{Re}}\left(\frac{\partial}{\partial z}\left[\int_0^h \tau_{xz}\,\mathrm{d}y\right] - \tau_{xz}|_{y=h}\frac{\partial h}{\partial z}\right). \quad \text{(F.12)}$$

Using (F.6) to (F.12) in (F.4) leads to (7.1):

$$\rho_h\left(h-\delta_1\right)\left[\frac{\partial u_h}{\partial t}+u_h\frac{\partial u_h}{\partial x}\right] + u_h\frac{\partial}{\partial t}\left[\rho_h(\delta_\rho-\delta_1)\right] - \frac{\partial}{\partial x}\left[\rho_h u_h^2\delta_2\right] + \frac{\partial}{\partial z}\left[\int_0^h \rho u w\,\mathrm{d}y\right] - u_h\frac{\partial}{\partial z}\left[\int_0^h \rho w\,\mathrm{d}y\right] = \frac{\partial}{\partial x}\left[p_h\left(\delta_p-h\right)\right] + \frac{\mu_h}{\mathrm{Re}}\left[\left.\frac{\partial v}{\partial x}\right|_{y=h} + \left.\frac{\partial u}{\partial y}\right|_{y=h}\right] - \frac{1}{2}C_f\rho_h u_h^2 + \frac{1}{\mathrm{Re}}\frac{\partial}{\partial x}\left[\int_0^h \tau_{xx}\,\mathrm{d}y\right] + \frac{1}{\mathrm{Re}}\left(\frac{\partial}{\partial z}\left[\int_0^h \tau_{xz}\,\mathrm{d}y\right] - \tau_{xz}|_{y=h}\frac{\partial h}{\partial z}\right). \quad \text{(F.13)}$$

G. Series expansions of the oblique-shock relations

G.1 Expansion of $\sin^2(\iota+\theta)$

To derive the following series expansions in terms of η/h_0, the notations presented in figure 7.6 will be used. From this figure, one can write the geometrical relations:

$$\tan\alpha = \frac{h_0}{l_0}, \tag{G.1a}$$

$$\sin\iota = \frac{h_0+\eta}{\sqrt{(h_0+\eta)^2+(l_0-\varepsilon+s)^2}}, \tag{G.1b}$$

$$\cos\iota = \frac{l_0-\varepsilon+s}{\sqrt{(h_0+\eta)^2+(l_0-\varepsilon+s)^2}}. \tag{G.1c}$$

From (7.14) and (7.15) it is straightforward to show that:

$$s-\varepsilon = \eta\underbrace{\left[\frac{1-k}{k\tan\beta}\right]}_{K_0}. \tag{G.2}$$

From trigonometric identities, one can write:

$$\sin^2(\iota+\theta) = \sin^2\iota\cos^2\theta+\cos^2\iota\sin^2\theta+\sin\iota\cos\iota\sin(2\theta). \tag{G.3a}$$

Using (G.1 b,c) and (G.2),

$$\begin{aligned}\sin^2(\iota+\theta) = {} & \frac{1}{h_0^2+\eta^2+2h_0\eta+l_0^2+K_0^2\eta^2+2l_0K_0\eta}\left\{\left(h_0^2+\eta^2+2h_0\eta\right)\cos^2\theta\right.\\ & +\left(l_0^2+K_0^2\eta^2+2l_0K_0\eta\right)\sin^2\theta\\ & \left.+\left(h_0l_0+h_0K_0\eta+l_0\eta+K_0\eta^2\right)\sin(2\theta)\right\}.\end{aligned} \tag{G.3b}$$

Upon multiplying both the numerator and denominator of the RHS of (G.3b) by $1/h_0^2$ and defining $q \equiv \eta/h_0$, (G.3b) becomes:

$$\begin{aligned}\sin^2(\iota+\theta) &= \frac{1}{1+q^2+2q+(l_0/h_0)^2+K_0^2q^2+2(l_0/h_0)K_0q}\left\{\left(1+q^2+2q\right)\cos^2\theta\right.\\ &\quad+\left((l_0/h_0)^2+K_0^2q^2+2(l_0/h_0)K_0q\right)\sin^2\theta\\ &\quad\left.+\left(l_0/h_0+K_0q+(l_0/h_0)q+K_0q^2\right)\sin(2\theta)\right\}. \qquad \text{(G.3c)}\end{aligned}$$

Substituting (G.1a) into the above equation gives:

$$\begin{aligned}\sin^2(\iota+\theta) &= \frac{1}{1+q^2+2q+1/\tan^2\alpha+K_0^2q^2+2K_0q/\tan\alpha}\left\{\left(1+q^2+2q\right)\cos^2\theta\right.\\ &\quad+\left(1/\tan^2\alpha+K_0^2q^2+2K_0q/\tan\alpha\right)\sin^2\theta\\ &\quad\left.+\left(1/\tan\alpha+K_0q+q/\tan\alpha+K_0q^2\right)\sin(2\theta)\right\}. \qquad \text{(G.3d)}\end{aligned}$$

Factorising (G.3d) by $1/(1+1/\tan^2\alpha)$ and noting that $\sin^2\alpha = 1/(1+1/\tan^2\alpha)$, one finds:

$$\begin{aligned}\sin^2(\iota+\theta) &= \frac{\sin^2\alpha}{1+2C_1q+C_2q^2}\left\{\left(1+2q+q^2\right)\cos^2\theta\right.\\ &\quad+\left(1+2K_1q+K_1^2q^2\right)\sin^2\theta/\tan^2\alpha\\ &\quad\left.+\left(1+q\left(1+K_1\right)+K_1q^2\right)\sin(2\theta)/\tan\alpha\right\}, \qquad \text{(G.3e)}\end{aligned}$$

where $C_1 \equiv \left(K_1+\tan^2\alpha\right)/\left(1+\tan^2\alpha\right)$, $C_2 \equiv \left(K_1^2+\tan^2\alpha\right)/\left(1+\tan^2\alpha\right)$ and $K_1 \equiv K_0\tan\alpha$. If the study is restricted to shock oscillations such that $q \ll 1$, one can expand the fractional term, i.e. :

$$\frac{1}{1+2C_1q+C_2q^2} = 1-2C_1q+\left(4C_1^2-C_2\right)q^2+\mathcal{O}(q^3). \qquad \text{(G.4)}$$

Using (G.4) in (G.3e) and retaining only terms up to the first order in q, one finds:

$$\begin{aligned}\sin^2(\iota+\theta) &= \sin^2\alpha\left\{\left[1+2q\left(1-C_1\right)\right]\cos^2\theta\right.\\ &\quad+\left[1+2q\left(K_1-C_1\right)\right]\sin^2\theta/\tan^2\alpha\\ &\quad\left.+\left[1+q\left(1+K_1-2C_1\right)\right]\sin(2\theta)/\tan\alpha\right\}+\mathcal{O}(q^2), \qquad \text{(G.5a)}\end{aligned}$$

which upon regrouping terms of similar orders gives:

$$\begin{aligned}\sin^2(\iota+\theta) &= \overbrace{\sin^2\alpha\cos^2\theta+\cos^2\alpha\sin^2\theta+\sin(2\theta)\sin\alpha\cos\alpha}^{\sin^2(\alpha+\theta)}\\ &\quad+\left\{2\left(1-C_1\right)\cos^2\theta\sin^2\alpha+2\left(K_1-C_1\right)\sin^2\theta\cos^2\alpha\right.\\ &\quad\left.+\left(1+K_1-2C_1\right)\sin(2\theta)\sin\alpha\cos\alpha\right\}q+\mathcal{O}(q^2). \qquad \text{(G.5b)}\end{aligned}$$

It is relatively straightforward to see that $K_1 - C_1 = \sin^2\alpha\,(K_1 - 1)$ and $1 - C_1 = (1 - K_1)\cos^2\alpha$, which if combined gives $1 + K_1 - 2C_1 = (1 - K_1)\cos(2\alpha)$ using the relation $\cos(2\alpha) = \cos^2\alpha - \sin^2\alpha$. Based on those remarks and after few manipulations of trigonometric identities, (G.5b) simplifies to:

$$\sin^2(\iota+\theta) \;=\; \sin^2(\alpha+\theta) + \left\{\frac{1-K_1}{2}\sin(2\alpha)\sin(2\alpha+2\theta)\right\} q + \mathcal{O}(q^2). \quad \text{(G.5c)}$$

Using the definitions of K_1 and K_0, (G.5c) becomes:

$$\begin{aligned}\sin^2(\iota+\theta) \;=\;& \sin^2(\alpha+\theta) \\ &+\frac{1}{2}\left[1+\frac{\tan\alpha}{\tan\beta}\left(1-\frac{1}{k}\right)\right]\sin(2\alpha)\sin(2\alpha+2\theta)\; q + \mathcal{O}(q^2). \quad \text{(G.5d)}\end{aligned}$$

If we now assume that k can be modelled according to (7.31), (G.5d) becomes:

$$\begin{aligned}&\sin^2(\iota+\theta) = \sin^2(\alpha+\theta) + \frac{1}{2}\varkappa(\alpha,\beta,\theta)\, q + \mathcal{O}(q^2) \text{ with,} \\ &\qquad\qquad \varkappa(\alpha,\beta,\theta) = \frac{\tan\alpha + \tan\beta}{\tan\beta\,(1 - 1/\tan\alpha) - 1}\sin(2\alpha)\sin\left[2\,(\alpha+\theta)\right]. \quad \text{(G.6)}\end{aligned}$$

G.2 Expansion of p_3/p_1

The pressure in region 3 varies according to:

$$\frac{p_3}{p_1} = \frac{p_2^+}{p_1}\left\{1 + \frac{2\gamma}{1+\gamma}\left[\mathrm{M}_2^2\sin^2(\iota+\theta) - 1\right]\right\}. \quad \text{(G.7)}$$

Using (G.6), (G.7) can be expanded as:

$$\frac{p_3}{p_1} = \frac{p_2^+}{p_1}\left\{1 + \frac{2\gamma}{1+\gamma}\left[\mathrm{M}_2^2\left(\sin^2(\alpha+\theta) + \frac{1}{2}\varkappa(\alpha,\beta,\theta)\frac{\eta}{h_0}\right) - 1\right]\right\} + \mathcal{O}\left(\frac{\eta^2}{h_0^2}\right), \quad \text{(G.8a)}$$

where the mean pressure in region 3 (i.e. $\bar{p}_3$) can be identified:

$$\frac{p_3}{p_1} = \frac{\bar{p}_3}{p_1} + \frac{p_2^+}{p_1}\frac{\gamma}{1+\gamma}\mathrm{M}_2^2\varkappa(\alpha,\beta,\theta)\frac{\eta}{h_0} + \mathcal{O}\left(\frac{\eta^2}{h_0^2}\right). \quad \text{(G.8b)}$$

Hence:

$$\frac{p_3}{p_1} = \frac{\bar{p}_3}{p_1} + A\,\frac{\eta}{h_0} + \mathcal{O}\left(\frac{\eta^2}{h_0^2}\right), \text{ with } A = \frac{p_2^+}{p_1}\frac{\gamma\varkappa\mathrm{M}_2^2}{1+\gamma}. \quad \text{(G.9)}$$

G.3 Expansion of ρ_3/ρ_1

The density in region 3 varies according to:

$$\frac{\rho_3}{\rho_1} = \frac{\rho_2^+}{\rho_1}\left\{\frac{(\gamma+1)\,\mathrm{M}_2^2\sin^2(\iota+\theta)}{2+(\gamma-1)\,\mathrm{M}_2^2\sin^2(\iota+\theta)}\right\}. \tag{G.10}$$

Substituting (G.6) into (G.10) gives:

$$\frac{\rho_3}{\rho_1} = \frac{\rho_2^+}{\rho_1}\left[\frac{a_0}{b_0}+\frac{\gamma+1}{2b_0}\mathrm{M}_2^2\varkappa\, q+\mathcal{O}(q^2)\right]\left[1+\frac{\gamma-1}{2b_0}\mathrm{M}_2^2\varkappa\, q+\mathcal{O}(q^2)\right]^{-1}, \tag{G.11a}$$

where $a_0 \equiv (\gamma+1)\,\mathrm{M}_2^2\sin^2(\alpha+\theta)$, and $b_0 \equiv 2+(\gamma-1)\,\mathrm{M}_2^2\sin^2(\alpha+\theta)$. The term with power -1 can be expanded, leading to:

$$\begin{aligned}\frac{\rho_3}{\rho_1} &= \frac{\rho_2^+}{\rho_1}\left[\frac{a_0}{b_0}+\frac{\gamma+1}{2b_0}\mathrm{M}_2^2\varkappa\, q+\mathcal{O}(q^2)\right]\left[1-\frac{\gamma-1}{2b_0}\mathrm{M}_2^2\varkappa\, q+\mathcal{O}(q^2)\right], &\text{(G.11b)}\\ &= \frac{\rho_2^+}{\rho_1}\frac{a_0}{b_0}\left[1-\frac{\gamma-1}{2b_0}\mathrm{M}_2^2\varkappa\, q+\frac{\gamma+1}{2a_0}\mathrm{M}_2^2\varkappa\, q\right]+\mathcal{O}(q^2). &\text{(G.11c)}\end{aligned}$$

Noting that $a_0/b_0 = \bar{\rho}_3/\rho_2^+$, (G.11c) can be written:

$$\begin{aligned}\frac{\rho_3}{\rho_1} &= \frac{\bar{\rho}_3}{\rho_1}+B\,\frac{\eta}{h_0}+\mathcal{O}\left(\frac{\eta^2}{h_0^2}\right),\\ &\text{with } B=\varkappa\left[\frac{1}{2\sin^2(\alpha+\theta)}-\frac{(\gamma-1)\,\mathrm{M}_2^2}{4+2\,(\gamma-1)\,\mathrm{M}_2^2\sin^2(\alpha+\theta)}\right]\frac{\bar{\rho}_3}{\rho_1}.\end{aligned} \tag{G.12}$$

G.4 Expansion of $\mathrm{M}_3/\mathrm{M}_1$

The Mach number in region 3 is computed according to:

$$\frac{\mathrm{M}_3}{\mathrm{M}_1} = \frac{1}{\mathrm{M}_1\sin\iota}\sqrt{\frac{1+(1/2)\,(\gamma-1)\,\mathrm{M}_2^2\sin^2(\iota+\theta)}{\gamma\mathrm{M}_2^2\sin^2(\iota+\theta)-(\gamma-1)/2}}. \tag{G.13}$$

Substituting (G.6) and denoting $\varkappa(\alpha,\beta,0)$ by $\varkappa_0$, one finds:

$$\begin{aligned}\frac{\mathrm{M}_3}{\mathrm{M}_1} &= \frac{1}{\mathrm{M}_1}\left[\sin^2\alpha+\frac{1}{2}\varkappa_0\, q+\mathcal{O}(q^2)\right]^{-\frac{1}{2}}\left[1+\frac{\gamma-1}{2}\mathrm{M}_2^2\left(\sin^2(\alpha+\theta)+\frac{1}{2}\varkappa\, q+\mathcal{O}(q^2)\right)\right]^{\frac{1}{2}}\\ &\quad\times\left[\frac{1-\gamma}{2}+\gamma\mathrm{M}_2^2\left(\sin^2(\alpha+\theta)+\frac{1}{2}\varkappa\, q+\mathcal{O}(q^2)\right)\right]^{-\frac{1}{2}}.\end{aligned} \tag{G.14a}$$

Each terms in powers of $\pm 1/2$ can be expanded up to the first order:

$$\frac{\mathrm{M}_3}{\mathrm{M}_1} = \frac{1}{\mathrm{M}_1}\left[\frac{1}{\sin\alpha} - \frac{\varkappa_0}{4\sin^3\alpha}\,q + \mathcal{O}(q^2)\right]\left[\sqrt{\frac{b_0}{2}} + \frac{(\gamma-1)\,\mathrm{M}_2^2\varkappa}{8\sqrt{b_0/2}}\,q + \mathcal{O}(q^2)\right] \times \left[\frac{1}{\sqrt{c_0}} - \frac{\gamma\mathrm{M}_2^2\varkappa}{4\,c_0^{3/2}}\,q + \mathcal{O}(q^2)\right], \tag{G.14b}$$

where b_0 is the same as in (G.11a) and $c_0 = (1-\gamma)/2 + \gamma\mathrm{M}_2^2\sin^2(\alpha+\theta)$. Regrouping terms of similar orders in q, one finds:

$$\frac{\mathrm{M}_3}{\mathrm{M}_1} = \frac{\overline{\mathrm{M}}_3}{\mathrm{M}_1}\left\{1 + \frac{1}{4}\left[\frac{(\gamma-1)\,\mathrm{M}_2^2\varkappa}{b_0} - \frac{\gamma\mathrm{M}_2^2\varkappa}{c_0} - \frac{\varkappa_0}{\sin^2\alpha}\right] q\right\} + \mathcal{O}(q^2), \tag{G.14c}$$

where $\overline{\mathrm{M}}_3 = \sqrt{b_0/(2c_0\sin^2\alpha)}$. Hence:

$$\frac{\mathrm{M}_3}{\mathrm{M}_1} = \frac{\overline{\mathrm{M}}_3}{\mathrm{M}_1} + C\,\frac{\eta}{h_0} + \mathcal{O}\left(\frac{\eta^2}{h_0^2}\right),$$
$$\text{with } C = \frac{\overline{\mathrm{M}}_3}{\mathrm{M}_1}\left\{\varkappa\left[\frac{(\gamma-1)\,\mathrm{M}_2^2}{8+4\,(\gamma-1)\,\mathrm{M}_2^2\sin^2(\alpha+\theta)} - \frac{\gamma\mathrm{M}_2^2}{2\,(1-\gamma)+4\gamma\mathrm{M}_2^2\sin^2(\alpha+\theta)}\right] - \frac{(\tan\alpha+\tan\beta)\cos^2\alpha}{\tan\beta\,(1-1/\tan\alpha)-1}\right\} \tag{G.15}$$

G.5 Expansion of $\rho_3 u_3(1-u_3/u_1)/(\rho_1 u_1)$

To expand $\rho_3 u_3(1-u_3/u_1)/(\rho_1 u_1)$, let us first note that:

$$\frac{\rho_3 u_3}{\rho_1 u_1}\left(1 - \frac{u_3}{u_1}\right) = \frac{\mathrm{M}_3}{\mathrm{M}_1}\left(\sqrt{\frac{\rho_3 p_3}{\rho_1 p_1}} - \frac{\mathrm{M}_3 p_3}{\mathrm{M}_1 p_1}\right). \tag{G.16}$$

Using (G.9), (G.12) and (G.15), (G.16) becomes:

$$\frac{\rho_3 u_3}{\rho_1 u_1}\left(1 - \frac{u_3}{u_1}\right) = \left[\frac{\overline{\mathrm{M}}_3}{\mathrm{M}_1} + C\,q + \mathcal{O}(q^2)\right]\left\{\left[\left(\frac{\bar\rho_3}{\rho_1} + B\,q + \mathcal{O}(q^2)\right)\left(\frac{\bar p_3}{p_1} + A\,q + \mathcal{O}(q^2)\right)\right]^{\frac{1}{2}} - \left(\frac{\overline{\mathrm{M}}_3}{\mathrm{M}_1} + C\,q + \mathcal{O}(q^2)\right)\left(\frac{\bar p_3}{p_1} + A\,q + \mathcal{O}(q^2)\right)\right\}. \tag{G.17a}$$

Expanding the square root and the products inside the curly brackets leads to:

$$\frac{\rho_3 u_3}{\rho_1 u_1}\left(1 - \frac{u_3}{u_1}\right) = \left[\frac{\overline{\mathrm{M}}_3}{\mathrm{M}_1} + C\,q + \mathcal{O}(q^2)\right]\left\{\sqrt{\frac{\bar\rho_3\bar p_3}{\rho_1 p_1}} + \frac{1}{2}\sqrt{\frac{\rho_1 p_1}{\bar\rho_3\bar p_3}}\left(\frac{\bar\rho_3}{\rho_1}A + \frac{\bar p_3}{p_1}B\right) q - \frac{\overline{\mathrm{M}}_3\bar p_3}{\mathrm{M}_1 p_1} - \left(\frac{\overline{\mathrm{M}}_3}{\mathrm{M}_1}A + \frac{\bar p_3}{p_1}C\right) q + \mathcal{O}(q^2)\right\}. \tag{G.17b}$$

The last product is then expanded to give:

$$\begin{aligned}\frac{\rho_3 u_3}{\rho_1 u_1}\left(1-\frac{u_3}{u_1}\right) &= \frac{\overline{\mathrm{M}}_3}{\mathrm{M}_1}\left(\sqrt{\frac{\bar\rho_3\bar p_3}{\rho_1 p_1}}-\frac{\overline{\mathrm{M}}_3\bar p_3}{\mathrm{M}_1 p_1}\right)+\frac{\overline{\mathrm{M}}_3}{\mathrm{M}_1}\left\{\frac{1}{2}\sqrt{\frac{p_1\bar\rho_3}{\bar p_3\rho_1}}\,A+\frac{1}{2}\sqrt{\frac{\rho_1\bar p_3}{\bar\rho_3 p_1}}\,B\right.\\ &\quad\left.-\frac{\overline{\mathrm{M}}_3}{\mathrm{M}_1}A-\frac{\bar p_3}{p_1}C+\frac{\mathrm{M}_1}{\overline{\mathrm{M}}_3}C\left(\sqrt{\frac{\bar\rho_3\bar p_3}{\rho_1 p_1}}-\frac{\overline{\mathrm{M}}_3\bar p_3}{\mathrm{M}_1 p_1}\right)\right\}q\\ &\quad+\mathcal{O}(q^2).\end{aligned}\tag{G.17c}$$

The first term in (G.17c) is $\bar\rho_3\bar u_3(1-\bar u_3/u_1)/(\rho_1 u_1)$, so that:

$$\begin{aligned}\frac{\rho_3 u_3}{\rho_1 u_1}\left(1-\frac{u_3}{u_1}\right) &= \frac{\bar\rho_3\bar u_3}{\rho_1 u_1}\left(1-\frac{\bar u_3}{u_1}\right)+\frac{\overline{\mathrm{M}}_3}{\mathrm{M}_1}\left\{\left(\frac{1}{2}\sqrt{\frac{p_1\bar\rho_3}{\bar p_3\rho_1}}-\frac{\overline{\mathrm{M}}_3}{\mathrm{M}_1}\right)A+\frac{1}{2}\sqrt{\frac{\rho_1\bar p_3}{\bar\rho_3 p_1}}\,B\right.\\ &\quad\left.+C\left(\frac{\mathrm{M}_1}{\overline{\mathrm{M}}_3}\sqrt{\frac{\bar\rho_3\bar p_3}{\rho_1 p_1}}-2\frac{\bar p_3}{p_1}\right)\right\}q+\mathcal{O}(q^2).\end{aligned}\tag{G.17d}$$

Hence:

$$\begin{aligned}&\frac{\rho_3 u_3}{\rho_1 u_1}\left(1-\frac{u_3}{u_1}\right)=\frac{\bar\rho_3\bar u_3}{\rho_1 u_1}\left(1-\frac{\bar u_3}{u_1}\right)+D\,\frac{\eta}{h_0}+\mathcal{O}\left(\frac{\eta^2}{h_0^2}\right),\\ &\quad\text{with } D=\frac{\overline{\mathrm{M}}_3}{\mathrm{M}_1}\left\{\left(\frac{1}{2}\sqrt{\frac{p_1\bar\rho_3}{\bar p_3\rho_1}}-\frac{\overline{\mathrm{M}}_3}{\mathrm{M}_1}\right)A+\frac{1}{2}\sqrt{\frac{\rho_1\bar p_3}{\bar\rho_3 p_1}}\,B+\left(\frac{\mathrm{M}_1}{\overline{\mathrm{M}}_3}\sqrt{\frac{\bar\rho_3\bar p_3}{\rho_1 p_1}}-2\frac{\bar p_3}{p_1}\right)C\right\},\end{aligned}\tag{G.18}$$

where A, B and C are defined in (G.9), (G.12) and (G.15).

Bibliography

Ackeret, J., Feldmann, F., and Rott, N. (1947). *Investigations of compression shocks and boundary layers in gases moving at high speed*. NACA TM 1113.

Adams, N. A. (1997). DNS of shock boundary-layer interaction – Preliminary results for compression ramp flow. CTR Annual Research Briefs 1997, Center for Turbulence Research, Stanford University and NASA Ames Research Center, Stanford, California.

Adams, N. A. (2000). Direct simulation of the turbulent boundary layer along a compression ramp at $M = 3$ and $\mathrm{Re}_\theta = 1685$. *J. Fluid Mech.*, 420:47–83.

Adamson, Jr, T. C. and Messiter, A. F. (1980). Analysis of two-dimensional interactions between shock waves and boundary layers. *Ann. Rev. Fluid Mech.*, 12:103–138.

Anderson, Jr, J. D. (1990). *Modern compressible flow: with historical perspective*. McGraw Hill, New York, NY.

Andreopoulos, J. and Muck, K. C. (1987). Some new aspects of the shock wave/boundary layer interaction in compression ramp flows. *J. Fluid Mech.*, 180:405–428.

Beresh, S. J., Clemens, N. T., and Dolling, D. S. (2002). Relationship between upstream turbulent boundary-layer velocity fluctuations and separation shock unsteadiness. *AIAA Journal*, 40(12).

Berselli, L. C., Iliescu, T., and Layton, W. J. (2005). *Mathematics of large eddy simulation of turbulent flows*. Springer–Verlag New York, LLC, first edition.

Boin, J.-P. and Robinet, J.-C. (2004). Three-dimensional unsteady laminar shock-wave/boundary layer interaction. NATO RTO-AVT-111 10–1/10–10.

Boin, J.-P., Robinet, J.-C., Corre, C., and Deniau, H. (2006). 3D steady and unsteady bifurcations in shock-wave/laminar boundary layer interaction: a numerical study. *Theor. Comput. Fluid Dyn.*, 20(3).

Borodai, S. G. and Moser, R. D. (2001). The numerical decomposition of turbulent fluctuations in a compressible boundary layer. *Theoret. Comput. Fluid Dynamcis*, 15(1):35–63.

Carpenter, M. H., Nordstrom, J., and Gottlieb, D. (1998). A stable and conservative interface treatment of arbitrary spatial accuracy. NASA/CR-1998-206921, February 1998.

Chan, S. C. (1994). *Planar laser scattering imaging of shock wave turbulent boundary layer interactions*. PhD thesis, Dept. of Aerospace Engineering and Engineering Mechanics, University of Texas at Austin.

Chapman, D. R., Kuehn, D. M., and Larson, H. K. (1958). Investigation of separated flows in supersonic and subsonic streams with emphasis on the effect of transition. *NACA Rept. 1356*.

Coleman, G. N., Kim, J., and Moser, R. D. (1995). A numerical study of turbulent supersonic isothermal-wall channel flow. *J. Fluid Mech.*, 305:159–183.

Crouch, J. D., Garbaruk, A., and Magidov, D. (2007). Predicting the onset of flow unsteadiness based on global instability. *Journal of Computational Physics*, 224:924–940.

Culick, F. E. C. and Rogers, T. (1983). The response of normal shocks in diffusers. *AIAA Journal*, 21(10).

Dallmann, U. (1988). Three-dimensional vortex structures and vorticity topology. *Fluid Dynamics Research*, pages 183–189.

Dennis, D. J. C. and Nickels, T. B. (2008). On the limitations of Taylor's hypothesis in constructing long structures in a turbulent boundary layer. *J. Fluid Mech.*, 614:197–206.

di Mare, L., Klein, M., Jones, W. P., and Janicka, J. (2006). Synthetic turbulence inflow conditions for large-eddy simulation. *Physics of Fluids*, 18(2).

Doligalski, T. L., Smith, C. R., and Walker, D. A. (1994). Vortex interactions with walls. *Annu. Rev. Fluid Mech.*, 26:573–616.

Dolling, D. S. (2001). Fifty years of shock-wave/boundary-layer interaction research: what next? *AIAA Journal*, 39(8).

Donaldson, C. P. (1944). *Effects of interaction between normal shock waves and boundary layer*. NACA CB 4A27.

Ducros, F., Ferrand, V., Nicoud, F., Weber, C., Darracq, D., Gacherieu, C., and Poinsot, T. (1999). Large-eddy simulation of the shock/turbulence interaction. *Journal of Computational Physics*, 152:517–549.

Dupont, P., Haddad, C., and Debiève, J. F. (2006). Space and time organization in a shock-induced separated boundary layer. *J. Fluid Mech.*, 559:255–277.

Dupont, P., Piponniau, S., Sidorenko, A., and Debiève, J. F. (2008). Investigation by particle image velocimetry measurements of oblique shock reflection with separation. *AIAA Journal*, 46(6).

Dupont, P., Piponniau, S., Sidorenko, A., and Debiève, J.-F. (January 2007). Investigation of an oblique shock reflection with separation by PIV measurements. 45$^{\text{th}}$ *AIAA Aerospace Sciences Meeting and Exhibit*.

Dussauge, J.-P. (2001). Compressible turbulence and energetic scales: what is known from experiments in supersonic flows? *Flow, Turbulence and Combustion*, 66(4):373–391.

Dussauge, J.-P., Dupont, P., and Debiève, J.-F. (2006). Unsteadiness in shock wave boundary layer interaction with separation. *Aerospace Science and Technology*, 10:85–91.

Dussauge, J.-P. and Piponniau, S. (2008). Shock/boundary-layer interactions: possible sources of unsteadiness. *Journal of Fluids and Structures*, 24:1166–1175.

Eckert, E. R. G. (1955). Engineering relations for friction and heat transfer to surfaces in high velocity flow. *Journal of the Aeronautical Sciences*, 22(8):585–587.

Edwards, J. R. (2008). Numerical simulations of shock/boundary layer interactions using time-dependent modeling techniques: a survey of recent results. *Progress in Aerospace Sciences*, 44:447–465.

Edwards, J. R., Choi, J., and Boles, J. A. (2008). Large-eddy/Reynolds-averaged navier–stokes simulation of a Mach 5 compression-corner interaction. *AIAA Journal*, 46(4).

Erengil, M. E. and Dolling, D. S. (1993). Physical causes of separation shock unsteadiness in shock-wave/turbulent boundary layer interactions. *AIAA Paper 93–3134*.

Erlebacher, G., Hussaini, M. Y., Speziale, C. G., and Zang, T. A. (1992). Toward the large-eddy simulation of compressible turbulent flows. *J. Fluid Mech.*, 238(1):155–185.

Fage, A. and Sargent, R. F. (1947). Shock wave and boundary layer phenomena near a flat surface. *Proceedings of the Royal Society of London, Series A: Mathematical and Physical Sciences*, 190(1020):1–20.

Ferri, A. (1940). *Experimental results with airfoils tested in the high speed tunnel at Guidonia*. NACA TM 946 (translation).

Ganapathisubramani, B., Clemens, N. T., and Dolling, D. S. (2007a). Effect of upstream coherent structures on low-frequency motion of shock-induced turbulent separation. In 45st *Aerospace Sciences Meenting and Exhibit*, number AIAA paper 2007–1141.

Ganapathisubramani, B., Clemens, N. T., and Dolling, D. S. (2007b). Effects of upstream boundary layer on the unsteadiness of shock-induced separation. *J. Fluid Mech.*, 585:369–394.

Ganapathisubramani, B., Clemens, N. T., and Dolling, D. S. (2009). Low-frequency dynamics of shock-induced separation in a compression ramp interaction. *J. Fluid Mech.*, 585:397–425.

Garnier, E. (2009). Stimulated detached eddy simulation of three-dimensional shock-/boundary layer interaction. *Shock Waves*, 19(6):479–486.

Garnier, E., Sagaut, P., and Deville, M. (2002). Large eddy simulation of shock/boundary-layer interaction. *AIAA Journal*, 40(10).

Gaster, M., Kit, E., and Wygnanski, I. (1985). Large-scale structures in a forced turbulent mixing layer. *J. Fluid Mech.*, 150:23–39.

Germano, M., Piomelli, U., Moin, P., and Cabot, W. H. (1991a). A dynamic subgrid-scale eddy viscosity model. *Physics of Fluids*, 3(7):1760–1765.

Germano, M., Piomelli, U., Moin, P., and Cabot, W. H. (1991b). Erratum: a dynamic subgrid-scale eddy viscosity model. *Physics of Fluids*, 3(12):3128–3128.

Gerritsen, M. and Olsson, P. (1996). Designing an efficient solution strategy for fluid flows: 1. A stable high order finite difference scheme and sharp shock resolution for the Euler equations. *Journal of Computational Physics*, 129:245–262.

Gerritsen, M. and Olsson, P. (1998). Designing an efficient solution strategy for fluid flows: II. Stable high-order central finite difference scheme on composite adaptive grids and sharp shock resolution. *Journal of Computational Physics*, 147:293–317.

Gramann, R. A. (1989). *Dynamics of separation and reattachment in a Mach 5 unswept compression ramp flow*. PhD thesis, Dept. of Aerospace Engineering and Engineering Machanics, University of Texas at Austin.

Guarini, S. E., Moser, R. D., Shariff, K., and Wray, A. (2000). Direct numerical simulation of a supersonic turbulent boundary layer at Mach 2.5. *J. Fluid Mech.*, 414:1–33.

Holder, D. W., Pearcey, H. H., and Gadd, G. E. (1954). The interaction between shock wave and boundary layers. *British Aeronautical Research Council Current Paper*, 180.

Hou, Y. X., Clemens, N. T., and Dolling, D. S. (2003). Wide-field PIV study of shock-induced turbulent boundary layer separation. In 41st *Aerospace Sciences Meenting and Exhibit*, number AIAA paper 2003–0441.

Huang, P. G., Coleman, G. N., and Bradshaw, P. (1995). Compressible turbulent channel flows: DNS results and modelling. *J. Fluid Mech.*, 305:185–218.

Hudy, L. M., Naguib, A. M., and Humphreys, Jr, W. M. (2003). Wall-pressure measurements beneath a separating/reattaching flow region. *Physics of Fluids*, 15(3).

Humble, R. A., Elsinga, G. E., Scarana, F., Ringuette, M. J., and van Oudheusden, B. W. (2009). Three-dimensional instantaneous structure of a shock wave/turbulent boundary layer interaction. *J. Fluid Mech.*, 622:33–62.

Hunt, D. and Nixon, D. (1995). Very large eddy simulation of an unsteady shock-wave/turbulent boundary-layer interactions. *AIAA Paper 95–2212*.

Inagaki, M., Kondoh, T., and Nagano, Y. (January 2005). A mixed-time-scale SGS model with fixed model-parameters for practical LES. *Journal of Fluids Engineering*, 127:1–13.

Jacquin, L., Cambon, C., and Blin, E. (1993). Turbulence amplification by a shock wave and rapid distortion theory. *Physics of Fluids*, 5(10):2539–2550.

Jarrin, N., Benhamadouche, S., Laurence, D., and R., P. (2006). A synthetic-eddy-method for generating inflow conditions for large-eddy simulations. *Heat and Fluid Flow*, 27:585–593.

Johansson, P. S. and Andersson, H. I. (2004). Generation of inflow data for inhomogeneous turbulence. *Theor. Comput. Fluid Dynamics*, 18(5):371–389.

Jones, L. E. (2008). *Numerical study of the flow around an airfoil at low Reynolds number*. PhD thesis, School of Engineering Sciences, University of Southampton.

Katzer, E. (1989). On the lengthscales of laminar shock/boundary-layer interaction. *J. Fluid Mech.*, 206:477–496.

Keating, A., Piomelli, U., Balaras, E., and Kaltenbach, H.-J. (2004). *A priori* and *a posteriori* tests of inflow conditions for large-eddy simulation. *Physics of Fluids*, 16(12).

Kempf, A., Klein, M., and Janicka, J. (2005). Efficient generation of initial- and inflow-conditions for transient turbulent flows in arbitrary geometries. *Flow, Turbulence and Combustion*, 74(1):67–84.

Kistler, A. L. (1964). Fluctuating wall pressure under a separated supersonic flow. *Journal of the Acoustical Society of America*, 36(3):543–550.

Klein, M., Sadiki, A., and Janicka, J. (2003). A digital filter based generation of inflow data for spatially developing direct numerical or large eddy simulations. *Journal of Computational Physics*, 186:652–665.

Knight, D. D. and Degrez, G. (Dec. 1998). Shock wave boundary layer interactions in high Mach number flows. a critical survey of current numerical prediction capabilities. *Advisory Rept. 319, AGARD*, 2:1.1–1.35.

Kornev, N. and Hassel, E. (2007). Method of random spots for generation of synthetic inhomogeneous turbulent fields with prescribed autocorrelations functions. *Commun. Numer. Meth. Engng*, 23(1):35–43.

Lee, S., Lele, S., and Moin, P. (1992). Simulation of spatially evolving compressible turbulence and application of Taylor's hypothesis in compressible flow. *Physics of Fluids*, pages 1521–1530.

Lee, S., Lele, S. K., and Moin, P. (1997). Interaction of isotropic turbulence with shock waves: effect of shock strength. *J. Fluid Mech.*, 340:225–247.

Lele, S. K. (1994). Compressibility effects on turbulence. *Annu. Rev. Fluid Mech.*, 26:211–54.

Li, D. (2007). Shock reflection and oblique shock waves. *Journal of Mathematical Physics*, 48(12).

Li, Q. (2003). *Numerical study of Mach number effects in compressible wall-bounded turbulence*. PhD thesis, School of Engineering Sciences, University of Southampton.

Liepmann, H. W. (1946). The interaction between boundary layer and shock wave in transonic flow. *Journal of Aerospace Sciences*, 13:623–638.

Lighthill, M. J. (1953). On boundary layers and upstream influence II. Supersonic flows without separation. *Proceedings of the Royal Society of London. Series A, Mathematical and Physical Sciences*, 217(1131):478–507.

Loginov, M. S., Adams, N. A., and Zheltovodov, A. A. (2006). Large eddy simulation of shock-wave/turbulent-boundary-layer interaction. *J. Fluid Mech.*, 565:135–169.

Lund, T. S., Wu, X., and Squires, K. D. (1998). Generation of turbulent inflow data for spatially-developing boundary layer simulations. *Journal of Computational Physics*, 140:233–258.

Mahesh, K., Lele, S. K., and Moin, P. (1997). The influence of entropy fluctuations on the interaction of turbulence with a shock wave. *J. Fluid Mech.*, 334:353–379.

Martin, M. P. (2007). Direct numerical simulation of hypersonic turbulent boundary layers. Part 1. Initialization and comparison with experiments. *J. Fluid Mech.*, 570:347–364.

Matsumoto, M. and Nishimura, T. (1998). Mersenne twister: a 623-dimensionally equidistributed uniform pseudorandom number generator. *ACM Trans. on Modeling and Computer Simulation*, 8(1):3–30.

McClure, W. B. (1992). *An experimental study of the driving mechanism and control of the unsteady shock induced turbulent separation in a Mach 5 compression corner flow.* PhD thesis, Dept. of Aerospace Engineering and Engineering Machanics, University of Texas at Austin.

McKenzie, J. F. and Westphal, K. O. (1968). Interaction of linear waves with oblique shock waves. *Physics of Fluids*, 11(11):2350–2362.

Moin, P., Squires, K., Cabot, W., and Lee, S. (1991). A ynamic subgrid-scale model for compressible turbulence and scalar transport. *Physics of Fluids*, 3(11):2746–2757.

Neiland, V. Y. (1971). Flow behind the boundary layer separation point in a supersonic stream. *Fluid Dynamics*, 6(3):378–384.

Pagella, A., Babucke, A., and Rist, U. (2004). Two-dimensional numerical investigations of small-amplitude disturbances in a boundary layer at $Ma = 4.8$: Compression corner versus impinging shock wave. *Physics of Fluids*, 16(7).

Pagella, A. and Rist, U. (2003). Direct numerical simulation of shock-boundary layer interaction at $Ma = 6$. from the Internet.

Pasha, A. A. and Sinha, K. (2008). Shock-unsteadiness model applied to oblique shock wave/turbulent boundary-layer interaction. *International Journal of Computational Fluid Dynamics*, 22(8):569–582.

Peridier, V. J., Smith, F. T., and Walker, J. D. A. (1991a). Vortex-induced boundary-layer separation. Part 1. The unsteady limit problem $\mathrm{Re} \rightarrow \infty$. *J. Fluid Mech.*, 232:99–131.

Peridier, V. J., Smith, F. T., and Walker, J. D. A. (1991b). Vortex-induced boundary-layer separation. Part 2. Unsteady interacting boundary-layer theory. *J. Fluid Mech.*, 232:133–165.

Piponniau, S., Dussauge, J.-P., Debiève, J.-F., and Dupont, P. (2009). A simple model for low-frequency unsteadiness in shock-induced separation. *J. Fluid Mech.*, 629:87–108.

Pirozzoli, S., Beer, A., Bernardini, M., and Grasso, F. (2009). Computational analysis of impinging shock-wave boundary layer interaction under conditions of incipient separation. *Shock Waves*, 19(6):487–497.

Pirozzoli, S. and Grasso, F. (2006). Direct numerical simulation of impinging shock wave/turbulent boundary layer interaction at $M = 2.25$. *Physics of Fluids*, 18(6).

Plotkin, K. J. (1975). Shock wave oscillation driven by turbulent boundary-layer fluctuations. *AIAA Journal 1036–1040*, 13(8).

Poggie, J. and Smits, A. J. (2001). Shock unsteadiness in a reattaching shear layer. *J. Fluid Mech.*, 429:155–185.

Poggie, J. and Smits, A. J. (2005). Experimental evidence for plotkin model of shock unsteadiness in separated flow. *Physics of Fluids*, 17(1).

Polivanov, P. A., Sidorenko, A. A., and Maslov, A. A. (2009). Experimental study of unsteady effects in shock wave/turbulent boundary layer interaction. In 47^{th} *AIAA Aerospace Sciences Meeting*, Orlando, Florida, USA.

Priebe, S., Wu, M., and Martin, M. P. (2009). Direct numerical simulation of a reflected-shock-wave/turbulent-boundary-layer interaction. *AIAA Journal*, 47(5):1174–1185.

Ringuette, M. J., Wu, M., and Martin, M. P. (2008). Coherent structures in direct numerical simulation of turbulent boundary layers at Mach 3. *J. Fluid Mech.*, 594:59–69.

Risken, H. (1989). *The Fokker–Plank equation*. Springer–Verlag, Second edition.

Robinet, J.-C. (1999). *Stabilité linéaire d'un écoulement présentant une onde de choc*. PhD thesis, (Thèse de Doctorat), École Nat. Sup. de l'Aéronautique et de l'Espace.

Robinet, J.-C. (2007). Bifurcations in shock-wave/laminar-boundary-layer interaction: global instability approach. *J. Fluid Mech.*, 579:85–112.

Robinet, J.-C. (Juin 2001). Étude des instabilités dans une couche limite décollée incompressible et compressible et réponse de choc oblique à une perturbation. Rapport de Post Doctorat, Groupe Supersonique, IUSTI, Marseille.

Robinet, J.-C. and Casalis, G. (2001). Critical interaction of a shock wave with an acoustic wave. *Physics of Fluids*, 13(4).

Sagaut, P. (2005). *Large eddy simulations for incompressible flows*. Springer–Verlag New York, LLC, third edition.

Sagaut, P., Garnier, E., Tromeur, E., Larchevêque, L., and Labourasse, E. (2004). Turbulence inflow conditions for large-eddy simulation of compressible wall-bounded flows. *AIAA Journal*, 42(3).

Sandham, N. D. (1991). An alternative formulation of the outer law of the turbulent boundary layer. *DLR report*.

Sandham, N. D., Li, Q., and Yee, H. C. (2002). Entropy splitting for high-order numerical simulation of compressible turbulence. *Journal of Computational Physics*, 178:307–322.

Sandham, N. D., Yao, Y. F., and Lawal, A. A. (2003). Large-eddy simulation of transonic turbulent flow over a bump. *International Journal of Heat and Fluid Flow*, 24:584–595.

Sandhu, H. S. and Sandham, N. D. (1994). Boundary conditions for spatially growing compressible shear layers. Technical Report QMW-EP-1100, Queen Mary University of London, 1994.

Settles, G. S. and Dodson, L. J. (1991). Hypersonic shock/boundary layer database. *NASA CR 177577*.

Simone, A., Coleman, G. N., and Cambon, C. (1997). The effect of compressibility on turbulent shear flow: a rapid-distortion-theory and direct-numerical-simulation study. *J. Fluid Mech.*, 330:307–338.

Smirnov, A., Shi, S., and Celik, I. (2001). Randon flow generation technique for large eddy simulations and particle-dynamics modeling. *Journal of Fluids Engineering*, 123:359–371.

Souverein, L. J., Dupont, P., Debiève, J.-F., Dussauge, J.-P., van Oudheusden, B. W., and Scarano, F. (2009a). Effect of interaction strength on the unsteady behavior of shock wave boundary layer interactions. In 39$^{\text{th}}$ *Fluid Dynamics Conference and Exhibit*, San Antonio, Texas, USA.

Souverein, L. J., van Oudheusden, B. W., Scarano, F., and Dupont, P. (2008). Unsteadiness characterization in a shock wave turbulent boundary layer interaction through dual-PIV. In 38$^{\text{th}}$ *Fluid Dynamics Conference and Exhibit*, Seattle, Washington, USA.

Souverein, L. J., van Oudheusden, B. W., Scarano, F., and Dupont, P. (2009b). Application of a dual-plane particle image velocimetry (dual-PIV) technique for the unsteadiness characterization of a shock wave turbulent boundary layer interaction. *Measurement Science and Technology*, 20(7).

Spalart, P. R. (1988). Direct simulation of a turbulent boundary layer up to $\mathrm{Re}_\theta = 1410$. *J. Fluid Mech.*, 187.

Spalding, D. B. (1961). A single formula for the 'law of the wall'. *J. Appl. Mech.*, 28:455–458.

Stewartson, K. and Williams, P. G. (1969). Self-induced Separation. *Proceedings of the Royal Society of London. Series A, Mathematical and Physical Sciences*, 312:181–206.

Stewartson, K. and Williams, P. G. (1973). Self-induced separation II. *Mathematika*, 20:98–108.

Teramoto, S. (2005). Large eddy simulation of transitional boundary layer with impinging shock wave. *AIAA Journal*, 43(11).

Theofilis, V., Hein, S., and Dallman, U. (2000). On the origins of unsteadiness and three-dimensionality in a laminar separation bubble. *Proceedings of the Royal Society of London. Series A, Mathematical and Physical Sciences*, 358(1777):3229–3246.

Thivet, F., Knight, D. D., Zheltovodov, A. A., and Maksimov, A. I. (2000). Some insights in turbulence modeling for crossing-shock-wave/boundary-layer interactions. *AIAA Paper 2000–131.*

Thomas, F. O., Putnam, C. M., and Chu, H. C. (1994). On the mechanism of unsteady shock wave/turbulent boundary layer interactions. *Experiments in Fluids*, 18(1/2):69–81.

Thompson, K. W. (1987). Time dependent boundary conditions for hyperbolic systems. *Journal of Computational Physics*, 68(1):1–24.

Touber, E. and Sandham, N. D. (2008a). Large-eddy simulations of an oblique shock impinging on a turbulent boundary layer: low-frequency mechanisms. In 18^{th} *International Shock Interaction Symposium*, Rouen, France.

Touber, E. and Sandham, N. D. (2008b). Oblique shock impinging on a turbulent boundary layer: low-frequency mechanisms. In 38^{th} *Fluid Dynamics Conference and Exhibit*, number AIAA paper 2008–4170.

Touber, E. and Sandham, N. D. (2009a). Comparison of three large-eddy simulations of shock-induced turbulent separation bubbles. *Shock Waves*, 19(6):469–478.

Touber, E. and Sandham, N. D. (2009b). Large-eddy simulation of low-frequency unsteadiness in a turbulent shock-induced separation bubble. *Theor. Comput. Fluid Dyn.*, 23:79–107.

Touber, E. and Sandham, N. D. (2009c). Large-eddy simulations of an oblique shock impinging on a turbulent boundary layer: effect of the spanwise confinement on the low-frequency oscillations. In 2nd *International Conference on Turbulence and Interactions*, Sainte–Luce, Martinique.

Touber, E. and Sandham, N. D. (2009d). Low-order stochastic modelling of low-frequency motions in reflected shock-wave/boundary-layer interactions. Submitted to the Journal of Fluid Mechanics.

Turcat, A. (2003). *Concorde. Essais d'hier, batailles d'aujourd'hui*. Le Cherche midi éditeur.

Ünalmis, O. H. and Dolling, D. S. (1994). Decay of wall pressure field and structure of a Mach 5 adiabatic turbulent boundary layer. *AIAA Paper 94–2363*.

Urbin, G. and Knight, D. (2001). Large-eddy simulation of a supersonic boundary layer using an unstructured grid. *AIAA Journal*, 39(7):1288–1295.

van Driest, E. R. (1956). On turbulent flow near a wall. *AIAA Journal Special Supplement: Centennial of Powered Flight*, 23(11):1007–1011.

Veloudis, I., Yang, Z., McGuirk, J. J., Page, G. J., and Spencer, A. (2007). Novel implementation and assessment of a digital filter based approach for the generation of LES inlet conditions. *Flow, Turbulence and Combustion*, 79(1):1–24.

Vreman, B. (1995). *Direct and large-eddy simulation of the compressible turbulent mixing layer*. PhD thesis, Department of Applied Mathematics, University of Twente.

Vreman, B., Geurts, B., and Kuerten, H. (July 1995). A priori tests of large eddy simulation of the compressible plane mixing layer. *J. Eng. Math.*, 29(4):299–327.

White, F. M. (1991). *Viscous fluid flow*. McGraw-Hill, Second edition.

Wu, M. and Martin, M. P. (2007). Direct numerical simulation of supersonic turbulent boundary layer over a compression ramp. *AIAA Journal*, 45(4).

Wu, M. and Martin, M. P. (2008a). Analysis of shock motion in shockwave and turbulent boundary layer interaction using direct numerical simulation data. *J. Fluid Mech.*, 594:71–83.

Wu, M. and Martin, M. P. (2008b). Analysis of shock motion in shockwave and turbulent boundary layer interaction using direct numerical simulation data. *J. Fluid Mech.*, 594:71–83.

Wu, P. and Miles, R. B. (2000). Mega hertz rate vizualization of separation shock-wave structure. *AIAA Paper 2000–647*.

Xie, Z. T. and Castro, I. P. (2008). Efficient generation of inflow conditions for large-eddy simulation of street-scale flows. *Flow, Turbulence and Combustion*, 81(3):449–470.

Yao, Y. F. and Sandham, N. D. (Spain, 2002). DNS of turbulent flow over a bump with shock/boundary-layer interactions. 5^{th} *Int. Symp. on Eng. Tur. Modelling and Measurements*.

Yee, H. C., Sandham, N. D., and Djomehri, M. J. (1999). Low-dissipative high-order shock-capturing methods using characteristic-based filters. *Journal of Computational Physics*, 150:199–238.